Search for Physics Beyond the Standard Model in the Trilepton Signature in pbar-p collisions at sqrt s = 1.96 TeV with CDF II

by

Marcelo A. Vogel

B.S., University of Chile, 2000
B.S., Physics, University of New Mexico, 1991

DISSERTATION

Submitted in Partial Fulfillment of the
Requirements for the Degree of

Doctor of Philosophy
Physics

The University of New Mexico

Albuquerque, New Mexico

May, 2012

Search for Physics Beyond the Standard Model in the Trilepton Signature in pbar-p collisions at sqrt s = 1.96 TeV with CDF II

by

Marcelo A. Vogel

B.S., University of Chile, 2000
B.S., Physics, University of New Mexico, 1991

Ph.D., Physics, University of New Mexico, 2012

Abstract

The standard model (SM) of particles and fields is a theory that has proven very accurate in the currently accessible collider energies. Nonetheless, the SM is theoretically incomplete in the sense that it leaves many questions and problems unanswered, for example, the origin of electroweak symmetry breaking (EWSB). The Higgs boson is introduced to the SM to provide a mechanism for electroweak symmetry breaking and masses to quarks and leptons. However, the introduction of the Higgs mechanism has the undesirable effect of introducing the hierarchy problem which is characterized by quadratically divergent contributions to the Higgs mass squared. Supersymmetry (SUSY) has been postulated as a way to solve the problem of the fine-tuning of the Higgs self-interactions, and additionally to provide a possible mechanism for EWSB. The golden search channel for mSUGRA is the $\chi^{\pm}{}_1\chi^0_2 \to 3\ell$ (three leptons)

channel. It offers a reasonable signal $\sigma \times BR$ with very small contributions from Standard Model backgrounds. This thesis, presents a search for chargino-neutralino production within the mSUGRA framework.

Contents

List of Figures

List of Tables

Chapter 1

Introduction

The standard model (SM) of particles and fields is a theory that has proven very accurate in the currently accessible collider energies. To this date, experimental results have confirmed many features of the theory to a high degree of precision, e.g., the predicted mass of the W boson. The current experimental frontier has advanced into the TeV range with no unambiguous hints of additional structure. Nonetheless, the SM is theoretically incomplete in the sense that it leaves many questions and problems unanswered, for example, the origin of electroweak symmetry breaking (EWSB). The Higgs boson is introduced to the SM to provide a mechanism for electroweak symmetry breaking and masses to quarks and leptons. However, the introduction of the Higgs mechanism has the undesirable effect of introducing the hierarchy problem which is characterized by quadratically divergent contributions to the Higgs mass squared. Supersymmetry (SUSY) has been postulated as a way to solve the problem of the fine-tuning of the Higgs self-interactions, and additionally to provide a possible mechanism for EWSB. Supersymmetry postulates that for every SM boson there exists a corresponding supersymmetric fermion with the same internal quantum numbers, except for spin which differs by 1/2, and vice-versa for SM fermions. That is, for each SM degree of freedom, there is a corresponding

SUSY degree of freedom. A new quantum number, called R-parity (R_p [119]), is introduced to avoid conflict with measured limits on the proton's lifetime. All SM particles have $R_p = +1$ and sparticles have $R_p = -1$. In an unbroken supersymmetry, standard model particles and their supersymmetric partners would share the same mass. The fact that no superpartners have been detected so far implies that, if SUSY is a symmetry of nature, it must be a broken symmetry with heavier superpartners than their SM counterparts. The minimal supersymmetric standard model (MSSM) respects the same $SU(3)\otimes SU(2)\otimes U(1)$ gauge symmetries as the SM, and it increases the number of free parameters in the theory to over 100. Various models have been postulated which provide a different mechanism for SUSY breaking, for example, in Supergravity (SUGRA), the force of gravity communicates the origins of SUSY breaking from a high mass scale to the electroweak scale. In a particular SUGRA model, the so-called minimal SUGRA model (mSUGRA [120]), grand unification is presumed at a high mass scale ($\simeq 10^{16}$ GeV) and the MSSM spectrum can be fully characterized by 4 parameters and a sign at the grand unification theory (GUT) scale [121]: a common scalar mass (m_0), a common gaugino mass ($m_{\frac{1}{2}}$), a common trilinear coupling value (A_0), the ratio of the vacuum expectation values of the two Higgs doublets ($\tan\beta$), and the sign of μ, where μ is the Higgsino mass parameter.

Events with multiple, isolated leptons are predicted in many models of physics beyond the Standard Model. In many of these models the leptons are predicted to be produced with low p_T. For example, trilepton events ($ee+\ell$ or $\mu\mu+\ell$, where $\ell = e$, μ or τ) are a promising signature for supersymmetric chargino-neutralino production in SUGRA models [122]. The "golden" search channel for mSUGRA is the $\chi^{\pm}{}_1\chi^0_2 \rightarrow 3\ell$ (three leptons) channel. It offers a reasonable signal $\sigma \times BR$ with very small contributions from Standard Model backgrounds. This thesis, presents a search for chargino-neutralino production within the mSUGRA framework. Nevertheless, the kinematic characteristics of the expected supersymmetric signal were kept as generic as possible, as opposed to model-constrained, in order to optimize the discovery

potential of the analysis. The results were ultimately interpreted in the context of the most attractive and promising regions of mSUGRA parameter space.

Chapter 2

Theoretical Framework

The present chapter describes the popular theoretical framework that motivates this thesis. It contains a brief introduction to the SM, and one of its most famous extensions, the Minimal Supersymmetric extension of the Standard Model (MSSM). We also discuss the resulting MSSM event signatures searched for in this thesis.

2.1 The Standard Model

The currently accepted, experimentally accurate, model of the fundamental constituents and interactions of matter is called the "The Standard Model of Particles and Fields," or simply, SM. The SM is a theory that has proven very accurate in the currently accessible low energy spectrum and which describes many experimental results to an unprecedented level of precision [1]. A complete description of the theory can be easily found in the scientific literature [2, 3]. Its two major components Quantum Chromodynamics (QCD) [4] and the electroweak theory of Weinberg, Salam, and Glashow [5] describe the interactions of fundamental particles. The production cross sections and the decay branching ratios for the various interactions are accu-

rately predicted. However, despite its many successes, important questions remain unanswered about the Standard Model. Among these, the so-called *hierarchy problem* serves as the motivation for one of the most popular beyond the Standard Model frameworks which is the main topic of this thesis.

2.1.1 Introduction to SM particles and interactions

In order to motivate the discussion leading to the introduction of beyond the standard model physics, a brief introduction to the SM is given here. For a detailed description the reader is refered to Gaillard et al. [1].

In the Standard Model of the electromagnetic, weak and strong interaction the fundamental particles are categorized into three groups; leptons, quarks and gauge bosons [1]. There are three known forces governing the interactions of matter at low energies: strong, electromagnetic and weak (Figure 2.1). The fourth force of nature, the gravitational interaction, is negligible for particles at the electroweak energy scale and it is currently not a part of the SM. The properties of all four forces are shown in Table 2.1. The strength by which particles couple to fields is called the coupling constant. The SM is a quantum field theory based on the symmetry

Interaction	Mediator	Coupling Constant	Range (m)
Strong	gluon	≤ 1	$\leq 10^{-15}$
Electromagnetic	γ	$1/137$	∞
Weak	$W^{\pm}, Z^0$	10^{-6}	10^{-18}
Gravitational	graviton	10^{-40}	∞

Table 2.1: Fundamental interactions. The particle acting as a mediator, the coupling constant and the range of the interaction are also shown.

group $SU(3)_c \otimes SU(2)_L \otimes U(1)_Y$. Interactions arise by requiring invariance under the gauge transformations described by the generators of each group. The $SU(3)_c$

symmetry group describes the strong interaction while $SU(2)_L \otimes U(1)_Y$ describes the electroweak interaction, which is spontaneously broken to $U(1)_{EM}$ by the Higgs mechanism [6] [7]. The strong interaction is mediated by gluons and binds quarks in

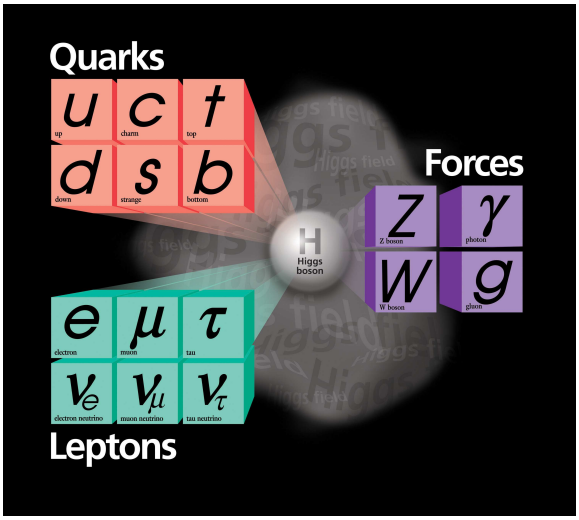

Figure 2.1: Elementary particles in the Standard Model. (Image courtesy of Fermilab Visual Media Services)

neutrons, protons and other hadrons. Furthermore, protons and neutrons are bound in atomic nuclei also through the action of the strong force. The source of the mass of hadrons is the binding energy in the field of the strong force ("sea" of virtual quarks and gluons), and not the Higgs mechanism.

The electromagnetic interaction is mediated by photons between particles possessing electric charge. The weak interaction is mediated by three gauge bosons, $W^{\pm}$ and Z^0, and it interacts with all known particles with the exception of gluons. The weak interaction is manifested, for example, in the decay of free neutrons with a mean lifetime of about 882 seconds. The force with the weakest strength is the gravitational interaction with a coupling strength about 40 orders of magnitude that of the strong interaction. Its effects are only apparent when large masses are involved,

such as astronomical objects, and at energies near the Planck scale $\sim 10^{19}$ GeV/c^2.

The fundamental particles of the standard model fall into two groups: boson and fermions. Bosons are particles that obey Bose-Einstein statistics with wave functions that are symmetric under the exchange of two particles. Fermion are particles that obey Fermi-Dirac statistics with wave functions that are anti-symmetric under the exchange of two particles. The spin-statistics theorem relates the intrinsic angular momentum of particles with the type of statistics they obey. Fermions have half-integer spin while bosons have integer spin.

The Standard Model recognizes two types of elementary spin 1/2 fermions: quarks and leptons. While quarks can interact via the strong, electromagnetic and weak interaction, leptons only feel the electromagnetic and the weak interaction.

Quarks and leptons

Quarks are spin 1/2 particles and have a fraction of the electric charge of the electron. There are six known quarks in nature arranged in three families or generations. Their names from first to last generation are: up (u) and down (d), charm(c) and strange (s), and top (t) and bottom (b). The last four quarks are unstable particles that decay into the lighter quarks. Each generation consists of a doublet of particles that share all the gauge quantum numbers. The different generations or families differ only by mass as a result of their different couplings to the Higgs field.

Quarks form stable and semi-stable bound states with integer total charge called hadrons, which can be divided into baryons and mesons according to the number of quarks in them. Mesons are composed of a quark-antiquark pair while baryons contain three quarks. Besides mass, electric charge, and spin, quarks have another intrinsic property unique to them called color charge. It is possible to distinguish three types of color through the strong interaction, red (R), blue (B) and green (G),

with the strong force resulting from the exchange of color charge in the form of 8 colored gluons.

Leptons are colorless, spin 1/2 particles. The muon (μ) and the tau (τ) have the electric charge of the electron and interact along with the electron through the weak and electromagnetic force. The electron-neutrino (ν_e), the muon-neutrino (ν_μ) and the tau-neutrino (ν_τ) have no electric charge and interact only via the weak force with other particles. In a manner analogous to quarks, the leptons are arranged in three generations or families, with the electron and electronic neutrino being the lightest, hence stable particles. There is experimental evidence that neutrinos have a small mass [8]. Table 2.2 lists the quarks and leptons of the SM.

	1^{st} Generation	2^{nd} Generation	3^{rd} Generation
quarks	Up (u) 1.5-3.0 MeV/c^2	Charm (c) 1.25±0.09 GeV/c^2	Top (t) 173.1±1.3 GeV/c^2
	Down (d) 3.0-7.0 MeV/c^2	Strange (s) 95±25 MeV/c^2	Bottom (b) 4.20±0.07 GeV/c^2
leptons	Electron neutrino (ν_e) < 2 eV/c^2	Muon neutrino (ν_μ) < 0.19 MeV/c^2	Tau neutrino (ν_τ) < 18.2 MeV/c^2
	Electron (e) 0.511 MeV/c^2	Muon (μ) 105.66 MeV/c^2	Tau (τ) $1776.99^{+0.29}_{-0.26}$ MeV/c^2

Table 2.2: The fermion sector of the SM. All masses are taken from the Particle Data Group (PDG) [9], except for the top quark mass, where the last Tevatron combination is quoted in [10].

Gauge bosons

Gauge bosons are spin 1 particles which are the mediators of the forces. The strong interaction is mediated by gluons, the electromagnetic interaction is mediated by photons and the weak interaction is mediated by the $W^\pm$ and Z^0 bosons. Table 2.3 list the gauge bosons of the SM and their masses.

All fermions and massive gauge boson are subject to the weak interaction. The mediators of the weak interaction are quite heavy with $W^{\pm}$ and Z^0 bosons having masses around 81 and 91 GeV/c^2, respectively. W bosons decay to lepton-neutrino pairs or to up-type quark and down-type quark pairs, while Z bosons decay to a fermion and its antiparticle. Flavor changing neutral currents (FCNC) do not exist in leading order in the SM; they do appear at second or higher order, hence they are suppressed. Strict experimental limits have been set on FCNC [11].

Weak isospin couples only to left-handed particles. For this reason the leptons and quarks are distinguished into left-handed doublets and right-handed singlets. Furthermore, in order to explain strangeness- and bottomness-changing weak interactions, the left-handed quarks are not arranged in their mass eigenstates, rather they are expressed as linear combinations of the physical quark states through a non diagonal 3×3 mixing matrix named the CKM matrix (Cabibbo, Kobayashi and Maskawa matrix) [12]. The CKM matrix has one CP (Charge-Parity) violating phase and CP violation has been observed in the decay of neutral kaons and b mesons [13].

Interaction	Particle	Mass
electromagnetic	photon, γ	0
strong	gluon, g	0
weak	$W^{\pm}$	80.403±0.029 GeV/c^2
	Z^0	91.188±0.002 GeV/c^2

Table 2.3: The gauge bosons of the SM and their associated interactions [10].

2.1.2 Lagrangian formulation of the SM

In quantum field theory particles are described field quanta and their interactions are expressed in the Lagrangian density $\mathcal{L}$. The motivation to start from a Lagrangian

formulation lies in the fact that conserved quantities can be associated to symmetries. According to the theorem of Noether [14], each continuous symmetry of a system corresponds to a conserved quantity. In field theory any continuous transformation in the field ψ that leaves unchanged the action (S) of the Lagrangian, defined as $S = \int \mathcal{L}(\psi, \delta\psi)dx$ is associated with a conserved quantity.

Lagrangian formulation of quantum electrodynamics (QED)

Quantum Electrodynamics (QED) was developed in the late 1940's and early 1950's chiefly by Feynman, Schwinger, Tomonaga and Dyson [15], describing electromagnetic interactions of electrons and photons through a quantum, relativistic, renormalizable theory. The Dirac Lagrangian for a free spinor field is given by

$$\mathcal{L} = i\bar{\psi}\gamma^{\mu}\partial_{\mu}\psi - m\bar{\psi}\psi \tag{2.1}$$

The requirement of global invariance of the field results in charge conservation. Global invariance is obtained when the field is changed by the same amount in every point in space-time, e.g., the transformation $\psi(x) \rightarrow e^{iq\alpha}\psi(x)$ is a global transformation for any value of α. In group theory all the transformations of the type $\psi(x) \rightarrow e^{iq\alpha}\psi(x)$ obtained by changing the value of α are said to belong to the global U(1) gauge group. The SM, however, is based upon local (as opposed to global) gauge invariance. Local U(1) invariance is obtained when the Lagrangian is invariant to transformations of the type $\psi(x) \rightarrow e^{iq\alpha(x)}\psi(x)$ where now α depends on the space-time position x, i.e., the transformation is independent at each point in space-time. It is clear that the Dirac Lagrangian cited above is not invariant to this transformation. Applying this transformation to the Dirac Lagrangian above results in

$$\mathcal{L}^{'} = i\bar{\psi}\gamma^{\mu}(\partial_{\mu} + iq\partial_{\mu}\alpha)\psi - m\bar{\psi}\psi \tag{2.2}$$

If we insist on imposing invariance of the Lagrangian under local gauge transformations we must seek a different derivative, one that transforms like ψ itself, i.e., $D_\mu\psi \rightarrow e^{iq\alpha(x)}D_\mu\psi$. This can be accomplished with the following definition:

$$D_\mu \equiv \partial_\mu - iqA_\mu \tag{2.3}$$

$$A_\mu \rightarrow A_\mu + \frac{1}{q}\partial_\mu\alpha(x) \tag{2.4}$$

As long as A_μ transforms as Equation 2.4 the derivative D_μ will transform as $D_\mu = \partial_\mu - iqA_\mu$ and the Lagrangian defined as

$$\mathcal{L} = i\bar{\psi}\gamma^\mu D_\mu\psi - m\bar{\psi}\psi \tag{2.5}$$

$$= \bar{\psi}(i\gamma^\mu\partial_\mu - m)\psi + q\bar{\psi}\gamma^\mu\psi A_\mu \tag{2.6}$$

is invariant under the local gauge transformation. The vector field A_μ introduced by demanding local phase invariance is called the gauge field. Hence, by demanding local invariance one is forced to introduced the gauge field, which couples to charged particles in the same way as the photon field does. If this field is to be regarded as the physical photon field, a new term corresponding to the photon kinetic energy must be added to the Lagrangian. Because this new term must be invariant to the transformation of Equation 2.4, it can only involve the gauge invariant field tensor $F_{\mu\nu} = \partial_\mu A_\nu - \partial_\nu A_\mu$. The local invariant Lagrangian obtained in this way is then:

$$\mathcal{L}_{QED} = \bar{\psi}(i\gamma^\mu\partial_\mu - m)\psi + q\bar{\psi}\gamma^\mu\psi A_\mu - \frac{1}{4}F_{\mu\nu}F^{\mu\nu} \tag{2.7}$$

By requiring the Dirac Lagrangian for a free spinor field to be locally invariant under U(1) phase transformations, the Lagrangian for Dirac spinor fields interacting with the electromagnetic potential is obtained. The last two terms above appear in the classical Maxwell Lagrangian, where the charge density is identified with $J^{em}_\mu =$

$q(\bar{\psi}\gamma_\mu\psi)$. Thus, in this theory the electromagnetic interaction is described by two quantum fields: one for the charged particles and one for the photon. The strength of the interaction is usually described by the coupling constant α_{em} whose value depends on the momentum transfer q^2 in an interaction. At $q^2 \to 0$ (or low energies) the coupling constant value is that of the fine structure constant, $\alpha_{\rm em} = \frac{e^2}{4\pi/hc} = \frac{1}{137}$. At larger energy scales (shorter distances) its value increases, being $\alpha_{em}(m_Z) \approx \frac{1}{128}$ at the scale given by the mass of the Z boson.

Lagrangian formulation of the electro-weak theory

As we saw in the previous section, Quantum electrodynamics can be derived by requiring $U_q(1)$ Lagrangian invariance, where the subindex q in $U_q(1)$ refers to the charge conservation that results from the symmetry. Furthermore, the imposition of local $U_q(1)$ invariance leads to the introduction of the A_μ field. With the same idea, the authors of the GWS theory originally tried to explain the weak (neutral and charged) currents as resulting from the imposition of a $SU(2)_L$ group symmetry.

An isospin triplet of weak currents can be defined as

$$J^i_\mu(x) = \bar{\chi}_L\gamma_\mu\frac{1}{2}\sigma_i\chi_L \tag{2.8}$$

where σ_i are the usual Pauli spin matrices and $\chi_L = \begin{pmatrix} \nu \\ e^- \end{pmatrix}_L$ is the doublet of left-handed fermions. For each current the corresponding charge (T^i) is obtained by integrating the $0^{\rm th}$ component of the current over space;

$$T^i = \int J^i_0 d^3x \tag{2.9}$$

and it can be shown that the charges satisfy

$$[T^i, T^j] = i\epsilon_{ijk}T^k \tag{2.10}$$

The commutation relation between the charges indicates the nature of the symmetry generated by them; in this case $SU(2)_L$. The sub-index L reminds us of that the weak isospin current couples only to left-handed Weyl spinors.

In the Fermi theory of the weak interaction, the charged and neutral currents are obtained from experiment. The weak neutral current J_μ^{NC} is given by

$$J_\mu^{NC} = \bar{u}\gamma_\mu \tfrac{1}{2}(C_V - C_A\gamma^5)u \tag{2.11}$$

where the values C_V and C_A depend on whether the u's are lepton or quarks. The charged currents can be expressed as

$$J_\mu^{+}(x) = \bar{\chi}_L\gamma_\mu\sigma_+\chi_L \tag{2.12}$$

$$J_\mu^{-}(x) = \bar{\chi}_L\gamma_\mu\sigma_-\chi_L \tag{2.13}$$

where $\sigma_\pm = \frac{1}{2}(\sigma_1 \pm i\sigma_2)$. Therefore, the currents $J_\mu^1(x)$ and $J_\mu^2(x)$ defined in Equation 2.8 are simply linear combinations of the positive and negative charged currents of the Fermi theory. However, the neutral current $J_\mu^3(x)$ does not contain the right handed component experimentally found in the weak neutral current J_μ^{NC} [16], which is not pure $V - A$. This problem is overcome by introducing the electromagnetic current J_μ^{em} which is a neutral current with with right- as well as left-handed components. Since neither J_μ^{NC} nor J_μ^{em} respect the $SU(2)_L$ symmetry, two orthogonal combinations are formed that do have definite transformation properties. One combination, J_μ^3, completes the weak isospin triplet, and the other, j_μ^Y, is unchanged by $SU(2)_L$ and thus it is a weak isospin singlet. j_μ^Y is called the weak hypercharge current and it is defined by

$$j_\mu^Y = \bar{\psi}\gamma_\mu Y\psi \tag{2.14}$$

where Y is the weak hypercharge defined by the Gell-Mann-Nishijima formula

$$Q = T^3 + \frac{Y}{2} \tag{2.15}$$

Just as the charge Q generates the group $U(1)_{em}$, the weak-hypercharge operator Y generates the symmetry group $U(1)_Y$. In this context the electromagnetic current is written as

$$j_\mu^{em} = J_\mu^3 + \frac{1}{2} j_\mu^Y \tag{2.16}$$

With the introduction of the electromagnetic interaction the symmetry group has been enlarged to $SU(2)_L \otimes U(1)_Y$, and the $U(1)_{em}$ group of electromagnetism is now contained in it. Each group: $SU(2)_L$ and $U(1)_Y$ couples with its own strength, and in addition to the electron charge, another coupling constant is needed to fully specify the electro-weak interaction. Therefore, the two interactions are partially unified under the group $\mathrm{SU(2)_L \otimes U(1)_Y}$.

By requiring global invariance under $SU(2)_L$, the T_i generators of Equation 2.9 introduce a new quantum number called the *w*eak isospin (T). This number is associated to different spin-like multiplets. Since the weak isospin only interacts with left-handed particles (right-handed antiparticles), the left-handed fermions transform as doublets while the right handed ones transform as singlets:

$$f_L^i = \begin{pmatrix} \nu_L^i \\ l_L^i \end{pmatrix} \quad , \quad \begin{pmatrix} u_L^i \\ d_L^i \end{pmatrix} \tag{2.17}$$

$$f_R^i = l_R^i, u_R^i, d_R^i \tag{2.18}$$

where $i = 1, 2, 3$ corresponds to the family index. Hence, the weak interaction is divided into a "charged part" (that is, exchanging the components of the doublet) and a "neutral part" (that is, leaving the doublets as they are).

Following the analogy with QED, the SM electroweak Lagrangian is obtained by requiring invariance under local gauge transformations to obtain an interacting field theory. This follows from the free particle Lagrangian density

$$\mathcal{L}_0 = i\bar{\psi}\gamma^\mu \partial_\mu \psi \tag{2.19}$$

by demanding invariance under the following local phase transformations:

$$\bar{\psi}_L \rightarrow e^{ig\boldsymbol{\alpha}(x)\cdot\mathbf{T}+ig'\beta(x)Y}\psi_L, \quad \bar{\psi}_R \rightarrow e^{ig'\beta(x)Y}\psi_R \tag{2.20}$$

where $\psi_L = \frac{1}{2}(1-\gamma^5)\psi$ and $\psi_R = \frac{1}{2}(1+\gamma^5)\psi$ are the chiral lef- and right-handed components of ψ respectively. The parameter $\boldsymbol{\alpha}(x)$ is an arbitrary three-component vector and $\mathbf{T} = (T_1, T_2, T_3)^t$ is the weak isospin operator whose components T_i are the generators of $SU(2)_L$ symmetry transformations. The matrix representations are given by $T_i = \frac{\sigma_i}{2}(i = 1, 2, 3)$ where σ_i are the Pauli matrices. The T_i do not commute and satisfy $[T^i, T^j] = i\epsilon_{ijk}T^k$, making the $SU(2)_L$ group non-Abelian. $\beta(x)$ is an arbitrary one-dimensional function of the space-time coordinate x. Y is the weak hypercharge as defined by the relation of Equation 2.15 and the generator of the group $U(1)_Y$. Q is the electric charge and the generator of the group $U(1)_{em}$.

Requiring the Lagrangian $\mathcal{L}_0$ to be invariant under the combined $SU(2)_L \otimes U(1)_Y$ (Equation 2.20) requires the introduction to the free Lagrangian of four additional vector (spin 1) fields: the isotriplet $\mathbf{W}_\mu = (W_{1\mu}, W_{2\mu}, W_{3\mu})^t$ for $SU(2)_L$ and B_μ for $U(1)_Y$. This is achieved by replacing the derivative ∂_μ in $\mathcal{L}_0$ by the covariant derivative

$$D_\mu \equiv \partial_\mu + ig\mathbf{T}\cdot\mathbf{W}_\mu + ig'\frac{Y}{2}B_\mu \tag{2.21}$$

where g and g' are the coupling constants corresponding to $SU(2)_L$ and $U(1)_Y$, respectively. To complete the Lagrangian, the kinetic energy terms of the gauge fields are added: $-\frac{1}{4}W^i_{\mu\nu}W^{\mu\nu}_i - \frac{1}{4}B_{\mu\nu}B^{\mu\nu}$. The field tensors $W^i_{\mu\nu}$ and $B_{\mu\nu}$ for $SU(2)_L$ and $U(1)_Y$ are defined by: $W^i_{\mu\nu} \equiv \partial_\mu W^i_\nu - \partial_\nu W^i_\mu - g\epsilon^{ijk}W^j_\mu W^k_\nu$ and $B_{\mu\nu} \equiv \partial_\mu B_\nu - \partial_\nu B_\mu$. Since $SU(2)_L$ is a non-Abelian group, it allows self-interactions of these gauge fields.

The interaction electro-weak Lagrangian density expressed in terms of the charged and neutral currents is

$$\mathcal{L}_{int} = -ig\mathbf{J}_\mu\cdot\mathbf{W}^\mu - i\frac{g'}{2}j^Y_\mu B^\mu \tag{2.22}$$

The physical bosons of the theory ($W^{\pm}_{\mu}, Z_{\mu}$ and A_{μ}) are constructed from the $SU(2)_L \otimes U(1)_Y$ gauge bosons :

$$W^{\pm}_{\mu} = \frac{1}{\sqrt{2}}\left(W^1_{\mu} \pm iW^2_{\mu}\right) \tag{2.23}$$

$$Z_{\mu} = W^3_{\mu} cos(\theta_W) - B_{\mu} sin(\theta_W) \tag{2.24}$$

$$A_{\mu} = W^3_{\mu} sin(\theta_W) + B_{\mu} cos(\theta_W) \tag{2.25}$$

where θ_W is defined such that $\tan(\theta_W) = g'/g$. Rewriting Equation 2.22 in terms of the physical bosons gives

$$\begin{aligned} \mathcal{L}_{int} &= -\frac{ig}{\sqrt{2}}\left(J^-_{\mu}W^{\mu+} + J^+_{\mu}W^{\mu-}\right) - \frac{ig}{cos(\theta_W)}\left(J^3_{\mu} - sin^2(\theta_W)J^{em}_{\mu}\right)Z^{\mu} \\ &- igsin(\theta_W)J^{em}_{\mu}A^{\mu} \end{aligned} \tag{2.26}$$

The last term in Equation 2.26 is the photon coupling to an electromagnetic current, and allows the identification of $gsin(\theta_W)$ to the electron charge, $e = g\sin\theta_W = g'\cos\theta_W$. Writing out the currents explicitly,

$$J^{\pm}_{\mu} = \bar{\psi_L}\gamma_{\mu}\sigma^{\pm}\psi_L \tag{2.27}$$

$$J^3 = \bar{\psi_L}\gamma_{\mu}\sigma^3\psi_L \tag{2.28}$$

$$J^{em} = \bar{\psi_L}\gamma_{\mu}Q\psi_L \tag{2.29}$$

Where Q is the charge operator and σ^i are the Pauli spin matrices. If one examines the weak charged term and the weak neutral term (first and second terms in Equation 2.26) and re-interprets them in the context of the old V-A theory one finds

$$m_W = \left(\frac{g^2\sqrt{2}}{8G_F}\right)^{1/2} = \left(\frac{e^2\sqrt{2}}{8G_F sin^2(\theta_W)}\right)^{1/2} \tag{2.30}$$

$$m_Z = \frac{m_W}{cos(\theta_W)} \tag{2.31}$$

Hence, the global and local conservation of weak-isospin and hypercharge naturally imply charge conservation, as required by QED. Table 2.4 shows the assignment of the standard model fermions to weak isospin doublets (T=1/2) and isospin singlets (T=0). The upper (lower) component of the doublet has T^3 =+1/2 (-1/2), and the isospin assignments for the second and third generation are identical. The first

Lepton	T	T^3	Q	Y	Quarks	T	T^3	Q	Y
ν_e	1/2	1/2	0	-1	u_L	1/2	1/2	2/3	1/3
e_L^-	1/2	-1/2	-1	-1	d_L	1/2	-1/2	-1/3	1/3
					u_R	0	0	2/3	4/3
e_R^-	0	0	-1	-2	d_R	0	0	-1/3	-2/3

Table 2.4: Weak isospin doublets and singlets.

relatively accurate measurement of $sin^2(\theta_W)$ of 0.23±0.01 was obtained in 1981 using the rates of charged and neutral current reactions in low energy neutrino experiments. This quantity allowed the first prediction of the $W^{\pm}$ and Z^0 boson masses to about 83 and 94 GeV/c^2 respectively. These bosons were first observed two years later by studying proton-antiproton collisions with the UA1 and UA2 detectors in the $Sp\bar{p}S$ collider at CERN [17, 18]. The $W^{\pm}$ was observed through its decay into a high energy lepton and missing transverse energy from the neutrino, and the Z^0 through its decay to a pair of charged leptons. The final measurement of the masses were in good agreement with the predicted values.

Lagrangian formulation of quantum chromodynamics (QCD)

The theory of the strong interaction, Quantum Chromodynamics (QCD), is one of the cornerstones of the Standard Model. Following the success of QED and of Yang-Mills theories, QCD was developed in 1973 [19] in the context of a Quantum Field Theory based on the $SU(3)_C$ symmetry group [20], where C refers to the quark's

color and the dimension indicates its three possible degrees of freedom. It is a non-abelian theory that describes the strong interaction of colored quarks and gluons[1]. The QCD Lagrangian is written as

$$\mathcal{L}_{QCD} = \sum_{flavor} \bar{q_a}(i\gamma^\mu D_\mu - m_q)_{ab} q_b - \frac{1}{4} F^A_{\alpha\beta} F^{\alpha\beta}_A, \tag{2.32}$$

where the sum runs over the six different quark flavors and the quark fields q are :

$$\begin{pmatrix} q_1 \\ q_2 \\ q_3 \end{pmatrix}$$

The covariant derivative required to make the Lagrangian invariant under $SU(3)_C$ transformations is given by

$$D_\mu = \left(\partial_\mu - i g_s \frac{\lambda^\alpha}{2} A^\alpha_\mu\right) \tag{2.33}$$

The quantities $\frac{\lambda^\alpha}{2}$ are the generators of the $SU(3)_C$ group given by 3×3 traceless hermitian matrices and A^α_μ are the gluons fields, with $\alpha = 1, \ldots, 8$. The energy in the gluon field is given by the last term in the Lagrangian where the gluon field strength tensor is

$$F^\alpha_{\mu\nu} = \partial_\mu A^\alpha_\nu - \partial_\nu A^\alpha_\nu + g_s f^{\alpha\beta\gamma} A_{\mu\beta} A_{\nu\gamma} \tag{2.34}$$

where g_s is the coupling constant which determines the strength of the interaction between colored quanta, and $f^{\alpha\beta\gamma}$ are the structure constants of the SU(3) color

[1]The charge associated with the strong interaction is the color charge. The color property was introduced for quarks to satisfy the requirement of the Pauli exclusion principle [2]. Later experimental results proved the validity of the color hypothesis.

group. The third term in Equation 2.34 shows the non-abelian nature of QCD. This term describes the property of interaction between gluons, resulting in the very different behavior of the strong force when compared to the electromagnetic interactions. This self-coupling is the reason why the strong coupling constant, $\alpha_s = \frac{g^2}{4\pi}$, is large at small energies (large distances) and decreases at high energies (small distance). This characteristic running of α_S is used to explain the observed behavior of the strong interaction:

- Asymptotic freedom: At high energies (small distance) the strong interaction proceeds via a color field of reduced strength and the quarks and gluons behave as essentially free, non-interacting particles.
- Confinement: At low energies (or large distance) the strength of the color field is increasing, since the potential behaves as $V(r) \sim \lambda r$, and as a consequence the quarks and gluons can never be observed as free particles. If two interacting partons are separated, the energy of the field increases to the point that new interacting particles are created resulting in colorless hadrons containing the partons. Therefore partons are not observed as free particles.

It is important to note that the asymptotic freedom property allows the application of perturbation theory to calculate cross section measurements in scattering processes where quarks and gluons are involved.

2.1.3 The Standard Model Higgs mechanism

In the electroweak theory any gauge boson mass term will enter the Lagrangian as $m_W^2 W^\mu W_\mu$. This term would destroy the $SU(2)_L \otimes U(1)_Y$ invariance unless the boson mass m_W is zero. This implies that all the gauge bosons of the electroweak theory must have vanishing mass if the invariance is to be kept. Thus, without

any other mechanism, electroweak theory lacks the ability to put mass into gauge bosons. One could argue that invariance is required for aesthetics purposes only, and that one could add such mass terms to the Lagrangian and ignore the symmetry breaking effects. This however inserts nonrenormalizable divergences to all orders rendering the theory meaningless. The solution is to invoke a mechanism developed by Petter Higgs et al.[21] known as the *Higgs mechanism*. In this mechanism a scalar field ϕ, with non-vanishing vacuum expectation value, is inserted into the theory of massless gauge bosons. To keep the Lagrangian invariant the field must belong to a $SU(2)_L \otimes U(1)_Y$ multiplet. The field ϕ will add a contribution $\mathcal{L}_2$ to the Lagrangian of the theory equal to

$$\mathcal{L}_2 = |D_\mu \phi|^2 - V(\phi) \tag{2.35}$$

In order to conserve $SU(2)_L \otimes U(1)_Y$ invariance the covariant derivative D_μ must be

$$D_\mu = \partial_\mu + ig\mathbf{T} \cdot \mathbf{W}_\mu + ig'\frac{1}{2}B_\mu Y \tag{2.36}$$

To obtain a theory in which the $W^\pm$ and Z^0 bosons get mass while the electromagnetic field remains massless, the choice of 4 real scalar fields is made, arranged in a doublet of complex scalars with hypercharge $Y = 1$.

$$\phi = \begin{pmatrix} \phi^+ \\ \phi^0 \end{pmatrix} \begin{array}{l} \phi^+ \equiv (\phi_1 + i\phi_2)/\sqrt{2} \\ \phi^0 \equiv (\phi_3 + i\phi_4)/\sqrt{2} \end{array} \tag{2.37}$$

Where the ϕ_i's are four real fields. When the Higgs potential is minimized, the neutral component of the Higgs field acquires a vacuum expectation value (VEV). The phase of the Higgs field can be chosen such that the VEV is real and positive. The minimum of the Higgs field is represented by ϕ_0,

$$\phi_0 = <0|\phi|0> = \frac{1}{\sqrt{2}} \begin{pmatrix} 0 \\ v \end{pmatrix} \tag{2.38}$$

A scalar potential $V(\phi)$ is chosen so as to have a vacuum expectation value

$$V(\phi) = \mu^2\phi^\dagger\phi + \lambda(\phi^\dagger\phi)^2 \tag{2.39}$$

This potential has a minimum at $v = \sqrt{\mu^2/\lambda}$ if $\lambda > 0$ and $\mu^2 < 0$. The potential of Equation 2.39 is commonly known as the *Mexican hat potential* due to its shape (see Figure 2.2). Choosing one of a set of degenerate states of minimum energy breaks the gauge symmetry. As stated by the Goldstone theorem [2], fields that acquire a VEV will have an associated massless Goldstone boson which will "disappear" transformed into the longitudinal component of a massive gauge boson.

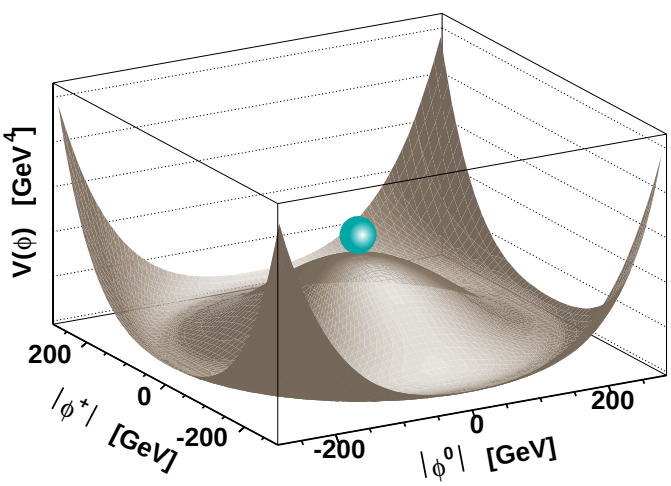

Figure 2.2: The minimum of the Higgs potential occurs at $-\mu^2/(2\lambda)$, not at zero.

If we expand the field ϕ around its VEV value,

$$\phi = \frac{1}{\sqrt{2}} \begin{pmatrix} 0 \\ v + h(x) \end{pmatrix} \tag{2.40}$$

and substitute it into the Lagrangian of Equation 2.35, rewriting the W^i_μ's and B_μ

as functions of the physical bosons (see Equation 2.23 to 2.25), we get :

$$\mathcal{L}_2 = \frac{1}{2}(\partial_\mu \phi)^2 + (\frac{gv}{2})^2 W_\mu^+ W^{-\mu} + \frac{1}{2}\left(\frac{gv}{2cos(\theta_W)}\right)^2 Z_\mu Z^\mu - \lambda v^2 h^2 + \dots \quad (2.41)$$

As a consequence of the VEV of the scalar field the symmetry has been broken resulting in $W^\pm$ and Z^0 bosons with masses, and a massless photon.

$$\begin{aligned} m_W &= gv/2 && (2.42)\\ m_Z &= gv/2cos(\theta_W) = v(g^2 + g'^2)^{1/2}/2 && (2.43)\\ m_A &= 0 && (2.44)\\ m_h &= \sqrt{2\lambda v^2} = \sqrt{-2\mu^2} && (2.45)\\ v^2 &= 4m_Z^2/(g^2 + g'^2) = 4m_W^2/g && (2.46) \end{aligned}$$

In addition, the introduction of the scalar field also resulted in a new scalar boson with a mass of $\sqrt{2\lambda v^2}$. This boson is denoted by the symbol h_{sm} and named the *Higgs boson* after Peter Higgs who was the first to understand this mechanism. It should be noted that while the value of v can be deduced from the $W^\pm$ mass (yielding $v = 246$ GeV), the mass of the Higgs itself remains unknown since it includes the unknown value of λ. The Higgs mechanism just described also provides a way to generate masses for the quarks and leptons. It is clear that the addition of a fermionic mass term such as $-m_e\bar{e}e = m_e(\bar{e_R}e_L + \bar{e_L}e_R)$ is not gauge invariant, since e_L and e_R belong to different representations of $SU(2)$ and have different $U(1)$ hypercharges. But an invariant mass term can be written by including a Yukawa-like coupling to the Higgs field ϕ,

$$\mathcal{L}_3 = -\lambda_e \left[(\bar{\nu_e}, \bar{e})_L \begin{pmatrix} \phi^+ \\ \phi^0 \end{pmatrix} e_R + \bar{e_R} \left(\phi^-, \bar{\phi^0}\right) \begin{pmatrix} \nu_e \\ e \end{pmatrix}_L \right] \quad (2.47)$$

Using Equation 2.40 to break the symmetry gives

$$\begin{aligned} \mathcal{L}_3 &= -\frac{\lambda_e}{\sqrt{2}} v \left(\bar{e}_L e_R + \bar{e}_R e_L\right) - \frac{\lambda_e}{\sqrt{2}} \left(\bar{e}_L e_R + \bar{e}_R e_L\right) h \\ &= m_e \bar{e} e - \frac{m_e}{v} \bar{e} e h \end{aligned} \tag{2.48}$$

where $m_e = \frac{\lambda_e v}{\sqrt{2}}$

This mechanism can be extended to all fermions. A fermion f will then acquire mass through interactions with the Higgs field via its coupling constant λ_f, which is proportional to the fermion's mass. Since the values of λ_f's are arbitrary, the value of the fermion masses are not predicted. In fact, each coupling must now be tuned to achieve the experimentally measured fermion mass. Our theoretical ignorance about the origin of the fermion masses has now been merely re-interpreted as a theoretical ignorance about the Higgs field coupling constants.

This brings the number of unspecifed Standard Model parameters to 22 namely

- Three gauge coupling constants
- Six quark masses
- Six lepton masses
- Three quark mixing angles and one phase in the CKM matrix (θ_{12}, θ_{23}, θ_{13} and the CP-violating phase δ).
- QCD vacuum angle
- The two scalar potential constants (μ, λ)

These parameters must be determined experimentally.

2.2 Supersymmetry and the Minimal Supersymmetric Standard Model

2.2.1 The hierarchy problem

The Standard Model of high-energy physics, augmented by neutrino masses, provides a remarkably successful description of presently known phenomena with no clear hints of additional structure well into the TeV energy scale. The SM has endured rigorous experimental testing and made many successful predictions, among them the discovery of the charm, bottom, and top quarks, the discovery of the Z^0 boson and the absence of flavor changing neutral currents. In spite of these successes the Standard Model is widely considered to be a low energy effective theory and not a fundamental one. Low energy here means energies achievable in existing and proposed particle experiments of the order of 15 TeV. The Higgs mechanism provides a successful model by which electroweak symmetry is broken allowing the gauge bosons and fermions of the SM to obtain mass. However, the Standard Model will have to be extended to describe physics at the reduced Planck scale $M_{\rm P} = (8\pi G_{\rm Newton})^{-1/2} = 2.4 \times 10^{18}$ GeV/c^2, where quantum gravitational effects become important. Furthermore, it is expected that new physics exists in the 16 orders of magnitude in energy between the electroweak scale, M_W, and the Planck scale. It is in this region that the *hierarchy problem* manifests itself as a disturbing sensitivity of the Higgs potential to any new physics [16]. The electrically neutral part of the Standard Model Higgs field is a complex scalar ϕ^0 with a classical potential

$$V = \mu^2|\phi^0|^2 + \lambda|\phi^0|^4 \tag{2.49}$$

The Standard Model requires a non-vanishing vacuum expectation value (VEV) for ϕ^0 at the minimum of the potential in order to provide for a mechanism of elec-

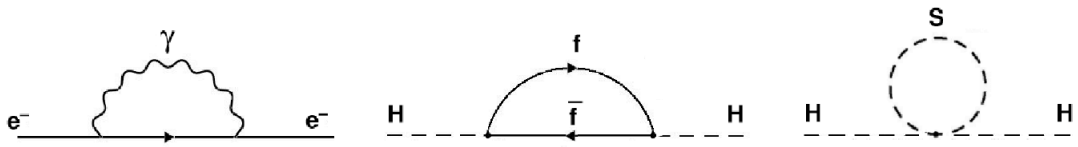

Figure 2.3: One-loop quantum corrections to the electron mass in QED (left), and to the Higgs squared mass parameter m_H^2 due to a Dirac fermion f (middle). Scalar one-loop contribution to the Higgs mass (right).

troweak symmetry breaking. This is guaranteed if $\lambda > 0$ and $\mu^2 < 0$, resulting in $\langle 0|\phi||0\rangle = \sqrt{-\mu^2/\lambda}$. Since we know from experiments[2] that $\langle 0|\phi|0\rangle$ is approximately 246 GeV/c^2, and that $\lambda \approx 1$ to ensure unitarity, it must be that μ^2 is very roughly of order $-(100\ \text{GeV}/c^2)^2$. The problem is that μ^2 receives large quantum corrections from the virtual effects of every particle that couples to the Higgs field.

The divergences in a quantum field theory can be managed by the renormalization process, which is any of a collection of techniques used to treat infinities arising in calculated quantities. This process is based on the assumption that SM parameters such as masses and coupling constants could be themselves divergent. What is really measured are not the "bare" (at tree level) parameters, but rather effective parameters that include the bare parameters and their corrections according to the theory. In a sense, the renormalization process arranges the divergences in the couplings and the bare masses to exactly cancel the high-momentum infinities.

An example of divergencies and renormalization is illustrated by the electron's one-loop self energy diagram shown in Figure 2.3 (left). The energy contribution to the electron mass according to the QED theory is [22]:

$$m_e = m_e^0 \left[1 + \frac{3\alpha}{2\pi} ln\left(\frac{\Lambda}{m_e^0}\right)\right] \tag{2.50}$$

[2]The masses of the $W^{\pm}$ and Z^0 bosons are related to the Higgs potential VEV v through $gv/2$ and $gv/2cos(\theta_W)$, respectively.

where m_e^0 is the bare mass of the electron and Λ is the cutoff value of the integral that runs over the photon momenta. This integral is logarithmically divergent and passes its behavior to the correction of the electron mass. It is interesting to note that if taking Λ to be the Planck Mass ($\sim 10^{19}$ GeV/c^2) the shift in the electron mass is only $m_e \simeq 1.7 m_e^0$. This shows that the normalization process of absorbing divergences into renormalized parameters is reasonable, at least when dealing with logarithmic divergences.

However, in the case of the Higgs field, these cancelations would require an unnatural cancelation of the bare Higgs mass and the radiative quantum corrections. Due to these corrections, the Higgs mass would be

$$m_{h_{SM}}^2 = (m_h^2)_0 + \Delta M_H^2 \tag{2.51}$$

where $(m_h^2)_0$ is the bare Higgs mass and ΔM_H^2 is the radiative correction. For example, in Figure 2.3 (middle) we have a correction to m_H^2 from a loop containing a Dirac fermion f with mass m_f, which can represent any of the leptons and quarks of the Standard Model. The correction to the mass of the Higgs boson due to this loop is [16]:

$$\Delta M_H^2 = -\frac{|\lambda_f|^2}{16\pi^2}\left[2\Lambda^2 + 6m_f^2 \ln\left(\Lambda/m_f\right) + \ldots\right] \tag{2.52}$$

In this case the correction is quadratic in the cut-off variable Λ. Here, a cut-off value such as the Planck scale (10^{19} GeV/c^2) would result in a mass correction 30 orders of magnitude larger than the expected physical mass of the Higgs of about (100 GeV/c^2). One may argue that this correction could be re-normalized into the bare mass of the Higgs boson, but this would require an enormous bare mass that would need to cancel very precisely the large correction. Furthermore, there are contributions similar to Equation 2.66 from the virtual effects of any arbitrarily heavy particles that might exist. For example, a hypothetical heavy complex scalar particle S with mass m_S could couple to the Higgs via the diagram of Figure 2.3 (right). The

contribution to the Higgs mass in this case is

$$\Delta M_H^2 \;=\; \frac{\lambda_S}{16\pi^2}\left[\Lambda^2 - 2m_S^2\ln(\Lambda_{\rm UV}/m_S) + \ldots\right] \tag{2.53}$$

Because the scalar S is a boson, this correction has the opposite sign as Equation 2.66, however, it is also quadratic. Therefore, $m^2_{h_{SM}}$ is sensitive to the masses of the *heaviest* particles that H couples to; if m_S is very large, it is difficult to understand why m_H^2 is so small. A complete cancellation of these corrections at all orders would call for an incredible "fine tunning" which seems very unlikely [23]. In a model with spontaneous electroweak symmetry breaking, this problem affects not only the Higgs mass but also its vacuum expectation value and, therefore, the masses of all particles that acquire mass through the Higgs mechanism such as the electro-weak bosons, quarks and charged leptons. Hence, it seems unnatural to have all the SM particle masses at the electroweak scale unless the model is somehow cut off or embedded into a richer structure at energies no larger than the TeV scale.

The need for a new symmetry

A richer particle spectrum is proposed by an extension of the SM called Supersymmetric Theory or Supersymmetry, which provides the means for an automatic cancellation of the radiative corrections to the Higgs mass. The problem of the self-energy of the electron is solved in QED by the existence of the positron [24]. The contribution to the electron's self-energy due to virtual photons is exactly cancelled by the contribution of virtual electron-positron pairs due to vacuum fluctuations. In a manner analogous to this chiral symmetry of QED, *supersymmetry* avoids large power corrections to the Higgs mass by introducing a fundamental symmetry between fermions and bosons.

2.2.2 Supersymmetry

Supersymmetry (SUSY) is a symmetry which relates masses and couplings of bosons and fermions via spin-$\frac{1}{2}$ operators [16]. In SUSY, particles are combined into superfields and an operator Q generates the transformation of converting fermions to bosons and vice versa:

$$Q|Boson\rangle = |Fermion\rangle \qquad Q^\dagger|Fermion\rangle = |Boson\rangle \tag{2.54}$$

The single-particle states of a supersymmetric theory fall into irreducible representations of the supersymmetry algebra, called *supermultiplets*. Each supermultiplet contains both fermion and boson states, which are commonly known as *superpartners* of each other. By definition of supermultiplet, if $|\Omega\rangle$ and $|\Omega'\rangle$ are members of the same supermultiplet, then $|\Omega'\rangle$ is proportional to some combination of Q and $Q^\dagger$ operators acting on $|\Omega\rangle$, up to a spacetime translation or rotation.

Consider a left-handed two-component Weyl fermion ψ and its superpartner a scalar field ϕ. The simplest possibility for the transformation of the scalar field is

$$\delta\phi = \epsilon\psi, \qquad \delta\phi^* = \epsilon^\dagger\psi^\dagger, \tag{2.55}$$

where ϵ is an infinitesimal, anticommuting, two-component Weyl fermion object parameterizing the supersymmetry transformation. The following choice for the transformation of the Weyl fermion ψ guarantees that a free Lagrangian with this minimal particle content will remain invariant

$$\delta\psi_\alpha = -i(\sigma^\mu\epsilon^\dagger)_\alpha\,\partial_\mu\phi + \epsilon_\alpha F, \qquad \delta\psi^\dagger_{\dot\alpha} = i(\epsilon\sigma^\mu)_{\dot\alpha}\,\partial_\mu\phi^* + \epsilon^\dagger_{\dot\alpha}F^*, \tag{2.56}$$

where $\alpha = 1, 2$ and $\dot\alpha = 1, 2$ are distinct spinor indices, and σ^μ are the Pauli matrices. An auxiliary field F is introduced to in order to make the supersymmetric algebra

close off-shell, that is

$$(\delta_{\epsilon_2}\delta_{\epsilon_1} - \delta_{\epsilon_1}\delta_{\epsilon_2})X \;\; = \;\; i(-\epsilon_1\sigma^\mu\epsilon_2^\dagger + \epsilon_2\sigma^\mu\epsilon_1^\dagger)\,\partial_\mu X, \tag{2.57}$$

for each of the fields $X = \phi, \phi^*, \psi, \psi^\dagger, F, F^*$. F has no kinetic Lagrangian term and transforms according to

$$\delta F = -i\epsilon^\dagger\overline{\sigma}^\mu\partial_\mu\psi, \qquad\qquad \delta F^* = i\partial_\mu\psi^\dagger\overline{\sigma}^\mu\epsilon, \tag{2.58}$$

where

$$\begin{aligned}
\sigma^0 = \overline{\sigma}^0 &= \begin{pmatrix} 1 & 0 \\ 0 & 1 \end{pmatrix}, \qquad & \sigma^1 = -\overline{\sigma}^1 &= \begin{pmatrix} 0 & 1 \\ 1 & 0 \end{pmatrix}, \\
\sigma^2 = -\overline{\sigma}^2 &= \begin{pmatrix} 0 & -i \\ i & 0 \end{pmatrix}, \qquad & \sigma^3 = -\overline{\sigma}^3 &= \begin{pmatrix} 1 & 0 \\ 0 & -1 \end{pmatrix}.
\end{aligned} \tag{2.59}$$

By Noether's theorem we have conserved currents J^μ and $J^{\dagger\mu}$, where K^μ is any object whose divergence satisfies $\delta\mathcal{L} = \partial_\mu K^\mu$

$$\epsilon J^\mu + \epsilon^\dagger J^{\dagger\mu} \;\; \equiv \;\; \sum_X \delta X\,\frac{\delta\mathcal{L}}{\delta(\partial_\mu X)} - K^\mu. \tag{2.60}$$

From these currents one constructs the conserved charges which are the generators of supersymmetry transformations

$$Q_\alpha = \sqrt{2}\int d^3\vec{x}\,J^0_\alpha, \qquad\qquad Q^\dagger_{\dot\alpha} = \sqrt{2}\int d^3\vec{x}\,J^{\dagger 0}_{\dot\alpha}. \tag{2.61}$$

Therefore Q is a complex anticommuting spinor which is a generator of supersymmetric transformations. Both Q and its hermitian conjugate $Q^\dagger$ are fermionic in nature (they carry spin angular momentum 1/2) and form a Lie superalgebra [25] with the

four-momentum and the Lorentz transformation generators in a generalization of the space-time symmetries of quantum field theory and of the Lorentz group [26].

$$\{Q_\alpha, Q^\dagger_{\dot\alpha}\} = -2\sigma^\mu_{\alpha\dot\alpha} P_\mu \tag{2.62}$$

$$\{Q_\alpha, Q_\beta\} = 0 \tag{2.63}$$

$$\{Q^\dagger_{\dot\alpha}, Q^\dagger_{\dot\beta}\} = 0 \tag{2.64}$$

$$[Q_\alpha, P^\mu] = 0, \qquad [Q^\dagger_{\dot\alpha}, P^\mu] = 0. \tag{2.65}$$

The squared-mass operator commutes with the operators Q, $Q^\dagger$, and with all space-time rotation and translation operators, so it follows immediately that particles inhabiting the same irreducible supermultiplet must have equal eigenvalues of the squared-mass operator, and therefore equal masses.

The supersymmetry generators $Q, Q^\dagger$ also commute with the generators of gauge transformations. Therefore particles in the same supermultiplet must also be in the same representation of the gauge group, and so must have the same electric charges, weak isospin, and color degrees of freedom. In this situation, each chiral fermion $f_{L,R}$ has a scalar partner $\tilde{f}_{L,R}$ and for each massless gauge boson A_μ, with helicity states ± 1, there is a massless spin 1/2 partner, with helicity states $\pm\frac{1}{2}$. Therefore, each supermultiplet contains an equal number of fermion and boson degrees of freedom $n_B = n_F$.

2.2.3 Supersymmetry and the hierarchy problem

The SM hierarchy problem presented in Section 2.2.1 is elegantly solved after introducing supersymmetric theory [16, 27]. For every correction to the Higgs squared

mass $m^2_{h_{SM}}$ due to a fermion f (two spin degrees of freedom) of the form

$$\Delta M_H^2 = -\frac{|\lambda_f|^2}{16\pi^2}\left[2\Lambda^2 + 6m_f^2 \ln\left(\Lambda/m_f\right) + \ldots\right] \tag{2.66}$$

There is a complex scalar boson contribution of opposite sign (two degrees of freedom) that also couples to the Higgs and contribute a mass correction term of the form

$$\Delta M_H^2 \;=\; \frac{\lambda_S}{16\pi^2}\left[\Lambda^2 - 2m_S^2 \ln(\Lambda_{\rm UV}/m_S) + \ldots\right] \tag{2.67}$$

If we require that $\lambda_S = |\lambda_f^2|$, then the two quadratic contributions cancel each other exactly. This relationship between the couplings is actually guaranteed by supersymmetry where fermions and bosons are related by construction in superfields. In this manner, in principle, all fermionic quadratic radiative corrections are cancelled exactly by the bosonic contributions of their superpartners, thus solving the problem of divergent radiative corrections to the Higgs mass.

2.2.4 The Minimal Supersymmetric Standard Model

The MSSM is a supersymmetric extension of the SM with minimal field content [28]. The MSSM obeys the same $\mathrm{SU(3)}_C \otimes \mathrm{SU(2)}_L \otimes \mathrm{U(1)}_\mathrm{Y}$ gauge symmetries of the Standard Model but doubles the spectrum of new particles; for every particle in the SM, a superpartner is postulated which differs by half a unit of spin. The superpartners are conveniently described by a notation with close correspondence to the SM notation for bosons and fermions. The names for the spin-0 partners of the quarks and leptons are constructed by prepending an "s", for scalar. So, generically they are called *squarks* and *sleptons*, or sometimes *sfermions*. The symbols for the squarks and sleptons are the same as for the corresponding fermion, but with a tilde ($\tilde{}$) used to denote the superpartner of a Standard Model particle. For example, the superpartners of the left-handed and right-handed parts of the electron Dirac field

are called left- and right-handed selectrons, and are denoted $\widetilde{e}_L$ and $\widetilde{e}_R$. A spinor such as the electron has two degree of freedom, its left- and right-handed parts, therefore it superpartner is a complex scalar field, composed of two real fields each with one degree of freedom. Therefore, the "R" in $\widetilde{e}_R$ refers to the chirality of its SM counterpart, the right-handed electron; $\widetilde{e}_R$ is a scalar field, not a spinor, and therefore has no chirality. A similar nomenclature applies for smuons and staus: $\widetilde{\mu}_L$, $\widetilde{\mu}_R$, $\widetilde{\tau}_L$, $\widetilde{\tau}_R$. The Standard Model neutrinos (neglecting their very small masses) are always left-handed, so the sneutrinos are denoted generically by $\widetilde{\nu}$, with a possible subscript indicating which lepton flavor they carry: $\widetilde{\nu}_e$, $\widetilde{\nu}_\mu$, $\widetilde{\nu}_\tau$. In addition, a complete list of the squarks is $\widetilde{q}_L$, $\widetilde{q}_R$ with $q = u, d, s, c, b, t$. The gauge interactions of each of these squark and slepton fields are the same as for the corresponding Standard Model fermions; for example, the left-handed squarks $\widetilde{u}_L$ and $\widetilde{d}_L$ couple to the W boson, while $\widetilde{u}_R$ and $\widetilde{d}_R$ do not. Finally, the fermionic partners of the bosons finish with the suffix "ino" (e.g. gluino is the superpartner of the gluon).

All the fermions of the standard model and their superpartners reside in *chiral* supermultiplets. The simplest possibility for a chiral or *scalar* supermultiplet, which is consistent with $n_B = n_F$, has a single two-component Weyl fermion (with two spin helicity states, so $n_F = 2$) and a complex scalar field with two real parts (each with $n_B = 1$). In order to see how the fermions of the SM and their superpartners fit into chiral supermultiplets, we consider the case of one generation of quarks, leptons and their superpartners. One can define $\hat{Q}$ as the superfield containing an $\mathrm{SU}(2)_L$ doublet of quarks:

$$Q = \begin{pmatrix} u_L \\ d_L \end{pmatrix} \tag{2.68}$$

The "hat" above Q was left out to avoid unecessary clatter. The scalar partners

which are also in an $\mathrm{SU}(2)_L$ doublet are,

$$\tilde{Q} = \begin{pmatrix} \tilde{u}_L \\ \tilde{d}_L \end{pmatrix} \tag{2.69}$$

In an analogous form, the superfield $\hat{U}^c$ ($\hat{D}^c$) contains the right-handed up (down) anti-quark, $\bar{u}_R$ ($\bar{d}_R$), and its scalar partner, $\tilde{u}_R^*$ ($\tilde{d}_R^*$). Following the same pattern, leptons are contained in the $SU(2)_L$ doublet superfield $\hat{L}$ which contains the left-handed fermions,

$$L = \begin{pmatrix} \nu_L \\ e_L \end{pmatrix} \tag{2.70}$$

and their scalar partners,

$$\tilde{L} = \begin{pmatrix} \tilde{\nu}_L \\ \tilde{e}_L \end{pmatrix} \tag{2.71}$$

Finally, the superfield $\hat{E}^c$ contains the right-handed anti-electron, $\bar{e}_R$, and its scalar partner, $\tilde{e}_R^*$.

Since the Higgs scalar boson has spin 0, it must reside in a chiral supermultiplet. Actually, it turns out that just one chiral supermultiplet is not enough. Because of the structure of supersymmetric theories, only a $Y = 1/2$ Higgs chiral supermultiplet can have the Yukawa couplings necessary to give masses to charge $+2/3$ up-type quarks (up, charm, top), and only a $Y = -1/2$ Higgs can have the Yukawa couplings necessary to give masses to charge $-1/3$ down-type quarks (down, strange, bottom) and to the charged leptons. Thus, two Higgs doublets are needed in order to generate both up-like and down-like quark masses.

We will call the $SU(2)_L$-doublet complex scalar fields with $Y = 1/2$ and $Y = -1/2$ by the names $\hat{H}_u$ and $\hat{H}_d$, respectively. The weak isospin components of $\hat{H}_u$

Names		spin 0	spin 1/2	$SU(3)_C$, $SU(2)_L$, $U(1)_Y$
squarks, quarks	$\hat{Q}$	$(\widetilde{u}_L \;\; \widetilde{d}_L)$	$(u_L \;\; d_L)$	$(\mathbf{3}, \mathbf{2}, \frac{1}{6})$
(×3 families)	$\hat{U}$	$\widetilde{u}^*_R$	$u^\dagger_R$	$(\overline{\mathbf{3}}, \mathbf{1}, -\frac{2}{3})$
	$\hat{D}$	$\widetilde{d}^*_R$	$d^\dagger_R$	$(\overline{\mathbf{3}}, \mathbf{1}, \frac{1}{3})$
sleptons, leptons	$\hat{L}$	$(\widetilde{\nu} \;\; \widetilde{e}_L)$	$(\nu \;\; e_L)$	$(\mathbf{1}, \mathbf{2}, -\frac{1}{2})$
(×3 families)	$\hat{E}$	$\widetilde{e}^*_R$	$e^\dagger_R$	$(\mathbf{1}, \mathbf{1}, 1)$
Higgs, higgsinos	$\hat{H}_u$	$(H^+_u \;\; H^0_u)$	$(\widetilde{H}^+_u \;\; \widetilde{H}^0_u)$	$(\mathbf{1}, \mathbf{2}, +\frac{1}{2})$
	$\hat{H}_d$	$(H^0_d \;\; H^-_d)$	$(\widetilde{H}^0_d \;\; \widetilde{H}^-_d)$	$(\mathbf{1}, \mathbf{2}, -\frac{1}{2})$

Table 2.5: Chiral supermultiplets in the Minimal Supersymmetric Standard Model. The spin-0 fields are complex scalars, and the spin-1/2 fields are left-handed two-component Weyl fermions.

with $T_3 = (1/2, -1/2)$ have electric charges 1, 0 respectively, and are denoted (H^+_u, H^0_u). Similarly, the $SU(2)_L$-doublet complex scalar $\hat{H}_d$ has $T_3 = (1/2, -1/2)$ components (H^0_d, H^-_d). The neutral scalar that corresponds to the physical Standard Model Higgs boson is in a linear combination of H^0_u and H^0_d. The fermionic superpartners of the Higgs scalars are called higgsinos. They are denoted by $\widetilde{H}_u$, $\widetilde{H}_d$ for the $SU(2)_L$-doublet left-handed Weyl spinor fields, with weak isospin components $\widetilde{H}^+_u$, $\widetilde{H}^0_u$ and $\widetilde{H}^0_d$, $\widetilde{H}^-_d$. The chiral supermultiplets of a minimal, phenomenologically viable extension of the Standard Model are summarized in Table 2.5, classified according to their transformation properties under the Standard Model gauge group $SU(3)_C \otimes SU(2)_L \otimes U(1)_Y$, which combines u_L, d_L and ν, e_L degrees of freedom into $SU(2)_L$ doublets. It is also useful to have a symbol for each of the chiral supermultiplets as a whole; these are indicated in the second column of Table 2.5 by the symbols: $\hat{Q}, \hat{U}, \hat{D}, \hat{L}, \hat{E}, \hat{H}_u$ and $\hat{H}_d$.

The vector bosons of the Standard Model reside in *gauge* supermultiplets. The simplest possibility for a gauge supermultiplet contains a spin-1 vector boson. A massless spin-1 boson has two helicity states, so the number of bosonic degrees of

Names		spin 1/2	spin 1	$SU(3)_C$, $SU(2)_L$, $U(1)_Y$
gluino, gluon	$\hat{G}_a$	$\widetilde{g}_a$	g_a	(**8**, **1** , 0)
winos, W bosons	$\hat{W}$	$\widetilde{W}^{\pm}$ $\widetilde{W}^0$	$W^{\pm}$ W^0	(**1**, **3** , 0)
bino, B boson	$\hat{B}$	$\widetilde{B}^0$	B^0	(**1**, **1** , 0)

Table 2.6: Gauge supermultiplets in the Minimal Supersymmetric Standard Model.

freedom is $n_B = 2$. Its superpartner is therefore a massless spin-1/2 Weyl fermion, again with two helicity states, so $n_F = 2$. Gauge bosons must transform as the adjoint representation of the gauge group, so their fermionic partners must also. Since the adjoint representation of a gauge group is always its own conjugate, the fermionic partners must have the same gauge transformation properties for left-handed and for right-handed components. Such a combination of spin-1/2 gauginos and spin-1 gauge bosons is called a gauge or *vector* supermultiplet.

The superpartners of the gauge bosons are generically referred to as gauginos. The $SU(3)_C$ color gauge interactions of QCD are mediated by the gluon, whose spin-1/2 color-octet supersymmetric partner is the gluino. The symbols for the gluon and gluino are g_a and $\widetilde{g}_a$ respectively. The electroweak gauge symmetry $SU(2)_L \otimes U(1)_Y$ is associated with spin-1 gauge bosons W^+, W^0, W^- and B^0, with spin-1/2 superpartners $\widetilde{W}^+, \widetilde{W}^0, \widetilde{W}^-$ and $\widetilde{B}^0$, called *winos* and *bino*. After electroweak symmetry breaking, the W^0, B^0 gauge eigenstates mix to give mass eigenstates Z^0 and γ. The corresponding gaugino mixtures of $\widetilde{W}^0$ and $\widetilde{B}^0$ are called zino ($\widetilde{Z}^0$) and photino ($\widetilde{\gamma}$); if supersymmetry were unbroken, they would be mass eigenstates with masses m_Z and 0. Table 2.6 summarizes the gauge supermultiplets of a minimal supersymmetric extension of the Standard Model. A symbol for each of the gauge superfields is included in second column of the table: $\hat{G}^a$, $\hat{W}$ and $\hat{B}$.

The chiral and gauge supermultiplets in Tables 2.5 and 2.6 make up the particle

content of the Minimal Supersymmetric Standard Model (MSSM). If supersymmetry were unbroken, then there would have to be selectrons $\widetilde{e}_L$ and $\widetilde{e}_R$ with masses exactly equal to $m_e = 0.511$ MeV. These particles would have been extraordinarily easy to detect a long time ago. Therefore, if supersymmetry is a symmetry of nature, it must be a broken symmetry. As we saw in Section 2.2.3, unbroken supersymmetry guarantees that the quadratic divergences in scalar squared masses must vanish to all orders in perturbation theory. Now, if broken supersymmetry is still to provide a solution to the hierarchy problem, then the relationships between dimensionless couplings that were required in an unbroken supersymmetric theory must be maintained ($\lambda_S = |\lambda_f|^2$). Otherwise, there would be quadratically divergent radiative corrections to the Higgs scalar masses of the form

$$\Delta m_H^2 = \frac{1}{8\pi^2}(\lambda_S - |\lambda_f|^2)\Lambda_{\mathrm{UV}}^2 + \dots . \tag{2.72}$$

In a broken supersymmetry, some of the terms that do not cancel automatically are of the form:

$$\Delta M_H^2 = \frac{\lambda^2}{16\pi^2}\left|m_S^2 - m_f^2\right| \tag{2.73}$$

where some smaller contributions have been omitted. Since these corrections must not be much greater than $m_{h_{SM}}$, then in order to avoid too much fine tuning we must have that [29, 30]

$$\left|m_S^2 - m_f^2\right| \lesssim 1\mathrm{TeV}^2 \tag{2.74}$$

Hence, one associates $\Lambda \sim 1$ TeV as the scale where the SM is no longer valid and must be substituted by its supersymmetric extension. This is however only a qualitative argument and does not help to predict with any certainty whether new particles should appear at 900 GeV or at 2 TeV.

Since supersymmetry is a broken symmetry of nature, we are therefore led to consider Lagrangian terms that will break supersymmetry at tree level. This is achieved by introducing terms by hand to the supersymmetry-conserving MSSM Lagrangian. The so-called "soft" terms are chosen to break supersymmetry explicitly which do not introduce unwanted effects such quadratically divergent terms. Therefore, the effective MSSM Lagrangian will have the form

$$\mathcal{L} = \mathcal{L}_{\text{SUSY}} + \mathcal{L}_{\text{soft}} \tag{2.75}$$

where $\mathcal{L}_{\text{SUSY}}$ contains all of the gauge and Yukawa interactions and preserves supersymmetry invariance, and $\mathcal{L}_{\text{soft}}$ violates supersymmetry but contains only mass terms and coupling parameters with *positive* mass dimension. Soft supersymmetry breaking will be discussed in more detail in Section 2.2.6.

An important feature of the MSSM is that the superpartners listed in Tables 2.5 and 2.6 are not necessarily the mass eigenstates of the theory. This is because after electroweak symmetry breaking and supersymmetry breaking effects are included, there can be mixing between the electroweak gauginos and higgsinos, and within the various sets of squarks and sleptons and Higgs scalars that have the same electric charge. The lone exception is the gluino, which is a color octet fermion and therefore does not have the appropriate quantum numbers to mix with any other particle.

The physical mass eigenstates that result from from the mixing of gauginos and higgsinos are model-dependent linear combinations of these states, called *charginos* and *neutralinos*, which are obtained by diagonalizing the corresponding mass matrices. There are two charginos ($\tilde{\chi}_i^{\pm}$) and four neutralinos ($\tilde{\chi}_i^0$), which are by convention ordered in masses ($\tilde{\chi}_1^{\pm}$ is the lowest chargino and $\tilde{\chi}_1^0$ is the lowest neutralino). Depending on whether the chargino or neutralino eigenstate approximates a particular gaugino or higgsino state, they can become more photino-like or bino-like.

The supersymmetric partners of the quarks and leptons are spin-zero bosons and the resulting squarks and sleptons can also mix their left- and right-handed components yielding the mass eigenstates (denoted by the indices 1,2 instead of L, R). This mixing is proportional to the mass of the SM partner quark or lepton and to $\tan\beta$ (to be defined later). Thus, the mixing can lead to an important splitting in the mass spectrum of heavy squarks, specially at large $\tan\beta$. In contrast, the first two families can be considered degenerate in mass. All physical particles of the MSSM are given in Table 2.7.

2HDM particle		**spin**	**SUSY particle**		**spin**
quarks:	q	$\frac{1}{2}$	squarks:	$\tilde{q}_1,\ \tilde{q}_2$	0
leptons:	l	$\frac{1}{2}$	sleptons:	$\tilde{l}_1,\ \tilde{l}_2$	0
gluons:	g_a	1	gluinos:	$\tilde{g}_a$	$\frac{1}{2}$
gauge bosons:	$W^{\pm}$, Z^0, γ	1	neutralinos:	$\tilde{\chi}_1^0,\ \tilde{\chi}_2^0,\ \tilde{\chi}_3^0,\ \tilde{\chi}_4^0$	$\frac{1}{2}$
Higgs bosons:	$h^0,\ H^0,\ A^0,\ H^{\pm}$	0	charginos:	$\tilde{\chi}_1^{\pm},\ \tilde{\chi}_2^{\pm}$	$\frac{1}{2}$

Table 2.7: The particle content of the MSSM.

2.2.5 MSSM Lagrangian and R-parity

The MSSM Lagrangian is constructed using the already defined particle content and following an analogous prescription used with the $\mathcal{L}_{\rm SM}$. Using a similar notation as in the SM, the kinetic term of the Lagrangian can be written as:

$$\begin{aligned}\mathcal{L}_{KE} &= \sum_i \left\{ (D_\mu S_i)^\dagger (D^\mu S_i) + \frac{i}{2}\bar{\psi}_i \gamma^\mu D_\mu \psi_i \right\} \\ &+ \sum_A \left\{ -\frac{1}{4} F^A_{\mu\nu} F^{\mu\nu A} + \frac{i}{2}\bar{\lambda}_A D \lambda_A \right\}\end{aligned} \tag{2.76}$$

Here, S_i (ψ_i) is the scalar (fermion) component of the i^{th} chiral superfield, D is the $SU(3)_C \otimes SU(2)_L \otimes\ U(1)_Y$ gauge invariant derivative, $F^A_{\mu\nu}$ is the Yang-Mills gauge field and λ_A is the gaugino superpartner of the corresponding gauge boson. It is worth noticing that the $\sum_i$ is a sum over all fermion fields of the SM, the scalar partners and the 2 Higgs doublets with their fermion partners. On the other hand, $\sum_A$ is over the $SU(3)_c$, $SU(2)_L$ and $U(1)_Y$ gauge fields with their fermion partners, the gauginos.

The interactions between bosons and fermions are completely determined by the gauge symmetries and by the supersymmetry:

$$\begin{aligned}\mathcal{L}_{int} = \quad & -\sqrt{2}\sum_{i,A} g_A \left[S_i^* T^A \bar{\psi}_{iL} \lambda_A + \text{h.c.}\right] \\ & -\tfrac{1}{2}\sum_A \left(\sum_i g_A S_i^* T^A S_i\right)^2\end{aligned} \tag{2.77}$$

where $\psi_L \equiv \frac{1}{2}(1-\gamma_5)\,\psi$, T^A is the matrix of the group generators and g_A the gauge coupling constants. It can be seen that there are no adjustable parameter, hence, all interaction strengths are completely fixed in terms of SM coupling constants.

Once the superfields and the gauge symmetries are chosen, the only freedom in constructing $\mathcal{L}_{MSSM}$ is contained in a function called the *superpotential*, $\mathcal{W}$ which contains all possible supersymmetry-resptecting interactions. This is an analytic function[3] of the chiral superfields, $\hat{S}$, that has the form:

$$\mathcal{W} = \epsilon_{ij}\mu \hat{H}_u^i \hat{H}_d^j + \epsilon_{ij}\left[y_E \hat{H}_d^i \bar{\hat{L}}^j \bar{\hat{E}} + y_D \hat{H}_d^i \hat{Q} \bar{\hat{D}} + y_U \hat{H}_u^j \hat{Q}^i \bar{\hat{U}}\right] + W_{RP} \tag{2.78}$$

where i and j are $SU(2)_L$ doublet indices and $\epsilon_{ij} = -\epsilon_{ji}$ (with $\epsilon_{12} = 1$) contracts the $SU(2)_L$ doublet fields. The term $\mu \hat{H}_u^i \hat{H}_d^j$ gives mass terms for the Higgs bosons and thus μ is often called the Higgs mass parameter. The terms in the square brackets

[3]The superpotential is analytic in the sense that it does not have complex conjugate fields

that are proportional to y_E, y_D and y_U give the usual Yukawa interactions of the fermions with the Higgs bosons.

The Yukawa matrices determine the current masses and the CKM mixing angles of the ordinary quarks and leptons after the neutral scalar components of H_u and H_d get VEVs. Since the top quark, bottom quark and tau lepton are the heaviest fermions in the Standard Model, it is often useful to make an approximation that only the $(3,3)$ family components of each of $\mathbf{y_u}$, $\mathbf{y_d}$ and $\mathbf{y_e}$ are important:

$$\mathbf{y_u} \approx \begin{pmatrix} 0 & 0 & 0 \\ 0 & 0 & 0 \\ 0 & 0 & y_t \end{pmatrix}, \qquad \mathbf{y_d} \approx \begin{pmatrix} 0 & 0 & 0 \\ 0 & 0 & 0 \\ 0 & 0 & y_b \end{pmatrix}, \qquad \mathbf{y_e} \approx \begin{pmatrix} 0 & 0 & 0 \\ 0 & 0 & 0 \\ 0 & 0 & y_\tau \end{pmatrix}. \tag{2.79}$$

In this limit, only the third family and Higgs fields contribute to the MSSM superpotential. It is instructive to write the superpotential in terms of the separate $SU(2)_L$ weak isospin components [$\hat{Q}_3 = (t\, b)$, $\hat{L}_3 = (\nu_\tau\, \tau)$, $\hat{H}_u = (H_u^+\, H_u^0)$, $\hat{H}_d = (H_d^0\, H_d^-)$, $\hat{U}_3 = \overline{t}$, $\hat{D}_3 = \overline{b}$, $\hat{E}_3 = \overline{\tau}$], so:

$$\begin{aligned} \mathcal{W} \;\approx\; & y_t(\overline{t}tH_u^0 - \overline{t}bH_u^+) - y_b(\overline{b}tH_d^- - \overline{b}bH_d^0) - y_\tau(\overline{\tau}\nu_\tau H_d^- - \overline{\tau}\tau H_d^0) \\ & +\mu(H_u^+ H_d^- - H_u^0 H_d^0) \end{aligned} \tag{2.80}$$

However, the dimensionless interactions determined by the superpotential are usually not the most important ones of direct interest for phenomenology. This is because the Yukawa couplings are already known to be very small, except for those of the third family (top, bottom, tau). Instead, production and decay processes for superpartners in the MSSM are typically dominated by the supersymmetric interactions of gauge-coupling strength. The couplings of the Standard Model gauge bosons (photon, $W^\pm$, Z^0 and gluons) to the MSSM particles are determined completely by the gauge

invariance of the kinetic terms in the Lagrangian. The gauginos also couple to (squark, quark) and (slepton, lepton) and (Higgs, higgsino) pairs.

In the most general superpotential, one can add more terms that are gauge-invariant and analytic in the chiral superfields, which are grouped under W_{RP} in Equation 2.78. These terms are of the form:

$$W_{RP} = \lambda_{\alpha\beta\gamma}\hat{L}^{\alpha}\hat{L}^{\beta}\bar{\hat{E}}^{\gamma} + \lambda'_{\alpha\beta\gamma}\hat{L}^{\alpha}\hat{Q}^{\beta}\bar{\hat{D}}^{\gamma} + \lambda''_{\alpha\beta\gamma}\bar{\hat{U}}^{\alpha}\bar{\hat{D}}^{\beta}\bar{\hat{D}}^{\gamma} + \mu'\hat{L}\hat{H} \tag{2.81}$$

where the indices α, β and γ label the 3 generations of quarks and leptons. These terms constitute a problem in the sense that the first two contribute to lepton number violation interactions, and the third one to baryon number violation interactions[4]. The possible existence of such terms might seem rather disturbing, since corresponding B- and L-violating processes have not been seen experimentally. The chiral supermultiplets carry baryon number assignments B = +1/3 for $\hat{Q}_i$, B = −1/3 for $\hat{U}_i, \hat{D}_i$ and B = 0 for all others. The total lepton number assignments are L = +1 for $\hat{L}_i$, L = −1 for $\hat{E}_i$, and L = 0 for all others. Therefore, the first two terms in eq. (2.81) violate total lepton number by 1 unit (as well as the individual lepton flavors) and the third term violates baryon number by 1 unit. The combination of lepton and baryon violation terms can contribute to the proton decay at tree level through the exchange of the scalar partner of the down quark, which would violate both B and L by 1 unit. Since this process is experimentally restricted [32, 33, 34, 35, 36, 37, 38, 39] it puts into question the validity of the model. If both λ' and λ'' couplings were present and unsuppressed, then the lifetime of the proton would be extremely short. For example, these terms would lead to decays such as $p^+ \to e^+\pi^0$ or e^+K^0 or $\mu^+\pi^0$ or μ^+K^0 or $\nu\pi^+$ or νK^+ etc. depending on which components of λ' and λ'' are largest.

[4]The fourth term can be ignored since one can implement a rotation in the lepton field $\hat{L}$ such that this term vanishes [31].

As a rough estimate based on dimensional analysis, for example,

$$\Gamma_{p\to e^+\pi^0} \sim m^5_{\rm proton} \sum_{i=2,3} |\lambda'^{11i}\lambda''^{11i}|^2/m^4_{\tilde{d}_i}, \tag{2.82}$$

which would be a tiny fraction of a second if the couplings were of order unity and the squarks had masses of order 1 TeV. In contrast, the decay time of the proton into lepton+meson final states is known experimentally to be in excess of 10^{32} years. Therefore, at least one of λ'^{ijk} or λ''^{11k} for each of $i = 1, 2$; $j = 1, 2$; $k = 2, 3$ must be extremely small. Many other processes also give strong constraints on the violation of lepton and baryon numbers [40, 41].

One could simply try to take B and L conservation as a postulate in the MSSM. However, this is clearly a step backward from the situation in the Standard Model, where the conservation of these quantum numbers is *not* assumed, but is rather a consequence of the fact that there are no possible renormalizable Lagrangian terms that violate B or L. Furthermore, there is a quite general obstacle to treating B and L as fundamental symmetries of Nature, since they are known to be necessarily violated by non-perturbative electroweak effects [42] (even though those effects are calculably negligible for experiments at ordinary energies). The preferred solution, however, is to introduce a new symmetry to the MSSM called R-parity [40, 43, 44, 45, 46, 47, 48], which has the effect of eliminating the possibility of B and L violating terms in the renormalizable superpotential. R-parity (R_p) is a multiplicative quantum number defined as:

$$R = (-1)^{3(B-L)+2s}\ , \tag{2.83}$$

where B and L are the baryon and lepton quantum numbers and s is the spin of the particle. Thus, all SM particles have $R_p = +1$ while their SUSY partners have $R_p = -1$. The R-parity assignment is very useful for phenomenology because all of the

Standard Model particles and the Higgs bosons have even R-parity ($P_R = +1$), while all of the squarks, sleptons, gauginos, and higgsinos have odd R-parity ($P_R = -1$). The R-parity odd particles are known as "supersymmetric particles" or "sparticles" for short, and they are distinguished by a tilde (see Tables 2.5 and 2.6).

If R-parity is exactly conserved, then there can be no mixing between the sparticles and the $P_R = +1$ particles. Furthermore, every interaction vertex in the theory contains an even number of $P_R = -1$ sparticles. This has three extremely important phenomenological consequences:

- The lightest sparticle with $P_R = -1$, called the "lightest supersymmetric particle" or LSP, must be stable. If the LSP is electrically neutral, it interacts only weakly with ordinary matter, and so can make an attractive candidate [49] for the non-baryonic dark matter that seems to be required by cosmology[5].
- Each sparticle other than the LSP must eventually decay into a state that contains an odd number of LSPs (usually just one).
- In collider experiments, sparticles can only be produced in even numbers (usually two-at-a-time).

2.2.6 SUSY breaking

Because supersymmetric particles have not been observed, the exact symmetry would need to be hidden at low energies in a manner analogous to electroweak symmetry. Otherwise, squarks and quarks would have equal masses and gluinos would be massless. Since this is not the case in nature, supersymmetry should be an exact symmetry that is broken. As we saw at the end of Section 2.2.4, it is instructive

[5]Due to cosmological constraints, a cold dark matter candidate need to be stable and neutral [50, 41].

to introduce terms into the Lagrangian that explicitly break supersymmetry without having to specify their possible origin. The supersymmetry-breaking couplings should be soft (of positive mass dimension) in order to be able to naturally maintain a hierarchy between the electroweak scale and the Planck (or any other very large) mass scale. This means in particular that dimensionless supersymmetry-breaking couplings should be absent. To prevent dangerous quadratic divergences, only a certain subset of supersymmetry-breaking terms are allowed to be present in the theory and their couplings are denoted as *soft* parameters. Then, the so-called soft Lagrangian which breaks SUSY is (first generation only):

$$\begin{aligned}
-\mathcal{L}_{soft} = & \frac{1}{2}\left[M_3\hat{g}\hat{g} + M_2\hat{W}\hat{W} + M_1\hat{B}\hat{B}\right] \\
& + \epsilon_{\alpha\beta}\left[-bH_d^\alpha H_u^\beta - H_u^\alpha \hat{Q}_i^\beta \hat{A}_{u_{ij}}\bar{\hat{U}}_j + H_d^\alpha \hat{Q}_i^\beta \hat{A}_{d_{ij}}\bar{\hat{D}}_j + H_d^\alpha \hat{L}_i^\beta \hat{A}_{e_{ij}}\bar{\hat{E}}_j + \text{h.}c.\right] \\
& + m_{H_d}^2|H_d|^2 + m_{H_u}^2|H_u|^2 + \hat{Q}_i^\alpha m_{Q_{ij}}^2 \hat{Q}_j^{\alpha *} \\
& + \hat{L}_i^\alpha m_{L_{ij}}^2 \hat{L}_j^{\alpha *} + \bar{\hat{U}}_i^* m_{U_{ij}}^2 \bar{\hat{U}}_j + \bar{\hat{D}}_i^* m_{D_{ij}}^2 \bar{\hat{D}}_j + \bar{\hat{E}}_i^* m_{E_{ij}}^2 \bar{\hat{E}}_j \ ,
\end{aligned} \tag{2.84}$$

where i and j are the $SU(2)_L$ doublet indices. It has been shown rigorously that a softly broken supersymmetric theory with $\mathcal{L}_{\text{soft}}$ as given by Equation (2.84) is indeed free of quadratic divergences in quantum corrections to scalar masses, to all orders of perturbation theory [51]. If the largest mass scale associated with the soft terms is denoted by m_{soft}, then the mass splittings between the known Standard Model particles and their superpartners cannot be too large, setting an upper limit to m_{soft} of the order of the TeV scale. Otherwise, we would lose our successful cure for the hierarchy problem, since the m_{soft}^2 corrections to the Higgs scalar squared mass parameter would be unnaturally large compared to the square of the electroweak breaking scale of 174 GeV. Therefore, we expect

$$M_1,\, M_2,\, M_3,\, \hat{A}_{u_{ij}},\, \hat{A}_{d_{ij}},\, \hat{A}_{e_{ij}} \sim m_{\text{soft}}, \tag{2.85}$$

$$m_{Q_{ij}}^2,\, m_{L_{ij}}^2,\, m_{U_{ij}}^2,\, m_{D_{ij}}^2,\, m_{E_{ij}}^2,\, m_{H_u}^2,\, m_{H_d}^2,\, b \sim m_{\text{soft}}^2, \tag{2.86}$$

with a characteristic mass scale m_{soft} that is not much larger than 1 TeV. The expression in Equation (2.84) is the most general soft supersymmetry-breaking Lagrangian that is compatible with gauge invariance and R-parity conservation in the MSSM, and that it does not introduce quadratic divergences.

Unlike the supersymmetry-preserving part of the Lagrangian, the above $\mathcal{L}_{\text{soft}}^{\text{MSSM}}$ introduces many new parameters that were not present in the ordinary Standard Model. A careful count [52] reveals that there are 105 masses, phases and mixing angles in the MSSM Lagrangian that cannot be rotated away by redefining the phases and flavor basis for the quark and lepton supermultiplets, and that have no counterpart in the ordinary Standard Model. Thus, in principle, supersymmetry *breaking* (as opposed to supersymmetry itself) appears to introduce a tremendous arbitrariness in the Lagrangian. The scalar and gaugino mass terms have the desired effect of breaking the mass degeneracy between the particles and their SUSY partners. The tri-linear A terms affect primarily the particles of the third generation. The b term mixes the scalar components of the two Higgs doublets. All of the quantities in $\mathcal{L}_{soft}$ receive radiative corrections and thus are scale-dependent, satisfying known Renormalisation Group Equations (RGEs).

However, a soft supersymmetry-breaking Lagrangian cannot be arbitrary or random. This is because most of the new parameters in eq. (2.84) allow flavor mixing or CP violating processes that are severely restricted by experiment [53]-[54]. For example, if $\mathbf{m_E^2}$ were not diagonal in the basis $(\widetilde{e}_R, \widetilde{\mu}_R, \widetilde{\tau}_R)$ of sleptons, then slepton mixing would occur and the individual lepton numbers would not be conserved. There are also contributions to $\mu \to e\gamma$ that depend on the off-diagonal elements of the left-handed slepton squared-mass matrix $\mathbf{m_L^2}$, therefore, the slepton squared-mass matrices should not have significant mixings for $\widetilde{e}_L, \widetilde{\mu}_L$ either. Furthermore, after the Higgs scalars get VEVs, the $\mathbf{\hat{A}_e}$ matrix could imply squared-mass terms that mix left-handed and right-handed sleptons with different lepton flavors, which would also

contribute to $\mu \to e\gamma$ through $(\hat{A}_e)_{12}$ and $(\hat{A}_e)_{21}$ and therefore are required to be small.

All of these potentially dangerous flavor-changing and CP-violating effects in the MSSM soft Lagrangian can be avoided if one assumes that supersymmetry breaking is suitably "universal," that is, the squark and slepton squared-mass matrices are flavor-blind, each proportional to the 3×3 identity matrix in family space:

$$\mathbf{m_Q^2} = m_Q^2 \mathbf{1}, \quad \mathbf{m_U^2} = m_U^2 \mathbf{1}, \quad \mathbf{m_D^2} = m_D^2 \mathbf{1}, \quad \mathbf{m_L^2} = m_L^2 \mathbf{1}, \quad \mathbf{m_E^2} = m_E^2 \mathbf{1}. \tag{2.87}$$

Then all squark and slepton mixing angles are rendered trivial, because squarks and sleptons with the same electroweak quantum numbers will be degenerate in mass. Supersymmetric contributions to flavor-changing neutral current processes will therefore be very small in such an idealized limit, up to mixing induced by $\mathbf{\hat{A}_u}$, $\mathbf{\hat{A}_d}$, $\mathbf{\hat{A}_e}$. Making the further assumption that the (scalar)^3 couplings are each proportional to the corresponding Yukawa coupling matrix,

$$\mathbf{\hat{A}_u} = A_{u0}\, \mathbf{y_u}, \qquad \mathbf{\hat{A}_d} = A_{d0}\, \mathbf{y_d}, \qquad \mathbf{\hat{A}_e} = A_{e0}\, \mathbf{y_e}, \tag{2.88}$$

will ensure that only the squarks and sleptons of the third family can have large (scalar)^3 couplings. Finally, one can avoid large CP-violating effects by assuming that the soft parameters do not introduce new complex phases. This is automatic for $m_{H_u}^2$ and $m_{H_d}^2$, and for m_Q^2, m_U^2, etc. if eq. (2.87) is assumed. One can also fix μ in the superpotential and b in eq. (2.84) to be real, by appropriate phase rotations of fermion and scalar components of the H_u and H_d supermultiplets. If one then assumes that

$$\arg(M_1),\, \arg(M_2),\, \arg(M_3),\, \arg(A_{u0}),\, \arg(A_{d0}),\, \arg(A_{e0}) \;=\; 0 \text{ or } \pi, \tag{2.89}$$

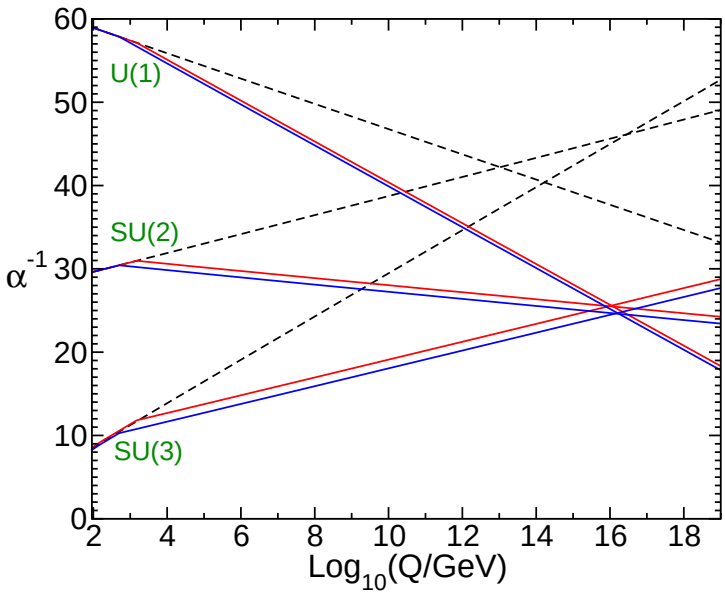

Figure 2.4: RG evolution of the inverse gauge couplings $\alpha_a^{-1}(Q)$ in the Standard Model (dashed lines) and the MSSM (solid lines). In the MSSM case, the sparticle mass thresholds are varied between 250 GeV and 1 TeV, and $\alpha_3(m_Z)$ between 0.113 and 0.123. Two-loop effects are included.

then the only CP-violating phase in the theory will be the usual CKM phase found in the ordinary Yukawa couplings.

The conditions of eqs. (2.87)-(2.89) make up what is called the hypothesis of *soft supersymmetry-breaking universality*. These equations could be interpreted as an assumed underlying simplicity or symmetry of the Lagrangian at some very high energy scale Q_0, such as the GUT scale; therefore, they should be viewed as boundary conditions on the running soft parameters at that input scale, which is likely very far removed from direct experimental probes. We must then RG-evolve all of the soft parameters, the superpotential parameters, and the gauge couplings down to the electroweak scale or comparable scales where experiments are performed. At the electroweak scale, Equations (2.87) and (2.88) will no longer hold exaclty, however, to a good approximation, key flavor- and CP-conserving properties remain.

An interesting result in favor of the MSSM is its apparent unification of gauge couplings at a scale $M_U \sim 2 \times 10^{16}$ GeV [55]. Figure 2.4 compares the RG evolution of the α_a^{-1}, including two-loop effects, in the Standard Model (dashed lines) and the MSSM (solid lines). Unlike the Standard Model, the MSSM includes just the

right particle content to ensure that the gauge couplings can unify, at a scale $M_U \sim 2 \times 10^{16}$ GeV. While the apparent unification of gauge couplings at M_U might be just an accident, it may also be taken as a strong hint in favor of a grand unified theory (GUT) which accommodates gauge coupling unification below $M_{\rm P}$.

The basic question to be addressed next regards the nature of the explicit soft supersymmetry breaking mechanism which results in the $\mathcal{L}_{soft}$ parameters. Various models have been postulated which provide a different mechanism for SUSY breaking, for example, in Supergravity (SUGRA), the force of gravity communicates the origins of SUSY breaking from a high mass scale to the electroweak scale. In a particular SUGRA model, the so-called minimal SUGRA model (mSUGRA), grand unification is presumed at a high mass scale ($\simeq 10^{16}$ GeV) and the MSSM spectrum can be fully characterized by 4 parameters and a sign at the grand unification theory (GUT): a common scalar mass (m_0), a common gaugino mass ($m_{\frac{1}{2}}$), a common trilinear coupling value (A_0), the ratio of the vacuum expectation values of the two Higgs doublets ($\tan\beta$), and the sign of μ, where μ is the Higgsino mass parameter. A more detailed introduction to mSUGRA will follow in Chapter 3.

A different possibility is that the flavor-blind mediating interactions for supersymmetry breaking are the ordinary electroweak and QCD gauge interactions. In this *gauge-mediated supersymmetry breaking* (GMSB) models [56, 57], the MSSM soft terms come from loop diagrams involving some *messenger* particles. The messengers are new chiral supermultiplets that couple to a supersymmetry-breaking VEV, and also have $SU(3)_C \times SU(2)_L \times U(1)_Y$ interactions, which provide the necessary connection to the MSSM. In contrast to mSUGRA, GMSB can be understood entirely in terms of loop effects in a renormalizable framework. This model is beyond the scope of this thesis.

2.2.7 Neutralinos and charginos

The higgsinos and electroweak gauginos mix with each other because of the effects of electroweak symmetry breaking. The neutral higgsinos ($\widetilde{H}_u^0$ and $\widetilde{H}_d^0$) and the neutral gauginos ($\widetilde{B}$, $\widetilde{W}^0$) combine to form four mass eigenstates called *neutralinos*. The charged higgsinos ($\widetilde{H}_u^+$ and $\widetilde{H}_d^-$) and winos ($\widetilde{W}^+$ and $\widetilde{W}^-$) mix to form two mass eigenstates with charge ± 1 called *charginos*. We will denote the neutralino and chargino mass eigenstates by $\widetilde{\chi}_i^0$ ($i = 1, 2, 3, 4$) and $\widetilde{\chi}_i^\pm$ ($i = 1, 2$). By convention, these are labeled in ascending order, so that $m_{\widetilde{\chi}_1^0} < m_{\widetilde{\chi}_2^0} < m_{\widetilde{\chi}_3^0} < m_{\widetilde{\chi}_4^0}$ and $m_{\widetilde{\chi}_1^\pm} < m_{\widetilde{\chi}_2^\pm}$. The lightest neutralino, $\widetilde{\chi}_1^0$, is usually assumed to be the LSP, unless there is a lighter gravitino or unless R-parity is not conserved.

In the gauge-eigenstate basis $\psi^0 = (\widetilde{B}, \widetilde{W}^0, \widetilde{H}_d^0, \widetilde{H}_u^0)$, the neutralino mass part of the Lagrangian is

$$\mathcal{L}_{\text{neutralino mass}} = -\frac{1}{2}(\psi^0)^T \mathbf{M}_{\widetilde{\chi}^0} \psi^0 + \text{c.c.}, \tag{2.90}$$

where

$$\mathbf{M}_{\widetilde{\chi}^0} = \begin{pmatrix} M_1 & 0 & -g'v_d/\sqrt{2} & g'v_u/\sqrt{2} \\ 0 & M_2 & gv_d/\sqrt{2} & -gv_u/\sqrt{2} \\ -g'v_d/\sqrt{2} & gv_d/\sqrt{2} & 0 & -\mu \\ g'v_u/\sqrt{2} & -gv_u/\sqrt{2} & -\mu & 0 \end{pmatrix}. \tag{2.91}$$

The entries M_1 and M_2 in this matrix come directly from the MSSM soft Lagrangian [see eq. (2.84)], while the entries $-\mu$ are the supersymmetric higgsino mass terms. The terms proportional to g, g' are the result of Higgs-higgsino-gaugino couplings,

with the Higgs scalars replaced by their VEVs: v_u and v_d. This can also be written as

$$\mathbf{M}_{\widetilde{\chi}^0} = \begin{pmatrix} M_1 & 0 & -c_\beta\, s_W\, m_Z & s_\beta\, s_W\, m_Z \\ 0 & M_2 & c_\beta\, c_W\, m_Z & -s_\beta\, c_W\, m_Z \\ -c_\beta\, s_W\, m_Z & c_\beta\, c_W\, m_Z & 0 & -\mu \\ s_\beta\, s_W\, m_Z & -s_\beta\, c_W\, m_Z & -\mu & 0 \end{pmatrix} \tag{2.92}$$

Here we have introduced abbreviations $s_\beta = \sin\beta$, $c_\beta = \cos\beta$, $s_W = \sin\theta_W$, and $c_W = \cos\theta_W$. The mass matrix $\mathbf{M}_{\widetilde{\chi}^0}$ can be diagonalized by a unitary matrix $\mathbf{N}$ to obtain mass eigenstates:

$$\widetilde{\chi}_i^0 = \mathbf{N}_{ij}\psi_j^0, \tag{2.93}$$

where $\mathbf{N}_{ij}$ is the mixing matrix, so that

$$\mathbf{N}^*\mathbf{M}_{\widetilde{N}}\mathbf{N}^{-1} = \begin{pmatrix} m_{\widetilde{\chi}_1^0} & 0 & 0 & 0 \\ 0 & m_{\widetilde{\chi}_2^0} & 0 & 0 \\ 0 & 0 & m_{\widetilde{\chi}_3^0} & 0 \\ 0 & 0 & 0 & m_{\widetilde{\chi}_4^0} \end{pmatrix} \tag{2.94}$$

has real positive entries on the diagonal. These are the magnitudes of the eigenvalues of $\mathbf{M}_{\widetilde{\chi}^0}$, or equivalently the square roots of the eigenvalues of $\mathbf{M}_{\widetilde{\chi}^0}^\dagger\mathbf{M}_{\widetilde{\chi}^0}$. The indices (i, j) on $\mathbf{N}_{ij}$ are (mass, gauge) eigenstate labels.

The chargino spectrum can be analyzed in a similar way. In the gauge-eigenstate basis $\psi^{\pm} = (\widetilde{W}^{+}, \widetilde{H}_u^{+}, \widetilde{W}^{-}, \widetilde{H}_d^{-})$, the chargino mass terms in the Lagrangian are

$$\mathcal{L}_{\text{chargino mass}} = -\frac{1}{2}(\psi^{\pm})^T \mathbf{M}_{\widetilde{\chi}^{\pm}} \psi^{\pm} + \text{c.c.} \tag{2.95}$$

where, in 2×2 block form,

$$\mathbf{M}_{\widetilde{\chi}^{\pm}} = \begin{pmatrix} \mathbf{0} & \mathbf{X}^T \\ \mathbf{X} & \mathbf{0} \end{pmatrix}, \tag{2.96}$$

with

$$\mathbf{X} = \begin{pmatrix} M_2 & g v_u \\ g v_d & \mu \end{pmatrix} = \begin{pmatrix} M_2 & \sqrt{2} s_\beta \, m_W \\ \sqrt{2} c_\beta \, m_W & \mu \end{pmatrix}. \tag{2.97}$$

The mass eigenstates are related to the gauge eigenstates by two unitary 2×2 matrices $\mathbf{U}$ and $\mathbf{V}$ according to

$$\begin{pmatrix} \widetilde{\chi}_1^{+} \\ \widetilde{\chi}_2^{+} \end{pmatrix} = \mathbf{V} \begin{pmatrix} \widetilde{W}^{+} \\ \widetilde{H}_u^{+} \end{pmatrix}, \qquad \begin{pmatrix} \widetilde{\chi}_1^{-} \\ \widetilde{\chi}_2^{-} \end{pmatrix} = \mathbf{U} \begin{pmatrix} \widetilde{W}^{-} \\ \widetilde{H}_d^{-} \end{pmatrix}. \tag{2.98}$$

Note that the mixing matrix for the positively charged left-handed fermions is different from that for the negatively charged left-handed fermions. They are chosen so that

$$\mathbf{U}^* \mathbf{X} \mathbf{V}^{-1} = \begin{pmatrix} m_{\widetilde{\chi}_1^{\pm}} & 0 \\ 0 & m_{\widetilde{\chi}_2^{\pm}} \end{pmatrix}, \tag{2.99}$$

with positive real entries $m_{\widetilde{\chi}_i^\pm}$. Because these are only 2×2 matrices, it is not hard to solve for the masses explicitly:

$$\begin{aligned} m^2_{\widetilde{\chi}_1}, m^2_{\widetilde{\chi}_2} &= \frac{1}{2}\Big[|M_2|^2 + |\mu|^2 + 2m_W^2 \\ &\quad \mp\sqrt{(|M_2|^2 + |\mu|^2 + 2m_W^2)^2 - 4|\mu M_2 - m_W^2 \sin 2\beta|^2}\Big]. \end{aligned} \tag{2.100}$$

These are the (doubly degenerate) eigenvalues of the 4×4 matrix $\mathbf{M}^\dagger_{\widetilde{\chi}^\pm}\mathbf{M}_{\widetilde{\chi}^\pm}$, or equivalently the eigenvalues of $\mathbf{X}^\dagger\mathbf{X}$, since

$$\mathbf{V}\mathbf{X}^\dagger\mathbf{X}\mathbf{V}^{-1} = \mathbf{U}^*\mathbf{X}\mathbf{X}^\dagger\mathbf{U}^T = \begin{pmatrix} m^2_{\widetilde{\chi}_1^\pm} & 0 \\ 0 & m^2_{\widetilde{\chi}_2^\pm} \end{pmatrix}. \tag{2.101}$$

Note that the discussion above yields the tree-level masses.

If the gaugino masses and the gauge couplings unify at the GUT scale [58], then

$$\frac{M3}{g_s^2} = \frac{M2}{g_2^2} = \frac{M1}{5/3g_Y^2} = \frac{m_{1/2}}{g^2(MGUT)} \tag{2.102}$$

which is invariant under the application of the renormalization group equation [16]. Using Equation 2.46 this implies that

$$\frac{M_1(m_Z)}{M_2(m_Z)} = \frac{5}{3}\tan^2\theta_W \approx \frac{1}{2} \tag{2.103}$$

In the limit of $\mu \gg |M_i| \gg m_Z$, $i = 1, 2$, the lightest neutralino $\widetilde{\chi}_1^0$ is mostly Bino, the next to lightest $\widetilde{\chi}_2^0$ neutralino is mostly neutral Wino and the neutralinos $\widetilde{\chi}_i^0$, $i = 3, 4$, are mostly neutral Higgsinos. The lighter chargino $\widetilde{\chi}_1^\pm$ is mostly charged Wino, while the heavier chargino is mostly charged Higgsino. Their respective masses roughly satisfy

$$m_{\widetilde{\chi}_1^\pm} \approx m_{\widetilde{\chi}_2^0} \approx 2 \cdot m_{\widetilde{\chi}_1^0}, \quad |\mu| \approx m_{\widetilde{\chi}_3^0} \approx m_{\widetilde{\chi}_4^0} \approx m_{\widetilde{\chi}_2^\pm} \gg m_{\widetilde{\chi}_1^\pm} \tag{2.104}$$

In the limit of $\mu \ll |M_i|$, $i = 1, 2$, the neutralinos $\widetilde{\chi}_i^0$, $i = 1, 2$, are mostly neutral Higgsinos and the neutralinos $\widetilde{\chi}_i^0$, $i = 3, 4$, are mostly Bino and neutral Wino, respectively. The lighter chargino $\widetilde{\chi}_1^\pm$ is mostly charged Higgsino and the heavier chargino $\widetilde{\chi}_2^\pm$ is mostly charged Wino. Their masses satisfy

$$m_{\widetilde{\chi}_1^\pm} \approx m_{\widetilde{\chi}_1^0} \approx m_{\widetilde{\chi}_2^0} \approx |\mu|, \quad 2 \cdot m_{\widetilde{\chi}_3^0} \approx m_{\widetilde{\chi}_4^0} \approx m_{\widetilde{\chi}_2^\pm} \tag{2.105}$$

2.2.8 Decays of neutralinos and charginos

As we saw in Section 2.2.7, each neutralino and chargino contains at least a small component of the electroweak gauginos $\widetilde{B}$, $\widetilde{W}^0$ or $\widetilde{W}^\pm$. So $\widetilde{\chi}_i^\pm$ and $\widetilde{\chi}_i^0$ inherit couplings of weak interaction strength to (scalar, fermion) pairs. The relevant couplings of the chargino and neutralino components are listed in Figure 2.5. It has to be noted that the charged Wino $\widetilde{W}^\pm$ couples only to left-handed sleptons and that the Higgsino $\widetilde{H}$ has a Yukawa coupling to third generation particles. If sleptons or squarks are

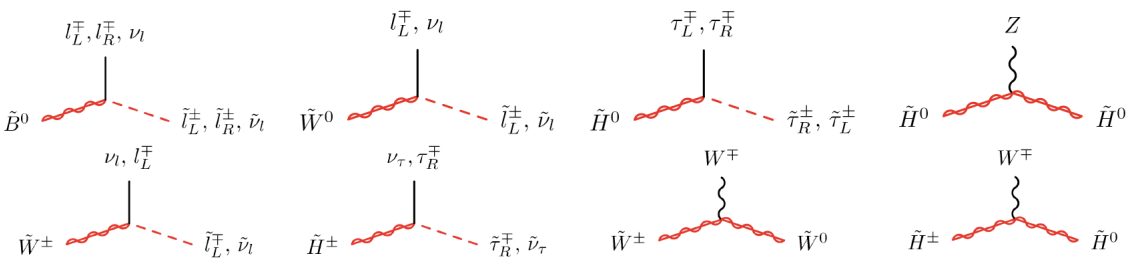

Figure 2.5: Relevant couplings of the components of chargino and neutralino.

sufficiently light, a neutralino or chargino can therefore decay into lepton+slepton or quark+squark. If sleptons are lighter than squarks, the lepton+slepton final states are favored. A neutralino or chargino may also decay into any lighter neutralino or chargino and a Higgs scalar or an electroweak gauge boson, because they inherit the gaugino-higgsino-Higgs and $SU(2)_L$ gaugino-gaugino-vector boson couplings of their

components. So, the possible two-body decay modes for neutralinos and charginos in the MSSM are:

$$\widetilde{\chi}_i^0 \to Z\widetilde{\chi}_j^0, \;\; W\widetilde{\chi}_j^\pm, \;\; h^0\widetilde{\chi}_j^0, \;\; \ell\widetilde{\ell}, \;\; \nu\widetilde{\nu}, \;\; [A^0\widetilde{\chi}_j^0, \;\; H^0\widetilde{\chi}_j^0, \;\; H^\pm\widetilde{\chi}_j^\pm, \;\; q\widetilde{q}], \tag{2.106}$$

$$\widetilde{\chi}_i^\pm \to W\widetilde{\chi}_j^0, \;\; Z\widetilde{\chi}_1^\pm, \;\; h^0\widetilde{\chi}_1^\pm, \;\; \ell\widetilde{\nu}, \;\; \nu\widetilde{\ell}, \;\; [A^0\widetilde{\chi}_1^\pm, \;\; H^0\widetilde{\chi}_1^\pm, \;\; H^\pm\widetilde{\chi}_j^0, \;\; q\widetilde{q}'], \tag{2.107}$$

where ν, ℓ, q represent neutrinos, charged leptons, and quarks respectively. The final states in brackets are the most kinematically restricted. Since the Higgs scalar h^0 is required to be light, it is also the most likely of the Higgs particles to appear in the final state.

If two-body decays are kinematically forbidden for a given chargino or neutralino, especially for $\widetilde{\chi}_1^\pm$ and $\widetilde{\chi}_2^0$, then three-body decays may occur

$$\widetilde{\chi}_i^0 \to ff\widetilde{\chi}_j^0, \quad \widetilde{\chi}_i^0 \to ff'\widetilde{\chi}_j^\pm, \quad \widetilde{\chi}_i^\pm \to ff'\widetilde{\chi}_j^0, \quad \text{and} \quad \widetilde{\chi}_2^\pm \to ff\widetilde{\chi}_1^\pm, \tag{2.108}$$

through the same gauge bosons, Higgs scalars, sleptons, and squarks that appeared in the two-body decays of Equations (2.106) and (2.107), but now off-shell. Here f represents a lepton or quark, with f and f' being distinct members of the same $SU(2)_L$ multiplet, and where one of the them in each of these decays is an antifermion.

The Feynman diagrams for the decays of chargino and neutralino with $\widetilde{\chi}_1^0$ in the final state that seem most likely to be important are shown in figures 2.6 and 2.7. In many situations, the decays

$$\widetilde{\chi}_1^\pm \to \ell^\pm\nu\widetilde{\chi}_1^0, \qquad \widetilde{\chi}_2^0 \to \ell^+\ell^-\widetilde{\chi}_1^0 \tag{2.109}$$

can be particularly important for phenomenology, because the leptons in the final state would commonly result in clean signals. In parts of the parameter space of the

mSUGRA model these decays are more likely if the intermediate sleptons mediating the decay chain are relatively light, even if they cannot be on-shell.

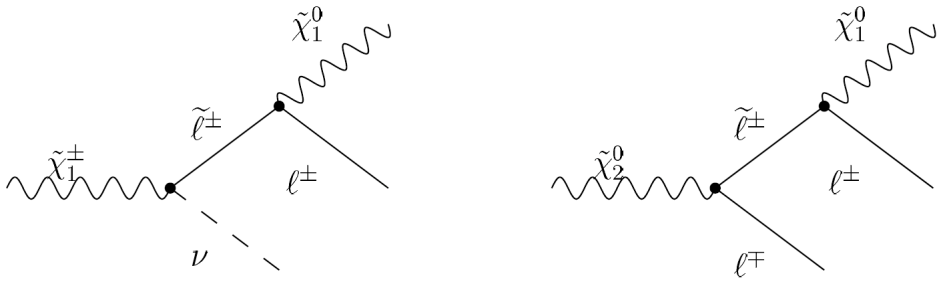

Figure 2.6: Two body decay modes for $\widetilde{\chi}_1^{\pm}$ (left) and $\widetilde{\chi}_2^0$ (right). These modes via real sleptons occur when the slepton mass is smaller than that of the chargino and neutralino.

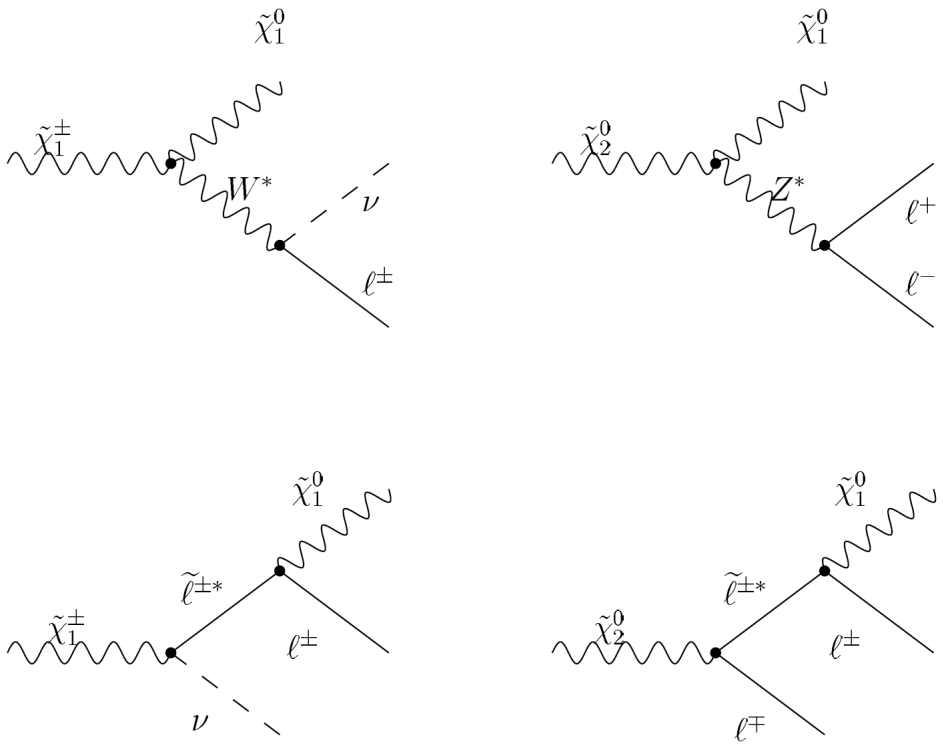

Figure 2.7: Three body decay modes for $\widetilde{\chi}_1^\pm$ (left) and $\widetilde{\chi}_2^0$ (right). These modes occur when the slepton mass is larger than the chargino and neutralino masses, so the decay occurs via virtual $W^\pm$ and Z^0 (top) or via virtual sleptons (bottom).

If the mSUGRA parameter tanβ is large, then τ and b Yukawa couplings become non-negligible as well, and as a result, $\widetilde{t}_1$ and $\widetilde{b}_1$ can be significantly lighter than first and second generation sleptons and squarks. The enhanced mixing of staus can often result in larger branching fractions for both $\widetilde{\chi}_2^0$ and $\widetilde{\chi}_1^\pm$ into final states with taus, rather than electrons or muons.

In the next chapter, we will discuss chargino and neutralino production and decay in the context of the mSUGRA model. An introduction to mSUGRA will be followed by a brief description of its phenomenology and of various constraints imposed on this phenomenology by independent physical measurements.

Chapter 3

mSUGRA

3.1 Origins of supersymmetry breaking

In the MSSM, supersymmetry breaking is simply introduced explicitly by adding soft susy breaking terms to the Lagrangian. However, as was discussed in Chapter 2, these soft parameters cannot be arbitrary. In oder to avoid potentially dangerous flavor-changing and CP-violating effects in the MSSM soft Lagrangian, supersymmetry breaking must be assumed "universal," that is, the squark and slepton squared-mass matrices must be flavor-blind and proportional to the 3×3 identity matrix in family space (Equation 2.87). Furthermore, the (scalar)^3 couplings must each be proportional to the corresponding Yukawa coupling matrix (Equation 2.88). Finally, one can avoid large CP-violating effects by assuming that the soft parameters do not introduce new complex phases (Equation 2.89). In order to understand how these patterns can emerge, it is necessary to consider models in which supersymmetry is spontaneously broken. By definition, this means that the vacuum state $|0\rangle$ is not invariant under supersymmetry transformations, so $Q_\alpha|0\rangle \neq 0$ and $Q^\dagger_{\dot{\alpha}}|0\rangle \neq 0$, where $\alpha = 1{,}2$ are spinor indices. Now, in global supersymmetry, the Hamiltonian operator

$H = P^0$ is related to the supersymmetry generators through the algebra:

$$\{Q_\alpha, Q^\dagger_{\dot\alpha}\} = -2\sigma^\mu_{\alpha\dot\alpha} P_\mu, \tag{3.1}$$

therefore,

$$H = P^0 = \frac{1}{4}(Q_1 Q_1^\dagger + Q_1^\dagger Q_1 + Q_2 Q_2^\dagger + Q_2^\dagger Q_2). \tag{3.2}$$

If supersymmetry is unbroken in the vacuum state, it follows that $H|0\rangle = 0$ and the vacuum has zero energy. Conversely, if supersymmetry is spontaneously broken in the vacuum state, then the vacuum must have positive energy, since

$$\langle 0|H|0\rangle = \frac{1}{4}\Big(\|Q_1^\dagger|0\rangle\|^2 + \|Q_1|0\rangle\|^2 + \|Q_2^\dagger|0\rangle\|^2 + \|Q_2|0\rangle\|^2\Big) > 0 \tag{3.3}$$

However, the field content of the MSSM does yield terms whose VEVs that can lead to an acceptable phenomenology and spectrum [16]. Therefore, the ultimate supersymmetry-breaking order parameter, or VEV, cannot belong to any of the MSSM supermultiplets. Supersymmetry breaking would need to occur in a "hidden sector" of particles that have only very small direct couplings to the "visible sector" chiral supermultiplets of the MSSM. However, the two sectors must share some interactions that are responsible for mediating supersymmetry breaking from the hidden sector to the visible sector, resulting in the MSSM soft terms. These terms would arise indirectly or radiatively, rather than from tree-level renormalizable couplings to the supersymmetry-breaking order parameters.

In a popular class of models the mediating interactions are associated with the new physics, including gravity, that enters near the Planck scale. In this "gravity-mediated", or *Planck-scale-mediated supersymmetry breaking* (PMSB) model, if supersymmetry is broken in the hidden sector by a VEV $\langle F\rangle$, then the soft terms in

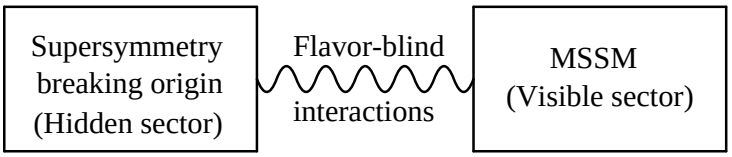

Figure 3.1: The presumed schematic structure for supersymmetry breaking

the visible sector should be roughly [16]

$$m_{\rm soft} \sim \langle F \rangle / M_{\rm P}, \tag{3.4}$$

For $m_{\rm soft}$ of order a few hundred GeV, one would therefore expect that the scale associated with the origin of supersymmetry breaking in the hidden sector should be roughly $\sqrt{\langle F \rangle} \sim 10^{10}$ or 10^{11} GeV.

A we saw in section 2.2.2, a supersymmetry transformation should turn a scalar boson field ϕ into a fermion field ψ_α.

$$\delta\phi = \epsilon\psi, \qquad \delta\phi^* = \epsilon^\dagger\psi^\dagger, \tag{3.5}$$

where ϵ^α is an infinitesimal, anticommuting, two-component Weyl fermion object parameterizing the supersymmetry transformation. However, taking into account gravity, supersymmetry can no longer be a global symmetry, but a local one. This means that the spinor parameter ϵ^α is no longer a constant, but a function of the space-time coordinate x. The resulting locally supersymmetric theory is called *supergravity* [152, 153], which unifies the spacetime symmetries of general relativity with local supersymmetry transformations.

3.2 mSUGRA (minimal SUper GRAvity)

In supergravity the spontaneous supersymmetry breaking sector connects with the MSSM sector through the effects of gravity. When supersymmetric theory is extended to include gravity, the resulting supergravity theory is non-renormalizable as a quantum field theory. These non-renormalizable interactions can be neglected for most phenomenological purposes, because they have couplings proportional to powers of $1/M_P$. However, these interactions may play an important role in understanding how supersymmetry breaking is transmitted to the MSSM.

A non-renormalizable supersymmetric Lagrangian for a gauge-invariant theory involving chiral and vector superfields can be constructed [16]. If we consider a globally supersymmetric effective Lagrangian, with the Planck scale suppressed effects that communicate between the two sectors included as non-renormalizable terms, it is possible to identify a soft supersymmetry-breaking Lagrangian in the low-energy effective theory. It has been popular to assume a "minimal" form for the normalization of kinetic and gauge interaction terms in the non-renormalizable Lagrangian [59]. This allows us to write the soft Lagrangian in terms of the superpotential parameters y^{ijk} and μ^{ij}, which are supersymmetry preserving, and a simplified version of the general parameters that embody the non-renormalizeable character of the general supergravity Lagrangian. These parameters in their simplified form are three dimensionless real couplings f, k, n, and two real dimensionless constants α and β. The "minimal" soft Lagrangian is then

$$\begin{aligned}\mathcal{L}_{\text{soft}} &= -\frac{\langle F\rangle}{2M_{\text{P}}} f\lambda^a\lambda^a - \frac{\langle F\rangle}{6M_{\text{P}}}(\alpha+3n)y^{ijk}\phi_i\phi_j\phi_k - \frac{\langle F\rangle}{2M_{\text{P}}}(\beta+2n)\mu^{ij}\phi_i\phi_j + \text{c.c.} \\ &\quad -\frac{|\langle F\rangle|^2}{M_{\text{P}}^2}(k+n^2)\phi^{*j}\phi_i, \end{aligned} \tag{3.6}$$

where ϕ_i and λ^a are the scalar and gaugino fields in the MSSM sector, and $\langle F\rangle$ is the VEV that breaks the supersymmetry in the hidden sector. If $\sqrt{\langle F\rangle} \sim 10^{10}$ or

10^{11} GeV, then the MSSM-sector soft terms ($m_{\text{soft}} \sim \langle F \rangle / M_{\text{P}}$) would be of order of a few hundred GeV. In principle, the original Lagrangian parameters that assumed a simplified form in f, k, n, α and β ought to be determined by the fundamental underlying theory. In this minimal scheme, it is possible to re-parametrize the soft terms in $\mathcal{L}_{\text{soft}}^{\text{MSSM}}$ in terms of only four parameters: $m_{1/2}$, m_0^2, A_0, B_0.

$$m_{1/2} = f\frac{\langle F \rangle}{M_{\text{P}}}, \qquad m_0^2 = (k+n^2)\frac{|\langle F \rangle|^2}{M_{\text{P}}^2}, \qquad A_0 = (\alpha + 3n)\frac{\langle F \rangle}{M_{\text{P}}}, \qquad B_0 = (\beta + 2n)\frac{\langle F \rangle}{M_{\text{P}}} \tag{3.7}$$

Rewriting the soft Lagrangian in terms of these parameters we get

$$\begin{aligned} \mathcal{L}_{\text{soft}} \;=\; & -\frac{m_{1/2}}{2}\lambda^a\lambda^a - \frac{A_0}{6}y^{ijk}\phi_i\phi_j\phi_k - \frac{B_0}{2}\mu^{ij}\phi_i\phi_j + \text{c.c.} \\ & -m_0^2\phi^{*j}\phi_i \end{aligned} \tag{3.8}$$

The Lagrangian of Equation 3.9 represents the soft Lagrangian of a supersymmetric theory with a general field content in a minimal supergravity framework. Therefore, for the field content of the MSSM, we can identify the parameters of Equation 3.9 with the coefficients appearing in the soft Lagrangian of Equation 2.84 at a renormalization scale $Q \approx M_{\text{P}}$.

$$M_3 = M_2 = M_1 = m_{1/2}, \tag{3.9}$$

$$\mathbf{m_Q^2} = \mathbf{m_{\bar{u}}^2} = \mathbf{m_{\bar{d}}^2} = \mathbf{m_L^2} = \mathbf{m_{\bar{e}}^2} = m_0^2\,\mathbf{1}, \qquad m_{H_u}^2 = m_{H_d}^2 = m_0^2, \tag{3.10}$$

$$\mathbf{a_u} = A_0\mathbf{y_u}, \qquad \mathbf{a_d} = A_0\mathbf{y_d}, \qquad \mathbf{a_e} = A_0\mathbf{y_e}, \tag{3.11}$$

$$b = B_0\mu, \tag{3.12}$$

This framework successfully evades the most dangerous types of flavor changing and CP violation as discussed in section 2.2.6. In particular, eqs. (3.10) and (3.11) are stronger versions of eqs. (2.87) and (2.88), respectively. If $m_{1/2}$, A_0 and B_0 all have the same complex phase, then eq. (2.89) will also be satisfied. These parameters should be viewed as RG boundary conditions on the soft parameters at the scale

$M_{\rm P}$, and their RG evolution down to the electroweak scale will then allow to predict the entire MSSM spectrum in terms of just five parameters $m_{1/2}$, m_0, A_0, B_0, and μ (plus the already-measured gauge and Yukawa couplings of the MSSM).

This theoretical framework has been the subject of the bulk of phenomenological and experimental studies of supersymmetry, and has become a benchmark scenario for experimental collider search limits. It is sometimes referred to as the *minimal supergravity* (mSUGRA) or *Constrained Minimal Supersymmetric Standard Model* (CMSSM) scenario for the soft terms.

3.3 Radiative electroweak symmetry breaking

In the mSUGRA framework, electroweak symmetry breaking is somewhat more complicated than in the SM because in the MSSM there are two Higgs doublets. In order to break electroweak symmetry, we need to find vacuum expectation values (VEVs) for the scalar potential V of the Higgs scalar fields.

$$\begin{aligned} V &= (|\mu|^2 + m_{H_u}^2)(|H_u^0|^2 + |H_u^+|^2) + (|\mu|^2 + m_{H_d}^2)(|H_d^0|^2 + |H_d^-|^2) \\ &\quad + [b\,(H_u^+ H_d^- - H_u^0 H_d^0) + \text{c.c.}] \\ &\quad + \frac{1}{8}(g^2 + g'^2)(|H_u^0|^2 + |H_u^+|^2 - |H_d^0|^2 - |H_d^-|^2)^2 + \frac{1}{2}g^2|H_u^+ H_d^{0*} + H_u^0 H_d^{-*}|^2 \end{aligned} \tag{3.13}$$

The terms proportional to $|\mu|^2$ and to g^2 and g'^2 come from the scalar potential of the supersymmetry preserving Lagrangian. On the other hand, the terms proportional to $m_{H_u}^2$, $m_{H_d}^2$ and b are just a rewriting of the last three terms of the MSSM soft Lagrangian (Equation 2.84). Terms for squark and slepton fields with large positive squared masses are left out of Equation 3.14 because they do not get VEVs. Furthermore, a possible VEV for one of the charged components of the Higgs scalar fields can be rotated away without any loss of generality through a $SU(2)_L$ gauge trans-

formation so that $H_u^+ = H_d^- = 0$ at the minimum of the potential. This is indeed desirable since it guarantees that at the minimum of the potential electromagnetism remains unbroken. Therefore, the only part of the potential that needs to get VEVs is

$$\begin{aligned} V &= (|\mu|^2 + m_{H_u}^2)|H_u^0|^2 + (|\mu|^2 + m_{H_d}^2)|H_d^0|^2 - (b\, H_u^0 H_d^0 + \text{c.c.}) \\ &\quad + \frac{1}{8}(g^2 + g'^2)(|H_u^0|^2 - |H_d^0|^2)^2 \end{aligned} \tag{3.14}$$

In models derived from mSUGRA, $m_{H_u}^2 = m_{H_d}^2$ is supposed to hold at tree level at the input scale; however, negative contributions to the RG equation for $m_{H_u}^2$ due to the effects of the large top Yukawa coupling pushes it to negative or small values $m_{H_u}^2 < m_{H_d}^2$ at the electroweak scale. Therefore, in these models electroweak symmetry breaking is actually driven by quantum corrections in what is known as *radiative electroweak symmetry breaking*. We can now require that the VEVs be compatible with the observed phenomenology of electroweak symmetry breaking, $SU(2)_L \otimes U(1)_Y \rightarrow U(1)_{EM}$. If we write

$$v_u = \langle H_u^0 \rangle, \qquad v_d = \langle H_d^0 \rangle. \tag{3.15}$$

then, these VEVs are related to the known mass of the Z^0 boson and the electroweak gauge couplings:

$$v_u^2 + v_d^2 = v^2 = 2m_Z^2/(g^2 + g'^2) \approx (174\,\text{GeV})^2. \tag{3.16}$$

The ratio of the VEVs is traditionally written as

$$\tan\beta \equiv v_u/v_d. \tag{3.17}$$

Now one can write down the conditions $\partial V/\partial H_u^0 = \partial V/\partial H_d^0 = 0$ under which the potential eq. (3.15) will have a minimum satisfying Equations (3.16) and (3.17):

$$m_{H_u}^2 + |\mu|^2 - b\cot\beta - (m_Z^2/2)\cos(2\beta) \;=\; 0, \tag{3.18}$$

$$m_{H_d}^2 + |\mu|^2 - b\tan\beta + (m_Z^2/2)\cos(2\beta) \;=\; 0. \tag{3.19}$$

These relations allow us to eliminate two of the Lagrangian parameters b and $|\mu|$ in Equation 3.12 in favor of $\tan\beta$, but do not determine the phase of μ. Therefore, to a reasonable approximation, the entire mass spectrum in mSUGRA models is determined by only five unknown parameters: m_0^2, $m_{1/2}$, A_0, $\tan\beta$, and $\mathrm{Arg}(\mu)$. As mentioned before, the soft parameters appearing in Equations 3.9 through 3.12 need to be RG evolved down to the electroweak scale in order to predict the MSSM spectrum. Figure 3.2 shows the RG running of scalar and gaugino masses in a typical model based on the mSUGRA boundary conditions imposed at $Q_0 = 2 \times 10^{16}$ GeV. The dot-dashed lines labeled H_u and H_d are the running values of the quantities $(\mu^2 + m_{H_u}^2)^{1/2}$ and $(\mu^2 + m_{H_d}^2)^{1/2}$, which appear in the Higgs potential.

As all components of the two SM Higgs doublets can be complex, eight degrees of freedom exist[60] and mix to form the five physical states of the Higgs spectrum and the three Goldstone bosons that provide the longitudinal components of the massive $W^\pm$ and Z^0 bosons via the Higgs mechanism. The remaining five Higgs scalar mass eigenstates consist of two CP-even neutral scalars h^0 and H^0, one CP-odd neutral scalar A^0, and a charge $+1$ scalar H^+ and its conjugate charge -1 scalar H^-. The gauge-eigenstate fields can be expressed in terms of the mass eigenstate fields as:

$$H^\pm = H_d^\pm \sin\beta + H_u^\pm \cos\beta \tag{3.20}$$

$$A^0 = \sqrt{2}(\mathrm{Im}H_d^0 \sin\beta + \mathrm{Im}H_u^0 \cos\beta \tag{3.21}$$

$$h^0 = -(\sqrt{2}\mathrm{Re}H_d^0 - v_d)\sin\alpha + (\sqrt{2}\mathrm{Re}H_u^0 - v_u)\cos\alpha \tag{3.22}$$

$$H^0 = (\sqrt{2}\mathrm{Re}H_d^0 - v_d)\cos\alpha + (\sqrt{2}\mathrm{Re}H_u^0 - v_u)\sin\alpha \tag{3.23}$$

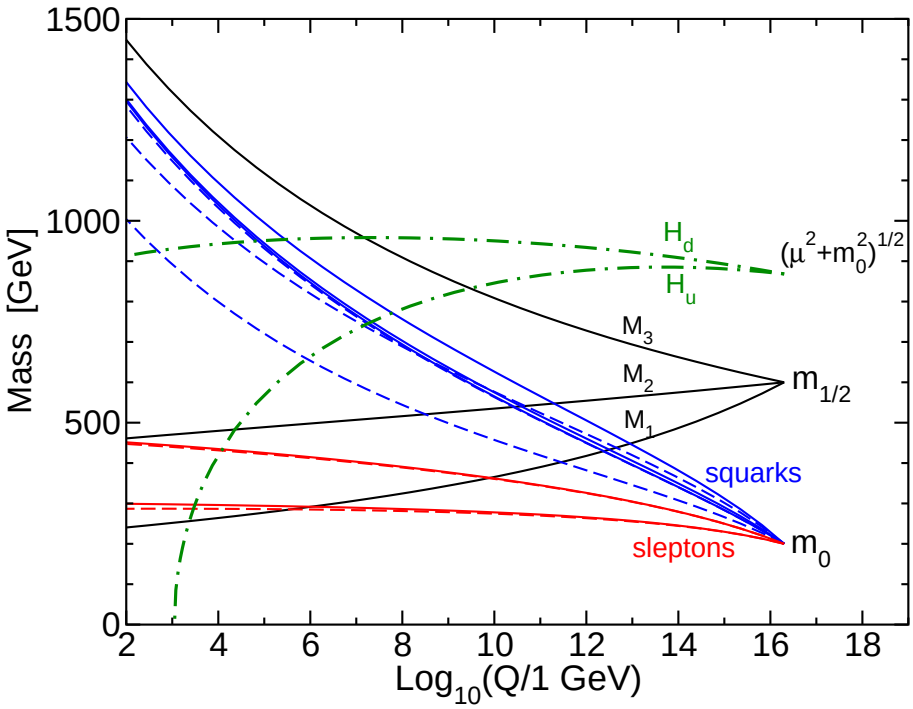

Figure 3.2: RG evolution of scalar and gaugino mass parameters in the MSSM with MSUGRA boundary conditions imposed at $Q_0 = 2 \times 10^{16}$ GeV. The parameter $\mu^2 + m_{H_u}^2$ runs negative, provoking electroweak symmetry breaking [16].

where α and β are the mixing angles. Their masses are given by

$$m_{A^0}^2 = 2b/\sin(2\beta) = 2|\mu|^2 + m_{H_u}^2 + m_{H_d}^2 \tag{3.24}$$

$$m_{h^0,H^0}^2 = \frac{1}{2}\Big(m_{A^0}^2 + m_Z^2 \mp \sqrt{(m_{A^0}^2 - m_Z^2)^2 + 4m_Z^2 m_{A^0}^2 \sin^2(2\beta)}\Big), \tag{3.25}$$

$$m_{H^\pm}^2 = m_{A^0}^2 + m_W^2. \tag{3.26}$$

The masses of A^0, H^0 and $H^\pm$ can in principle be arbitrarily large since they all grow with $b/\sin(2\beta)$. In contrast, the mass of h^0 is bounded above. From Equation (3.25), one finds at tree-level [61]:

$$m_{h^0} < m_Z|\cos(2\beta)| \tag{3.27}$$

3.4 mSUGRA phenomenology

Motivated by the observed suppression of flavor changing neutral currents and by the near unification of gauge coupling constants at $M_{GUT} \simeq 23 \times 10^{16}$ GeV, the mSUGRA model assumes a common mass m_0 for scalars and a common mass $m_{1/2}$ for gauginos at scale $Q = M_{GUT}$. In addition, the soft breaking trilinear A terms are also assumed unified to A_0 at $Q = M_{GUT}$. The magnitude of the superpotential μ term is determined by requiring radiative breaking of electroweak symmetry, which allows one to trade the bilinear b parameter for the parameter $\tan\beta \equiv v_u/v_d$. This assumed simplicity results in a significantly reduced number of parameters required to generate the entire supersymmetric mass spectrum and the possibility of estimating the cross section of various supersymmetric production processes. For example, the LEP2 limit on chargino mass $m_{\chi_1^\pm} > 95$ GeV [62] implies that gluinos and most squarks should have masses typically greater than 300 GeV, so that strong sparticle production at the Tevatron is expected to be suppressed. Then, $\chi_1^\pm \bar{\chi}_1^\pm$ production and $\chi_1^\pm \chi_2^0$ production are expected to be the dominant sparticle production mechanisms. In fact, it has become increasingly clear that the trilepton signal from $p\bar{p} \to \chi_1^\pm \chi_2^0$ followed by $\chi_2^0 \to ll\chi_1^0$ and $\chi_1^\pm \to l\nu\chi_1^0$ ($l = e, \mu$) is one of the most promising channels for discovery of supersymmetry at the Fermilab Tevatron collider [63, 69].

Figure 3.3 shows various production cross sections as a function of $m_{\tilde{g}}$ assuming five generations of degenerate squarks, for a) $m_{\tilde{q}} = m_{\tilde{g}}$ and b) $m_{\tilde{q}} = 2m_{\tilde{g}}$, with $\mu = +m_{\tilde{g}}$, and $\tan\beta = 3$. The region to the left of the vertical line is excluded by the LEP2 chargino mass limit $m_{\chi_1^\pm} > 95$ GeV [62]. It can be seen that electroweak production of charginos and neutralinos dominates over the strongly produced $\tilde{g}\tilde{g}, \tilde{q}\tilde{g}$, and $\tilde{q}\tilde{q}$ cross sections over practically all of the parameter space for which $|\mu| \gg M_1, M_2$. The cross section for $\chi_1^\pm \chi_1^0$ is relatively suppressed because χ_1^0 is dominantly a hypercharge, or bino-like, gaugino and it couples to W via its suppressed components, while the squark or gluino plus chargino or neutralino associated production reactions (dash-

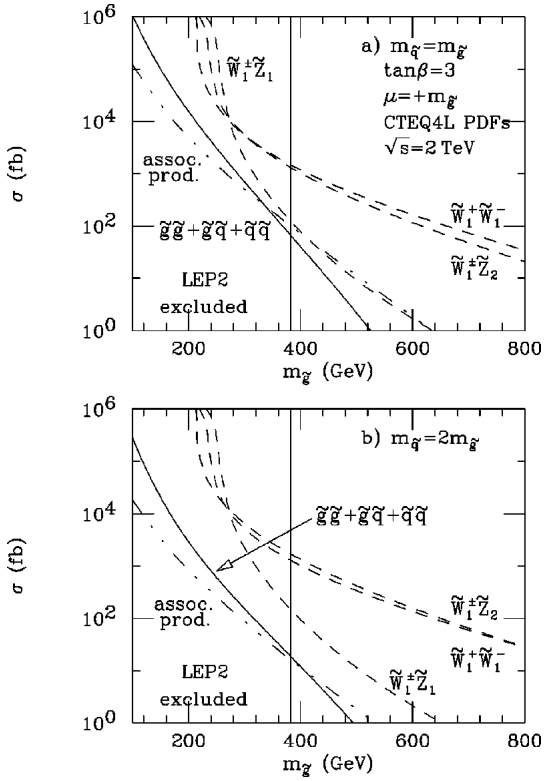

Figure 3.3: Sparticle production cross sections as a function of $m_{\tilde{g}}$ for $\mu = +m_{\tilde{g}}$ and $\tan\beta = 3$ [118].

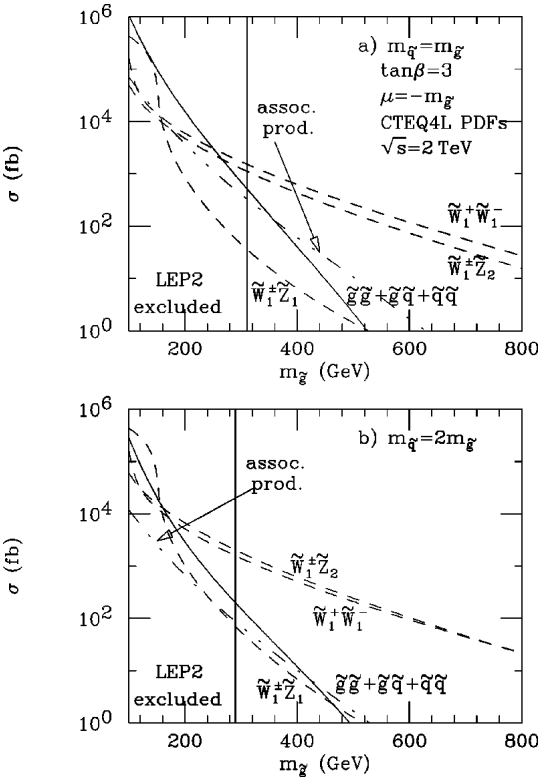

Figure 3.4: Sparticle production cross sections as a function of $m_{\tilde{g}}$ for $\mu = -m_{\tilde{g}}$ and $\tan\beta = 3$ [118].

dot-dot curves) occur at smaller rates. These general qualitative features hold for both regimes shown. Similar results are shown in Figure 3.4 for $\mu = -m_{\tilde{g}}$. In this case, for low values of $m_{\tilde{g}}$ with $m_{\tilde{q}} \simeq m_{\tilde{g}}$, the strong production cross sections can be dominant, but only in parameter space regions already excluded by LEP2. Since opposite sign dilepton or jet plus lepton signals from $\chi_1^+\bar{\chi}_1^-$ production suffer from large standard model backgrounds, many SUSY searches have focused on the clean trilepton signature from $\chi_1^\pm\chi_2^0$ production for which the SM background is expected to be small. The Feynman diagram for the production of chargino-neutralino is shown in Figure 3.5.

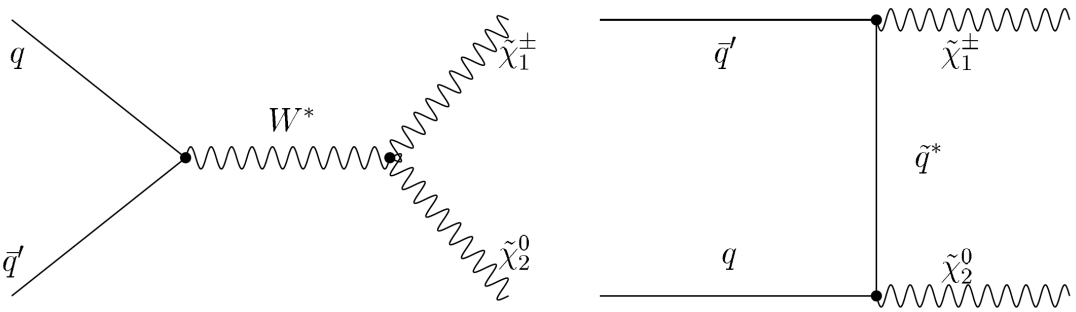

Figure 3.5: Associated $\widetilde{\chi}_1^\pm\widetilde{\chi}_2^0$ production through s-channel via virtual $W^\pm$ exchange (left) and t-channel via $\widetilde{q}$ exchange (right). For $\widetilde{\chi}_1^\pm$ and $\widetilde{\chi}_2^0$ masses near $W^\pm$ and Z^0 masses a measurable production rate can be expected. The two diagrams interfere destructively, therefore a large $\widetilde{q}$ leads to a higher production cross section.

The phenomenology of mSUGRA has been extensively studied yielding specific ranges of parameter space of more interest to trilepton analyses than others. Out of the 5 independent mSUGRA parameters, only two: m_0 and $m_{1/2}$, play a significant role in the sensitivity of trilepton analyses. Figure 3.6 shows the dependence of the masses of the MSSM particles on m_0 and $m_{1/2}$. This figure (and the ones that follow) were generated starting from a single mSUGRA point and varying one parameter at a time [156]. The benchmark point used corresponds to: $m_0 = 60$ GeV/c^2, $m_{1/2} = 190$ GeV/c^2, tan$\beta = 3$, $A_0 = 0$ and $\mu > 0$[1]. While the masses of sleptons and squarks depend strongly on m_0, the mass of chargino and neutralinos show almost no dependence on this parameter.

The decay branching ratios of $\widetilde{\chi}_1^\pm$ and $\widetilde{\chi}_2^0$ as functions of m_0 and $m_{1/2}$ are show in Figures 3.7 and 3.8 respectively. A strong dependence of the branching ratios on both of these parameters is observed. For example, for $m_0 = 60$ GeV/c^2, the branching ratio for the decay of $\widetilde{\chi}_1^\pm$ to an on-shell stau ($\widetilde{\chi}_1^\pm \rightarrow \widetilde{\tau}_1^\pm\nu_\tau$) is approximately 83%, while at $m_0 = 140$ GeV/c^2 the branching ratio for this same decay channel is nearly

[1]A similar dependence of the masses, branching ratios and cross-sections on the parameters is observed for $\mu < 0$ [156].

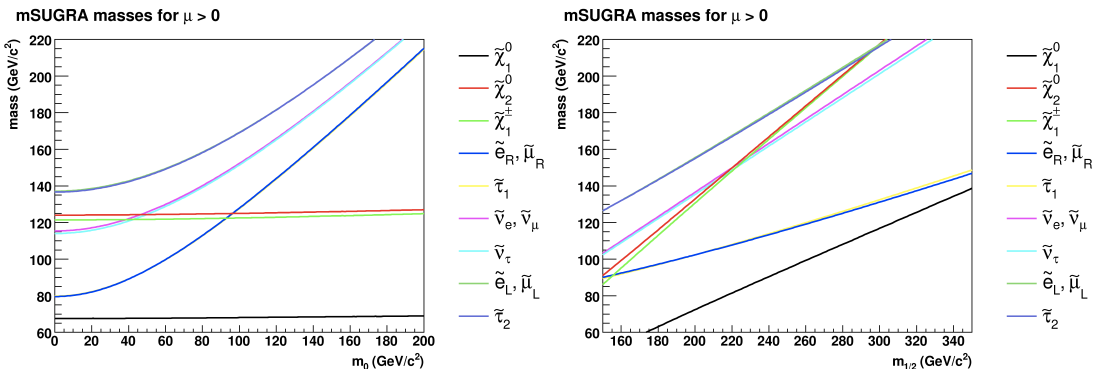

Figure 3.6: Mass of relevant supersymmetric particles as a function of m_0 (left) and $m_{1/2}$ (right) [156].

0% [156].

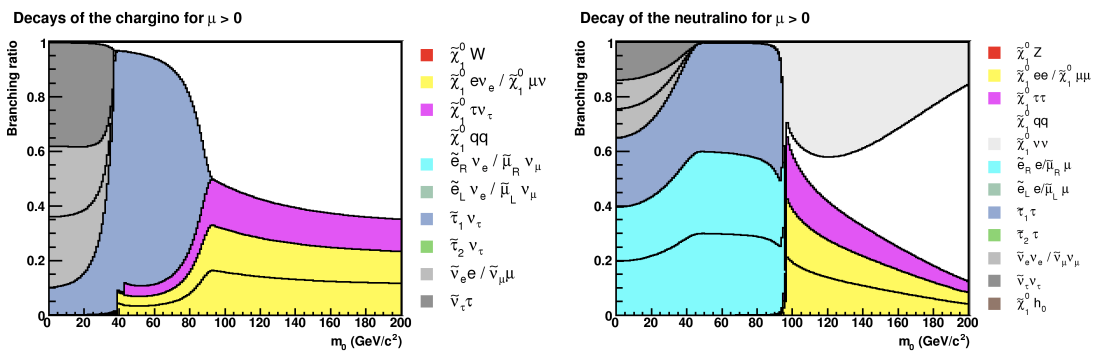

Figure 3.7: Decay branching ratios of $\widetilde{\chi}_1^{\pm}$ (left) and $\widetilde{\chi}_2^0$ (right) as functions of m_0 for $\mu > 0$ [156].

The cross-section for the associated production of chargino-neutralino in $\bar{p}p$ ($\sqrt{s} =$ 1.96 TeV) collisions at the Tevatron are show in Figure 3.9 as a functions of m_0 and $m_{1/2}$. The cross-sections were calculated with PROSPINO 2.0 and the particle spectrum was generated with ISAJET 7.75 [156].

By taking into account the dependence of the cross-section for the associated production of $\widetilde{\chi}_1^{\pm}\widetilde{\chi}_2^0$ on m_0 and $m_{1/2}$, and the dependence of the decay branching

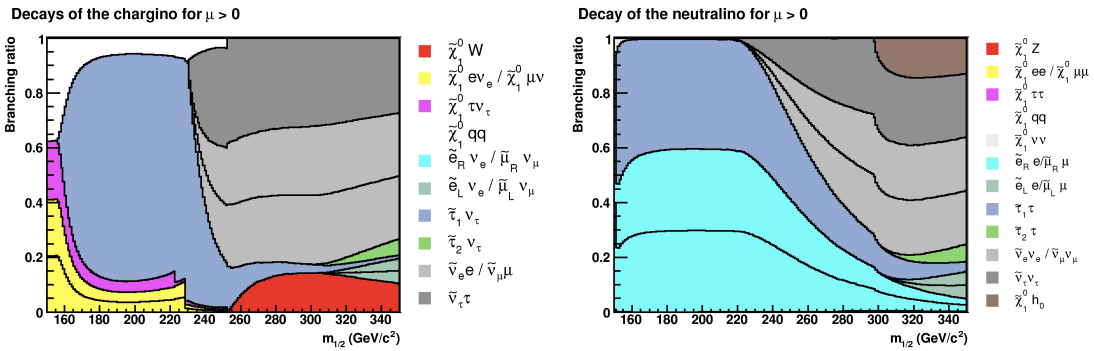

Figure 3.8: Decay branching ratios of $\widetilde{\chi}_1^{\pm}$ (left) and $\widetilde{\chi}_2^0$ (right) as functions of $m_{1/2}$ for $\mu > 0$ [156].

ratios of these particles on the same parameters, it is possible to divide the m_0-$m_{1/2}$ plane into regions with different sensitivity for a trilepton analysis. Three main re-

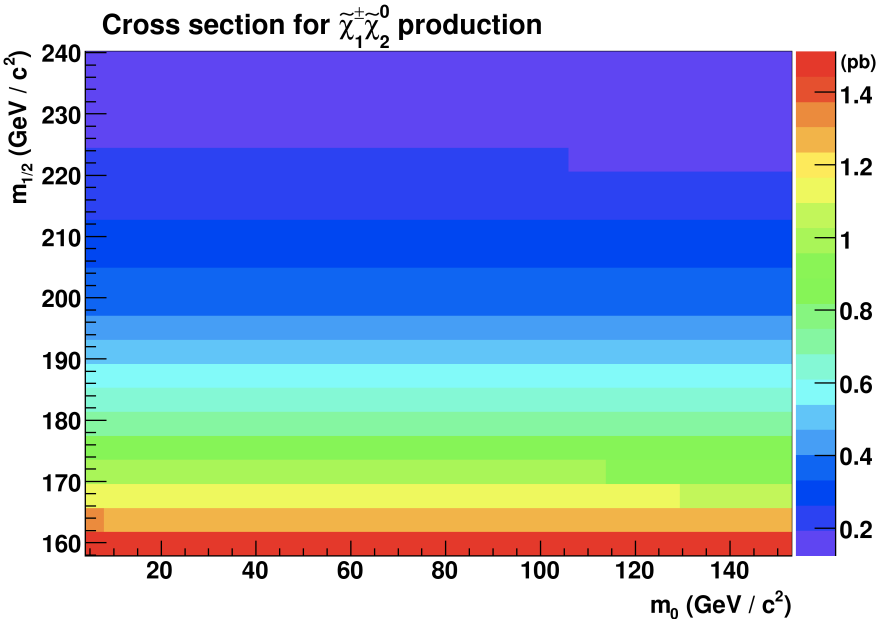

Figure 3.9: Cross section for the production of $\widetilde{\chi}_1^{\pm}\widetilde{\chi}_2^0$ in $\bar{p}p$ collisions at the Tevatron as a function of m_0 and $m_{1/2}$, for $\tan\beta = 3$, $A_0 = 0$ and $\mu > 0$ [156].

gions were identified in a previous work [156], each defined by the dominance of a particular decay mode of chargino and neutralino and by its final states. In each region $m(\widetilde{\chi}_2^0) \approx m(\widetilde{\chi}_1^\pm)$.

Region A: $m(\widetilde{\chi}_2^0) < m(\widetilde{l}_R^\pm) < m(\widetilde{\nu}) < m(\widetilde{l}_L^\pm)$. Only three-body decays via off-shell particles are possible. The decay via off-shell $W^\pm$ or Z^0 bosons is dominant for higher m_0; however, at the border of region A where $m(\widetilde{\chi}_2^0 \approx m(\widetilde{l}_R^\pm)$ the decay via off-shell sleptons ($\widetilde{e}_R$, $\widetilde{\mu}_R$, $\widetilde{\tau}_1$) is dominant.

$$\widetilde{\chi}_1^\pm \to \widetilde{\chi}_1^0 W^{\pm *} \to \widetilde{\chi}_1^0 \begin{pmatrix} l^\pm \nu_l \\ \\ q_1 \bar{q}_2 \end{pmatrix}, \qquad \widetilde{\chi}_2^0 \to \widetilde{\chi}_1^0 Z^{0*} \to \widetilde{\chi}_1^0 \begin{pmatrix} l^+ l^- \\ \\ q\bar{q} \\ \\ \nu\bar{\nu} \end{pmatrix} \tag{3.28}$$

$$\widetilde{\chi}_1^\pm \to \widetilde{l}_R^{\pm *} \nu_l \to \widetilde{\chi}_1^0 l^\pm \nu_l, \qquad \widetilde{\chi}_2^0 \to \widetilde{l}_R^{\pm *} l^\mp \to \widetilde{\chi}_1^0 l^+ l^- \tag{3.29}$$

Region B: $m(\widetilde{l}_R^\pm) < m(\widetilde{\chi}_2^0) < m(\widetilde{\nu}) < m(\widetilde{l}_L^\pm)$. As long as the mass of the slepton is lower than the mass of the decaying neutralino and chargino a sequential two-body decay via on-shell right-handed sleptons ($\widetilde{e}_R$, $\widetilde{\mu}_R$, $\widetilde{\tau}_1$) is dominant.

$$\widetilde{\chi}_1^\pm \to \widetilde{l}_R^\pm \nu_l \to \widetilde{\chi}_1^0 l^\pm \nu_l, \qquad \widetilde{\chi}_2^0 \to \widetilde{l}_R^\pm l^\mp \to \widetilde{\chi}_1^0 l^+ l^- \tag{3.30}$$

Region C: $m(\widetilde{l}_R^\pm) < m(\widetilde{\nu}) < m(\widetilde{\chi}_2^0) < m(\widetilde{l}_L^\pm)$. On-shell decays via right-handed sleptons ($\widetilde{e}_R$, $\widetilde{\mu}_R$, $\widetilde{\tau}_1$) and sneutrinos ($\widetilde{\nu}_e$, $\widetilde{\nu}_\mu$, $\widetilde{\nu}_\tau$) are available. Which of the two on-shell decay channels is dominant depends on the mixing of the chargino and neutralino.

$$\widetilde{\chi}_1^\pm \to \widetilde{\nu}_l l^\pm \to \widetilde{\chi}_1^0 l^\pm \nu_l, \qquad \widetilde{\chi}_2^0 \to \widetilde{\nu}_l \bar{\nu}_l \to \widetilde{\chi}_1^0 \nu_l \bar{\nu}_l \tag{3.31}$$

$$\widetilde{\chi}_1^\pm \to \widetilde{l}_R^\pm \nu_l \to \widetilde{\chi}_1^0 l^\pm \nu_l, \qquad \widetilde{\chi}_2^0 \to \widetilde{l}_R^\pm l^\mp \to \widetilde{\chi}_1^0 l^+ l^- \tag{3.32}$$

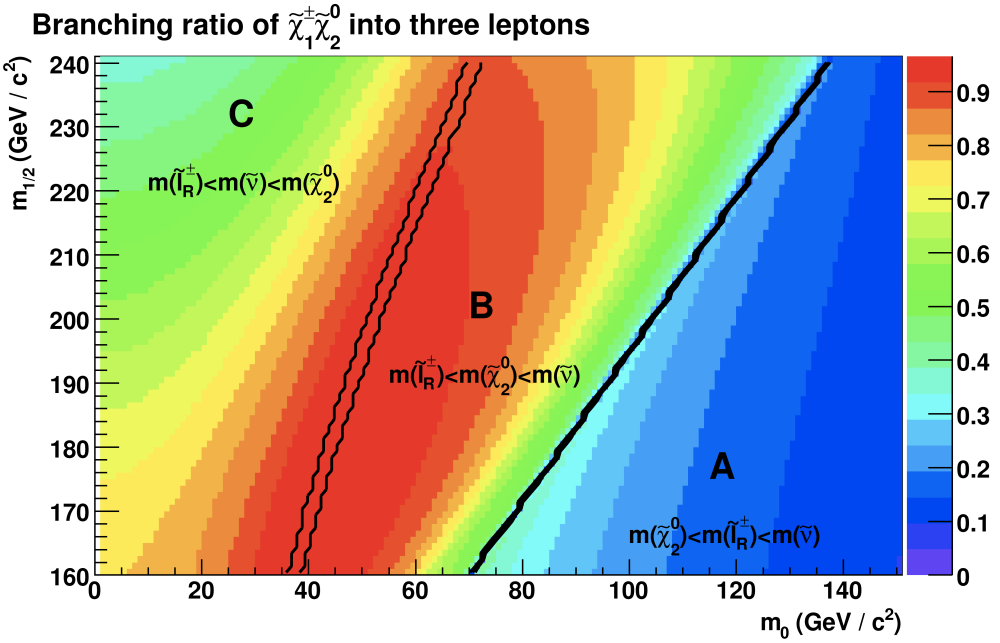

Figure 3.10: Branching ratio for the decay of a chargino-neutralino pair into three leptons, where leptons are electrons, muons and taus, for $\tan\beta = 3$, $A_0 = 0$ and $\mu > 0$ [156].

As the cross section for the associated production of $\tilde{\chi}_1^{\pm}\tilde{\chi}_2^0$ has a rather simple dependence on the mSUGRA parameters m_0 and $m_{1/2}$, the branching ratio into three leptons is the major factor that determines the sensitivity of a trilepton analysis and its potential to exclude parts of the mSUGRA parameter space. Figure 3.10 shows a color-coded map of the branching ratios in the m_0-$m_{1/2}$ plane [156]. Region A of parameter space shows the lowest branching ratios to trileptons. For high values of m_0 the decay is dominated by the exchange of an off-shell $W^{\pm *}$ or Z^{0*} boson. Given that these bosons can decay to final states with two neutrinos or quarks, the overall branching ratio to three leptons is low. At the border of region A and B, where $m(\tilde{\chi}_2^0) \approx m(\tilde{l}_R^{\pm})$, the decay via off-shell slepton becomes dominant. Since sleptons decay to leptons 100% of the time, the branching ratios of $\tilde{\chi}_1^{\pm}$ and $\tilde{\chi}_2^0$ into three leptons increases. In region B the decay via on-shell right-handed sleptons is

dominant. As this decay has 100% leptons in the final state, the branching ratio into three leptons increases, making this region of parameter space the most likely to produce a trilepton signature. Finally, In region C the decay via on-shell sneutrinos becomes available and the branching ratio decreases again. Therefore, the exclusion limit should be optimal in region B, which has motivated the choice of benchmark points with $m_0 = 60$ GeV/c^2 and $m_{1/2} = 190$ GeV/c^2 in SUSY trilepton analyses. The value of $\tan\beta = 3$ is chosen to ensure abundant decays to final states with electrons and muons; taus leptons are only used as third leptons in this analysis. Furthermore, the production cross-section of chargino-neutralino peaks at $\tan\beta = 3$ for $\mu > 0$. The trilinear coupling is chosen at $A_0 = 0$ to avoid decays of chargino to quarks in the final state at higher values of A_0, but low enough to include electrons and muons in the final state.

3.5 Experimental constraints on mSUGRA

Constraints on the parameter space of mSUGRA are found in a series of physical measurements. The combination of constraints points to favored regions of model parameter space where collider and non-accelerator SUSY searches may be more focused. These constraints come from:

- LEP2 direct limits
- The relic density of cold dark matter in the universe
- The branching fraction for the radiative $b \to s\gamma$ decay
- The muon anomalous magnetic moment
- The flavor violating decay $Bs \to \mu^+\mu^-$

Each of these quantities and their constraints on mSUGRA will be discussed next.

3.5.1 LEP direct limits

Based on negative searches for superpartners at LEP2, it is required that $m_{\widetilde{\chi}_1^\pm} > 103.5$ GeV/c^2 and $m_{\widetilde{e}} >\sim 100$ GeV/c^2, which is the most stringent of the slepton mass limits [158]. The LEP2 experiments also set a limit on the SM Higgs boson mass: $m_h > 114.4$ GeV/c^2 [157]. In our mSUGRA parameter space, the lightest SUSY Higgs boson h is almost always SM-like. The exception occurs when the value of m_A becomes low at very large values of tanβ.

3.5.2 Neutralino relic density

Measurements of galactic rotation curves, binding of galactic clusters, and the large scale structure of the universe all point to the need for significant amounts of non-baryonic Dark Matter (DM) in the universe. In addition, detailed analyses of the anisotropies of the cosmic microwave background (WMAP) point to a cold dark matter density [159]

$$0.106 < \Omega_{CDM} h^2 < 0.121 \tag{3.33}$$

In many R-parity conserving models such as mSUGRA, the lightest neutralino ($\widetilde{\chi}_1^0$) is also the lightest SUSY particle (LSP); as such, it is massive, neutral and stable. Therefore, relic neutralinos left over from the Big Bang provide an excellent candidate for the CDM (Cold Dark Matter) content of the universe. The upper limit above represents a true constraint, while the corresponding lower limit is flexible, since there may be additional sources of CDM. In the early universe, such neutralinos would exist in thermal equilibrium with matter and radiation. As the universe expanded and cooled, the thermal energy would no longer be sufficient to produce neutralinos at an appreciable rate, and annihilation and co-annihilation reactions to SM particles and Higgs bosons would reduce their relic density. Therefore, the mSUGRA parameter

space can be scanned for areas that are consistent with the observed best limits on $\Omega_{CDM}h^2$, while regions that would produce relic densities in excess can be ruled out.

3.5.3 $b \rightarrow s\gamma$ decay

The transition $b \rightarrow s\gamma$ is a flavor-changing neutral current process. In the SM, it is described by a penguin diagram in which a virtual W is exchanged in a loop with a top quark, with a photon emitted from any of the lines. There are large QCD corrections to the penguin diagram which have been calculated through some of the next-to-leading-logarithmic QCD corrections [163]. The Standard Model prediction is BR$(b \rightarrow s\gamma) = (3.54 \pm 0.49) \times 10^{-4}$. This decay rate has been measured by the BELLE [160], CLEO [161], and ALEPH[162] collaborations. A weighted averaging of these results yields BR$(b \rightarrow s\gamma) = (3.25 \pm 0.37) \times 10^{-4}$, which agrees very well with the SM prediction. The 95% CL range corresponds to $\pm 2\sigma$ away from the mean. To this an uncertainty in the theoretical evaluation is added of about 10%. Together, these imply the bounds, $2.16 \times 10^{-4} <$BR$(b \rightarrow s\gamma) < 4.34 \times 10^{-4}$.

The inclusive radiative B-decay is a sensitive probe of new physics, especially if related to the virtual exchange of a charged Higgs boson. This is particularly enhanced if the effect of the supersymmetric partners of the Higgs sector are included. These contributions can amount to a factor of 2-3 enhancement over the SM prediction. Given that the agreement between the observed and expected branching ratio for this decay are in very good agreement, this places strong constraints on the mSUGRA parameter space.

3.5.4 Muon anomalous magnetic moment

The Dirac equation predicts a muon magnetic moment

$$\vec{M} = g_\mu \frac{e}{2m_\mu} \vec{S} \tag{3.34}$$

with gyromagnetic ratio $g_\mu = 2$. Quantum loop effects lead to a small calculable deviation from $g_\mu = 2$, parameterized by the anomalous magnetic moment

$$a_\mu \equiv \frac{g_\mu - 2}{2} \tag{3.35}$$

This quantity can be accurately measured and, within the Standard Model (SM) framework, precisely predicted. The muon anomalous magnetic moment a_μ was measured to high precision by the E821 experiment [164]: $a_\mu^{exp} = 11659208.9(5.4)(3.3) \times 10^{-10}$, where the statistical and systematic uncertainties are given, respectively. The $g-2$ collaboration reported a 2.6σ deviation from the standard model value (Figure 3.11). For generic SUSY parameters, the chargino-sneutrino diagram provides a dominant contribution through loop effects. Assuming that the future data confirms the a_μ anomaly, the combined effects of $g_\mu - 2$ and $m_{\widetilde{\chi}_1^\pm} > 103.5$ GeV/c^2 then only allows $\mu > 0$ [170].

3.5.5 $B_s \to \mu^+\mu^-$ decay

The rare decay $B_s \to \mu^+\mu^-$ is both a Flavor Changing Neutral Current (FCNC) and helicity suppressed in the SM. Its branching ratio is precisely predicted within the the SM to $\mathrm{BR}(B_s \to \mu^+\mu^-) = (3.19 \pm 0.19) \times 10^{-9}$ [171, 172]

The present upper limit for this decay is $\mathrm{BR}(B_s \to \mu^+\mu^-) = 1.8^{+1.1}_{-0.9} \times 10^{-8}$ at 90% CL, set by the CDF Collaboration [173]. This limit is still one order of magnitude higher than the SM prediction and therefore there is still a large scope for new physics contributions.

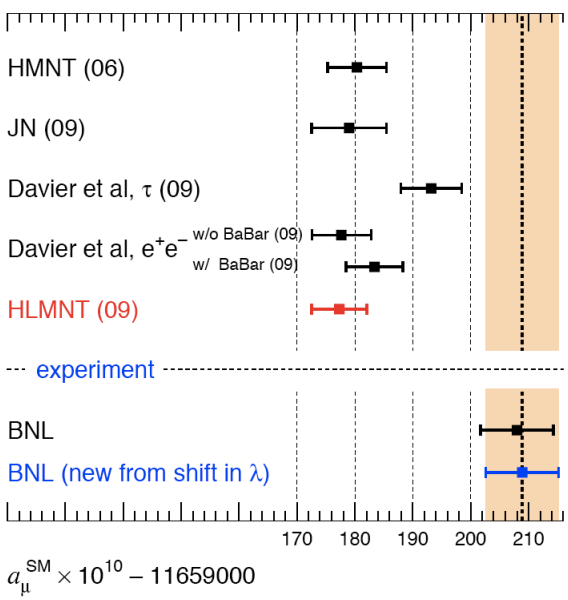

Figure 3.11: Comparison of recent predictions for $g-2$ compared to the BNL measurement [164]. Jegerlehner and Nyffeler [165], Davier et al. [166, 167, 168], Teubner et al. (HLMNT(09)) [169]

This observable is sensitive to physics beyond the SM involving an extended Higgs sector, such as mSUGRA with two Higgs doublets. A potentially important contribution to this decay is mediated by the neutral states in the Higgs sector where the amplitude for the Higgs-mediated decay of B_s grows as tanβ, and hence can completely dominate the SM contribution if tanβ is large according to the formula:

$$BR(B_s \to \mu^+\mu^-) \sim \frac{tan^6\beta}{m_A^4} \tag{3.36}$$

where m_A is the mass of the CP-odd neutral Higgs [170].

3.5.6 Application of constraints to phenomenology

The various experimental constraints on mSUGRA phenomenology are best illustrated on the m_0 versus $m_{1/2}$ plane of parameter space, where $A_0 = 0$ and $\mu > 0$ are assumed. For different values of $\tan\beta$, distinct regions are identified where the parameters lead to a phenomenology that is either inconsistent with, or favored by, the various physical measurements discussed earlier in this section. Figure 3.12 shows the constraints on parameter space for three different values of the top quark mass m_t and $\tan\beta = 10$. Also shown are contours of constant gluino and first generation squark mass. Figure 3.13 shows the constraints for different values of $\tan\beta$ with $m_t = 171.4$ GeV/c^2. In both figures, the following regions of parameter space are identified:

- The red-shaded regions are excluded because either the $\widetilde{\tau}_1$ becomes the lightest SUSY particle, in contradiction to negative searches for long lived, charged relics (left edge), or electroweak symmetry breaking (EWSB) is not correctly obtained (lower-right region).

- The blue-shaded region is excluded by LEP2 searches for chargino pair production ($m_{\widetilde{\chi}_1^\pm} < 103.5$ GeV/c^2)

- The region below the magenta contour line near the origin is excluded; the contour is roughly the LEP2 lower limit on m_h, the lightest SUSY Higgs boson h.

- The thin green regions at the boundary of the unshaded white region satisfies $0.094 < \Omega_{\widetilde{\chi}_1^0} h2 < 0.129$ where neutralino saturates the observed relic density. This region is preferred by standard cosmology.

- The yellow regions are not necessarily excluded because $\Omega_{\widetilde{\chi}_1^0} h2 < 0.094$, however they require multiple Dark Matter (DM) components to complete the

observed relic density. The white regions all have $\Omega_{\tilde{\chi}_1^0}h2 > 0.129$ and give too much thermal DM and are thus excluded unless neutralino decays either via small R-parity violating couplings, or neutralino is not the LSP.

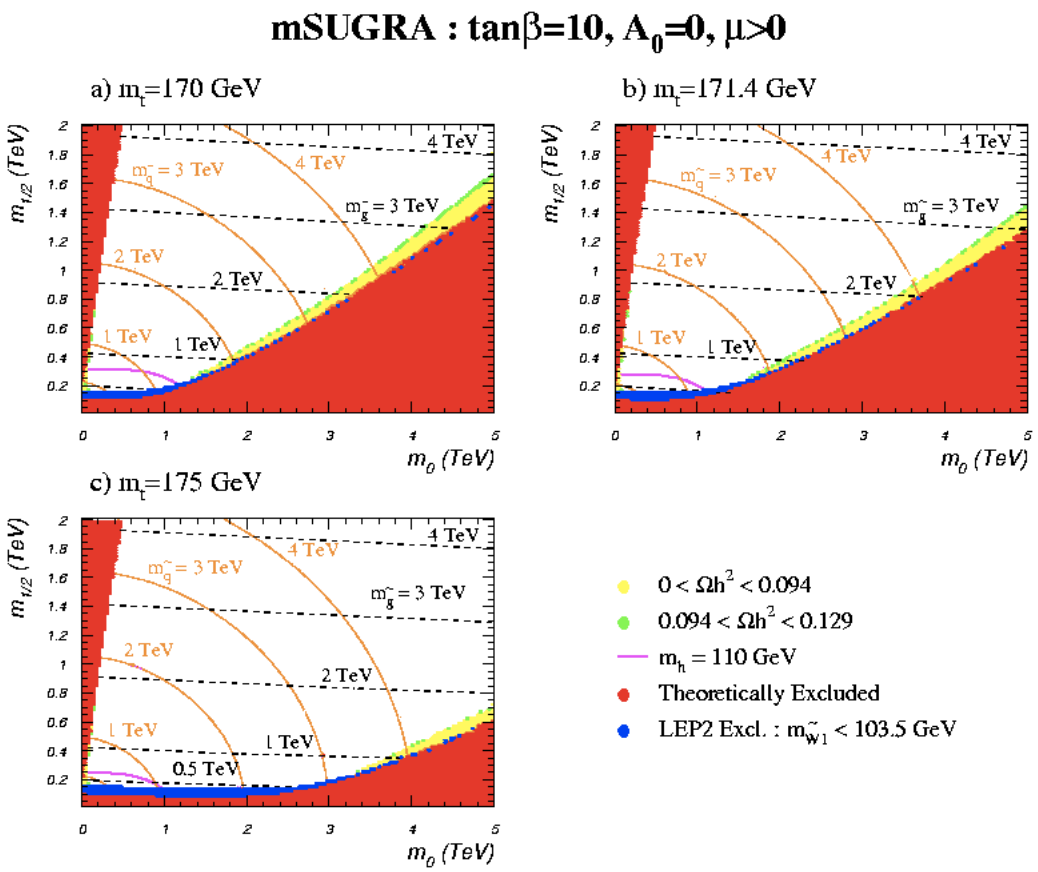

Figure 3.12: The m_0 vs. $m_{1/2}$ plane in mSUGRA for $A_0 = 0$, tan$\beta = 10$ with $\mu > 0$ and a) $m_t = 170$ GeV/c^2, b) $m_t = 171.4$ GeVc^2 and c) $m_t = 175$ GeVc^2. The red-shaded regions are excluded because electroweak symmetry is not correctly broken, or because the LSP is charged. Blue regions are excluded by direct SUSY searches at LEP2. Yellow and green shaded regions are WMAP-allowed, while white regions are excluded owing to $\Omega_{\tilde{\chi}_1^0}h^2 > 0.129$. Also shown are gluino and first generation squark mass contours, as well as a magenta contour below which $m_h \leq 110$ GeV/c^2. Source [174].

It is of interest to separate the region that is favored by the observed relic density of dark matter into different areas dominated by specific mechanisms of neutralino annihilation and co-annihilation. For $\tan\beta = 10$, three general areas can be identified. At very low m_0 and low $m_{1/2}$ values sleptons are quite light and the dominant neutralino annihilation process in the early universe occurs via t-channel slepton exchange to SM leptons $\widetilde{\chi_1^0}\widetilde{\chi_1^0} \to l\bar{l}$. This is the so-called bulk annihilation region [175]. At low m_0 and moderate $m_{1/2}$, and adjacent to the stau-LSP region, there is a thin strip of allowed region where neutralino and the light stau were in thermal equilibrium in the early universe. Here, neutralino co-annihilation with the light stau brings the neutralino relic density down to its observed value [176]. At large m_0, adjacent to the EWSB excluded region, the superpotential μ parameter becomes small and the higgsino-content of $\widetilde{\chi}_1^0$ increases significantly [174] and can annihilate efficiently via gauge couplings to its higgsino component. If $m_{\widetilde{\chi}_1^0} > M_W$ and M_Z, then $\widetilde{\chi}_1^0\widetilde{\chi}_1^0 \to WW$, ZZ, Zh is enhanced, and the correct measured relic density is obtained [177].

For values of $\tan\beta$ well beyond 10, the bottom and tau Yukawa couplings become large, and the value of m_A steadily drops. This effect can be observed in Figure 3.13 which shows the mSUGRA m_0 vs. $m_{1/2}$ plane for increasing values of $\tan\beta$. For $\tan\beta \sim 45 - 55$, the value of m_A is small enough so that $\widetilde{\chi}_1^0\widetilde{\chi}_1^0$ can annihilate into $b\bar{b}$ pairs through the s-channel A (and also H) resonance. This is the so-called A-funnel [178].

Figure 3.14 shows a typical parameter space for mSUGRA, with $\tan\beta = 40$ and 50. As in Figures 3.12 and 3.13, the model parameters are significantly constrained by different experimental results. The light Higgs mass bound of $m_h > 114.4$ GeV/c^2 excludes the region left to the red dotted contour line for $m_h = 114.4$ GeV/c^2. Likewise, the bound on the lightest chargino mass of $m_{\widetilde{\chi}_1^0} > 103.5$ GeV/c^2 from LEP2 excludes the region left to the black dashed line. The grey shaded region correspond

to points not satisfying the electroweak symmetry breaking condition, while the brick-colored region is excluded because the stau is lighter than the neutralino. The blue region represents the 2σ bound on the dark matter relic density from WMAP. Only two new constraints are shown in this figure and define the following regions:

- The $b \to s\gamma$ branching ratio excluded region is shown as a yellow shaded region (95% CL exclusion).
- The muon magnetic moment anomaly $a_\mu = (g_\mu - 2)/2$ is shown as a pink shaded region. This region is within 2σ of where one gets a 4σ deviation from the SM as suggested by the experimental result and the SM prediction [169].
- The CDF 90% CL contour of $\mathrm{Br}(B_s \to \mu^+\mu^-)$ is shown as a green shaded region [173]. This area represents points consistent with the current experimental limit on $\mathrm{Br}(B_s \to \mu^+\mu^-)$, which is one order of magnitude above the expectation. In addition, the 1σ contour is shown as dashed light-green lines in both figures.

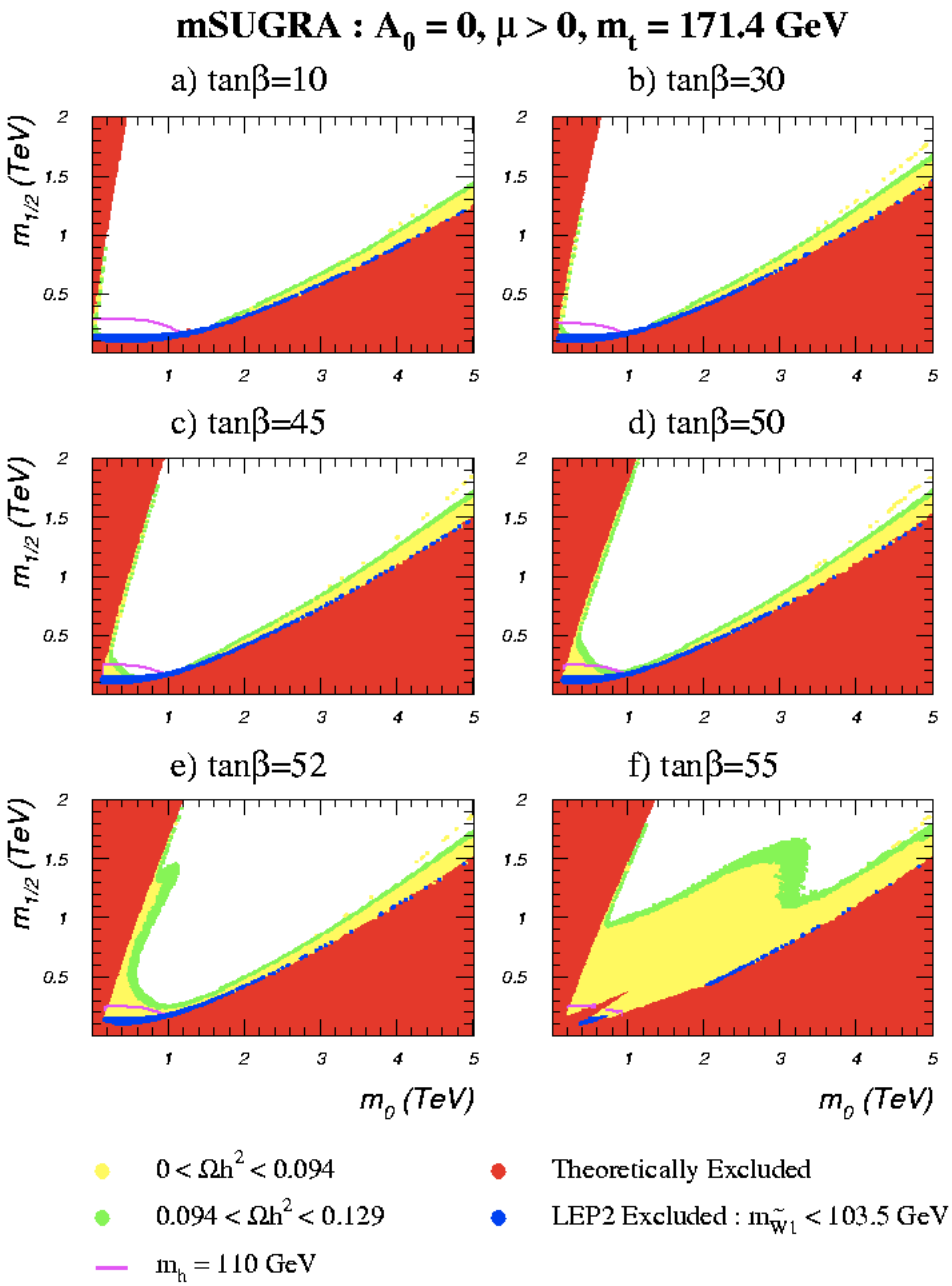

Figure 3.13: The m_0 vs. $m_{1/2}$ plane in mSUGRA for $A_0 = 0$ and various values of tanβ, with $\mu > 0$ and $m_t = 171.4$ GeV/c^2. The red-shaded regions are excluded because electroweak symmetry is not correctly broken, or because the LSP is charged. Blue regions are excluded by direct SUSY searches at LEP2. Yellow and green shaded regions are WMAP-allowed, while white regions are excluded owing $\Omega_{\tilde{\chi}_1^0} h^2 > 0.129$. Below the magenta contour in each frame, $m_h \leq 110$ GeV/c^2. Source [174]

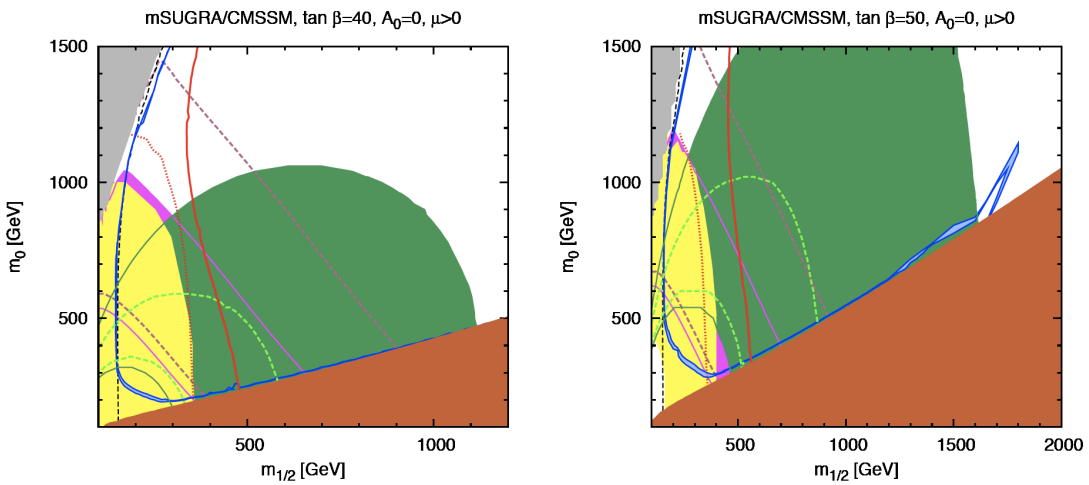

Figure 3.14: The mSUGRA parameter space is shown. The CDF allowed range of BR($B_s \to \mu^+\mu^-$) is shown by the green shaded region.The red solid line shows the neutralino-proton elastic scattering crosssection contour of 9×10^{-9} pb. We also show the 2σ contours from 3.2σ deviation based on [166] by slanted dashed purple lines. Other regions and lines are explained in the text. Source [170].

Chapter 4

Experimental Setup

4.1 The Fermilab accelerator

The Fermilab accelerator is a chain of circular and linear accelerators used to accelerate protons and antiprotons to an energy of 0.98 TeV as measured in the laboratory reference frame (1.96 TeV center of mass energy). The bunch crossing period or time between collisions is 396 ns. The accelerator is located at The Fermi National Accelerator Laboratory (Fermilab), 30 miles West of Chicago, Illinois. The Fermilab accelerator [74] accelerates particles using a chain of 8 separate accelerators which can be divided into 4 groups according to the their functionality: The Proton Source, The Anti-proton Source, The Main Injector and Recycler, and the Tevatron (Figure 4.1). Two detectors were designed to extract the full scientific potential of the proton-antiproton collisions: CDF, the Collider Detector at Fermilab, and D0. Both of them have the common structure of high energy physics experiments characterized by concentrical layers, with a tracker inside a solenoidal magnetic field, followed outward by a calorimeter and a muon spectrometer.

The results presented in the thesis make use of approximately 5.8 fb^{-1} of data

collected by CDF. A brief description of the accelerator chain and the detector is presented in the following sections.

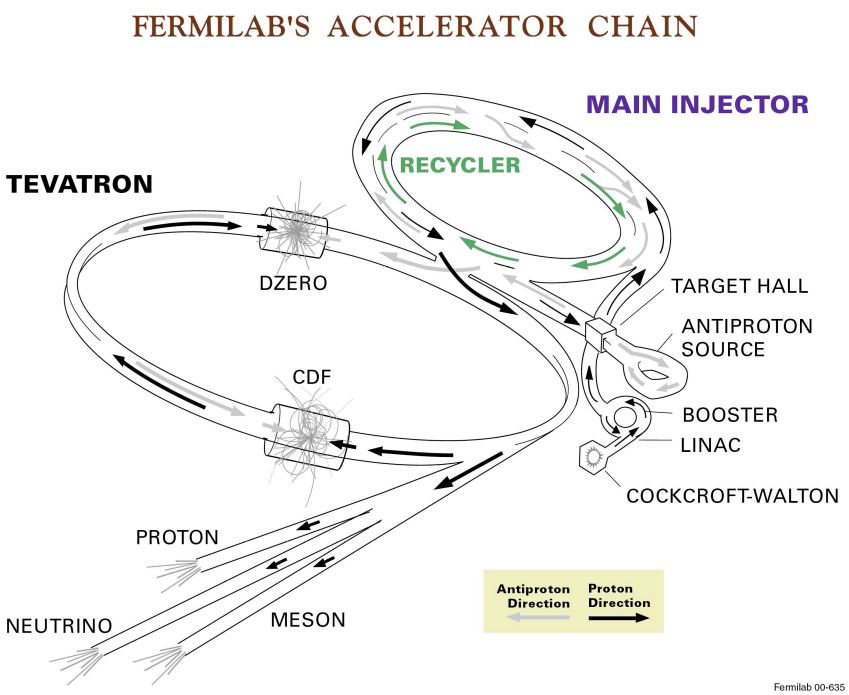

Figure 4.1: The Tevatron Collider Chain at Fermilab.

4.1.1 The Proton Source

The Proton Source consists of the Cockcroft-Walton, Linac and Booster accelerators. Protons accelerated at Fermilab come from a simple "C" size cylinder of compressed hydrogen gas (H_2). The acceleration processes begins with the production of Hydrogen ions (H^-) in a gas chamber where a voltage provided by a Cockcroft-Walton voltage multiplier is applied. This is a multistage diode/capacitor voltage multiplier providing 750 kV DC. The room housing the Cockcroft-Walton multiplier and the hydrogen chamber is shown in Figure 4.2. The negative hydrogen ions coming from

the Cockcroft-Walton are fed into the Linac [75] (linear accelerator), which consists of a series of drift tubes aligned in the direction of acceleration and separated by small gaps as shown in Figure 4.3. Radio-Frequency (RF) is applied to these drift tubes such that when the ions are traversing in between the drift tubes they increase their energy by an amount proportional to the peak-to-peak voltage of the RF signal. The length of the drift tubes and the RF frequency and phase are synchronized so that when the ions are between drift tubes the electric field is always maximum and in the same direction. The ions gain the same amount of energy each time they pass through a drift-tube gap, therefore, the gain in energy while traversing the entire Linac is proportional to the total number of gaps. At this point the beam is said to be "bunched since the ions need to be traveling in a closely-spaced arrangement for the accelerating scheme to work: particles that pass through the gap when the RF field is in the opposite direction are decelerated. The Linac is 130 meters long, has an RF frequency of 805 MHz and an electric field of about 3 Megavolt/meter, bringing the beam to 400 MeV in pulses of 20 ms before injection into the Booster.

In the booster [76] the H^- ions coming from the Linac are stripped of their two electrons by passing them though a thin carbon foil. The newly arrived hydrogen ions are injected into the booster via a bending magnet and "merged" into the existing beam (Figure 4.4 (right)) creating a mixture of protons and ions. This mixture is then cycled through the thin carbon foil until a beam of pure protons is achieved. While in the Booster, the protons are forced into a circular trajectory by means of dipole magnets, completing the circle when they re-enter the bending magnet. After all the bunches from the Linac have entered the Booster the ramping process begins. As with any synchrotron the Booster increases the energy by turning the RF cavities on while increasing the magnetic field in the dipole magnets so as to keep up with the larger momentum of the particles. The Booster is 475 meters in circumference and accelerates the protons from the Linac energy of 400 MeV to 8 GeV in a period of 0.033 seconds.

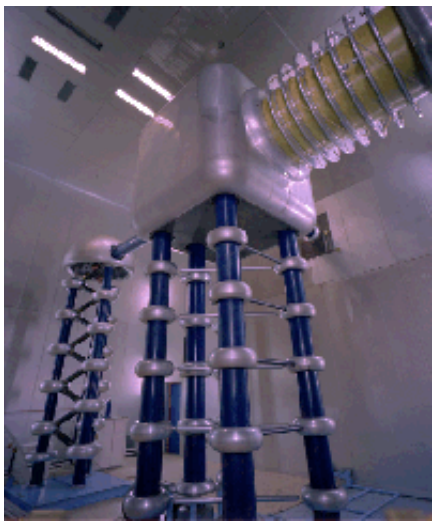

Figure 4.2: The Cockcroft-Walton accelerator. Two main components are shown. The Cockcroft-Walton accelerator itself (left-back) providing 750 kV DC to the hydrogen chamber (metallic cube atop insulator tower at center-front).

Figure 4.3: Drift tubes in the Linac.

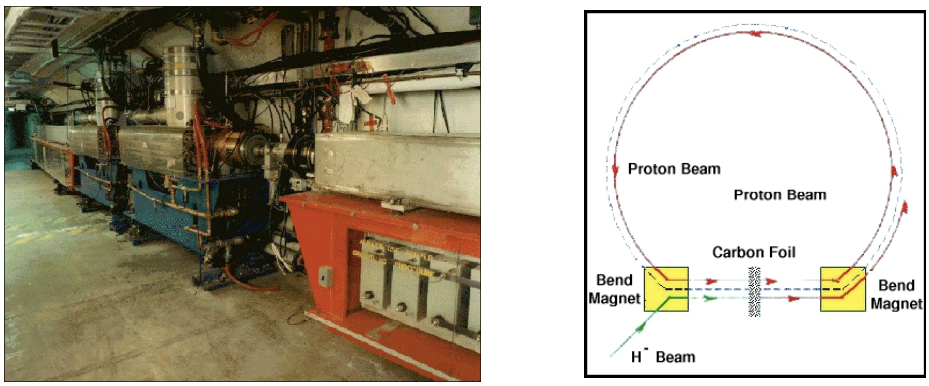

Figure 4.4: The Booster. Left: The photograph shows the RF cavities on the left side and the bank of capacitors inside the orange girder on the right side. Right: The diagram shows how the beam of H^- coming from the Linac is stripped and compacted in the Booster.

4.1.2 The main injector and recycler

Protons coming from the Booster at 8 GeV are injected into the Main Injector [76]. The Main Injector (Figure 4.5) has two important functions that are carried out at

Figure 4.5: Left: Aerial view of the Main Injector (front) and the Tevatron (back). Right: Main Injector Tunnel. The lower magnets are part of the Main Injector, the upper green magnets are part of the Recycler.

different times. The first one is to accelerate 8 GeV protons from the Booster to an energy of 120 GeV to be used in the production of antiprotons at the antiproton source facilities, which are then stored in the Accumulator. The second function of the Main Injector is to accelerate 8 GeV protons from the Booster (and later, antiprotons from the Accumulator) to an energy of 150 GeV for final injection into the Tevatron ring. The Main Injector tunnel also houses the Recycler [78], a fixed-energy storage ring for antiprotons placed directly above the Main Injector beamline (Figure 4.5 (right)). The purpose of the Recycler is to increase the luminosity of the Tevatron Collider over the maximum luminosity potential of the Main Injector. The Recycler consists of a ring of bricks of magnetized strontium ferrite which functions as a post-Accumulator ring for antiprotons. As the stack size in the Accumulator ring increases, there comes a point when the stacking rate begins to decrease. By emptying the contents of the Accumulator into the Recycler periodically, the Accumulator is always operating at its optimum antiproton intensity regime.

4.1.3 The anti-proton source

The antiproton source [79] [80] consist of The Target Station, The Debuncher, and The Accumulator (Figure 4.6). The bunched beam of 120 GeV protons from the Main Injector is directed to a Nickel Target where antiprotons are produced along a myriad of other particles[1]. These particles come off the target at many different angles and they are focused into a beamline with a Lithium lens. The antiprotons are then separated from the other particles in the beam by the use of a pulsed magnet, effectively acting as a charge-mass spectrometer. The separated antiprotons are then injected into the Debuncher, an 8 GeV synchrotron, which reduces the spread in the energy distribution of the antiprotons. The antiproton beam is then directed into the Accumulator, a storage ring in the Antiproton Source, where antiprotons are

[1]The production rate for 8 GeV antiprotons is about 18 $\bar{p}$ per 10^6 p

stored at an energy of 8 GeV and stacked to 10^{10} particles per bunch. Finally, the antiproton bunches are injected into the Main Injector and accelerated to 150 GeV.

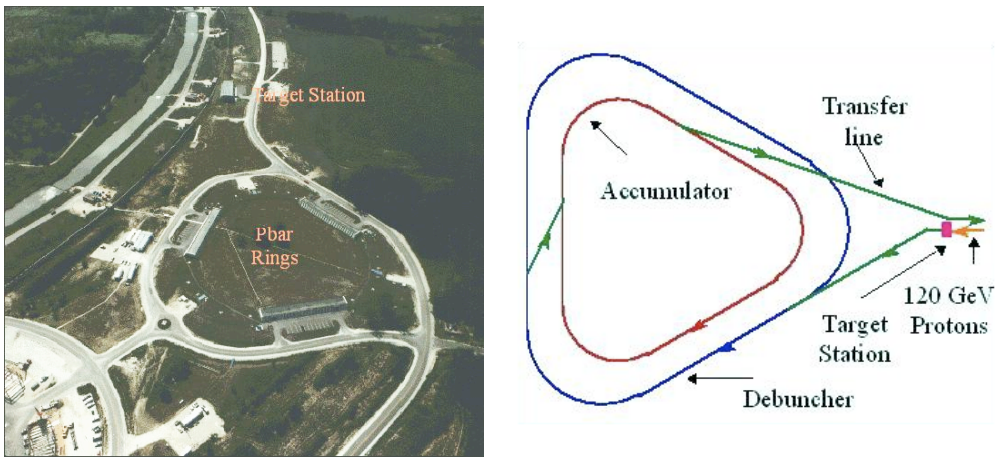

Figure 4.6: Aerial view of the Accumulator and Debuncher site (left). Schematic diagram. The Debuncher takes the antiprotons from the target, reduces their momentum spread and store them in the Accumulator (right).

4.1.4 The Tevatron

The Tevatron [81] is the final stage in the acceleration process. It receives 150 GeV antiprotons from the Main Injector, and then accelerates them to the final energy of 980 GeV. The Tevatron ring is a circular beam pipe of one kilometer radius. Along its total circumference of about 6.3 kms, the Tevatron holds 816 dipolar superconducting magnets made of a niobium-titanium alloy wire, which are kept at a temperature of 4.3 K cooled with liquid helium. At an energy of 980 GeV, the magnetic field of the dipolar magnets is about 4.2 Tesla with a 4000 Amperes current draw through the coils. Interleaved with the dipole magnets are 204 quadrupole magnets that focus the beam to achieve peak luminosity. The RF system of the Tevatron consist of an array of 8 RF cavities running at a frequency of 53.03 MHz. This frequency does not need to be changed during the ramping given the very small velocity difference

of the protons at 150 GeV and 980 GeV. It takes 9 cycles to fill the Tevatron with 36 bunches of protons (or antiprotons), and it takes about 40 seconds to ramp the energy from 150 GeV to 980 GeV. The typical number of protons (antiprotons) in a bunch is about $27 \times 10^{11}(30 \times 10^{10})$.

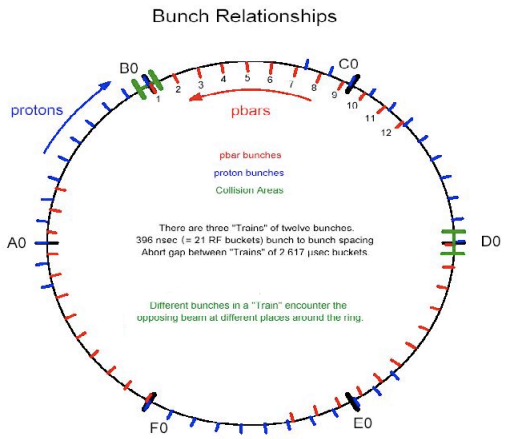

Figure 4.7: Bunch structure in 36×36 mode. Proton bunches go clockwise and are shown as blue marks outside the ring. Antiprotons go counter-clockwise and are shown as red marks inside the ring. Detectors are placed at B0 and D0 points.

4.1.5 The beam structure

During RunII the Tevatron is operated in 36×36 mode, which refers to the number of bunches of protons and antiprotons respectively. The beam configuration is shown in Figure 4.7. The 36 bunches are distributed in three trains of 12 bunches each. The bunches in a train are separated by 21 RF buckets (396 ns). Once all the proton bunches are injected, and before loading the antiprotons, a set of electrostatic separators are used to create a pair of non-intersecting helical, closed orbits with protons in one strand and the antiprotons to be loaded in the other. The helical configurations prevents the collisions between the beams all along the ring.

Antiprotons are then injected in their strand of the helix. With the two beams in the Tevatron the ramping up to 980 GeV is done. After some procedures to clean up the beam halo are finished, the injection helix is set to collision helix. This mode uses separator bumps close to the interaction points and phases the helix so that the proton and antiproton beams collide only at the center of the detectors. The bunch crossing occurs every 396 ns. There are two detectors in the Tevatron ring located at the points marked B0 and D0 where the helical orbits cross to produce the $\bar{p}p$ interaction that are observed. The detector used in this analysis is located at B0 and it is called CDF, the Collider Detector at Fermilab. In the absence of a crossing angle or position offset, the luminosity at the interaction points is given by the expression:

$$L = \frac{f_{bc} N_b N_p N_{\hat{p}}}{2\pi(\sigma_p^2 + \sigma_{\hat{p}}^2)} F \frac{\sigma_l}{\beta^*} \tag{4.1}$$

where f_{bc} is the revolution frequency, N_b is the number of bunches, $N_{p(\bar{p})}$ is the number of protons (antiprotons) per bunch, and $\sigma_{p(\bar{p})}$ is the transverse and longitudinal rms proton (antiproton) beam size at the interaction point. F is a form factor with a complicated dependence on the so-called beta function, β^*, and the bunch length, σ_l. The beta function is a measure of the beam width, and it is proportional to the beam's x and y extent in phase space. Table 4.1 shows the design Run II accelerator parameters [82].

Figure 4.8 and Figure 4.9 show, respectively, the evolution in the integrated luminosity, defined as $L = \int L dt$, and the instantaneous luminosity delivered by the Tevatron since its commissioning through July 2009.

Parameter	Run II
number of bunches (N_b)	36
revolution frequency [MHz] (f_{bc})	1.7
bunch rms [m] σ_l	0.37
bunch spacing [ns]	396
protons/bunch (N_p)	2.7×10^{11}
antiprotons/bunch ($N_{\bar{p}}$)	3.0×10^{10}
total antiprotons	1.1×10^{12}
β^* [cm]	35

Table 4.1: Accelerator parameters for Run II configuration.

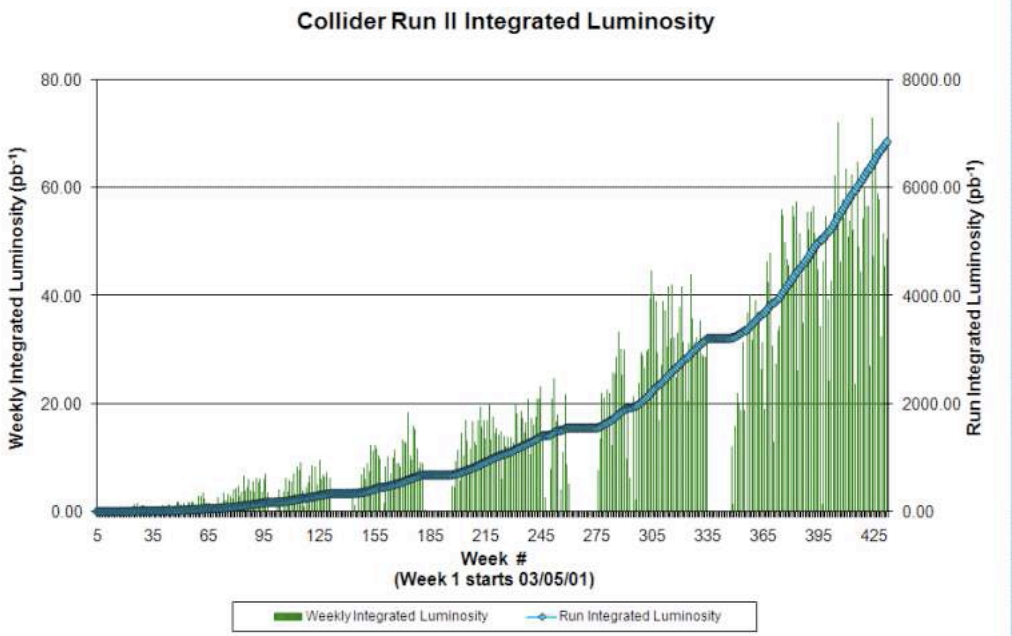

Figure 4.8: Tevatron Collider Run II integrated luminosity. The vertical green bar shows each weeks total luminosity as measured in pb^{-1}. The diamond connected line displays the integrated luminosity.

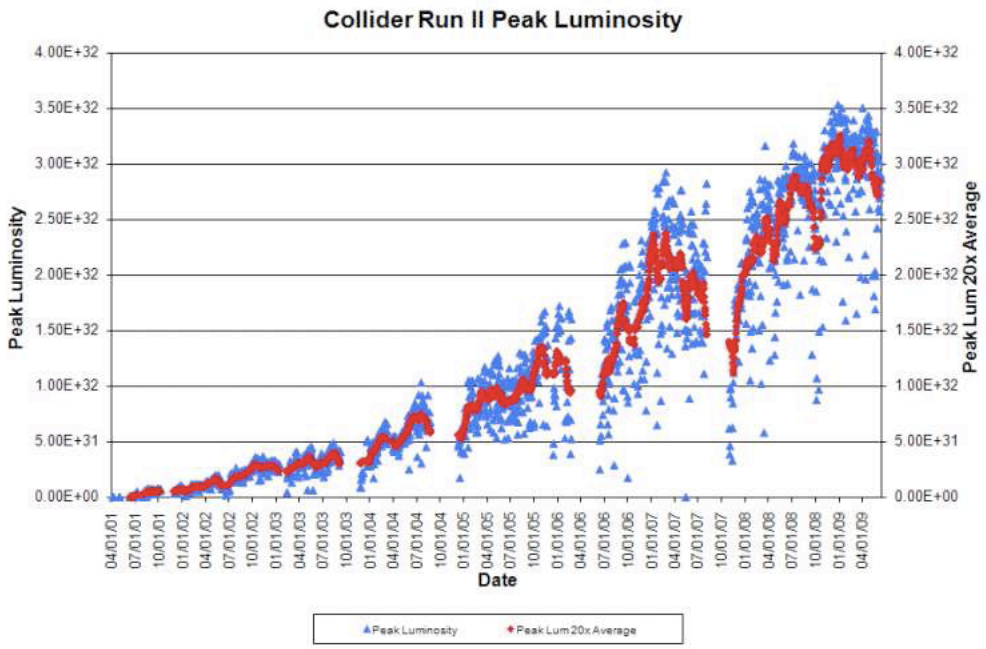

Figure 4.9: Tevatron Collider Run II Peak Luminosity. The blue squares show the peak luminosity at the beginning of each store and the red triangle displays a point representing the last 20 peak values averaged together.

4.2 The CDF II detector

Since the commissioning of the Tevatron, the CDF detector has undergone many changes. The current detector, used during Run II of data taking, is called CDF II (Figure 4.10). Its innermost subsystem is the Integrated Tracking System and consists outwardly of the Silicon Vertex Detectors, the Central Outer Tracker and the Solenoid. Surrounding the Integrated Tracking System is the Calorimetry System, which consists of the central and forward electromagnetic and hadronic calorimeters. The outermost sub-detectors are the Muon Chambers. Additionally, the Time of Flight System and the Cerenkov Luminosity Counter System are described. A more

detailed description of all the components can be found in [83].

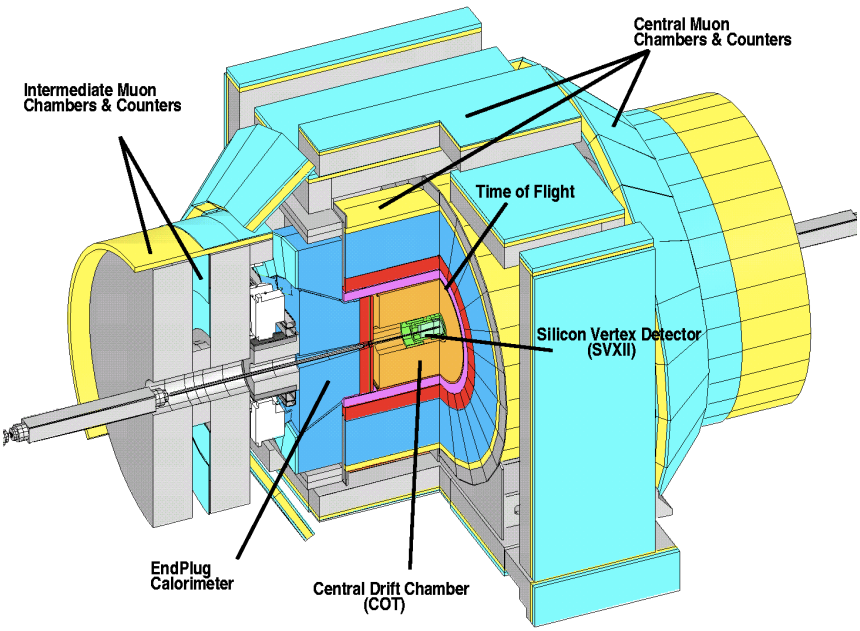

Figure 4.10: The CDF II.

4.2.1 Overview of coordinate systems and variables

The Cartesian coordinate system of CDF is defined as a right-ternary $(\hat{x}, \hat{y}, \hat{z})$ with its origin at the center of the detector which roughly coincides with the nominal collision point of the bunches.

The detector (see Figure 4.11) has cylindrical symmetry along the z axis and reflection symmetry about the (x, y) plane. The z direction is defined along the beam pipe such that protons move in the positive z direction. The y direction is defined transverse to the z direction with its positive side pointing up to the zenith of the detector. The x direction is then chosen to complete the right ternary, pointing its positive side away from the ring, parallel to the horizon. Given the symmetry of the

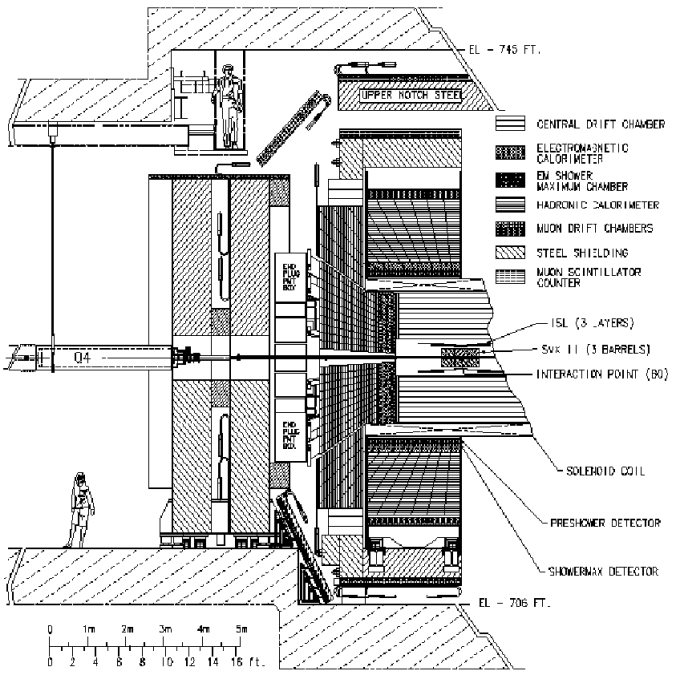

Figure 4.11: The CDF II lateral view.

detector and the fact that the colliding beams are not polarized make it convenient to work in cylindrical coordinates (r, ϕ, z). In this system r is defined transverse to the z axis. The azimuthal angle ϕ is defined on the (x, y) plane with $\phi = 0$ along the positive x direction. The z is defined as in the Cartesian system. The polar angle θ is taken from the positive direction of the z axis.

However, θ is not a good variable to use in this case because it is not Lorentz invariant. Due to the fact that the proton (and antiproton) is an extended object, the actual constituent partons will not be traveling at 980 GeV. Thus, the number of particles per unit angle ($dN/d\theta$) will not be the same for particles with different velocity. A more appropriate kinematic variable is *rapidity*, defined as

$$Y = \frac{1}{2}\log\left(\frac{E + p_z}{E - p_z}\right) \tag{4.2}$$

where E is the energy and p_z is the z component of the momentum of the particle.

In Phase-space we have,

$$\begin{aligned} d^3p/E &= dp_x dp_y dp_z/E \\ dp_x dp_y &= (1/2) dp_T^2 d\phi \\ dY &= dp_z/E \end{aligned} \tag{4.3}$$

then,

$$d^3p/E = (1/2) dp_T^2 d\phi (EdY)/E = (1/2) dp_T^2 d\phi dY. \tag{4.4}$$

For high energy particles, $p \gg m$ so $E \sim p$ and the rapidity is approximated by the *pseudorapidity*, defined as

$$\eta = -\log\left[\tan\left(\frac{\theta}{2}\right)\right] \tag{4.5}$$

In this case, the number of particles per unit rapidity ($dN/d\eta$) is invariant under boosts in the z direction. Typically, the position of objects (such as detector components) is described in terms of r, z and ϕ coordinates, while the direction of a particle is usually specified in (η, ϕ). As it is described later on, some sub-detectors in CDF II are divided into regions of constant Δ_η. The global CDF II coordinate system is defined with respect to the Central Outer Tracker (COT), which is part of the Tracking system to be described in the next section. The position of all other sub-detectors are measured with respect to the COT reference frame and this information is stored in alignment tables. Positions in a sub-detector are typically measured in the local frames and then converted to the global CDF II coordinate system via the appropriate alignment table.

4.2.2 Particle tracking

The trajectory of particles can give valuable information about the kinematics of a physical process, including charge sign and good momentum resolution if magnetic

fields are present. The process of reconstructing a particle trajectory is known as tracking. This section describes the sub-detectors that form the integrated tracking system of CDF II as shown in Figure 4.12, followed by a brief overview of the basics of tracking reconstruction.

Solenoid

All the tracking systems are contained in a superconducting solenoid of 1.5 m in radius and 4.8 m in length. The solenoid provides a very homogeneous axial magnetic field of 1.4 Tesla inside a useful volume of 2.8 m in diameter and 3.5 m along the negative z direction. In normal operating conditions its current consumption is about 4650 A. Inside the solenoid, and in direct contact with it, is located the Central Outer Tracker.

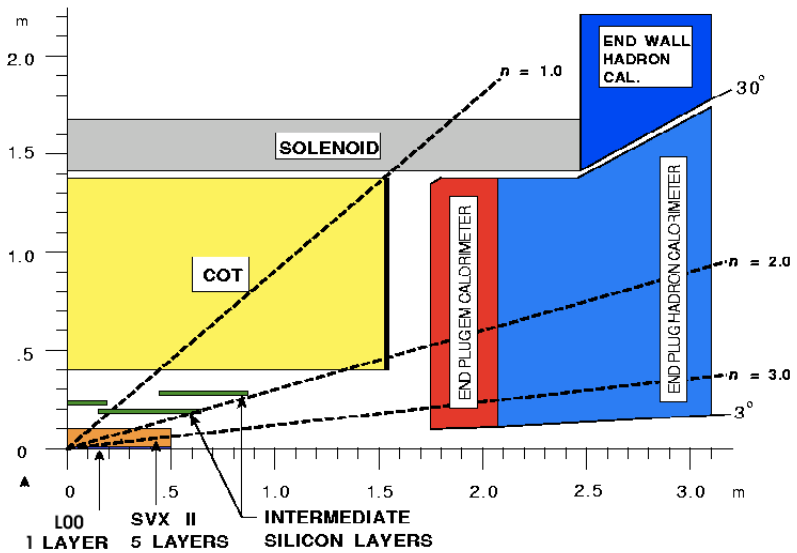

Figure 4.12: Longitudinal view of the CDF II tracking volume. Its main components are the Solenoid, the Central Outer Tracker (COT), and the silicon micro-strip detectors ISL, SVXII and L00.

Central Outer Tracker (COT)

As mentioned in Section 4.2.1, the COT position defines the global CDF II reference frame and it is the main component of the tracking system. It is located inside the solenoid in the region with $|z| < 155$ cm and between radii: 44 and 132 cm. The COT is a cylindrical multi-wire, open-cell drift chamber. It consists of 8 superlayers each made of a large number of cells as shown in Figure 4.13. Each cell is either an "axial" or a "stereo" cell. Superlayers 1, 3, 5, 7 (2, 4, 6, 8) are made completely of stereo (axial) cells. The main difference between these two types of cells is their orientation: axial cells are placed in a straight longitudinal direction, parallel to the z direction at constant ϕ, while stereo cells are obtained from an axial cell by rotating the two end-plates with respect to each other (each wire is rotated through six cells from the east end-plate to the west end-plate). Together, axial and stereo cells provide information about the z position of the hit. Particles originating from the interaction point having $|\eta| < 1$ pass through all 8 superlayers of the COT.

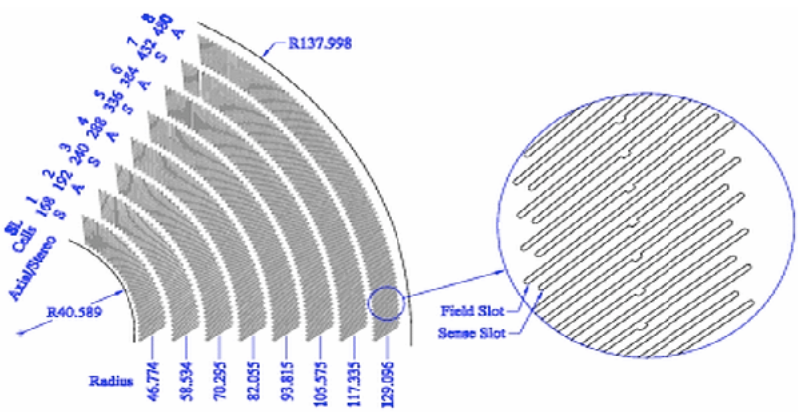

Figure 4.13: Schematic diagram of the 8 layers in a quadrant of the COT. The number of cells, the radius from the center to the beampipe and the type (Stereo or Axial) are shown for each superlayer.

Each cell has an approximate size of about 2 cm by 10 cm and a length of

310 cm spanning the whole longitudinal direction of the COT. The COT is filled with a 49.5:49.5:1 argon-ethane-isopropyl alcohol mixture as active medium. In this open-cell configuration all cells share the same active gas filling the COT volume. A transverse view of three cells in superlayer 2 is shown in Figure 4.14. The cells are separated from each other by field panels made of gold-plated mylar. Inside a cell wires run along its longitudinal direction, some of them are potential wires used to shape the electric field, while others are sense wires used to gather information about a particle's trajectory.

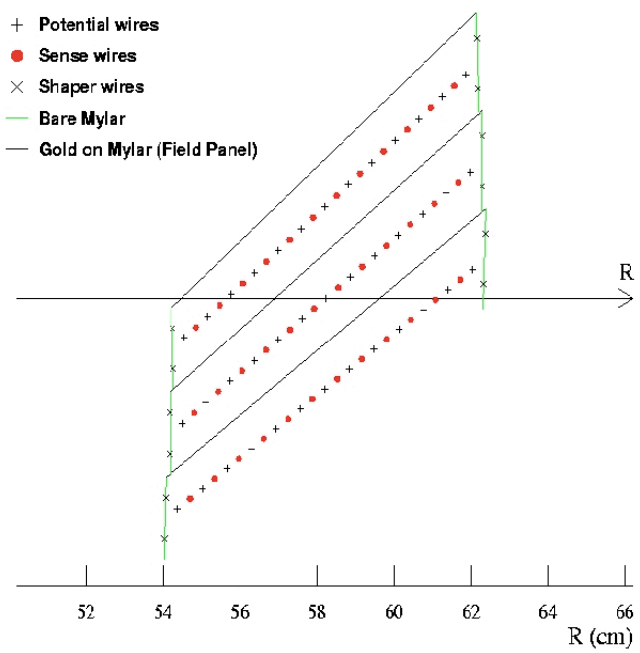

Figure 4.14: Schematic diagram of three cells in Superlayer 2 of the COT.

When a charged particle passes through the gas it leaves a trail of ionization electrons. These electrons drift towards the sense wires by virtue of the electric field created by the field panels and the potential wires (Figure 4.15 (left)). Once near a sense wire the electrons get strongly accelerated by the local $\frac{1}{r}$ electric field and produce more ionization electrons in a process known as "avalanche." The signal in

such a wire is analyzed in real time and depending on the charge collection the wire is said to have been "hit." The time from the moment the collision was expected to have occured to the time the signal was detected gives information about the distance between the particle's trajectory and the sense wire. The high voltage applied to the COT is such that the electric field drift is about 1.9 kV/cm. The drift velocity is about 54 μm/ns. In addition to the electric field due to the cell's field panel, the solenoid magnetic field permeates the COT volume. In such crossed fields charged particles originally at rest move on the plane perpendicular to the magnetic field at an angle α with respect to the electric field as shown in Figure 4.15 (right). This angle is know as the Lorentz angle and depends on the magnitude of the fields and on the properties of the active medium. In the COT the Lorentz angle $\alpha = 35^\circ$ and it is the reason why all the cells are tilted by 35° in the COT geometry, so ionization electrons will drift in the ϕ direction perpendicular to high p_T tracks, optimizing the overall resolution of the COT. The single hit position resolution of the COT has been measured to 140 μm, resulting into a transverse momentum resolution of

$$\frac{\Delta_{P_T}}{P_T} = 0.15\% \frac{P_T}{[GeV/c]}$$

Silicon detectors

At CDF II there are three silicon-based detectors named L00, SVXII and ISL. They differ in size, radius and number of active elements, but they all use silicon micro-strip technology. They enable us to measure the position of secondary vertexes like those produced in the decay of long lived hadrons (such as B mesons) with excellent resolution. In fact, 10 times better than what would be achieved with the COT alone. The best position resolution achieved is 9 μm in the SVXII and the impact

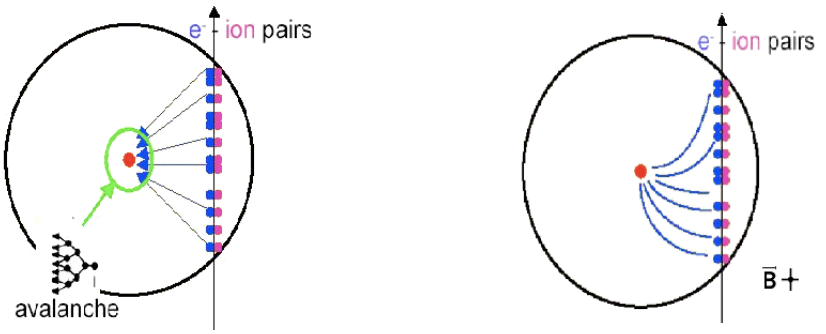

Figure 4.15: Schematic diagram of a single-wire drift chamber. The diagrams show the trail of ionization electrons left by the passage of a charged particle and the drift of the electrons with and without (right and left) the presence of a magnetic field.

parameter resolution, including L00, reaches 40 μm for tracks with $p_T > 3$ GeV/c. The silicon micro-strip detectors were used for the first time in a hadronic accelerator by CDF during Run I of data taking [85].

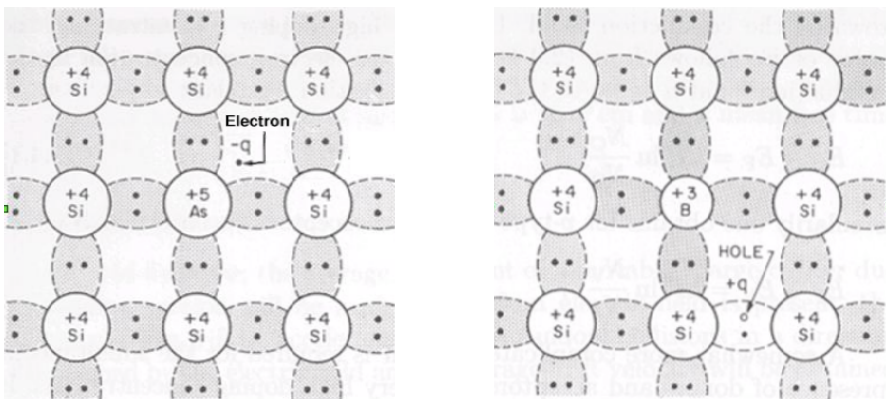

Figure 4.16: Impurities are added to the silicon crystalline structure to obtain n-type (left) and p-type (right) silicon.

The silicon detector takes advantage of the ionization products left by the passage of a charged particle. The semi-conductor properties of the silicon (energy gap between valence and conduction band is small), allows electron-holes produced by ionization to drift apart by means of an applied electric field. However, in pure

silicon the charge carriers outnumber the charge produced in the ionization process by 4 orders of magnitude, therefore the electron-hole pairs quickly recombine. In order to accurately measure the ionization signal it is essential to deplete the free charge carriers in the ionization volume. This is accomplished by exploiting the properties of $p-n$ junctions. A $p-n$ junction is the union of silicon n-type and silicon p-type. Silicon n-type is obtained by adding impurities of donor ions like phosphorus or arsenic to the molecular structure of the silicon crystal as shown in Figure 4.16 (left). The donors introduce energy levels close to the conduction band, resulting in electrons as the majority carriers. Silicon p-type is obtained by introducing acceptor ions like boron in the silicon crystal (see Figure 4.16 (right)). These acceptors introduce energy levels close to the valence band, resulting in holes as the majority carriers. The process of adding donors/acceptors to an otherwise pure material is refer to as "doping."

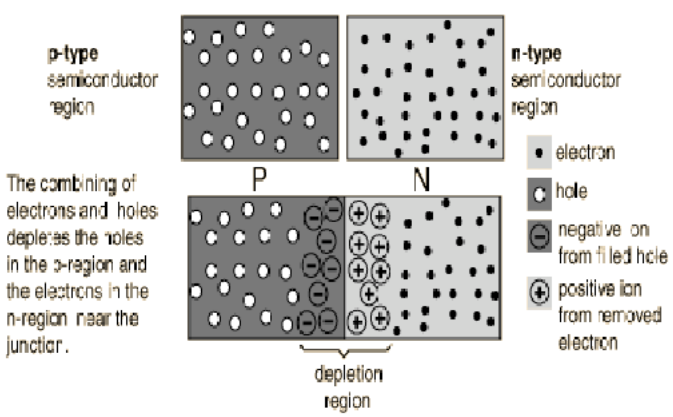

Figure 4.17: Junction of p-type and n-type silicon materials.

When brought together to form a $p-n$ junction, the gradient of electron and hole densities results in a migration of majority carries out of the junction. The junction is now left with net charge of opposite sign on each side, but otherwise depleted of majority carriers as shown in Figure 4.17. The region near the junction is called the

depletion zone. In this zone the electron-hole pairs produced by ionization will drift along the field lines generated by the net charges. In silicon detectors it is common to use a highly doped p-type (p^+) silicon and a lightly doped n-type (n^-) silicon that constitutes the bulk of the detector.

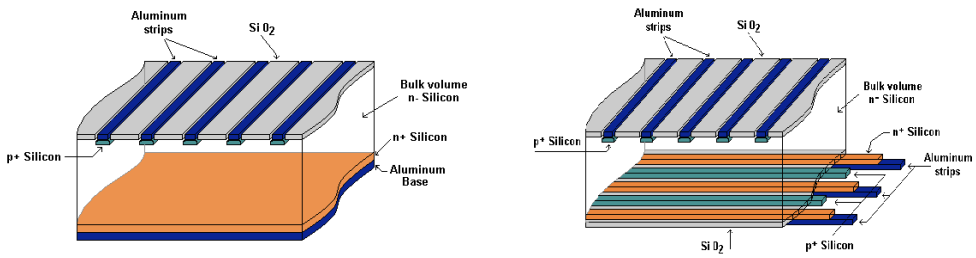

Figure 4.18: Silicon strip detector used for $(\rho - \phi)$ hit position identification (left). Silicon strip 90° detector used for $(\rho - \phi - z)$ hit position identification (right).

At CDF three types of modules made of silicon detectors are used. The first one is made by laying micro-strips of p^+ type silicon over a n^- bulk of silicon (Figure 4.18 (left)). The side of the silicon opposite to the p^+ strips is a highly doped n-type substrate (n^+). If the strips lie parallel to the z direction the module allows $(\rho - \phi)$ position identification. The second type is called a "90° stereo" module and it is similar to the first type, except that the n^+ substrate is replaced with n^+ strips that run perpendicular to the z direction. This allows for the measurement of the hit along the z direction, thus fully determining the position of the hit (Figure 4.18 (right)). The third type is called a small angle stereo which is essentially a $(\rho - \phi)$ module that lies quasi-parallel with respect to the z direction at an angle of only 1.2°. This type is used overlapped with a $(\rho - \phi)$ module allowing a full determination of the hit position, with only a slightly worse resolution in the z position that a 90° stereo module. All three module types are used in all three silicon sub-detectors (SVXII, ISL and L00). The signal is usually detected in a small number of consecutive strips and the hit position is determined by weighing the strip positions by the amount of charge collected by each.

SVXII

The silicon modules are supported with Rohacell foam in assemblies called ladders. Each ladder supports double-sided silicon modules, where on each side lies a string of 4 modules connected to each other by wire bonds, thus quadrupling the length of the strips. Twelve of these ladders are set in a circular configuration to form a layer that surrounds the beam pipe at a certain radius. The ladders are supported by two beryllium bulkheads in the arrangement shown in Figure 4.19. The bulkheads provide support for 60 ladders in 5 concentric layers, conforming a 29 cm long SVXII barrel. The SVXII is built by placing three barrels along the beampipe. Layers are numbered from 0 (innermost) to 4 (outermost). Layers 0, 1 and 3 combine $(\rho - \phi)$ modules on one side with 90° stereo on the other side. Layers 2 and 4 combine $(\rho - \phi)$ modules on one side with small angle stereo on the other. The single hit resolution of SVXII is about 9 μm.

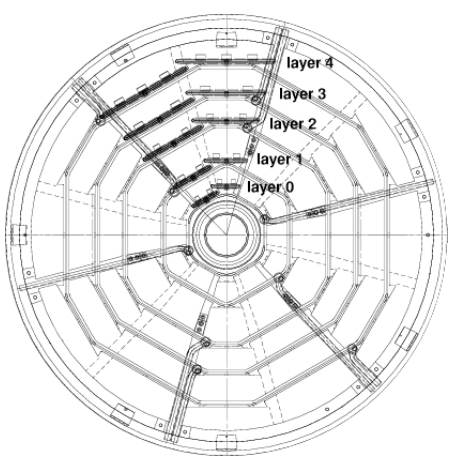

Figure 4.19: End view of the SVXII silicon bulkhead. The placement of ladders is shown in two adjacent wedges.

ISL

Consists of three layers as shown in Figure 4.12. In the central region ($|\eta| \leq 1$) a single layer is placed at a radius of 22 cm. Two more layers are located in the region $1 \leq |\eta| \leq 2$ at radii of 20 cm and 28 cm. The layers are double-sided with $(\rho - \phi)$ on one side and small angle stereo modules on the other. In order to reduce the total number of channels to 268,800 only one out of two channels is read. The ISL single hit resolution is about 20 μm.

L00

Consists of a single-sided layer of 12 ladders and is shown in Figure 4.20. Six of the ladders lie at a radius of 1.35 cm and the other six at 1.62 cm from the beamline. Each ladder is made of 6 sets of two wire-bonded modules each, spanning 95 cm in the z direction. The layer is supported by a carbon-fiber structure.

L00, SVXII and ISL have dedicated cooling lines running at a nominal temperature of $-6°C$. Special effort is made to align the silicon detectors to the beam, as opposed to the COT. The impact parameter[2] of a track is obtained using silicon hit information and is used for triggering purposes. A small misalignment of the COT would not result in a severe track misrecontruction. However, if the silicon detector were aligned with the COT, a misalignment in the latter would cause a non-desirable dependence on the ϕ coordinate of the impact parameter and the trigger.

Tracking and pattern recognition

Tracking Parameterization: In the plane perpendicular to a homogeneous magnetic field, such as the one provided by the CDF solenoid, the trajectory of a charged

[2]Distance of closest approach of a track to the beam.

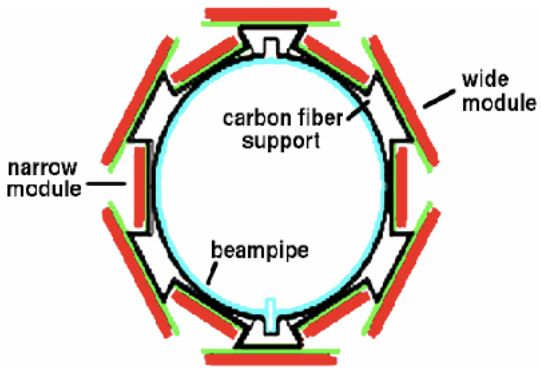

Figure 4.20: End view of the L00 detector.

particle follow a circular pattern. The longitudinal component of the particle's momentum is not modified by the axial magnetic field, thus in three spacial dimensions the trajectories of charged particles are helices. In three dimensions a helix can be parametrized with the use of five parameters, which for convenience are chosen as:

- C: the signed helix curvature defined as $C = \frac{sign(q)}{2R}$, where R is the radius of the circle in the transverse plane and q is the charge of the particle.
- z_0: the position of the point in the z axis which is closest to the track.
- d_0: signed quantity defined as $d_0 = sign(q)(r_C - R)$, where r_C is the position of the center of the circle on the transverse plane. Its magnitude is the distance from z_0 to the closest point on the track. This is the impact parameter.
- ϕ_0: direction of the transverse momentum of the particle in the point to closest approach to the z axis.
- $cot(\theta)$: the ratio of the longitudinal to the transverse momentum ($\frac{P_z}{P_T}$).

Pattern Recognition: Track reconstruction begins with the use of COT data. The algorithm is described in detail in [86], and it is cited here for reference. The

algorithm starts by finding in each superlayer the so-called 3-hit seeds, which are seeds with hits in three consecutive wires that pass some initial quality cuts. All seeds passing this initial selection are then used to search for hits on the remaining wires of the superlayer. Each seed that gives rise to a collection of hits in a superlayer forming a segment of a particle's track is called a segment. To build the segment each seed is fit to a line that defines the path for the hit search. For each hit wire on the path the time of the hit is compared to the expected time, and the hit is added to the segment only if the the time difference is within 20 ns. The procedure is repeated until all the wires in the superlayer are reached. After all the segments in a superlayer are found a list of segments is compiled and ordered in decreasing number of hits.

The next step is to obtain axial tracks (i.e., tracks without any z coordinate information) by linking the segments from the axial superlayers. The algorithm (named Segment Linking, or SL) starts by creating an initial set of tracks from the segments in the outer superlayer (SL8) assuming no impact parameter, and calculating its expected position and angle in the next inner axial superlayer (SL6). For each segment in the inner axial superlayer SL6 a search is done for those segments in SL8 whose expected position at SL6 matches the SL6 segment. The segments are matched if the angle between the expected track at SL6 (extrapolated from the SL8 segment) and the segment in SL6 is less than 0.05 rad, and the position is less than a specific threshold. If multiple matches are found for a given SL6 segment the best match is chosen based on the one with the smallest angular difference. Once the segments are linked the track is fit using only information from these two superlayers, obtaining the curvature, the d_0, the ϕ_0 and the covariance matrix. The information from the rest of the axial superlayers (SL4 and SL2) is now included by linking the tracks made from SL8 and SL6 to the segments in SL4 and SL2. The procedure is similar to that used in linking the SL8 segments to the SL6 segments, except that now the extrapolation path takes into account the d_0 parameter and the covariance

matrix of the tracks. The tracks extrapolated to SL4 and SL2 are compared to the segments found in those superlayers, and the matching is done requiring an angle difference less than 0.05 rad and a position difference less than 4 times the error of the extrapolated track. If a link is found the segment is added to the track and the track is refit to include the new segment information. In addition to the SL algorithm, a second track-reconstruction method named Histogram linking, or HL is run in parallel in order to get the maximum reconstruction efficiency out of the two methods. Essentially this algorithm starts by seeking segment with at least 8 hits and curvature greater than 0.008. The segment is then extrapolated defining a search path. For each layer the distance between the hit and the extrapolated segment is histogrammed. All the layers are then summed up to obtain a global histogram. The bin with the most hits defines the position of the track candidate. If the bin has more than 10 entries (hits) a track is made. At this point axial tracks were obtained by two different algorithms: SL and HL.

Now the stereo pattern recognition is applied. The stereo pattern algorithm starts by matching stereo segments to existing axial tracks (Figure 4.21). For each segment in the outer stereo superlayer a stereo fit is performed to the axial track. The stereo fit is done starting with a value of $z_0 = cot(\theta) = 0$, the z_0 and $cot(\theta)$ obtained as a result of the fit are then fed as inputs for a new fit, iterating up to ten times. All the stereo segments with $|z_0| \leq 175$ cm enter the list of candidate stereo matches. If there are no such segments in the outer stereo superlayer the next inner superlayer is searched. As before, these segment candidates are used to search for matching segments in the next inner stereo superlayers. A set of matching segments should have differences in ϕ of less than 0.01 rads. The matching stereo segments are then used to search for matching segment in the inner stereo superlayers. Other algorithms are applied at this stage to recover stereo information for axial tracks that have failed the stereo-matching algorithm.

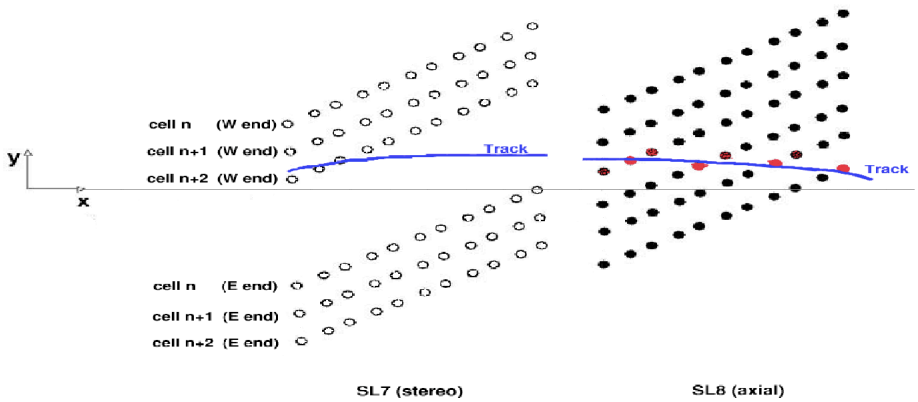

Figure 4.21: Stereo track reconstruction. A few cells of SL8 and SL7 are shown. The ϕ position of the cells in SL8 does not change as a function of the z coordinate. The cells number n, n+1 and n+2 are shown as a function of their z position. An axial track is first reconstructed from the hits (sense wires in red) in SL8. Another track is reconstructed with full z information from the hits in SL7. If the stereo track matches the axial track(as it happens in the diagram) the axial segment is appended to the stereo track and a new fit is performed.

At this point the fit of the three axial parameters and two stereo parameters of the track were done independently. The next step is to perform a full 5-parameter fit. Only tracks with at least two stereo hits and 12 axial hits are fit. The fit is defined to be a success only if all the following apply:

$$|C| \leq 0.1$$
$$|d_0| \leq 150\ cm$$
$$|z_0| \leq 300\ cm$$
$$|cot(\theta)| \leq 4$$

The final step is to remove residual hits from the track (i.e., hits on wires to which the track distance was larger than 600 microns) and make a final refit. If the new fit fails, the track keeps its old parameters. The final list of COT-only tracks is then made by

carefully removing duplicate tracks obtained from the SL and HL algorithms. The most complete track is obtained when the silicon detector hits are added to the COT track information. In general, and depending on the specifics of the analysis, both COT only or COT+SVXII tracks are used. The COT+SVXII track collection is made starting from the COT-only tracks and extrapolating each track through the silicon SVXII detector from the outer layers to the inner ones. At each layer the error matrix of the track parameters is updated to reflect the amount of material traversed. The silicon hits close to the extrapolated track are added to the track and a refit is performed. Each time a hit is appended a new track candidate is generated. Each of these tracks is further extrapolated until all the layers of the detector are searched. From the full list of track candidates associated with one COT track the best one is selected based on the number of hits and quality of the fit. The typical position resolution of a COT+SVXII track is about 40 μm for d_0 and 70 μm for z_0.

4.2.3 Calorimetry

The calorimeter system is located surrounding the CDF tracking volume, outside of the solenoid coil. The different calorimeters that compose the system are scintillator-based detectors, segmented into projective towers (or wedges) in $\eta \times \phi$ space which point to the interaction region. The total coverage of the system is 2π in ϕ and about $|\eta| < 3.64$ units in pseudorapidity. The calorimeter system is divided into two regions: central and plug. The central calorimeter covers the region $|\eta| < 1.1$ and it is divided into two halves at $|\eta| = 0$. It is conceived as a hybrid system of sampling scitilators and strip wire proportional chambers. The forward plug calorimeters cover the angular region $1.1 < |\eta| < 3.64$, as shown in Figure 4.22. Due to this structure, two "gap" regions are found at $|\eta| = 0$ and $|\eta| \sim 1.1$.

The energy resolution of each section was measured with different test beams,

and it can be parameterized in E (for normal incidence) with the following equation:

$$(\sigma/E)^2 = (\sigma_1/\sqrt{E})^2 + (\sigma_2)^2 \tag{4.6}$$

where the first term on the right comes from sampling fluctuations and the photo-statistics of photo-multiplier tubes (PMTs), and the second term comes from the non-uniform response of the calorimeter.

The CDF calorimeter system features 3 sub-systems: the Central, Wall and Forward (or Plug) calorimeters[3]. This section describes the mechanical and geometrical design of the CDF calorimeters. Table 4.2 summarizes the parameters characterizing the different systems.

Central calorimeter

The Central calorimeter has a cylindrical shape surrounding the beam pipe along the z direction. It is made by the union of two cylindrical pieces that join at $z = 0$ and extend over either side in the z direction covering the region $|\eta| \leq 1.1$ as shown in Figure 4.22. Each of these cylindrically-shaped pieces is in turn composed of 24 wedges arranged in two so-called arches with 12 wedges each. Each wedge spanning 15° in azimuth. The construction stage of one of the arches is shown in Figure 4.23 (left).

The basic structure of a central wedge is shown in Figure 4.23 (right). They measure 249 cm in the z direction and have an inner radius of 172 cm and an outer radius of 345 cm. The electromagnetic calorimeter (CEM, Central ElectroMagnetic) occupies the first inner 35 cm of each wedge, while the rest is used to place the hadronic calorimeter CHA (Central HAdronic). The CEM and the CHA are sampling calorimeters and they are built by stacking layers atop of each other. Each

[3]The MiniPlug calorimeter is not discussed in this thesis.

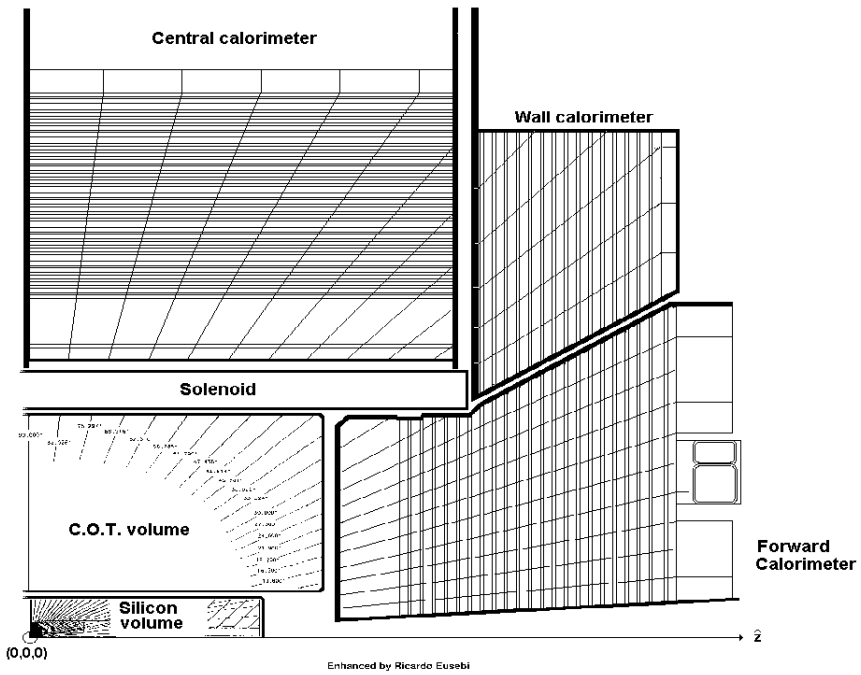

Figure 4.22: Calorimeter sub-systems. Schematic diagram showing a quadrant of the CDF detector. The CDF detector features four calorimeters, the Central, the End Wall, the Forward or Plug and the MiniPlug calorimeter (not shown). All lengths are in centimeters.

layer is made of two components carefully chosen to obtain the most accuracy for the type of measurement wanted. The CEM has 31 layers, each consisting of a 5 mm thick polystyrene scintillator (SCSN-38) together with a 3.175 mm thick lead sheet. The CHA is made of 32 layers, each with a 1 cm thick scintillator and a 2.54 cm thick iron sheet. While the iron and lead components are single-piece sheets running along the z direction, the scintillator is cut and isolated into several pieces (or tiles) along the z direction. The light from all the scintillator tiles in a single tower is collected separately from the CEM and CHA in order to distinguish between electromagnetic and hadronic energy. The total energy is then obtained for each tower by adding the two measurements. The segmentation in the CEM matches that of the CHA,

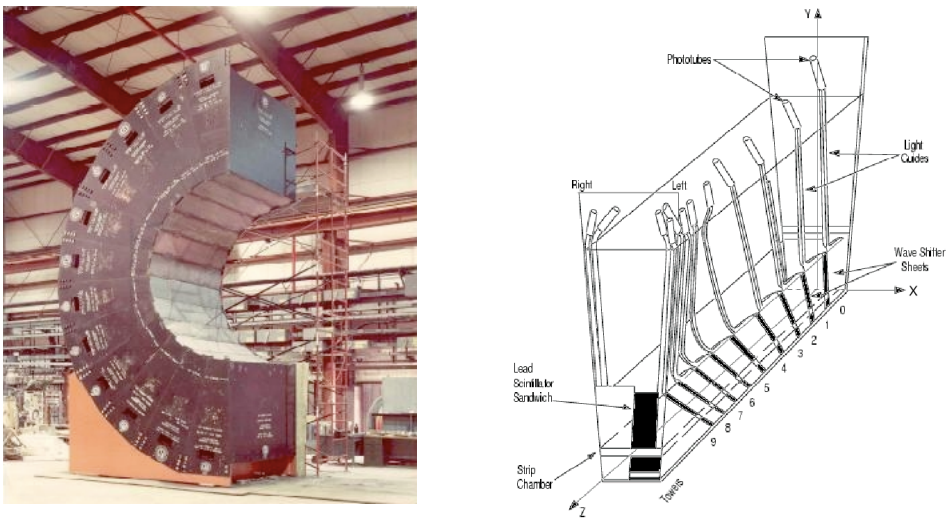

Figure 4.23: Construction stage of one arch. It contains 12 wedges and constitutes a quarter of the central calorimeter (left). Schematic diagram of one central wedge (right).

i.e., the η values of the centers of the towers match in both calorimeters. The angular difference between the centers of two consecutive towers is a constant $\delta_\eta = 0.11$ throughout the detector. The CEM has ten projective towers. The total radiation length for a particle traveling from the origin through the first tower ($\eta \leq 0.11$) is about $18{\chi_0}^4$, but this total length would be different for a particle following a trajectory with larger η as it has to traverse more material. To keep the total radiation length constant across all towers in a wedge, a fraction of the lead sheets are replaced with plastic ones. This proportion increases with the η of the tower, such that the last tower has approximately 20 lead sheets versus 31 found in the first tower. There-

[4]The radiation length χ_0 describes the characteristic amount of matter transversed, for a high-energy electron to lose all but $1/e$ of its energy by bremsstrahlung, which is equivalent to 7/9 of the length of the mean free path for e^+e^- pair production of high-energy photons. The average energy loss due to bremsstrahlung for an electron of energy E is related to the radiation length by $(dE/dx)_{brems} = -E/\chi_0$ and the probability for an electron pair to be created by a high-energy photon is $(7/9)\chi_0$.

fore, when looking out from the interaction point along different values of η within the same wedge, the same total thickness of material is encountered independently of η. This is what is called a projective tower geometry (Figure 4.22). The capabilities of the CEM are enhanced by the implementation of two extra detection systems in the CEM volume of the wedges: a proportional chamber named CPR (Central PReradiator) located just in front of the CEM (from the interaction point), and a Proportional strip detector (CES) at about $7\chi_0$ into the tower.

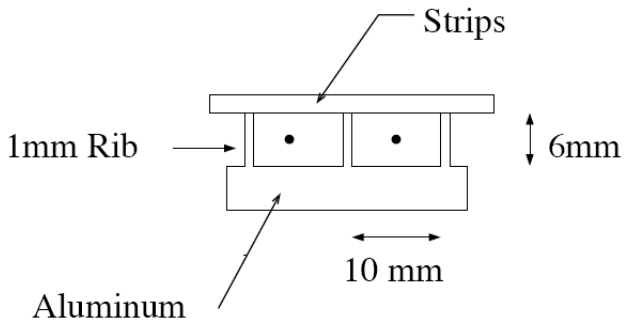

Figure 4.24: Chambers of the central electromagnetic shower detector.

The interaction of particles with the solenoid and tracking material before entering the calorimeter results in soft shower profiles that are measured in the CPR. This serves as a discriminator to distinguish pions and conversion electrons from electrons and photons coming from the primary vertex, helping to reduced the electron background. The CES is a two-dimensional shower profile detector located at the expected shower maximum of $7\chi_0$. It is made of wires running along the z direction and strips orthogonal to them (Figure 4.24). It provides valuable information used in the identification of electrons and photons. The position measurement can be matched to existing tracks while the transverse shower profile can be used to separate single photons from the two photon decays of π^0's.

When the particles of the shower pass through the scintillators they emit light.

In the CEM the light going out of the thin edge of the scintillator is collected by a flat Y7 Polymethylmethacrylate (Y7 PMMA) panels transverse to the scintillators. Two such panels located on each side of the wedge are used for each CEM tower. The upper edge of the panel is molded into a squared 3 cm by 3 cm section which is optically coupled to a long rod that extends radially passed the CHA and that ends in a Photo Multiplier Tube (PMT). The light collection design is shown in Figure 4.25 for the CEM and the CHA. The energy deposited in a CEM tower is then obtained by adding the information of both PMTs in the tower. The PMMA also acts as a wave shifter, reducing the frequency of the light emitted by the SCSN-38 scintillator to the optimum for the PMT. The energy resolution of the CEM is measured to be $\frac{\sigma(E_T)}{E_T} = \frac{13.5\%}{\sqrt{E_T}} + 1.5\%$, where $E_T = Esin\theta$ and θ is the angle of incidence of the test beam of high energy electrons and photons.

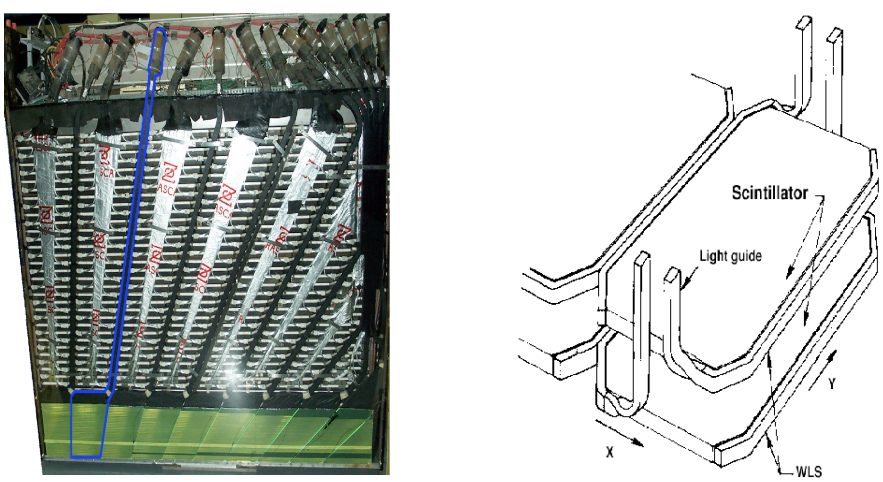

Figure 4.25: A detailed picture of the side of a central calorimeter wedge. The light is collected from the CEM by the flat panels at the bottom and redirected via a square light guide to the PMT on the upper side. In the CHA the light is collected from each tile and guided upwards to merge with a PMT (left). Detail of the light collection in CHA scintillator tile (right).

The CHA light collection is slightly different. The light coming out of each scintillator tile is collected by two square-shaped light guides that surround the tile

as shown in Figure 4.25 (right). In each hadronic tower the light guides on the same wedge side are joined together and extended until reaching the PMT. Details of this can be seen in Figure 4.25 (left). As with the CEM, the light in the CHA is collected using two PMTs per tower. Out of the ten CEM towers only 8 are properly projected into the CHA, the other two projecting outside the CHA at the far-z side. The total interaction absorption length for the first 8 towers is about $4.7\lambda_0$[5]. For the two towers that project outside the CHA, the absorption length is completed by a set of towers located in the WHA (Wall HAdronic calorimeter). Charged pions were used to obtain the energy resolution in the CHA and WHA detectors, which are $\frac{\sigma(E_T)}{E_T} = \frac{50\%}{\sqrt{E_T}} + 3\%$ and $\frac{\sigma(E_T)}{E_T} = \frac{75\%}{\sqrt{E_T}} + 4\%$, respectively.

Wall hadron calorimeter

The WHA extends the hadronic towers of the CHA to roughly complete $4.7\lambda_0$ per tower. The material components of the layers in the WHA are the same as those in the CHA. The physical characteristics however are different, as the WHA towers are made of layers that lie parallel to the (x, y) plane, and thus are perpendicular in orientation to those of the CHA as it is shown in Figure 4.22. The WHA uses 15 layers of 5 cm iron and 1.0 cm scintillator.

Forward calorimeter

The forward calorimeters are placed surrounding the beam pipe at 172 cm in the z axis at either sides of the interaction point (see Figure 4.22 and 4.26). It provides coverage in the region $1.1 \leq |\eta| \leq 3.6$. As with the central calorimeter the forward calorimeter has an electromagnetic (PEM) and a hadronic (PHA) section. As before

[5]An interaction length is the average distance a particle will travel before interacting with a nucleus $\lambda_0 = \frac{A}{\rho\sigma N_A}$ where A is the atomic weight, ρ is the material density, σ is the cross section and N_A is Avogadro's number.

both sections are made of stacked layers of scintillator and lead (for the PEM) or scintillator and iron (for the PHA). The layer orientation follows that of the WHA where the layers lie on the (x, y) plane. In the transverse plane the calorimeter is sectioned into 12 wedges of 30° in ϕ. A wedge section is shown in Figure 4.27 where the tower segmentation can be appreciated. The lines define the boundaries of the scintillator tiles. The tiles at the same position in different layers define the projective towers. The PEM has 23 layers, each composed of 4.5 mm thick lead and 4 mm thick SCSN38 scintillator, resulting in a total of about $21\chi_0$ at normal incidence. The PHA has also 23 layers of 5.08 cm iron and 6 mm scintillator resulting in about $7\lambda_0$[6]. Test beam measurements determined that the energy resolution of the PEM for electrons and photons is $\frac{\sigma(E)}{E} = \frac{16\%}{\sqrt{E}} + 1\%$. The PHA energy resolution is $\frac{\sigma(E)}{E} = \frac{80\%}{\sqrt{E}} + 5\%$ for charged pions that do not interact in the electromagnetic component.

The light is collected from the scintillator tiles by a wavelength shifting fiber (WLS) embedded in the scintillator. One fiber per tile is used, adding up to 40 fibers per layer per wedge. All the fibers of a single projective tower in the PEM are joined together into the tower's PMT. The same is done for the PHA towers, resulting in 480 PMTs for the PEM and another 480 for the PHA. The PEM is also implemented with a shower maximum detector (PES) similar to the one used in the CEM. This 2-D position sensitive detector is placed at a depth of $6\chi_0$ inside the PEM calorimeter and helps discriminate between electrons and di-gamma decays of π^0's. The PES covers a circular area of 2.6 m in diameter at 1.8 m from the origin of the detector. It is divided into 8 sections of 45° in ϕ, thus spanning three PEM wedges. Each sector (see Figure 4.28) contains two layers U and V of 5 mm pitch scintillator strips.

These layers are held together with 3.175 mm thick lexan material. The strips in the U and V layers lie at a 45° crossing angle allowing the 2-D position identification.

[6]In addition, the PEM material adds about $1\Lambda_0$ to the total interaction length.

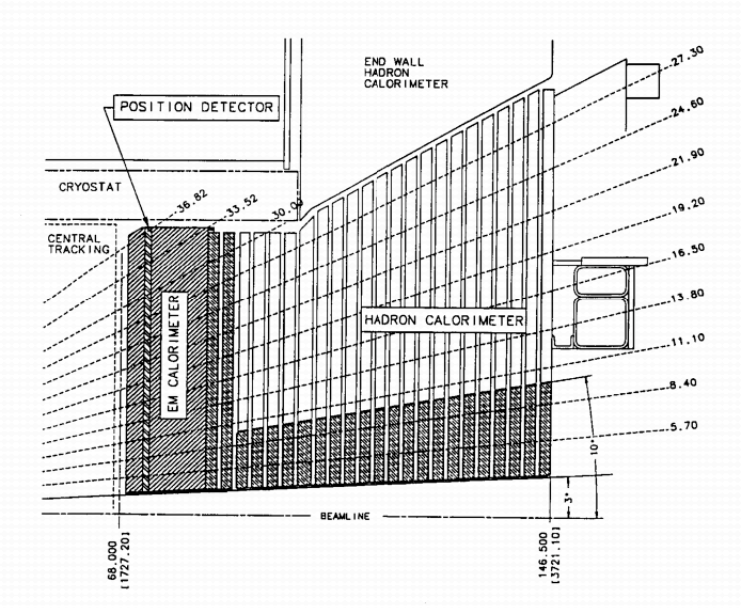

Figure 4.26: The forward calorimeter section. Detailed diagram showing the location of the electromagnetic and hadronic calorimeter, the shower maximum detector and the tower segmentation.

In order to reduce the occupancy of the strips expected from the underlying event the U and V layers are both divided into an upper and lower segments corresponding to $1.13 \leq |\eta| \leq 2.60$ and $2.60 \leq |\eta| \leq 3.50$ respectively. This η division line matches the PEM calorimeter inter-tile boundary. The occupancy expected in the lower segment is two to four times that of the upper one, but more segmentation is impractical if not physically impossible. The strips connect to a WLS fiber that carries the light to a channel in a Multiple Anode PMT (MAPMT) for readout. It should also be mentioned that the scintillator of the first layer of the PEM is 10 mm thick (as opposed to 4 mm thick) and made of BC408, a different scintillator type that yields about 1.6 times more light than the one used in the rest of the calorimeter. The larger thickness of the scintillator sheet and the larger light yield allow this layer to be used as a preradiator (PES), providing a good discriminator between gamma and

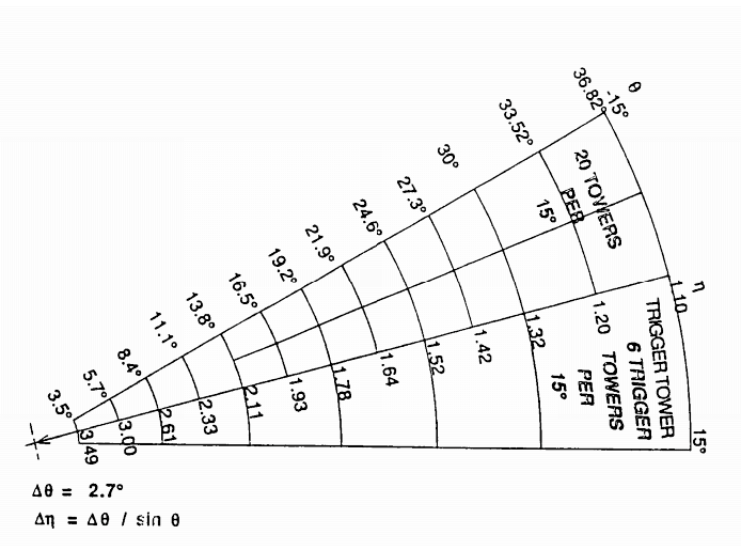

Figure 4.27: The section of a wedge in the forward detector. The physical scintillator tiles in the region $-15° < \theta < 0°$ are repeated but not shown in the region $0° < \theta < 15°$, where the diagram shows the logical towers used in the trigger system.

π^0's. This layer is read out separately and all the fibers are read out using Multiple Anode PMTs (MAPMT).

Calorimeter	Coverage	Thickness	Energy resolution (E in GeV)
CEM	$\|\eta\| < 1.1$	$18\chi_0$	$\frac{13.5\%}{\sqrt{E_T}} + 2\%$
CHA	$\|\eta\| < 0.9$	$4.7\lambda_0$	$\frac{50\%}{\sqrt{E_T}} + 3\%$
WHA	$0.9 < \|\eta\| < 1.3$	$4.7\lambda_0$	$\frac{75\%}{\sqrt{E_T}} + 4\%$
PEM	$1.1 < \|\eta\| < 3.6$	$21\chi_0$	$\frac{16\%}{\sqrt{E}} + 1\%$
PHA	$1.2 < \|\eta\| < 3.6$	$7\lambda_0$	$\frac{80\%}{\sqrt{E}} + 5\%$

Table 4.2: CDF II Calorimeter subsystems and characteristics. The energy resolution for the EM calorimeter is given for a single incident electron and that for the hadronic calorimeter for a single incident pion.

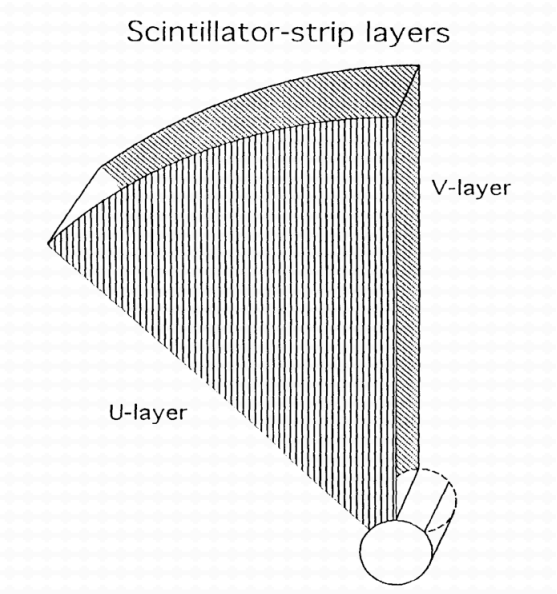

Figure 4.28: The U and V layers that conform the Shower maximum detector (PES) of the Plug forward Calorimeter.

4.2.4 Muon detectors

The muon system, which consists of sets of drift chambers and scintillators, is installed beyond the calorimeter system as the radially outermost component of CDF Run II (r$\sim$3.5 m). The muon system is divided into different subsystems: the Central Muon Detector (CMU), the Central Muon Upgrade Detector (CMP), the Central Muon Extension Detector (CMX) and the Intermediate Muon Detector (IMU).

Most particle detection systems are not specific to one particle. While the CEM is most sensitive to electrons it also detects photons. The detection of a shower in the CEM does not undoubtedly indicate the nature of the original particle. Similar statements can be made about the CHA and the tracking sub-systems. The properties of muons, on the other hand, allow for a clear and often unmistakable identification. For example, the large mass of the muon compared to that of the electron results

in a $\frac{M_{ele}^2}{M_{muo}^2} \sim \frac{1}{40000}$ relative suppression of electromagnetic bremsstrahlung [90], the primary process by which electromagnetic showers are created. Muons, as electrons, are weakly interacting particles which are not subject to the strong interactions with atomic nuclei that could result in hadronic showers. Despite its larger mass, the muon is still lighter than most other particles, therefore, its decay to particles that may interact hadronically is kinematically forbidden. This results in the muon's long decay time and its ability to pass through larger amounts of matter without interacting than any other charged particle.

CDF takes advantage of these properties of muons by positioning muon detectors behind large quantities of absorber. The only charged particle with the ability to pass through such absorbers with high efficiency is the muon, so a "hit" in these charged particle detectors is often a clear signal of a muon. The CDF muon systems typically consist of drift chambers stacked in a few layers in order to reconstruct the particle's track information. In a muon system a pair of adjacent stacks is called a tower, and the portion of a reconstructed track is called a stub. The timing information is obtained, when possible, by placing a scintillator in front of the drift chambers. However unlikely, there are other processes that can mimic a muon with "hits" in the muon system. To minimize these effects, CDF requires that the stub matches a COT track in order for the stub to be identified as a muon. The use of larger absorbers to reduce some of these contributions is not always advised. This is because the effect of multiple Coulomb scatterings grows with the material traversed, resulting in tracks reconstructed at the muon system that do not reflect the original muon direction, and thus do not match the corresponding COT track. Additionally, the muon also loses (little) energy while traversing the absorber.

At CDF four charged particle detection sub-systems form the overall CDF muon detection system. As mentioned at the beginning of this section, these systems are named: CMU (Central MUon Detector), CMP (Central Muon uPgrade), CMX

(Central Muon eXtension), and IMU (Intermediate MU Detector). The coverage of each of these systems is shown in Figure 4.29.

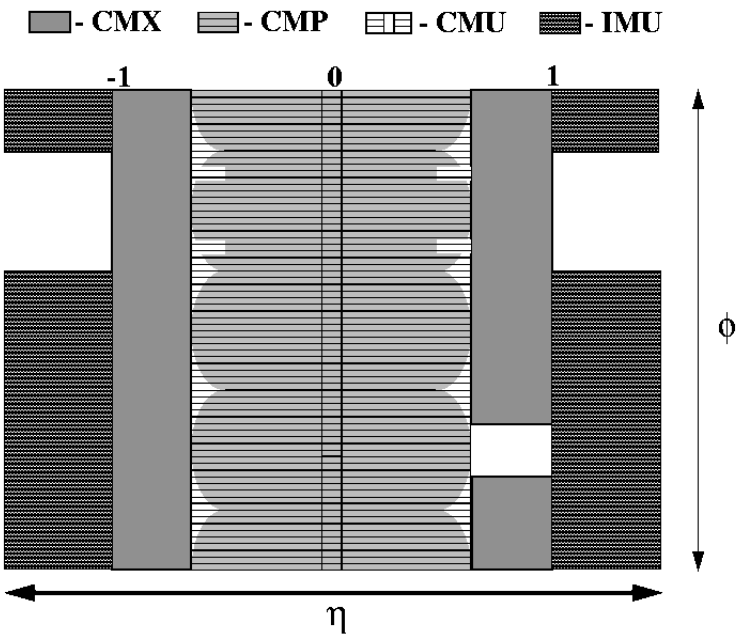

Figure 4.29: The coverage in $\eta - \phi$ coordinates is shown for the Muon system.

CMU

The Central muon system shown in Figure 4.30, is housed in the Central calorimeter wedges, described in Section 4.2.3. Like the central calorimeter, it has cylindrical shape and it is located at a minimum radius of 347 cm. The calorimeter serves as an absorber and the muon range-out threshold[7] is about 1.4 GeV/c, mostly due to the heavy calorimeter material. Because of geometrical and mechanical constraints only 12.6° (out of the total 15°) of the wedges are instrumented, leaving a 2.4° gap between chambers in consecutive wedges. A central gap of about 18 cm is also

[7]The transverse momentum value (p_T) below which a muon will not pass through an absorber is called the range-out threshold.

present between chambers in the east-side and west-side wedges. In each wedge the CMU system is segmented into three sections of 4.2° each, as shown in Figures 4.30 and 4.31. Each section consists of four stacked layers of drift chambers. Each layer has four single-wire drift cells. The cells run along the z direction and are filled with a mixture of argon-ethane-isopropyl in 49.5:49.5:1 proportions providing a drift velocity of about 54 μm/ns. Each sense wire is attached to a TDC to get timing information.

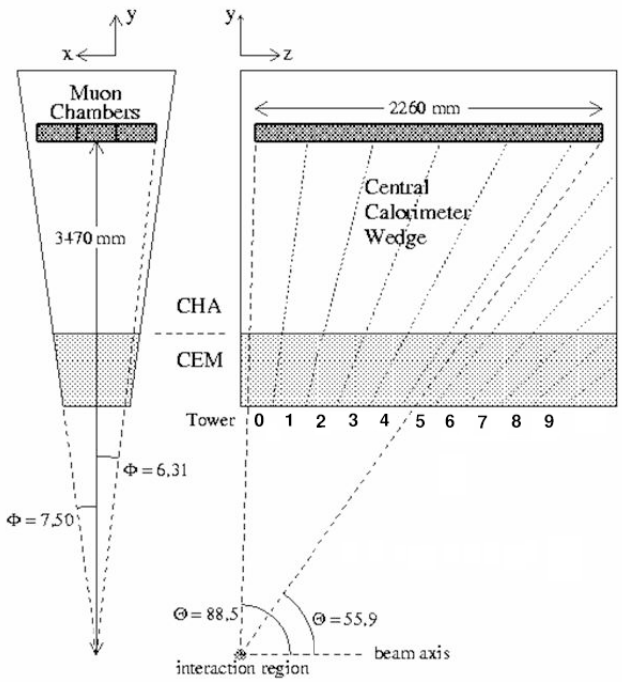

Figure 4.30: The CMU muon chambers are located in the Central Calorimeter wedge geometry, at a larger radius than the CHA.

The individual cells are made of aluminum and are held at -2500 V, while the sense wires are held at +2325 V. The upper two layers have slightly larger cells than the lower two, resulting in a slight offset of the sense wires between layers of up to 2 mm in the outer cells. This allows us to resolve the two-fold ambiguity

characteristic of drift chambers regarding which side of the wire the track passed through.

The CMU system also provides the z coordinate of the track by the charge division method. This method essentially consists of collecting the charge on both ends of the wire. Due to the wire resistivity the charge will differ according to the z position of the track. If $Q1$ and $Q2$ are the collected charges on both ends of the wire, the position z_0 of the track from the end in which $Q1$ was collected is $z_0 = L \times \frac{Q1-Q2}{Q1+Q2}$ where L is the total length of the wire. Wires of adjacent cells are also connected together on one end in order to perform charge division to find the z coordinate of the hit.

The two most significant limitations to the CMU system performance are: a) the short length of the absorber in front of it, i.e., the calorimeter. With only $5.5\chi_0$ the showers generated in the CHA are often extended beyond it, reaching the CMU system and producing "fake" muon signals. And b) the gaps between wedges, which add up to 57.6° or 16% of the $2\pi\phi$ coverage.

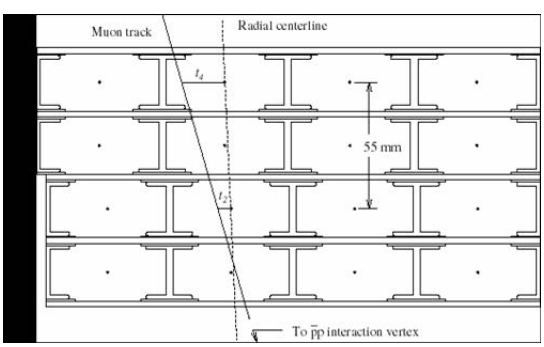

Figure 4.31: One CMU section (of the three) located in a central calorimeter wedge. The details of the cell are shown. The black line on the left is the lateral wall of the wedge.

CMP

The CMP (or Central Muon uPgrade) is designed to improve upon both limitations of the CMU system. The CMP scintillator-chambers are located outside the detector and are arranged on what can be thought of as the sides of a rectangular box (Figure 4.11). These chambers are preceded by a heavy steel absorber that adds $2.3\chi_0$ for a total of $7.8\chi_0$. With this additional absorber the range-out threshold reaches only 2.2 GeV/c, and is still well below typical muon energies from electro-weak sources. As can be seen in the diagram of Figure 4.32 and Figure 4.11, some portions of the system take advantage of already present steel, like the upper and lower solenoid return yokes, therefore, not all the sections lie on the same plane.

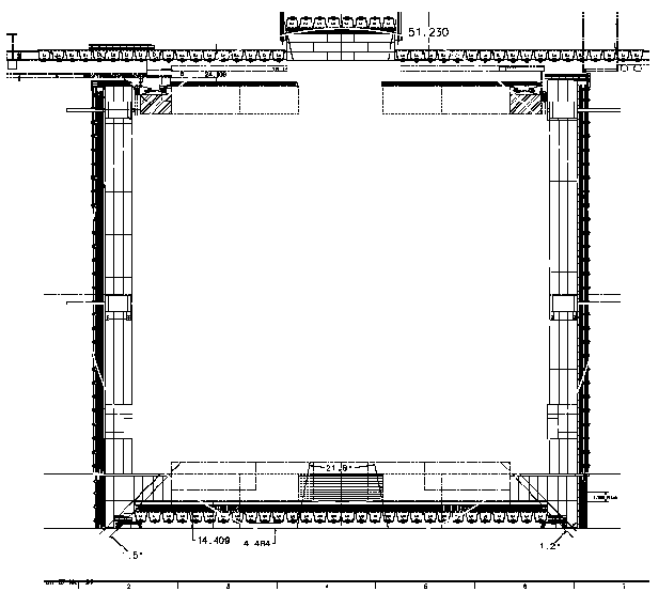

Figure 4.32: Positioning of the CMP system in the CDF detector hall.

The CMP also provides full coverage in ϕ. Due to its rectangular geometry the η coverage depends on the ϕ coordinate; as seen in Figure 4.29 it is roughly about $|\eta| \leq 0.6$. The CMP system is based on single wire drift chambers 2.5 cm

by 15 cm and 640 cm long as shown in Figure 4.33. The chambers are arranged in four layers with half-cell staggering between them. Behind the cell a scintillator system (named CSP Central Scintillator uPgrade) provides timing information. As with the CMU, each wire is read by a single TDC. With the inclusion of the CMP system a new handle for the evaluation of the number of CMU "fake" muons due to "punch-through" is at hand. In order to obtain cleaner samples of muons it is now common practice to require that CMU hits have a corresponding CMP hit, in addition to a matching COT track. This muons are informally called CMUP muons. While the CMP provides for a better discriminator of muons than the CMU alone, its η coverage is limited, and a big fraction of muons get lost in uninstrumented regions at larger η.

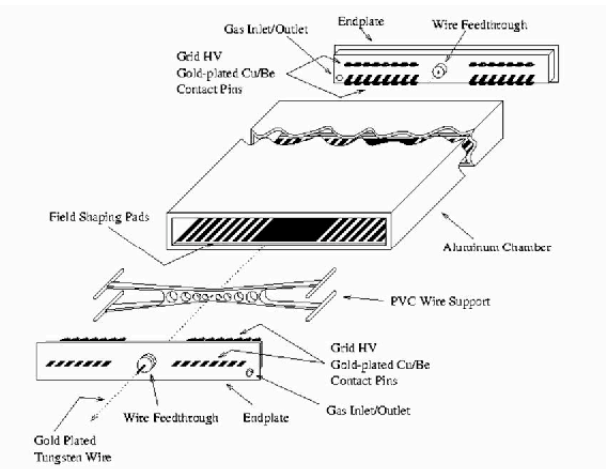

Figure 4.33: Drift chambers used in the CMP and CMX muon detector systems. The wire supports are used only in CMP.

CMX

The CMX (Central Muon eXtension) enlarges the coverage of the muon system, providing extra coverage in the region $0.6 \leq \eta \leq 1$, while slightly overlapping in the

region $\eta = 0.6$ with the CMU. The CMX consists of a pair of arches at each end of the detector. On each side, the CMX chambers follow the surface of an imaginary cone whose apex lies in the z axis further away from the detector; the aperture angle of the cone is about 45°. Figure 4.34 shows the arches during the detector assembly period. The two arches are complemented with two more chamber arrays at the top and bottom, which are not shown in Figure 4.34. While the upper chamber is made of the same components as the arches the lower one has a finer segmentation. In the arches and the upper chambers the CMX is segmented in wedges, each spanning 15° in ϕ. Each wedge is composed of 8 layers of a 180 cm long version of the drift chambers used in the CMP. The layers are staggered as shown in Figure 4.35 so that all particles will traverse at least 4 layers in order to accurately reconstruct the track. While no additional steel was added in front of this detector the large angle from the interaction point through the calorimeter, solenoid yoke, and support structures yields considerably more absorber material than in the central region. The CMX is also implemented with scintillators in what is called the CSX (Central Scintillator eXtension). In the arches the scintillators are installed both in the inside and outside of the chamber and are half-cell staggered. Each scintillator is read by a single PMT. In the lower chambers scintillators are placed only on one side, and read with two PMTs from both ends to allow the computation of a mean-time.

IMU

The main components of the IMU are the Barrel Chambers (BMU). This detector is shaped as two contiguous barrels of drift chambers located on the outer radius of the toroids (Figure 4.34). These chambers expand the muon coverage of CDF up to $|\eta| \simeq 1.5$, but only cover the upper 270° in azimuth. Sets of scintillators were also installed for trigger confirmation and spurious signal rejection. The central muon scintillator upgrade, CSP, are counters installed on the outer surface of the CMP chambers. Two

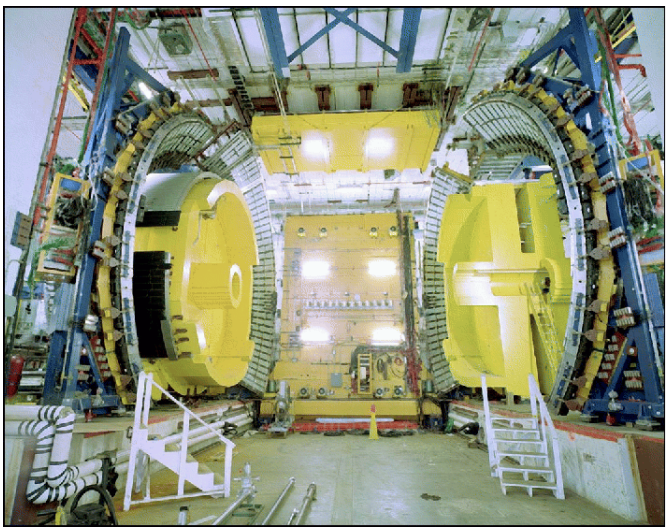

Figure 4.34: The CMX arches in the detector hall. The arches are still to be complemented at the top and bottom to give a full ϕ coverage. The rest of the CDF detector is yet to be put in between them. Part of the IMU system is also shown surrounding the yellow toroids.

layers of scintillators are mounted on the internal and external sides of the CMX, the so-called central muon extension scintillator, CSX. Finally, the IMU incorporates two scintillator systems: the barrel scintillator upgrade, BSU, and the Toroid Scintillator Upgrade, TSU. The BSU detector is made of rectangular scintillators mounted on the outside of the BMU chambers and with the same azimuthal coverage. The TSU detector is made of trapezoidal scintillators mounted on the inner face of the toroid and covering 2π in azimuth.

4.2.5 TOF

The TOF (Time Of Flight) is dedicated to measure the time of flight of the particles generated in the primary interaction. The TOF system consist of 216 scintillator bars 279 cm long arranged in a cylindrical geometry. The bars have a square cross

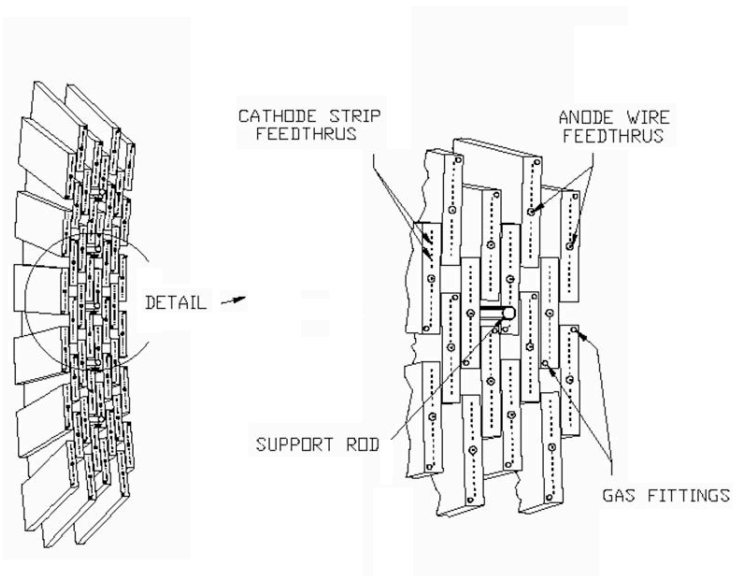

Figure 4.35: The eight-layer CMX drift chamber system.

section with an approximate side of 4 cm, and occupy the space between the COT and the cryostat of the solenoid (see Figure 4.36) at a radius of 138 cm. The bars are made of plastic scintillator BC-408, which provides a fast rise time and long decay time while having a bulk attenuation length of about 380 cm. The bars are placed next to each other providing full coverage in ϕ for $|\eta| \leq 1.0$. At each end, the bars are coupled to Winston cone light guides attached to fine mesh PMTs. The PMTs are located in situ and thus embedded in the solenoid's 1.4 T magnetic field. This reduces the PMTs gain to 2×10^4, about 500 less than if no magnetic field were present. To increase signal, a custom made amplifier with a gain of about 15 was appended to the output of the PMT.

The TOF measures the time of flight of the particle from the moment the interaction occurs to the moment the particle traverses the TOF bars. The time of the interaction is determined by the tracks in the event, and the TOF system provides the time at which the particle passed through a bar, taking into account necessary

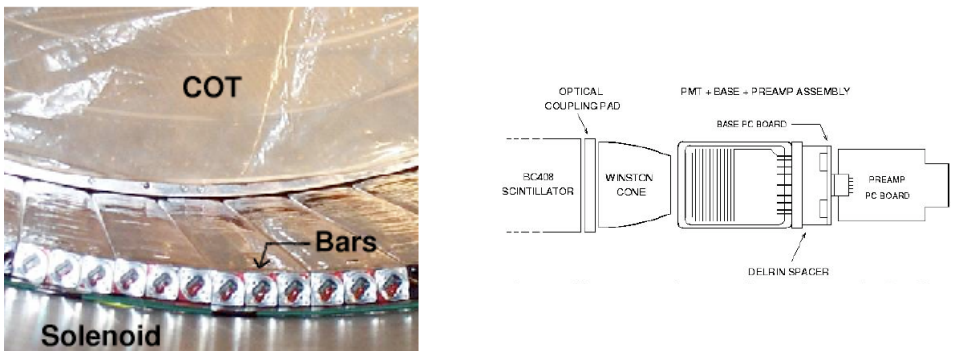

Figure 4.36: Left: TOF bars installed in the lower portion, between the superconducting solenoid (surface below) and the COT structure (above). Right: Detail of the read out design of the TOF bars.

corrections. The difference between these two times is the time of flight of the particle. Since the length of the track between these two points is known from the tracking systems, the TOF provides a direct measurement of the particle's velocity. For a given momentum the smaller the time difference, the larger the velocity and the smaller the mass. The mass can be directly calculated from $m = \frac{p}{c}\sqrt{\frac{c^2t^2}{L^2} - 1}$ where p and L are the momentum and length of the particle's track and t is the time of flight of the particle obtained from the TOF. In Figure 4.37 (left) the expected time of flight difference between charged π, K and p relative to one another is shown as a function of momentum. The time difference between pairs of particles is translated into a particle ID separation power with about 100 ps of resolution, which provides a two standard deviation separation between $K^{\pm}$ and $\pi^{\pm}$ for momenta $p < 1.6$ GeV/c . The performance of the TOF with early data is shown in Figure 4.37 (right) A more detailed description of the construction details is given in [91] and of its expected performance and impact in physics analysis in [92].

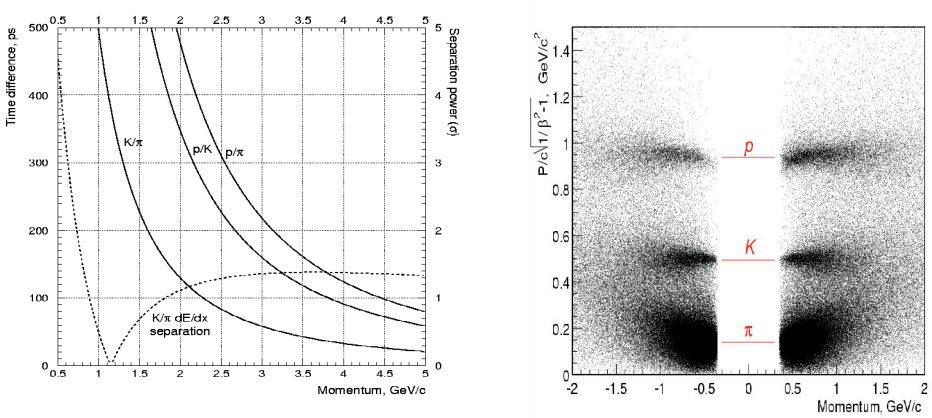

Figure 4.37: TOF performance. Expected time of flight difference (in ps) between charged π, K and p relative to one another as a function of momentum and separation power assuming 100ps resolution. The dashed line shows the K/π separation from dE/dx measurement by the COT. TOF recontructed mass versus momentum. The data clusters around the charged π, K and p masses with a 60:30:10 proportion. Data from Tevatron store 860 (12/23/2001).

4.2.6 CLC

In CDF, the beam luminosity is determined using gas Cerenkov counters located in the pseudorapidity region $3.7 < |\eta| < 4.7$, which measure the average number of inelastic interactions per bunch crossing. The Cherenkov Luminosity Counter (CLC) was designed for the Tevatron Run II in order to achieve a precision measurement of the instantaneous luminosity. The CLC is located at each side of the detector in the 3° gap between the plug calorimeter and the beam pipe as shown in Figure 4.38. It spans from 184 cm to 405 cm along the z axis. The CLC is composed of an array of Cherenkov counters in the shape of long cones (cone-modules). These are made of 2 layers of aluminized mylar rolled into a conical shape, and have on one end a light collector that directs the light to a PMT, and on the other a glued plastic cap. There are three types of cone-modules arranged in three concentric (and conic) layers with 16 cones each. The full CLC consists then of 48 conical counters

per detector side (Figure 4.39). The cones are supported by two plates, one at 390 cm from the detector center just outside the volume of the forward calorimeter, and the other located inside the volume of the detector at about 184 cm from the detector center. These plates align and support the cones such that they have a good proyective geometry with respect to the nominal collision point. The CLC is filled with isobutane gas at about 14.7 psig pressure. The conical geometry makes the CLC sensitive to particles coming from the collision point. More detailed information on the CLC is found in [93] and [94].

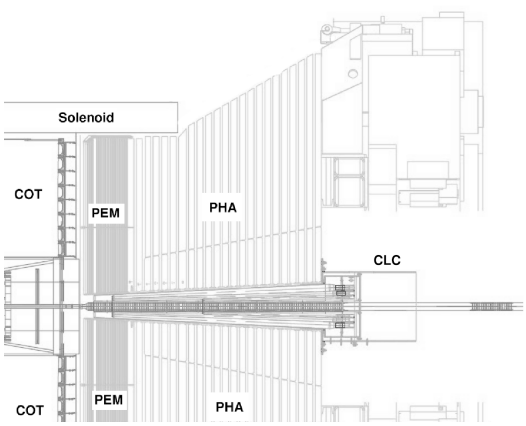

Figure 4.38: The CLC is located in the 3° gap between the plug calorimeter and the beam pipe.

The CLC measures the average number of primary interactions per bunch crossing (μ), and this information allows the computation of the instantaneous luminosity L. The average number of primary interactions, μ, is related to the instantaneous luminosity, L, by the expression:

$$\mu \cdot f_{bc} = \sigma_{tot} \cdot L \tag{4.7}$$

where f_{bc} is the bunch crossing frequency at the Tevatron, on average 1.7 MHz for 36 $\times$ 36 bunch operations, and σ_{tot} is the total $p\bar{p}$ cross section. Since the CLC is not

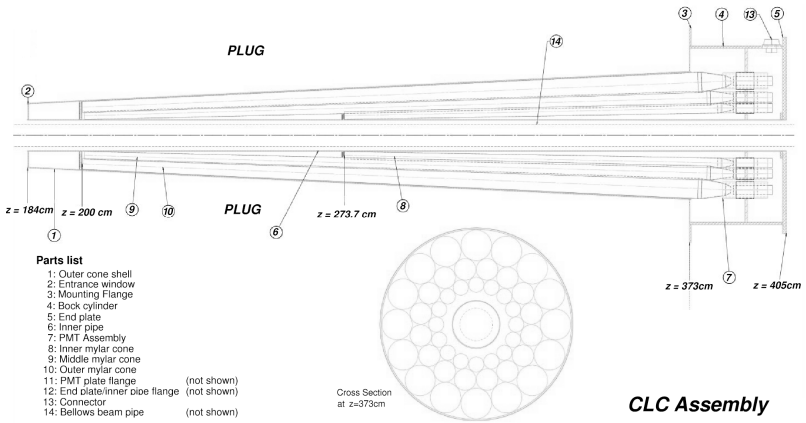

Figure 4.39: The CLC Assembly diagram. The cross section view at z=373 cm is also shown.

sensitive to the elastic component of the $p\bar{p}$ scattering, Equation 4.7 can be rewritten using the inelastic cross section, σ_{in}, as

$$L = \frac{\mu \cdot f_{bc}}{\sigma_{in}} \tag{4.8}$$

where now μ is the average number of inelastic $p\bar{p}$ interactions. The method used at CDF for the luminosity measurement is based on the counting of empty crossings [95]. This method determines μ by measuring the first bin of the distribution which corresponds to the probability of having zero inelastic interactions, P_0, through the relation:

$$P_0(\mu) = e^{-\mu} \tag{4.9}$$

which is correct if the acceptance of the detector and its efficiency were 100%. Given the limited accuracy of this statement, there is a need for some selection criteria, α, to define an "interaction." An "interaction" is defined as a $p\bar{p}$ crossing with hits above a fixed threshold on both sides of the CLC detector. Consequently, an empty crossing is defined as a $p\bar{p}$ crossing with no interactions. Given these selection criteria, the

experimental quantity P_0, called $P_0^{exp}\{\alpha\}$, is related to μ through:

$$P_0^{exp}\{\mu;\alpha\} = (e^{\epsilon_w \cdot \mu} + e^{-\epsilon_e \cdot \mu} - 1) \cdot e^{-(1-\epsilon_0)\cdot\mu} \tag{4.10}$$

where the acceptances ϵ_0 and $\epsilon_{w/e}$ are, respectively, the probability to have no hits in the combined east and west CLC modules and the probability to have at least one hit exclusively in the west/east CLC module. The evaluation of these parameters is based on Monte Carlo simulations, and typical values are $\epsilon_0 = 0.07$ and $\epsilon_{w/e} = 0.12$. To obtain the luminosity measurement using the Equation 4.8, the value of σ_{in} is still needed. At the beginning of Run II, an extrapolation to 2 TeV of the value measured at $\sqrt{s} = 1.8$ TeV by CDF [96] was used. The cross section would be $\sigma_{in} = 60.4$ mb. To facilitate the comparison of CDF and D0 cross section measurements in Run II, the collaborations agreed to use a common inelastic cross section [97], $\sigma_{in} = 59.3$ mb that is about 1.9% smaller than previous value. Since CDF never modified the actual luminosity value used internally within the collaboration, the CDF quoted luminosity is multiplied offline by a factor of 1.019. Different sources of uncertainties have been taken into account to evaluate the systematic uncertainties on the luminosity measurement [98]. The dominant contributions are related to the detector simulation and the event generator used, and have been evaluated to be about 3%. The total systematic uncertainty in the CLC luminosity measurements is 5.8%, which includes uncertainties on the measurement, 4.2%, and on the inelastic cross section value, 4%.

4.2.7 The trigger system and data flow

The CDF trigger system consists of three trigger levels, see Figure 4.40. The first two levels are hardware based, while the third one consists of a processor farm. The decisions taken by the system are based on increasingly more complex event information. The two hardware levels are monitored and controlled by the Trigger Supervisor Interface, TSI, which manages signals from the different sections of the

trigger and DAQ system, a global clock and bunch crossing signal.

As mentioned in Section 4.1.5 the proton and antiproton bunches cross every 396 ns. With the last Tevatron lumonisities of the order 4×10^{31} $\mathrm{cm}^{-2}\mathrm{s}^{-1}$ this amounted to about 1.6 interactions per bunch crossing, i.e., 1.6 interactions every 396 ns or about 2.5 Million events/second. There are two main reasons for which recording all the events produced is not feasible. First, with an average event size of about 100 kiloBytes, it would require throughput and storage capabilities of 250 GigaBytes/second, and there is currently no technology with such capacities. Second, even if such technology existed the detector would not be fast enough to read out and transfer all the information before the next bunch crossing occured. It typically takes about 2 μs for a complete CDF detector readout, but there is only 0.4 μs between bunch crossing. However, the majority of the events produced are of little interest to the current CDF physics program. Most of these events are protons and antiprotons passing right by each other with very little momentum transferred between the interacting partons. Only ocassionally there will be a hard parton-parton collision with outgoing particles with large transverse momentum. The non-elastic, soft interacting events are typically called "minimum bias events." The minimum bias events have a production cross section of the order of 10 mb, and are typically used for calibration purposes. The CDF physics program is interested in much more rare events, with production cross sections typically smaller than 100 μb. This is more than three orders of magnitude smaller than the total $p\bar{p}$ cross section. The $t\bar{t}$ production cross section is about 6.7 pb or nine orders or magnitude smaller than the minimum bias production cross section!

These problems are curcumvented by the implementation of the CDF trigger system, which selectively reads out and stores only those events considered of interest. A schematic diagram of the CDF trigger system is shown in Figure 4.40 (Left). The CDF global trigger system has a three-level structure. The Level-1 trigger filters

out the vast majority of the events without any interesting signatures. Since this level takes up to 5.5 μs to reach an accept/reject decision, the front-end electronics is equipped with a 14-event deep buffer to accomodate new events while the Level-1 decision is taken. The accepted events are further analysed by the Level-2 trigger. The Level-2 trigger takes more time and adds more information to make further decisions regarding the event. If accepted, the full information of the detector subsystems is read out and passed to the Event Builder. There, the different fragments of information from the different sub-detectors is collected, reordered and concatenated to build a single unit of information containing all the event information. The Event Builder then passes the full event directly to Level-3. Level-3 then makes the final decision and, if accepted, the event is tranfered to the Consumer Server Logger (CSL), a local mass storage system that temporarely stores the events. The CSL ultimately transfers the information to the Fermilab Feynman Computing Center (FCC) where it is written on tape. If the connection between the CSL and the FCC were to break the CSL can store up to 8 hours of information before reaching its maximum storage capacity. The CDF trigger system is descibed in detail in [100]. A detailed Description of the CSL and FCC can be found at [99]. In the following subsections a more detailed description of the parts that comprise the CDF Trigger system are discussed.

Level-1 trigger system

A block diagram of the Level-1/Level-2 trigger system is shown in Figure 4.40. These trigger levels are managed by the Trigger Supervisor Interface (the box marked TSI/CLK in the figure), which also provides a global clock. The Level-1 is a synchronous trigger system. On every bunch crossing, this trigger reads out the event information from the detector, stores it in the pipeline and makes a decision on an earlier event. The decision is made based on "primitives", a fast and rudimentary re-

construction of the raw information from all sub-detectors. The Level-1 trigger uses primitives made from measurements of energy in the calorimeters (Central, Wall, and Plug), tracks in the COT, stubs in the muon systems (CMU,CMP and CMX) and, not shown in the figure, coincidence hits in the CLC for minimum bias trigger and Time of Flight information. The first three are shown in Figure 4.40 (right) as the boxes labeled L1-CAL, L1-TRACK, and L1-MUON repectively.

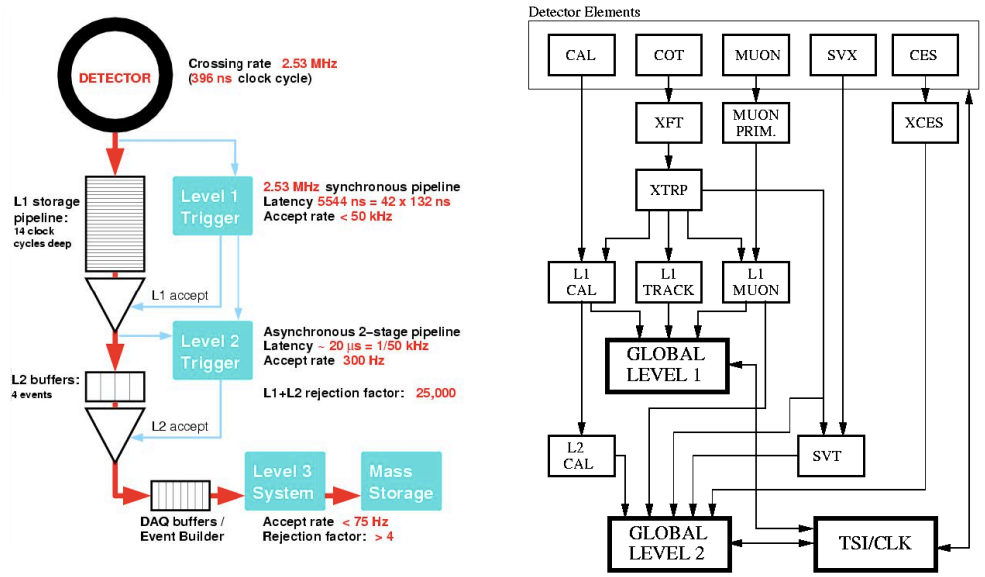

Figure 4.40: Schematic diagram of the CDF global Trigger system (left). Detailed block diagram of Level 1 and Level 2 trigger (right).

The L1-CAL information sets an array of 8 bits per each 15° wedge, representing 8 momentum thresholds per wedge. Track extrapolation is done using look-up tables so that tracks crossing wedge boundaries are handled correctly. The L1-Muon basically informs what muon towers have fired[8], and makes use of the real granularity of the muon sub-detector systems, as opposed to logical (typically bigger) granularity units. These primitives are often combined to form electron, muon or jet objects, that are later to be used in the trigger decision process.

[8]A muon tower is said to have fired if at least one of the stacks has a stub.

In general tracking recontruction, even when done rudimentarily, is more complex and harder to achieve than the reconstructions of primitives based on calorimeter and muon information. The extra complexity involved in tracking is shown in Figure 4.40 (right) by the boxes labeled XFT and XTRP whose function is explained next.

XFT

XFT stands for eXtremely Fast Tracker, and is an online track processor to identify charged particles in the COT in time to take part in the Level-1 decision making process. The processor uses the information of the 4 axial superlayers only. The identification algorithm basically consists of two steps: Segment finding and segment linking. The segment finding portion classifies all the COT hits into either prompt hits (drift time <44 ns) or delayed (drift time between 44 ns and 132 ns). Then in each superlayer a set of predefined patterns of prompt/delayed hits are applied to find all the segments. These predefined patterns were obtained assuming impact parameter equal to zero. The track's charge is then determined by the ϕ position and the track's slope in the two outermost axial superlayers. The slope and the ϕ position conform a "pixel." The segment linking is then perform by matching all those pixels that appear to be part of the same track. If 4 or more pixels are found an estimate of the track parameters is obtained. The tracks found by the XFT are passed to the XTRP and a copy is made to be used later in Level-2 if the event were to pass Level-1.

XTRP

The XTRP, or the eXTRaPolator unit, performs a quick extrapolation of the XFT tracks to other sub-detector systems such as calorimeters and muon chambers. This

allows for a better identification of real physics objects (or particles) such as electrons, jets and muons; as opposed to detector objects such as tracks, showers in the calorimeters, etc. An algorithm that uses a particular logical combination of the primitives is called an individual (Level-1) trigger. These individual triggers are designed based on the desired event final state, or equivalently on the physics process to be studied. In order to cover the CDF physics program, 64 individual triggers are implemented. The Level-1 trigger system makes a decision for each of the 64 individual triggers, while also making a global Level-1 decision. If the event is accepted the event information is passed to the Level-2 system together with the 64 bits representing the accept/reject decision for the individual triggers. The Level-1 trigger rate of accepts is less than 50 kHz, much smaller than the total input rate of 2.5 MHz.

In summary, the three main components of the Level-1 trigger system are:

- The L1-CAL calorimeter trigger is employed to detect electrons, photons, jets, total transverse energy and missing transverse energy, $\not\!\!E_T$. The calorimeter triggers are divided into two types: object triggers (electron, photons and jets) and global triggers ($\sum E_T$ and $\not\!\!E_T$). The calorimeter towers are summed into trigger towers of 15° in ϕ and by approximately 0.2 in η. Therefore, the calorimeter is divided in 24 × 24 towers in $\eta \times \phi$ space. The object triggers are formed by applying thresholds to individual calorimeter trigger towers, while thresholds for the global triggers are applied after summing energies from all towers.

- The L1-TRACK trigger is designed to reconstruct tracks in the COT. An eXtremely Fast Tracker, XFT, uses hits from the 4 axial layers of the COT to find tracks with a p_T greater than some threshold, $\sim$ 2 GeV/c. The resulting track list is sent to the extrapolation box, XTRP, that distributes the tracks to the Level-1 and Level-2 trigger subsystems.

- L1-MUON system uses muon primitives, generated from various muon detector elements, and XFT tracks extrapolated to the muon chambers by the XTRP to form muon trigger objects. For the scintillators of the muon system, the primitives are derived from single hits or coincidences of hits. In the case of the wire chambers, the primitives are obtained from patterns of hits on projective wires with the requirement that the difference in the arrival times of signals be less than a given threshold. This maximum allowed time difference imposes a minimum p_T requirement for hits from single tracks.

Level-2 trigger system

The Level-2 trigger is an asynchronous system that processes events as they are received from Level-1. The Level-2 decision is based on Level-1 primitives as well as on more accurately processed information from the calorimeter, additional information from the shower maximum strip chambers (CES), and the axial strips of the Silicon vertex detector (SVXII). These are indicated in Figure 4.40 (right) by the boxes labeled L2CAL, XCES and SVT. The L2CAL hardware uses the trigger tower provided by L1CAL and further calculates the total energy of the clusters by summing the energy of the towers that comprise it. The clusters are obtained by identifying "seed" (energy above a seed threshold) and "shoulder" towers (which are contiguous to the seed tower, above a shoulder threshold and below the seed threshold).

The need for L2CAL also arises from the fact that jets are not fully contained in Level-1 trigger towers, and thus the Level-1 threshold is set to values much lower than those of jet energies. This results in rates that would be too high for Level-3 to handle, so the L2CAL provides a reduction in the jet trigger rates by calculating the total cluster energy (which should be close to the jet energy) and applying a filter based on jet energy. The L2CAL hardware also provides total tranverse energy and tranverse missing energy calculations. The XCES hardware takes the information

of the CES and generates a bitmap of strips with energy above a certain threshold. Then the XFT tracks, extrapolated by the XTRP, are matched with the bitmap to produce electron candidates. The SVT system significantly improves upon the XFT track parameters. It extrapolates the XFT track primitives to the volume inside the SVXII and recalculates the track parameters, this time adding the impact parameter information which is not present in the XFT primitives. It uses only the information of the axial strips of the SVXII. The impact parameter is an indication of a displaced vertex, which is a strong and clean signature in many physics processes. Currently, the number of possible individual triggers for Level-2 is 192. After the Level-2 global decision is made the event is transfered to the Event Builder [101] if accepted, and then to Level-3 togheter with the Level-1 and Level-2 primitives and individual trigger bits. The Level-2 hardware takes about 20 μs to make the global decision, and with the implementation of a set of 4 event buffers the total accept rate is below 300 Hz.

In summary, the Level-2 performs the following tasks:

- The L2-CAL hardware carries out the hardware cluster finder functions. It receives trigger tower energies from the L1-CAL and applies "seed" and "shoulder" thresholds for cluster finding. It is basically designed for triggering on jets, but specific reconstruction of clusters for triggering on electrons, taus, and photons is also performed.

- The shower maximum detector provides a much better spacial resolution than a calorimeter tower. The XCES boards perform sum of the energy on groups of four adjacent CES wires and compare them to a threshold (around 4 GeV). This information is matched to XFT tracks to generate a Level 2 trigger. This trigger hardware provides a significant reduction in combinatorial background for electrons and photons.

- Silicon Vertex Tracker, SVT, uses hits from the $r \times \phi$ strips of the SVX II and tracks from the XFT to find tracks in SVX II. SVT improves on the XFT resolution for ϕ and p_T and adds a measurement of the track impact parameter, d_0. Hereby the efficiency and resolution are comparable to those of the offline track reconstruction. The SVT enables triggering on displaced tracks, that have a large d_0.

Level-3 trigger system

The Level-3 trigger system is a large array of conventional PC's running on the Linux operating system. After an event is accepted at Level-2, it has to be read out completely. This operation involves collecting data from over a couple of hundred VME Readout Buffers (VRBs). The Event Builder assembles the event from pieces of data from the Level-2 system into complete events. The Level-3 is divided into 16 sub-farms, each consisting of a converter node (running the Event Builder) and 12 to 16 processor nodes. Once the event is built, it is sent to one node in the Level-3 sub-farm. The Level-3 trigger reconstructs the event following given algorithms. These algorithms take advantage of the full detector information and improved resolution not available to the lower trigger levels. This includes a full 3-dimensional track reconstruction and tight matching of tracks to calorimeter and muon-system information. Events that satisfy the Level-3 trigger requirements are then transfered onward to the Consumer Server/Data Logger (CSL) system for storage first on disk and later on tape. The average processing time per event in Level-3 is on the order of a few seconds. The Level-3 leads to a further reduction in the output rate, roughly 50 Hz.

A set of requirements that an event has to fulfill at Level 1, Level 2 and Level 3 constitutes a trigger path. The CDF II trigger system implements about 200 trigger paths. An event will be accepted if it passes the requirements of any one of these

paths and, depending on the trigger path, it will be stored in a trigger dataset. A complete description of the different datasets at CDF Run II can be found in [102].

Another important feature of the trigger system of CDF is that Level-1 and Level-2 accepts can be pre-scaled. This means that only a fraction of the events that fulfill the trigger requirements are actually accepted. Even if this implies loosing potentially useful events, it becomes necessary at high luminosity. Given the continuously improving performance of the Tevatron, pre-scaling trigger has become common practice in the last years. Moreover, the trigger system allows for dynamic pre-scaling of trigger accepts, meaning that the scaling factor varies with the instantaneous luminosity, so the output bandwidth is maximally utilized.

4.2.8 Data taking

From the operational point of view, data taking occurs in three basic steps. The first step is to "set up" the detector, which involves the initialization of the crates and front-end electronics and the download of settings to specialized electronic components for calibration and other purposes. The second step is the actual data-taking, which occurs in a fairly automatic way and could last in principle for as long as the operator decides. There are, however, a number of reasons to abort data-taking such as the approaching end of a store (Tevatron cycle), hardware malfunction, software problems, etc. The data collected from the moment the detector is set up until data taking finishes is called a "run," and is characterized by a single integer number. Each time the detector is setup the run number is incremented by one. In certain runs sub-detector systems could have malfunctioned, be turned off or be in a general bad state. When a run is finished, it is always properly marked to indicate the overall status of the sub-detector systems. This information is later used to decide what runs to exclude (if any) from the analysis data. The list of runs to be considered good is

called 'the "good run list" and depends on the choice of sub-detectors required to be working properly for a particular physics analysis.

Chapter 5

Event and particle reconstruction at CDF

Collisions of protons and antiprotons can result in the generation of a large variety of final state particles. In particular, this dissertation considers final states characterized by three isolated leptons plus missing energy, considered to be the "golden channel" for the search for Supersymmetry at the Tevatron. To perform a data analysis, the information obtained from the detector has to be processed in order to reconstruct observables. This section describes the requirements imposed on the information gathered from different sub-detectors, to efficiently identify the different particles in the energy rage of interest in this analysis.

5.1 Track and Primary Vertex Reconstruction

The trajectories of charged particles are found (in a first approximation) as a series of segments in the axial superlayers of the COT. Two complementary algorithms associate the segments lying on a common circle to define an axial track. Segments

in the stereo layers are associated with the axial tracks to reconstruct 3-D tracks. For muons and electrons used in this analysis, COT tracks are required to have at least 3 axial and 3 stereo segments with at least 5 hits per superlayer. The efficiency for finding isolated high momentum COT tracks in the COT fiducial volume with $p_T > 10$ GeV is measured using electrons from $W^{\pm} \to e^{\pm}\nu$ events and it is found to be $(98.3 \pm 0.1)\%$. Silicon hit information is added to reconstructed COT tracks using an "outside-in" tracking algorithm. The COT tracks are extrapolated to the silicon detector and the track is refitted using the information from the silicon measurements. The initial track parameters provide a width for a search region in a given layer. For each candidate hit in that layer, the track is refitted and used to define the search region into the next layer. The search uses the two best candidate hits in each layer to generate a small tree of final track candidates, and the one with the best fit χ^2 is selected. The efficiency to associate at least three silicon hits with an isolated COT track is found to be $(91 \pm 1)\%$. The primary vertex location for a given event is found by fitting well-measured tracks to a common point of origin. At high luminosities, more than one collision can occur on a given bunch crossing. For a luminosity of $\sim 10^{32}$ cm^{-2}s^{-1}, there are ~ 2.3 interactions per bunch crossing. The luminous region is long, with $\sigma_z = 29$ cm; therefore the primary vertices of each collision are typically separate in z. The first estimate of the primary vertices (x_V, y_V, z_V) is binned in the z coordinate, and the z position of each vertex is then calculated from the weighted average of the z coordinate of all tracks within 1 cm of the first iteration vertex, with a typical resolution of 100 μm. The primary vertex is determined event by event by an iterative algorithm which uses tracks around a seed vertex, defined as above, to form a new vertex. The χ^2 for all tracks relative to the new vertex is calculated, tracks with bad χ^2 are removed, and the cycle is repeated until all tracks have a good χ^2. The locus of all primary vertices defines the beamline, the position of the luminous region of the beam-beam collisions through the detector. A linear fit to (x_V, y_V) vs. z_V yields the beamline for each stable

running period. The beamline is used as a constraint to refine the knowledge of the primary vertex in a given event. The transverse beam cross section is circular, with a rms width of $\approx 30\mu$m at $z = 0$, rising to $\approx 50 - 60\mu$m at $|z| = 40$ cm. The beam is not necessarily parallel nor centered in the detector.

5.2 Electron reconstruction and identification

Electrons are measured in the Electromagnetic Calorimeters. Incident electrons induce showers across multiple calorimeter towers. The energy of the showers appears in clusters in the $\eta - \phi$ coordinate system. The clustering algorithm looks for EM-objects in the CEM. It starts by creating an E_T-ordered list of possible seed towers that are in the fiducial region and have $E_T^{em} > 2$ GeV. Then, towers within the fiducial regions (including seeds) adjacent to the available highest E_T seed are checked. They may belong to the cluster if they are in the same detector as the seed, and have not been already used. Clusters in CEM can grow only away by 1 physical tower from the seed. A cluster is found if the total EM-energy passes $E_T^{em} > 2$ GeV (default), and $E_T^{had}/E_T^{em} < 0.125$, where E_T^{had} is the hadronic energy within the seed tower in CEM. After all clusters are found, tracks from the default collection are matched with them computing the cluster center with the energy weighted average of the CES coordinates of the cluster towers. The central electron candidates must have a matching COT track.

The electron cluster is formed of a seed EM tower, defined as the tower where most of the energy is deposited, and a number of shoulder towers, which are added to the seed tower until the maximum cluster size is reached. The largest cluster spans two towers in pseudorapidity and on tower in azimuth.

The geometry of the CDF detector imposes the categorization of electrons into

two types according to the calorimeter in which the deposition takes place: central and plug electrons.

Central electrons. Central electrons traverse the central part of the detector, $|\eta| < 1.1$, leaving a track in the COT and depositing their energy in the CEM calorimeter. To identify central electrons some or all of the following requirements are applied:

- $E_T = E \cdot sin(\theta) > 5$ GeV. The transverse energy E_T is equal to the total electromagnetic energy deposited by the electron in the CEM cluster (E) multiplied by the $sin(\theta)$ of the COT track pointing to the seed tower of the cluster. The energy E is corrected to account for non-linear effects and known differences in response between different towers, as measured from $Z \rightarrow e + e^-$ candidates.

- $p_T > 4$ GeV. The transverse momentum of the COT track. The momentum resolution of the track is improved by constraining the track to originate from the beam line position (beam constrained) whenever possible.

- Fiduciality. This variable requires that the electron is reconstructed in a region of the CDF detector that is well instrumented.

- $E_{had}/E_{em} < 0.055 + 0.00045 \text{ GeV}^{-1} \cdot E_{total}$. The ratio of the energy deposited in the hadronic calorimeter cluster to that deposited in the electromagnetic cluster. The second term in the right hand side compensates for a drop in efficiency of the cut at very high energies, as the electron shower leaks into the hadronic calorimeter.

- $E/P < 2$, if $p_T > 50$ GeV. Ratio of the electromagnetic calorimeter energy to the momentum of the track as measured from the COT track. This cut helps reducing the number of jets that fake electrons. These jets typically contain a

π^0 that deposits its energy in the electromagnetic calorimeter. This cut also helps discard those electrons that radiate high energy photons. The photon is typically collinear with the electron track and generally deposits its energy in the same calorimeter tower and therefore the cluster energy does not differ much from the original energy of the electron. The p_T of track, however, is significantly reduced making the ratio E/P much larger than one.

- $Lshr < 0.2$. This quantity uses the lateral shower profile and compares it to what is expected from electromagnetic showers. It is defined as

$$L_{shr} = 0.14 \sum_i \frac{E_i^{measured} - E_i^{expected}}{\sqrt{(0.14\sqrt{E})^2 + \sigma^2_{E_i^{expected}}}} \tag{5.1}$$

  where the index i runs over adjacent towers, $E_i^{measured}$ is the energy measured in tower i and $E_i^{expected}$ is the energy expected from test beam data. The energy resolution in the CEM is represented by $0.14\sqrt{E}$, where E is the energy in the cluster, and $\sigma^2_{E_i^{expected}}$ is the error in $E_i^{expected}$. Typically $Lshr$ is a two-tower sum. Any extra particles accompanying the one responsible for the main EM shower will tend to add to the energy in adjacent towers and make $Lshr$ a larger number.

- -3.0 cm$< Q \cdot \Delta x < 1.5$ cm; $|\Delta z| < 3$ cm. The distance between the COT track extrapolated to the CES, and the best matching CES cluster is represented by Δx and Δz, where x and z are local CES variables. This requirement imposes a close match between the two. The cut on Δx has been multiplied by the charge of the track, Q, and it is asymmetric in $r - \phi$ to account for possible photon bremsstrahlung in the outward direction relative to the track.

- $\chi^2_{strip} < 10$. This quantity compares the shower profile in the shower maximum detector, CES, with the shower profile obtained from test beam electrons.

- Track quality cuts. A well reconstructed track should have at least 5 hits in each of three axial and two stereo superlayers of the COT.

- $|z_{vertex}| < 60$ cm. The position in z of the primary vertex interaction. The z_{vertex} is determined by the intersection of the track with the beam axis. The longitudinal spread of the event vertex about the nominal interaction point $z = 0$ is a Gaussian with $\sigma = 29$ cm.

- Not a conversion. The interaction of photons with the detector material can result in the conversion of photons into electron-positron pairs. These conversions can be identified by the presence of another electron candidate with opposite charge near the electron candidate. If both tracks are close in ϕ at the point of conversion the event is flagged as a conversion and rejected as a whole.

- Calorimeter isolation: $E_T^{iso}/E_T^{cluster} < 0.1$ (fractional isolation), if $E_T > 20$ GeV. The ratio of transverse energy in the electromagnetic and hadronic calorimeter contained in a cone of radius $\Delta R = \sqrt{(\Delta\eta)^2 + (\Delta\phi)^2} < 0.4$ which excludes the electron cluster energy to the electron cluster energy. This cut rejects electrons that are not isolated from hadronic activity, including those coming from semi-leptonic quark decays. If $E_T < 20$ GeV, then absolute isolation is used: $E_T^{iso} < 2.0$.

- Impact parameter: $|d_0, corr| < 0.02$ cm (with $N_{si\ hits} > 2$), or $|d_0, corr| < 0.2$ cm (with $N_{si\ hits} \leq 2$). The impact parameter is the distance of closest approach of a track to the the beam axis. This cut is particularly efficient at identifying leptons coming from displaced vertices, such as those resulting from the semi-leptonic decays of b quarks. By requiring the impact parameter to be small (not displaced), the leptons are most likely prompt electrons forming at the nominal interaction point. The value of d_0 is corrected before the cut is applied.

The efficiencies of central electron identification cuts are measured using a $Z/\gamma \rightarrow$

e^+e^- data sample. Events are required to have oppositely charged electrons, with an invariant mass of the electron pair in a ± 15 GeV range from the nominal Z mass. One electron is required to pass all the identification cuts, while the other is used to obtain the efficiency of the cuts. The central electron identification efficiencies for data and MC are measured by the collaboration and parametrized as functions of the period of data taking (PerfIDia [127]). On average, the identification efficiencies of tight central electrons (defined in Chapter 5) in data and MC are $(0.799 \pm 0.002)\%$ and $(0.814 \pm 0.001)\%$, respectively. In order to compensate for differences in the reconstruction of tight electrons in data and MC a scale factor of $\epsilon_{data}/\epsilon_{MC} = 0.981 \pm 0.003$ (stat.)± 0.004 (syst.) is applied to correct acceptances obtained from MC.

Plug electrons. Electron candidates depositing energy in the PEM calorimeter are called plug electrons. To identify plug electrons some or all of the following requirements are applied:

- $1.13 < |\eta| < 2.8$. The PEM allows the identification of electromagnetic clusters of energy at pseudorapidities up to $|\eta| < 2.8$. The charge misidentification rate of PEM can be very large as forward electrons may not traverse a large part of the COT, and track information is limited. The track efficiency is improved by using an algorithm named the Phoenix algorithm [104]. The algorithm starts by associating a track with energy observed in the PEM cluster. The track is constrained at the primary vertex and at the center of the cluster. Two tracks are constructed based on the two possible charges of the electron. The algorithm next looks for hits in the silicon that matches the tracks. If hits are matched the track is reconstructed. If both track are reconstructed the one with the best goodness of fit is taken. Electrons candidates with a cluster in the PEM and a Phoenix track are called Phoenix electrons.

- $E_T > 5$ GeV. The transverse energy of the PEM cluster, which is limited to two towers in pseudorapidity and two towers in azimuth, must be grater than 5 GeV.

- $E_{had}/E_{em} < 0.055$. Similar to the central electron requirement.

- $U_{5\times9} \geq 0.65$ and $V_{5\times9} \geq 0.65$ (Pes5x9). The variables $U_{5\times9}$ and $V_{5\times9}$ are isolation variables for the PES shower maximum detector. They are independently applied to both the U and V layers. The clustering in each layer is performed by ordering strips in decreasing energy with the highest-energy strips used as seeds. The PES cluster has a fixed width of nine strips. The quantities $U_{5\times9}$ and $V_{5\times9}$ represent the ratios of energy sum in the central 5 strips to the total energy in all the nine strips.

- $\chi^2_{PEM} < 10$. This variable compares the energy distribution in the 3×3 PEM towers around the seed tower to what was obtained from a test beam of electrons by means of a χ^2 test statistics.

- $\Delta R_{PES-PEM} < 3$ cm. This variable compares the position of the shower obtained from the χ^2_{PEM} fit to the intersection of the centroids in the layers U and V. The difference in pseudorapidity $\Delta\eta$, and in azimuth $\Delta\phi$, determines $(\Delta R_{PES})^2 = (\Delta\eta)^2 + (\Delta\phi)^2$.

- $N_{SiHits} \geq 3$. The number of hits in the silicon for Phoenix electrons.

- $|z_{vertex}| < 60$ cm. Same as the central electron requirement.

- Not a conversion. If it has a COT track.

- Calorimeter isolation: $E_T^{iso}/E_T^{cluster} < 0.1$.

- Impact parameter: $|d_0, corr| < 0.02$ cm (with $N_{si\ hits} > 2$), or $|d_0, corr| < 0.2$ cm (with $N_{si\ hits} \leq 2$).

The plug electron identification efficiencies are determined from a $Z/\gamma \rightarrow e^+e^-$ data sample. A central electron and a plug electron are required with the invariant mass of the two-electron system in a 20 GeV window around the Z mass. The central electron passes all the standard identification cuts for central electrons (tight electron) and the plug electron is used to measure the efficiencies of the plug identification cuts. The scale factors ($\epsilon_{data}/\epsilon_{MC}$) for this analysis were obtained from PerfIDia [127].

5.3 Muon reconstruction and identification

Muons are minimum ionizing particles which penetrate large amounts of material with little energy loss. Their passage through the detector is commonly characterized by a track in the COT, little energy deposition in the calorimeter, and hits in the muon chambers. Muons are detected by the muon-system placed in the outermost layer of the CDF detector because of the highly penetrating nature of muons. Hits in the muon detectors are linked together to form track segments called stubs; these track segments are matched to extrapolated COT tracks, thus reconstructing a basic muon object. Isolated tracks with $p_T > 10$ GeV that are not fiducial to any of the muon systems are also considered as muon candidates (called stubless muons).

Muons at CDF are categorized by the detector region through which they pass. In this dissertation CMU, CMP, CMX and BMU sub-detectors are used. Those reconstructed in the CMU detector are called CMU muons, and so on. Muons reconstructed in both the CMU and CMP detectors are called CMUP muons. In particular, central tracks that are not expected to pass (not fiducial) through any of the muon detectors are called Central Minimum Ionizing Objects or CMIO muons. They are also called stubless muons, to indicate that no stub was reconstructed in the muon detector. To identify central muons some or all of the following requirements

are applied:

- $p_T > 5$ GeV. The transverse momentum of the COT beam-constraint (if available) track.

- $E_{em} \leq 2$ GeV$+Max(0, 0.0115(P-100$ GeV$))$, if $p_T > 20$ GeV; $E_{em} \leq 2$ GeV, if $p_T < 20$ GeV. It requires the energy deposited in the electromagnetic calorimeter to be very small. A small P-dependent correction is introduced for muons with $P > 100$ GeV.

- $E_{had} \leq 6$ GeV$+Max(0, 0.0280(P - 100$ GeV$))$, if $p_T > 20$ GeV; $E_{had} \leq 3.5$ GeV$+p_T/8$, if $p_T < 20$ GeV. Requires the energy deposited in the hadronic calorimeter to be smaller than that of strongly interacting jets.

- Fiduciality. This variable requires that the track of the muon candidate extrapolates to the proper muon chamber. For stubless muons it requires the track to pass through well instrumented regions of the CDF detector and through no muon sub-detector.

- $|\Delta X|_{CMU} \leq 7$ cm, $|\Delta X|_{CMP} \leq 5$ cm and $|\Delta X|_{CMX} \leq 6$ cm, if $p_T > 20$ GeV; $|\Delta X|_{CMU} \leq 7$ cm, $|\Delta X|_{CMP} \leq 5$ cm and $|\Delta X|_{CMX} \leq 6$ cm, or $\chi^2_i < 9$, if $p_T < 20$ GeV, where $i =$ CMU, CMP or CMX. The distance in the $r-\phi$ plane between the COT track extrapolated to the stub segment, and the position of the reconstructed stub for the muons in different sub-detectors.

- $\rho_{COT} > 140$ cm. The radius at which the track leaves the COT. This track is used for CMX only, as tracks may leave the COT from the side. In general, data and Monte Carlo simulation do not agree for $\rho_{COT} \leq 140$ cm due to the data bias introduced by the XFT trigger which requires the track to have hits in at least 4 COT superlayers. Data and Monte Carlo agree for $\rho_{COT} > 140$ cm.

- Track quality cuts. Same as those for central electron.
- $|z_0| < 60$ cm. The z-position of the track.
- Isolation: $E_T^{iso}/p_T < 0.1$ (fractional isolation), if $p_T > 20$ GeV. The quantity E^{iso} is the energy of calorimeter towers in the cone of $\Delta R = 0.4$ without including the tower associated with the track. If $p_T < 20$ GeV, then absolute isolation is used: $E_T^{iso} < 2.0$.
- Impact parameter: $|d_0, corr| < 0.02$ cm (with $N_{si\ hits} > 2$), or $|d_0, corr| < 0.2$ cm (with $N_{si\ hits} \leq 2$). The impact parameter is the distance on the transverse plane of closest approach of a track to the the beamline. This cut is particularly efficient at identifying leptons coming from displaced vertices, such as those resulting from the semi-leptonic decays of b quarks. By requiring the impact parameter to be small (not displaced), the leptons are most likely prompt leptons forming at the nominal interaction point. This cut also substantially reduces cosmic muons that entered the detector in the time window of the collision and in-flight decays.
- Not a cosmic muon. Muons coming from cosmic backgrounds are identified as dimuon events with an angular separation close to 180° in ϕ. Cosmic rays enter the detector at random times and at random locations. As cosmic muons traverse the detector they leave single tracks in the COT, which are reconstructed as two separate tracks, and deposit energy in the calorimeter as they exit. The time difference between the energy deposited on both ends of the hadronic calorimeter can be analyzed to identify cosmic muons. In addition, a cut on the impact parameter of the track efficiently identifies cosmic muons. Events in which a muon is tagged as cosmic are rejected.

As with electrons, the muon identification efficiencies are measured using a $Z/\gamma \rightarrow \mu^+\mu^-$ data sample. One muon is required to pass tight cuts and is associated with the

Level-1 trigger. The other muon is chosen to be fiducial (i.e. the track points to the proper sub-detector) and used to measure the efficiency of each of the identification cuts. The scale factors ($\epsilon_{data}/\epsilon_{MC}$) for this analysis were obtained from PerfIDia [127].

5.4 Jet reconstruction

In a typical $p\bar{p}$ collision free quarks and gluons which carry color are created. They undergo a process called fragmentation where they create partons via a cascade of gluon emissions and decays. The fragmentation continues until the momentum square of the partons is of the order of the infrared cut-off scale. Due to color confinement they cannot exist individually and they hadronize resulting in streams of colorless particles. These particles are collimated along the direction of the original parton and, after traversing the tracker, deposit their energy in a cluster of towers in the calorimeter. This stream of particles is called a jet. Jets are reconstructed from the energy deposited in the calorimeter towers with a *jet clustering* algorithm, which starts by identifying a seed tower as the one with the largest energy deposition. The group of towers within the cone with $\Delta R = \sqrt{(\Delta\eta)^2 + (\Delta\phi)^2} = 0.4$ in (η, ϕ) space and centered at the seed tower are identified as part of the jet cluster. The cone size $\Delta R = 0.4$ is chosen to include most of the jet energy without including a large contribution from other event activity. The choice of cone size also depends on the type of physics. A cone 0.4 is optimal for high p_T physics (large $\sqrt{\hat{s}}$) such as in top physics. After the cluster is defined, the shower center in the plane (η, ϕ) of the calorimeter is determined as follows:

$$\eta_{centroid} = \frac{\sum_i E_T^i \eta^i}{E_T^i} \tag{5.2}$$

$$\phi_{centroid} = \frac{\sum_i E_T^i \phi^i}{\sum_i E_T^i} \tag{5.3}$$

where the sum runs over the towers in the cluster and $\eta^i(\phi^i)$ represent the $\eta(\phi)$ coordinate of the center of the tower. After the position of the shower is calculated a new cone is defined centered in the new coordinates and the calculation is repeated for the new cluster. This process is then iterated until the cluster remains unchanged. The transverse energy of the jet is calculated with the following equation:

$$E_T^{raw} = \sqrt{(\sum_i E_i sin(\theta_i) cos(\theta_i))^2 + (\sum_i E_i sin(\theta_i) sin(\theta_i))^2} \tag{5.4}$$

where E_i is the total energy in tower i and θ_i is taken with respect to the highest sum-p_T primary vertex. This quantity represents the energy deposited in the cluster, and does not include corrections to account for detector effects or other physics processes, and is thus referred to as the "raw" jet energy. The corrected value of the jet E_T is derived from the raw value E_T^{raw} by applying a set of multiplicative and additive correction factors resulting in a corrected value that is close to the energy of the original parton. The corrections are given by the following relation:

$$E_T = (E_T^{raw} \times f_{rel} \times f_{time} \times f_{scale} \times E_T^{MI}) \times f_{abs} - E_T^{UE} + E_T^{OC} \tag{5.5}$$

The seven factors are briefly explained below, (more detailed information can be found in [105]).

- Relative correction, f_{rel}. This factor takes into account the relative tower-to-tower differences in calorimeter response.
- Time dependent correction, f_{time}. The calorimeter response exhibits a decline with time. This correction factor depends on the date the event was recorded and properly assigns a multiplicative factor to account for the decline in response.
- Energy scale correction, f_{scale}. This factor account for the non-linear response of the calorimeter.

- Multiple Interaction, E_T^{MI}. With current luminosities, a single interaction per bunch crossing is expected on average. The number of interactions follows Poisson statistics and in a particular event this number can be larger than one, which means that the physics process under study may have an overlapping minimum bias event. The energy of the minimum bias event may fall in the jet clustering cone, and must be subtracted. This is calculated on an event-by-event basis.

- Absolute energy correction, f_{abs}. This factor corrects the energy of the jet to that of the original parton that generated it. It includes nuclear absorption and particle leakage effects that can reduce the total energy measured in the jet cluster.

- Underlying event correction, E_T^{UE}. Extra energy can be deposited in the jet cluster that is not coming from the original parton. This energy can originate from spectator partons, beam-beam soft interactions or beam remnants.

- Out of cone corrections, E_T^{OC}. Part of the energy of the initial parton may fall outside the cone resulting in a underestimation of its energy. This quantity is obtained from MC simulation of the physics process under study.

Each level of correction has a systematic error associated with it, and the combination of them result in the total systematic uncertainty of the jet E_T measurement.

5.5 Tau reconstruction and identification

Tau reconstruction refers to the process of identification of a hadronically decaying tau through its decay products. The hadronic decay of a tau lepton proceeds as $\tau \rightarrow X_h \nu_\tau$, where X_h can be $\phi^\pm$ or $K^\pm$ or some short-lived intermediate resonance

that decays to final states including $\pi^{\pm}$, π^0, $K^{\pm}$ or K^0. The fraction of tau decays containing $K^{\pm}$'s is much smaller than that containing $\pi^{\pm}$ and therefore all the charged tracks are considered pions in the tau reconstruction process. The decay products of high energy taus travel in a direction collimated around the tau momentum. The reconstruction algorithm begins by finding a seed calorimeter tower with transverse energy greater than 6 GeV. Then, neighboring towers with energy larger than 1 GeV are added to the cluster. Because the cluster is expected to be narrow, no more than 6 towers are allowed in the cluster. The algorithm then defines the seed track as the highest momentum track pointing to the calorimeter cluster. All other tracks inside a signal cone of 10° around the seed track, and whose z_0 position is close to that of the seed track, are associated with the tau candidate. Other tracks outside the signal cone and inside a larger cone of 30° are treated as isolation tracks. The region between 10° and 30° is called the isolation annulus. The signal cone and isolation annulus are depicted in Figure 5.1 for a non isolated tau candidate. More detailed information about the tau reconstruction algorithm is found in [106].

Neutral pions decay to diphoton around 98.8% of the time. The neutral pions coming from highly energetic taus (e.g. taus from the decay of W's or Z's) typically have energies larger than 10 GeV. For these high energy pions the angular separation between the two photons is very small, and the clusters of energy deposited in the calorimeter are generally overlaped and identified as one. The identification of a π^0/γ is done by a cluster in the shower max detector, CES. The CES cluster is required to have certain energy distribution and to have no track pointing to its center to reduce contamination from real electrons. The four momentum of the π^0 can be reconstructed assuming the vertex to be at the z_0 of the seed track. A de tailed description of π^0 reconstruction is given in [107]. The four momentum of the hadronic system can be calculated from the momentum of the tracks and the π^0's. The following is the set of extra requirements imposed over the tau candidates as found above:

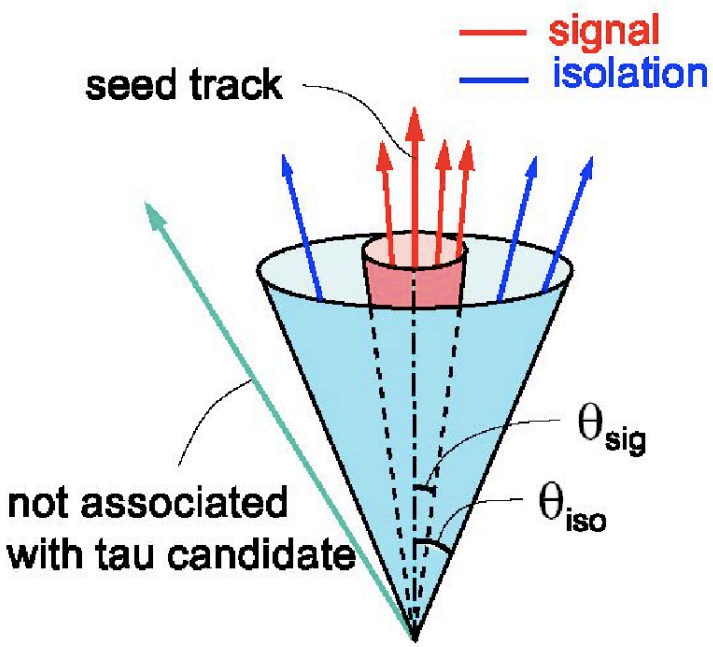

Figure 5.1: Tau identification cone, and isolation annulus. This particular set of track would not pass the tau cuts as there are tracks in the isolation annulus.

- Visible $E_T > 20$ GeV. E_T of the tau candidate calculated using tracks and π^0's associated with the tau candidate: $E_T = \pi^0 + \sum_{tracks=i} P_T^i$.
- E_T of the calorimeter cluster > 20 GeV.
- E_T of the seed tower > 10 GeV.
- Seed track $p_T > 10$ GeV.
- Cluster mass < 4 GeV. Cluster mass of the 4-vector defined by the energies and positions of the calorimeter towers comprising the tau cluster.
- $M_{tracks+\pi^0} < 1.8$ GeV/c^2. Invariant mass of the tracks and π^0's to be less than the tau mass.

- Calorimeter isolation:

$$\frac{E_T(0.4) - E_T(\tau)}{E_T(\tau)} < 0.1$$

  where $E_T(0.4)$ is the E_T of all the calorimeter towers within the cone of $\Delta R = 0.4$ centered at the tau candidate (τ).

- Seed track quality requirements:

  - N(axial COT segments with 5 or more hits) ≥ 3.
  - N(stereo COT segments with 5 or more hits) ≥ 3.
  - $\chi^2(COT)/N_{DOF} < 3$.
  - Seed track impact parameter $|d_0| < 1$ cm.
  - Absolute value of the seed track z coordinate $|z_0| < 60$ cm.
  - 9 cm $< z_{CES} <$ 230 cm. The z coordinate of the extrapolation of the seed track to the CES detector must be in the most sensitive CES region (fiduciality requirement).
  - $|x_{CES}| < 21.5$ cm. For 1-prong tau candidates only (same CES fiducial requirement as for electrons).

- Tracks in signal cone ($< 10^\circ$) = 1 or 3.

- Tracks in isolation annulus ($10^\circ - 30^\circ$) with $p_T > 1$ GeV = 0.

- $|\sum_{tracks=i} q^i| = 1$. The magnitude of the sum of the track charges must add up to one.

- Number of associated calorimeter towers ≤ 6.

- Electron veto: $\xi > 0.1$

$$\xi \equiv \frac{E_{tot}}{\sum |\vec{p}|}\left(1 - \frac{E_{em}}{E_{tot}}\right)$$

The variable ξ is defined in order to suppress electrons and muons depositing large amounts of energy in the electromagnetic calorimeter, where $\sum |\vec{p}|$ are the scalar momenta of tracks in the signal cone, while E_{tot} and E_{em} are the total and electromagnetic cluster energies respectively. The electron removal procedure is described in detail in [108].

5.6 Missing transverse energy

Although with an unknown magnitude, the momentum of the initial partons is known to be entirely along the beam direction. Momentum conservation thus requires that the energy of all the final states balances in the plane transverse to the beam line. Many interesting physical processes have neutrinos in their final state. Neutrinos escape the detector carrying significant amounts of energy, and the identification of the presence of a neutrino is possible by the detection of an imbalance in the transverse energy. The transverse energy, E_T, is a 2-D vectorial quantity defined as:

$$\vec{E}_T^{raw} = \sum_{cal.towers} E_i^{raw} sin(\theta_i i)\vec{n_i} \tag{5.6}$$

where the sum is over all the calorimeter towers, E_i^{raw} is the raw energy of each tower, θ_i is the polar angle to the center of the tower, and $\vec{n_i}$ is a transverse unit vector pointing to the center of the tower. On the transverse plane $\vec{E}_T^{raw}$ can be expressed in terms of its x and y components:

$$E_{T_x}^{raw} = \sum_{cal.towers} E_i^{raw} cos(\phi_i) \tag{5.7}$$

$$E_{T_y}^{raw} = \sum_{cal.towers} E_i^{raw} sin(\phi_i) \tag{5.8}$$

where the magnitude E_T^{raw} is given by:

$$E_T^{raw} = \sqrt{(E_{T_x}^{raw})^2 + (E_{T_y}^{raw})^2} \tag{5.9}$$

The value of $\vec{E}_T^{raw}$ defined above has to be corrected on an event-by-event basis. The first correction is related to the muons in the event. The amount of energy deposited by muons in the calorimeter is significantly less than the energy they carry. The estimation based on the calorimeter is then corrected to include the energy of the muon as measured by its track information. A second correction is related to the jets in the event. Since the jet cluster energy is corrected as explained above, in the calculation of the $\vec{E}_T^{raw}$ the raw energy of towers in the cluster has to be replaced by their corrected energies.

$$E_{T_x}^{corr} = E_{T_x}^{raw} + \sum_{i=0}^{N_{jets}} (E_x^{corr,i} - E_x^{raw,i}) \tag{5.10}$$

$$E_{T_y}^{corr} = E_{T_y}^{raw} + \sum_{i=0}^{N_{jets}} (E_y^{corr,i} - E_y^{raw,i}) \tag{5.11}$$

Finally, if there are electrons in the event, $\vec{E}_T^{raw}$ must also be corrected to account for corrections to the energies and momenta of the electrons. The corrected resulting transverse energy is refered to as $\vec{E}_T$. Since the energy is assumed to be balanced it is often more useful to talk in term of the "missing energy" defined simply as $\not\!\!\vec{E}_T = -\vec{E}_T$. If neutrinos are present in the final state, the $\not\!\!\vec{E}_T$ indicates the direction and magnitude of the vectorial sum of the neutrinos transverse energy in the event.

5.7 Lepton identification cuts

The signature for this analysis consists of three leptons and missing energy. As was mentioned in Chapter 2, there are only three leptonic flavors: e, μ, τ; however, muons and electrons can be classified further depending on which sub-detectors are involved in their reconstruction. As discussed earlier in this chapter, specific cuts are applied to variables associated with each sub-detector in order to increase the efficiency of reconstructing and finding leptons. Additional cuts may be required to further filter leptons with certain desired characteristics, such as those originating from the interaction point, as opposed to those coming from displaced vertices. The leptonic types described below satisfy the final selection criteria used in this dissertation. A summary of the cuts applied to each category is presented in tables.

Central electrons. Electrons reconstructed in the central region of the detector $|\eta| < 1.1$. Depending on the stringency of the identification cuts they can be divided into two categories: **tight** and **loose** electrons. Table 5.1 lists the cuts defining each category.

Plug electrons. Electrons reconstructed in the forward or plug region of the detector $|\eta| > 1.13$. Depending on the algorithm used to reconstruct their track they can be divided into two categories: **PEM** and **Phoenix** electrons. Table 5.2 lists the cuts defining each category.

Cut	CEMTIGHT	CEMLOOSE
Track p_T	> 4	
E_T	> 5	
Fiduciality	FidEleSmx()=1	
HAD/EM	$< 0.055 + 0.00045 \times E$	
Tracking	NStereoSegments(5) ≥ 2	
	NAxialSegments(5) ≥ 3	
Scaled CES χ^2_s	< 10	< 20
Lshr	< 0.2	—
ΔX	$-3.0 < \Delta X \times Q < 1.5$	—
ΔZ	$\lvert\Delta Z\rvert < 3.0$	—
E/P	< 2, for $p_T < 50$	—
Impact Parameter	$\lvert D0_{cor}\rvert < 0.02$, for nSvxHits$> 2$	
	$\lvert D0_{cor}\rvert < 0.2$, for nSvxHits$\leq 2$	
Vertex	$\lvert Z0\rvert < 60$	
Isolation	$\mathrm{ISO}_{frac} < 0.1$, for $E_T > 20$	
	ISO < 2, for $E_T < 20$	
Conversion Veto	$\Delta xy < 0.1$ AND $\Delta cot\theta < 0.02$	

Table 5.1: Central electron ID cuts for tight and loose selection.

Cut	PEM	PHOENIX
E_T	> 5	
PesEta	$1.13 \leq \lvert\eta_{PES}\rvert \leq 2.8$	
HAD/EM	< 0.055, for $E^{EM} < 100$ $< 0.055 + 0.0026 * log(E^{EM})$, for $E^{EM} \geq 100$	
χ^2_{PEM}	< 10	
Pes5x9 (both)	> 0.65	
Isolation	ISO< 4.0	
Track	default	Phoenix
Silicon Hits	—	≥ 3
Vertex	$\lvert Z0\rvert < 60$	
Impact Parameter	$\lvert D0_{cor}\rvert < 0.02$, for nSvxHits$> 2$ $\lvert D0_{cor}\rvert < 0.2$, for nSvxHits$\leq 2$	
Conversion Veto	$\Delta xy < 0.1$ AND $\Delta cot\theta < 0.02$	—

Table 5.2: Plug electron ID cuts. For the PEM category a default track is required, while for the Phoenix category a Phoenix track with at least three silicon hits is required.

Central muons. Muons reconstructed in the central region of the detector $|\eta| < 1.1$. Depending on which muon system they left stubs they are divided into the following categories: **CMU**, **CMUP** and **CMX**. The **CMIO** category is not fiducial to any muon chambers (stubless muons). Table 5.3 lists the cuts defining each category.

Cut	CMU	CMUP	CMX	CMIO
p_T	> 5			> 10
Fiduciality	CMU	CMU and CMP	CMX	non-finducial
Stub	CMU	CMU and CMP	CMX	—
Track-Stub $p_T > 20$	$\lvert\Delta X_{\rm CMU}\rvert < 7$	$\lvert\Delta X_{\rm CMP}\rvert < 5$	$\lvert\Delta X_{\rm CMX}\rvert < 6$	—
Track-Stub $p_T < 20$	$\chi^2_{\rm CMU} < 9$ or $\lvert\Delta X_{\rm CMU}\rvert < 7$	$\chi^2_{\rm CMU} < 9$ and $\chi^2_{\rm CMP} < 9$ or $\lvert\Delta X_{\rm CMP}\rvert < 5$	$\chi^2_{\rm CMX} < 9$ or $\lvert\Delta X_{\rm CMX}\rvert < 6$	—
EM	$< 2 + Max(0, 0.0115 \times (P - 100))$, for $p_T > 20$ < 2, for $p_T < 20$			
HAD	$< 6.0 + Max(0, 0.028 \times (P - 100))$, for $p_T > 20$ $< 3.5 + p_T/8$, for $p_T < 20$			
Tracking	NStereoSegments(5) ≥ 2 and NAxialSegments(5) ≥ 3			
Impact Parameter	$\lvert D0_{cor}\rvert < 0.02$, for nSvxHits$> 2$ $\lvert D0_{cor}\rvert < 0.2$, for nSvxHits$\leq 2$			
Vertex	$\lvert Z0\rvert < 60$			
Isolation	$\mathrm{ISO}_{frac} < 0.1$, for $E_T > 20$ $\mathrm{ISO} < 2$, for $E_T < 20$			

Table 5.3: Central muon ID cuts. For $p_T < 20$ muons are also accepted if $\chi^2 < 9$.

Forward muons. Muons reconstructed in the forward region of the detector with stubs in the Barrel Muon Detector (**BMU**). Table 5.4 lists the cuts defining this category.

Cut	BMU
Fiduciality	BMU
	BmuFidX()< 0
	BmuFidZ()< -13, for $\lvert\eta_{det}\rvert < 1.25$
	BmuFidZ()< -3, for $\lvert\eta_{det}\rvert \geq 1.25$
Stub	BMU Stub
Track-Stub	$\lvert\Delta X_{\rm BMU}\rvert < 9$
EM	$< 2 + Max(0, 0.0115 \times (P - 100))$, for $p_T > 20$
	< 2, for $p_T < 20$
HAD	$< 6.0 + Max(0, 0.028 \times (P - 100))$, for $p_T > 20$
	$< 3.5 + p_T/8$, for $p_T < 20$
Tracking	NStereoSegments(5) ≥ 2 and NAxialSegments(5) ≥ 1, for $\lvert\eta_{det}\rvert < 1.25$
	NStereoSegments(5) ≥ 1 and NAxialSegments(5) ≥ 1, for $\lvert\eta_{det}\rvert \geq 1.25$
Impact Parameter	$\lvert D0_{cor}\rvert < 0.02$, for nSvxHits$> 2$
	$\lvert D0_{cor}\rvert < 0.2$, for nSvxHits$\leq 2$
Vertex	$\lvert Z0\rvert < 60$
Isolation	$\mathrm{ISO}_{frac} < 0.1$, for $E_T > 20$
	ISO < 2, for $E_T < 20$

Table 5.4: BMU ID cuts.

Hadronic taus. As previously discussed, these are taus which decay hadronically into narrow jets of particles and which are reconstructed from its decay products. Only taus from the central region of the detector are considered ($|\eta| < 1.1$). Table 5.5 lists the cuts defining this category.

Cut	TAU
Visible E_T	> 20
Tower E_T	> 10
Seed Track p_T	> 10
$\lvert\eta_{det}\rvert$	< 1
Cluster mass	< 4
Visible mass	< 1.8
ISO_{frac}	< 0.1
Tracking	NStereoSegments(5) ≥ 3 NAxialSegments(5) ≥ 3
Seed Track $D0$	< 1
Vertex	$\lvert Z0\rvert < 60$
Seed Track $\lvert X_{CES}\rvert$	< 21.5, for 1-prong tracks only
Seed Track $\lvert Z_{CES}\rvert$	$9 < \lvert Z_{CES}\rvert < 230$
$\chi^2(COT)/N_{DOF}$	< 3
Charge	$=1$
Standard electron rejection	yes
Number of tracks in cone ($< 10^0$)	1 or 3
Number of tracks in annulus ($10^0 - 30^0$)	0 with $p_T > 1$
Number of associated cal. towers	≤ 6

Table 5.5: Hadronic tau ID cuts.

Isolated tracks. This category can be interpreted as a very loose lepton category. They are essentially good quality tracks that are isolated in p_T, that is, there are no other good quality tracks reconstructed near them. Table 5.6 lists the cuts defining this category.

Cut	Isolated Track
p_T	> 5
Tracking	NStereoSegments(5) ≥ 3 and NAxialSegments(5) ≥ 3
Vertex	$\|Z0\| < 60$
	$\|Z0$ (track) - $Z0$ (primary vertex)$\| < 5$
Isolation	ISO $(p_T) = 0$

Table 5.6: Isolated track ID cuts.

Chapter 6

Measurement of the fake rate of electrons, muons, taus and isolated tracks

Fake leptons are objects such as tracks and calorimetric energy depositions from light-flavor QCD activity that are mis-reconstructed by the detector and software as leptons that may pass the identification cuts of an analysis. However, when referring to the contribution of fakes to the backgrounds of various analyses, a much broader definition is applied. We may include along with the true fakes, non-prompt particles such as decay-in-flight muons and conversion electrons coming from light-flavored QCD. In the absence of a tuned MC simulation capable of reproducing the behavior of jets faking leptons in the different phase-space regions of interest, the probability that an object from QCD will fake a lepton is measured directly from the data. This probability or *fake rate*, is then applied to the analysis data in order to make a full estimation of the contribution of fakes.

6.1 Fake rate measurement

In an inclusive data sample of QCD events, we normally encounter the following sources of fake leptons:

- Fake leptons
  - Overlap of π^0 and a track $\rightarrow$ fake electrons
  - Interactive $\pi^{\pm} \rightarrow$ fake electrons
  - Punch-through hadron $\rightarrow$ fake muons
- Non-prompt leptons
  - Decay-in-flight muons from $\pi^{\pm}$ and $K^{\pm} \rightarrow$ muons
  - Photon coversions $\rightarrow$ electrons
  - (Semi-)Leptonic decay of heavy-flavor hadrons $\rightarrow$ leptons

The goal is to parametrize the probability per jet and per track that light-flavor QCD will result in leptons that will pass all the analysis identification cuts. In this context, the leptons from (semi-)leptonic decays of heavy-flavor hadrons and conversion electrons are considered contamination which needs to be reduced by standard procedures. The parameterization of this probability is what is generally referred to as a fake rate per jet for electrons and taus, and per track for muons and isolated tracks. Most of these fake rates are measured in data samples triggered by different jet energy thresholds, which are presumed to have very few real leptons. In the case of electrons and taus the measurement is performed for two different types of fakeable objects or denominators: CdfJets for both leptonic flavors and CdfEmObjects and CdfTaus for electrons and taus respectively. The fake rates for different energies are presented as the number of fake leptons per fakeable object for the various types of denominators used.

6.2 Datasets

The jet samples used in this study are the inclusive jet-triggered QCD data samples jet20, jet50, jet70 and jet100, corresponding to dataset ID's gjt1ah, gjt2ah, gjt3ah and gjt4ah respectively. The integrated luminosity of this sample is L= 387.7 pb^{-1}. Good run list version 27 (1,0,5,1) was used requiring electrons, muons and COT to be good. Additional datasets were used to measure the fake rates of BMU muons and isolated tracks. The jet triggered samples gjt1bd, gjt2bh, gjt3bi and gjt4bj were used for the fake rate of BMU, while the high-p_T single lepton triggered datasets bhelb and bhmub (periods d through j) were used for isolated tracks.

The jet-triggered data sets gjtxah and gjtxbj (x=1,..,4) are triggered by jets of different threshold energies: 20, 50, 70 and 100. The basic assumption made regarding these datasets is that the majority of the identified leptons found in their events are fake leptons. However, a small real lepton contamination is expected from conversions, heavy flavor and electroweak processes. These real leptons are removed from the datasets through the following actions:

- The missing energy in the events is required to be low to clean real leptons from W decays. $\not\!\!E_T < 15$
- Z-veto. Events with two or more leptons of the same flavor are not used. This cleans leptons from Z decays.
- An impact parameter cut is applied to clean leptons from semi-leptonic b-quark decays (heavy flavor).
- Standard conversion veto.

6.3 Fake Rate

The fake rate of a given lepton type is defined as the ratio between the number of fake leptons found in the jet sample to the number of objects that could potentially fake that lepton type, or fakeable objects.

$$\text{Fake rate (jet(or track)} \rightarrow \text{lepton)} = \frac{\text{Identified leptons}}{\text{Fakeable objects}} \tag{6.1}$$

When using jets (CdfJet) as denominator objects, a reconstructed lepton is counted in the numerator if it passes all the analysis ID cuts and it can be matched to a denominator jet passing some minimal quality cuts. The matching of electrons and taus to jets is done by requiring that the candidate lepton be within $\Delta R \leq 4$ of the fakeable object. On the other hand, when using CdfEmObject and CdfTau denominators, and also in the case of muon fake rates, all identified objects passing the analysis cuts are included in the numerator and no matching is required. In these cases, the denominator cuts are looser versions of the ID cuts, therefore, the numerator is always a subset of the denominator

We measure the fake rate of four different electron types: central tight, central loose, PEM (with default track) and Phoenix electrons. For muons we consider CMU, CMUP, CMX, CMIO and BMU. Finally, we measure the fake rate of isolated tracks, which can be thought of as avery loose leptons. The definitions of these objects are described in detail in Chapter 5. The fake rate is measured for each lepton type separately, where the numerator of Equation 6.1 passes all the identification cuts that define each category. Given that some object types are contained in others that are more loosely defined, i.e., all tight electrons are also loose, or they simply overlap as in the case of PEM and Phoenix, the following modified lepton types are used:

- Loose electrons that are not tight

- Phoenix electrons that are not PEM
- CMU muons that are not CMUP

The reason for this requirement of orthogonality is that leptons are uniquely identified with one and only one of these categories with the highest quality types having preference, i.e., electrons are tight if the pass all the tight cuts, and loose if they fail any of them (while passing all loose cuts).

6.3.1 Denominator objects and cuts

The denominators in Equation 6.1 can be collectively thought of as very loose lepton types. In the case of electron fake rates, two types of denominators are used: jet (CdfJet) and electron (CdfEm) objects. The CdfJet's correspod to a collection of loosely reconstructed jet objects consisting of energy depositions in the calorimeter with jet-like characteristics. Since fake electrons are actually real jets that are mis-reconstructed as electrons, it makes sense to use these jets in the denominator as *fakeable* objects, or objects that can fake electrons. On the other hand, CdfEmObject's are very loosely reconstructed electrons. This collection most likely includes real jets originating from QCD activity that, due to their electron-like characteristics, have a high probability of being reconstructed as identified electrons. In the same spirit, CdfTau objects are used as denominators for identified hadronic taus. Finally, the denominators for muons are tracks that are fiducial to specific areas of the muon system. Punch-through hadrons and in-flight decays of $\pi^{\pm}$ and $K^{\pm}$leave tracks in the tracking system and stubs in the muon chambers which are sometimes reconstructed as identified muons; therefore, isolated tracks are the best choice of fakeable object for muons.

Denominator object definitions: electrons and taus

Central and plug denominator jets (CdfJet) are required to have $E_T > 4$ GeV and are defined according to pseudorapidy:

- Central fakeable jet: $|\eta_{Det}| \leq 1.1$
- Plug fakeable jet: $1.2 \leq |\eta_{Det}| \leq 2.8$. Plug calorimeter coverage only for $|\eta_{Det}| \geq 1.2$.

CdfEmObject denominators are required to pass the following cuts depending on their location in the detector:

- Central CdfEmObject
  - Central Region: $|\eta_{Det}| \leq 1.1$
  - $E_T > 5$ GeV
  - FidEleSmx()=1
  - $E_{had}/E_{em} < 0.125 + 0.00045 \times E$
  - $Iso < 4.0$ for $P_T < 20$ GeV, or $Iso/E_T < 0.2$ for $P_T > 20$ GeV
  - Has default track
  - Not a conversion
- Plug CdfEmObject
  - Plug Region: $1.2 \leq |\eta_{Det}| \leq 2.8$ (PesEta)
  - $E_T > 5$ GeV
  - $E_{had}/E_{em} < 0.125 + 0.00045 \times E$

  - $Iso < 4.0$
  - Has default track (PHX track for PHOENIX category, with SVX hits ≥ 3 and $|Z0| < 60$)
  - Not a conversion (PEM category only)

CdfTau denominators are only required to be central in pseudorapidity.

- Central CdfTau: $|\eta_{Det}| \leq 1.0$

The use of CdfEmObject and CdfTau denominators is motivated by the fact that the CDF offline reconstruction software uses different algorithms to reconstruct leptons and jets. Therefore, the same object reconstructed as a jet and as an electron or tau will have different parameters (energy, electromagnetic fraction of the energy cluster, etc.) and any measurement of the fake rate "per jet" is complicated by this ambiguity. These differences pose an even bigger challenge while attempting to predict the kinematic distributions of fake leptons starting from jet denominators. This complication is avoided by defining the fake rate as the probability for a reconstructed electron or tau candidate (CdfEmObject or CdfTau) passing minimal denominator cuts to pass the full identification cuts of leptons.

Sample bias

The loose denominator cuts applied to CdfEmObjects are introduced to reduce observed differences in the kinematics of denominator objects among different jet samples [113], [114]. Due to differences between the offline and the trigger clustering algorithms, CdfEmObjects from higher jet-E_T trigger thresholds tend to have larger hadronic fractions. Therefore, the requirement that $E_{had}/E_{em} < 0.125$ improves the consistency in the electron fake rate denominator composition between different jet

samples (Figure 6.1). The same is true of the calorimeter isolation fraction with the jet100 sample having denominator objects (CdfEmObjects and tracks) with larger values of Iso/E_T for the same E_T than the jet20 sample (Figure 6.2). This is a large source of sample bias because identified leptons are required to be isolated and denominators in samples with higher trigger energies will be on average less likely to fake them. This sample bias is largely reduced by requiring denominators to be isolated.

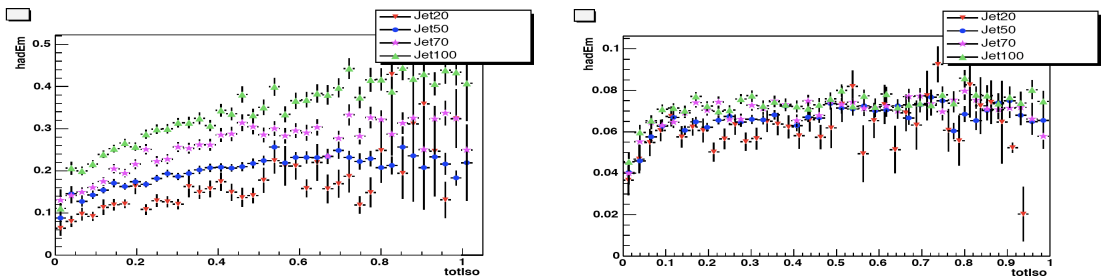

Figure 6.1: E_{had}/E_{em} as a function of the calorimeter fractional isolation (cone 0.4) for all CdfEmObjects (left) from jet20, jet50, jet70 and jet100, and for CdfEmObjects with $E_{had}/E_{em} < 0.125$ (right).

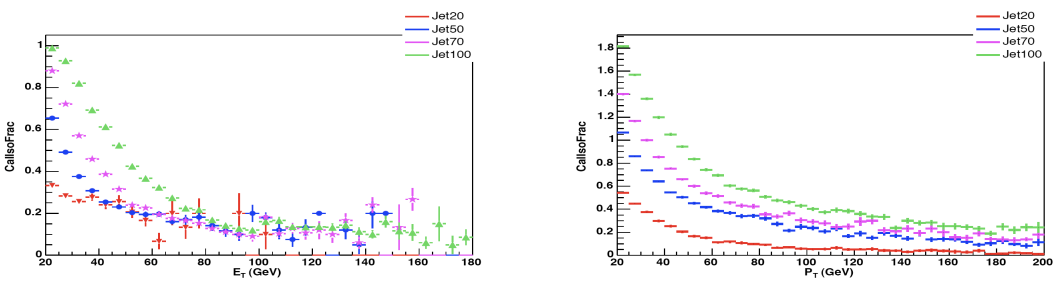

Figure 6.2: Calorimeter fractional isolation (cone 0.4) as a function of E_T for CdfEmObjects (left), and as a function of p_T for tracks (right).

Trigger bias

To avoid the trigger bias introduced by the trigger energy threshold of each jet sam-

ple, it is important to identify which fakeable objects and leptons are biased by the trigger. In order to accomplish this, it is first necessary to identify which jets in the event pass each of the L1, L2 and L3 trigger requirements listed in Table 6.1. These jets are most likely the jets that actually triggered the event and are denominated *trigger jets* accordingly. If there is a single trigger jet in the event, that jet is considered biased by the trigger while all other jets are considered to be unbiased. However, If an event has two or more trigger jets, then all the jets in the event are considered unbiased, including the trigger jets. On the other hand, if there are no trigger jets in the event, it could be said that all jets participated in the triggering and that they should all be considered biased; however, in this case it is more appropriate to consider only the highest energy jet in the event as biased.

Now that the trigger jets have been identified, it is possible to determine which numerator and denominator objects are biassed by the trigger. This is done by looking at the distance in phase space ΔR between each of the numerator and denominator objects and each of the trigger jets. If this distance is $\Delta R < 0.7$ the objects are considered to be biased by the trigger, as they most likely correspond to the same object reconstructed as a jet and as a lepton.

Trigger Jet Requirements					
Jet sample		Jet 20	Jet 50	Jet 70	Jet 100
L1	One calorimeter tower with	> 5 GeV	> 5 GeV	> 10 GeV	> 10 GeV
L2	One calorimeter cluster with	> 15 GeV	> 40 GeV	> 60 GeV	> 90 GeV
		$\|\eta\| < 3.6$	$\|\eta\| < 3.6$	$\|\eta\| < 3.6$	$\|\eta\| < 3.6$
L3	One cone 0.7 jet with	$E_T > 20$ GeV	$E_T > 50$ GeV	$E_T > 70$ GeV	$E_T > 100$ GeV

Table 6.1: Description of JET 20 (50/70/100) trigger. Online jets which satisfy all the three level requirements are called trigger jets.

Denominator object definitions: muons and isolated tracks

Denominator tracks are default tracks that pass all the track quality cuts of Table 5.3 for central muon types and of Table 5.4 for BMU. It is required that the denominator tracks of a given muon type be fiducial to the muon chambers corresponding to that muon type. This defines five types of fakeable tracks:

- CMU fakeable tracks: fiducial to CMU chambers.
- CMUP fakeable tracks: fiducial to CMU and CMP chambers.
- CMX fakeable tracks: fiducial to CMX chambers.
- BMU fakeable tracks: fiducial to BMU barrel chambers.
- CMIO fakeable tracks: not fiducial to CMU, CMP, CMX, and BMU chambers.

Fakeable tracks are also required to be isolated in the central or plug calorimeter in order to reduce an observed dependence of the fake rates on the particular jet sample used[109]. The track isolation is constructed by extrapolating the track to the central or plug calorimeter and calculating the energy in a cone of 0.4 around the track and subtracting the energy in the towers hit by the track. Then, a track is considered isolated if $E_T^{cone0.4} \leq 4$ or $E_T^{cone0.4}/p_T \leq 0.1$, where $E_T^{cone0.4}$ is the track isolation. An additional cut of $E/P \leq 1$ is applied to reduce electron contamination in the denominator tracks, where E is the energy in the towers hit by the track and P is the track momentum. The denominators of isolated tracks are required to pass all the track quality cuts of Table 5.6 except for the p_T-isolation requirement.

6.4 Electron Fake Rates

6.4.1 Jet denominators for electrons

The fake rates of central electrons as a function of jet energy are shown in Figure 6.3. The rates measured with different jet samples are shown in different colors. The measurements corresponding to samples jet20, jet50, jet70 and jet100 are treated as results of independent experiments and averaged using the formula below, which were used for all leptonic types. The average rates are shown in Figure 6.4.

$$\bar{x} = \frac{\sum x_i/\sigma_i^2}{\sum 1/\sigma_i^2} \tag{6.2}$$

$$\sigma_x^{-2} = \sum 1/\sigma_i^2 \tag{6.3}$$

The first two low-E_T bins are biased by the cut on the transverse energy at 5 GeV for tight and loose electrons. This occurs because of a smearing of the jet E_T when jets are reconstructed as fake electrons. That is, a jet with $E_T > 5$ GeV may reconstruct as an electron with $E_T < 5$ GeV and be excluded from the numerator of Equation 6.1, thus artificially decreasing the fake rate at energies close to this cutoff. Therefore, for the purpose of measuring the fake rate these biased bins are ignored and the fits are simply extrapolated down to 5 GeV.

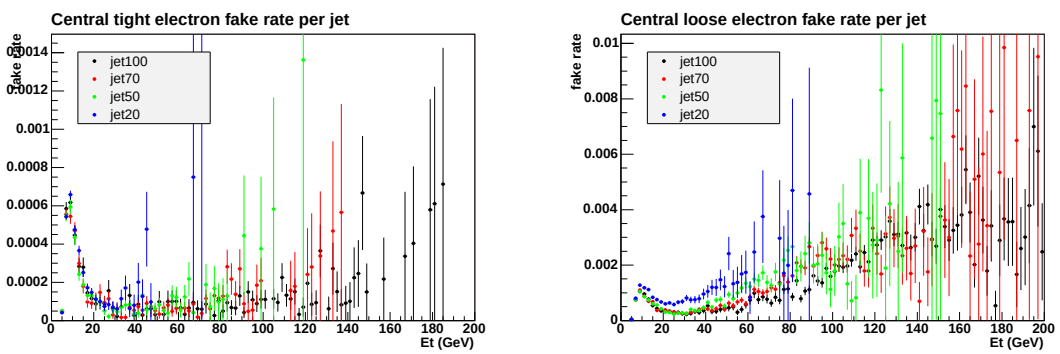

Figure 6.3: Tight (right) and loose (left) electron fake rates versus jet E_T for the jet20, jet50, jet70 and jet100 samples.

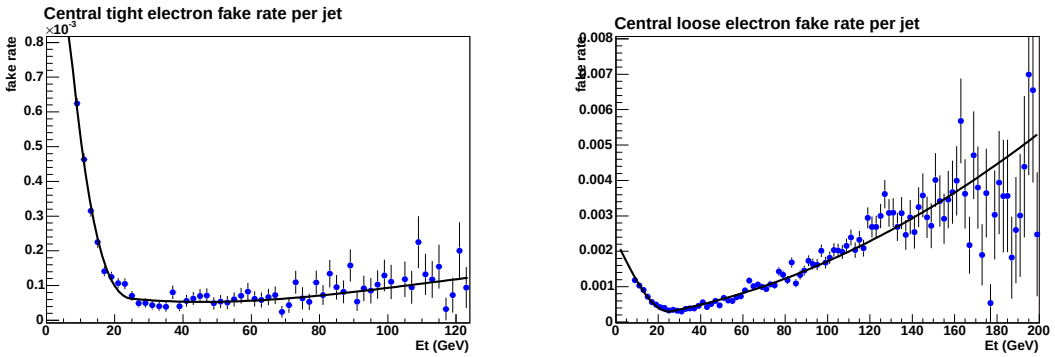

Figure 6.4: Tight (right) and loose (left) electron fake rates versus jet E_T for the average over the four jet samples. A fit to the combined fake rates is also shown.

The fake rates of plug electrons as a function of jet energy are shown in Figure 6.5. The rates measured with different jet samples are shown in different colors. It was shown in a previous measurement [109] that the fake rates of plug electrons are fairly independent of pseudorapidity for $|\eta| \geq 1.3$, but that they do show an enhancement for $1.2 \leq |\eta| \leq 1.3$. For this reason, the fake rates for these two regions are measured separately. The averaged rates are shown in Figure 6.6.

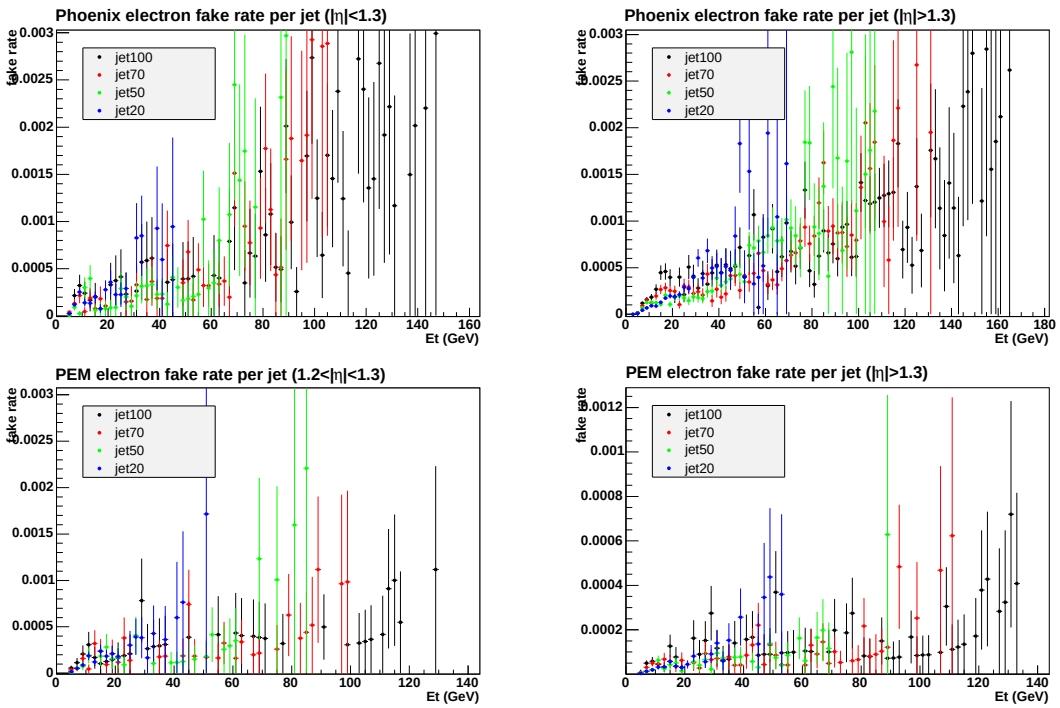

Figure 6.5: Phoenix (top) and pem (bottom) fake rates for the jet20, jet50, jet70 and jet100 samples. The fake rates were measured separately for $|\eta| < 1.3$ (left) and for $|\eta| > 1.3$ (right).

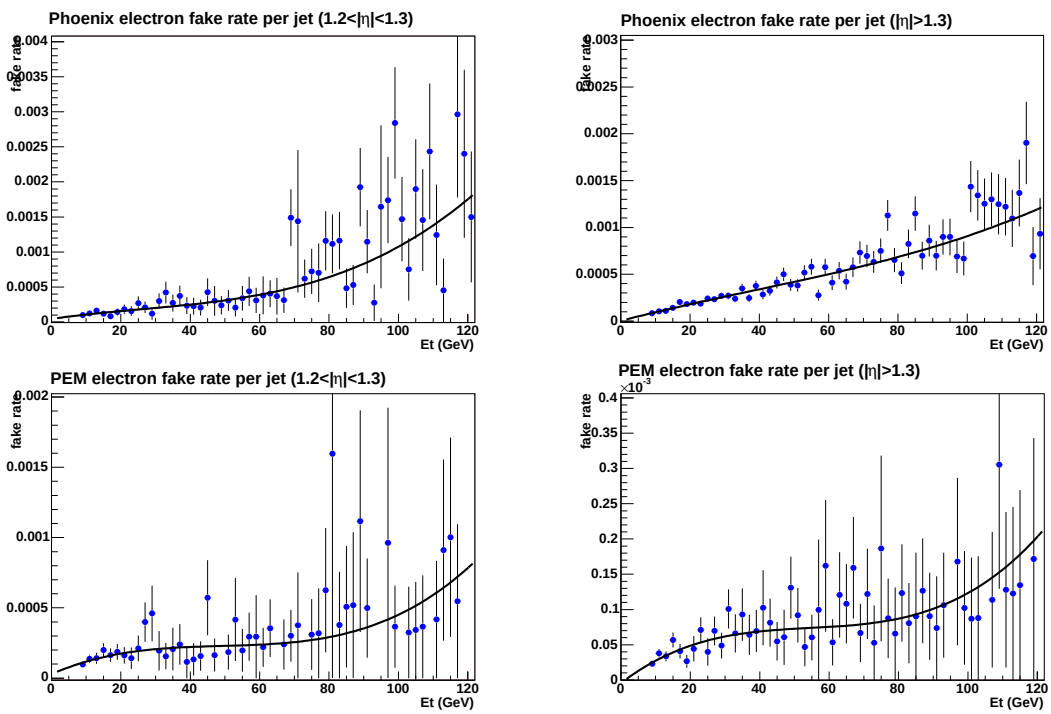

Figure 6.6: Phoenix (top) and pem (bottom) fake rates versus versus jet E_T for the average over the four jet samples. The fake rates are shown separately for $|\eta| < 1.3$ (left) and for $|\eta| > 1.3$ (right). A fit to the combined fake rates is also shown.

6.4.2 CdfEmObject denominators

The fake rates of central electrons as a function of raw electron energy are shown in Figure 6.7. The rates measured with different jet samples are shown in different colors. These measurements are averaged in the manner described in the previous section and are shown in Figure 6.8.

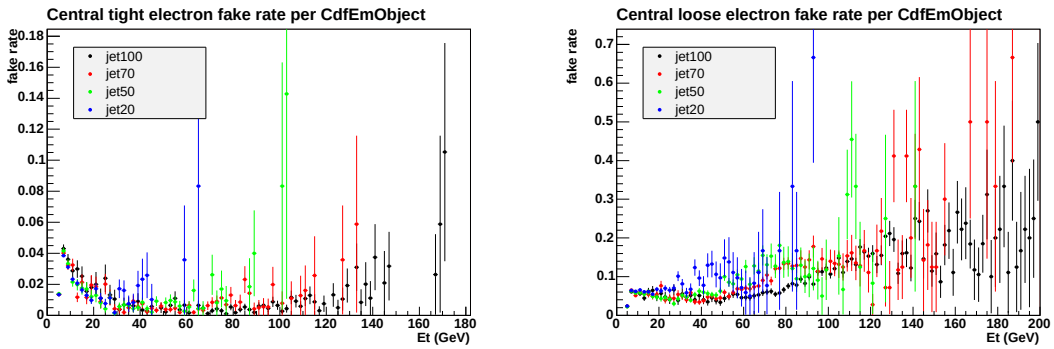

Figure 6.7: Tight (right) and loose (left) electron fake rates versus raw electron E_T for the jet20, jet50, jet70 and jet100 samples.

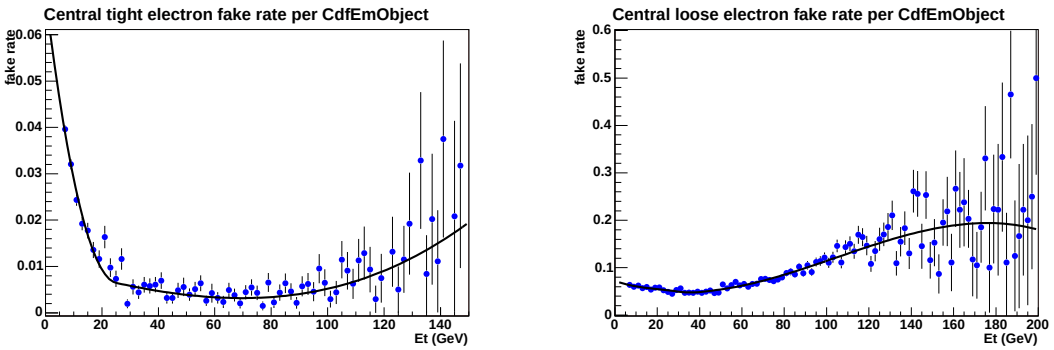

Figure 6.8: Tight (right) and loose (left) electron fake rates versus raw electron E_T for the average over the four jet samples. A fit to the combined fake rates is also shown.

As was the case in the previous section with jet denominators, the first bins in the fake rate of central electrons with electromagnetic clusters denominators are biased

by the cut on the transverse energy at 5 GeV, and on the transverse momentum of their track at 4 GeV. Several corrections are applied to the energy of fully identified electrons, and these corrections behave as an effective smear on the energy of the fakeable objects. Here again the first bins are simply when fitting the histograms.

The fake rates of plug electrons as a function of raw electron energy are shown in Figure 6.9. The rates measured with different jet samples are shown in different colors. As in the previous section, the fake rates are measured for two separate regions of pseudorapidity, mainly, for $1.2 \leq |\eta| \leq 1.3$ and $|\eta| \geq 1.3$. The averaged rates are shown in Figure 6.10.

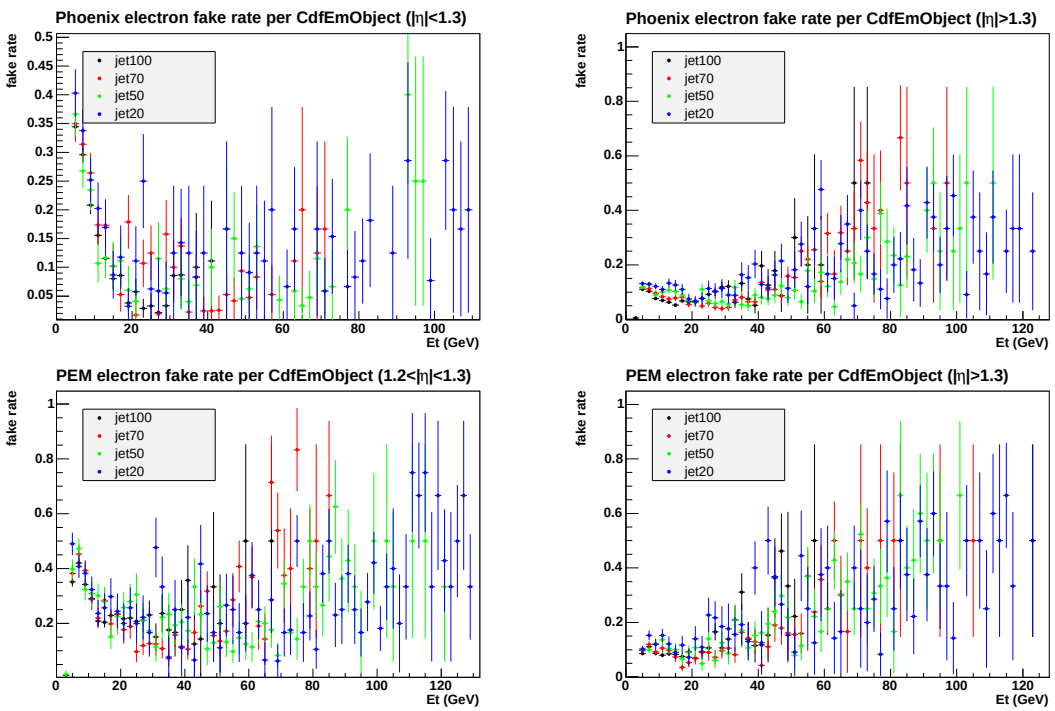

Figure 6.9: Phoenix (top) and pem (bottom) fake rates versus raw electron E_T for the jet20, jet50, jet70 and jet100 samples. The fake rates were measured separately for $|\eta| < 1.3$ (left) and for $|\eta| > 1.3$ (right).

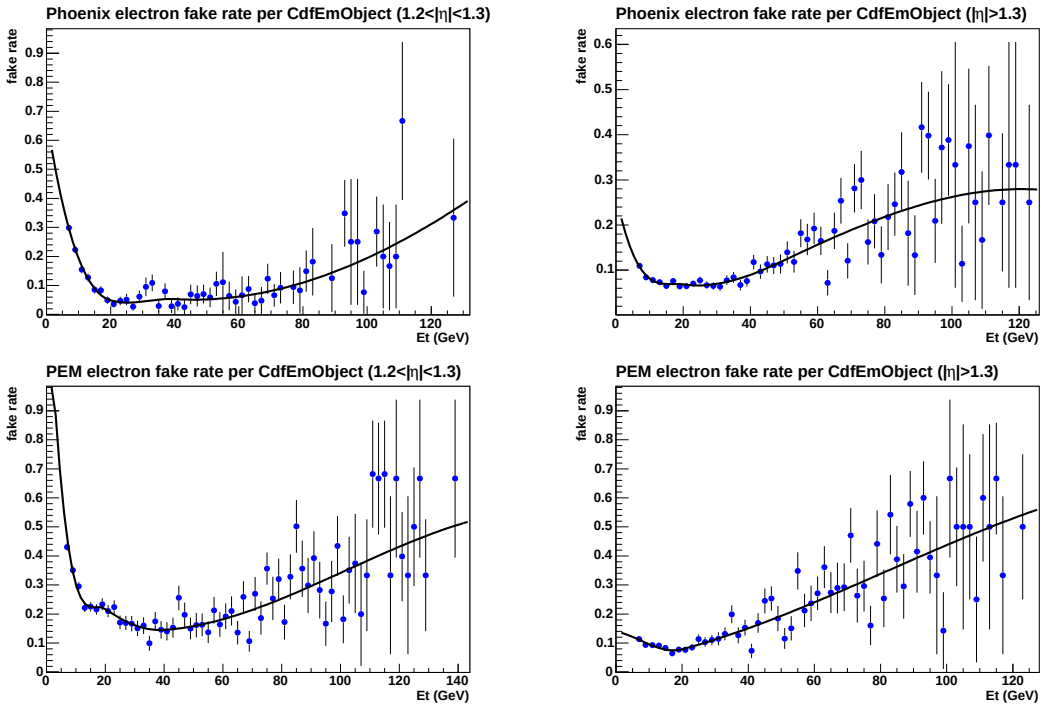

Figure 6.10: Phoenix (top) and pem (bottom) fake rates versus raw electron E_T for the average over the four jet samples. The fake rates are shown separately for $|\eta| < 1.3$ (left) and for $|\eta| > 1.3$ (right). A fit to the combined fake rates is also shown.

6.5 Muon Fake Rates

The fake rates of muons as a function of track p_T are shown in Figure 6.11. The rates corresponding to different jet samples are plotted using different colors. The average rates over the samples are calculated in the same way as for electrons and are shown in Figure 6.12.

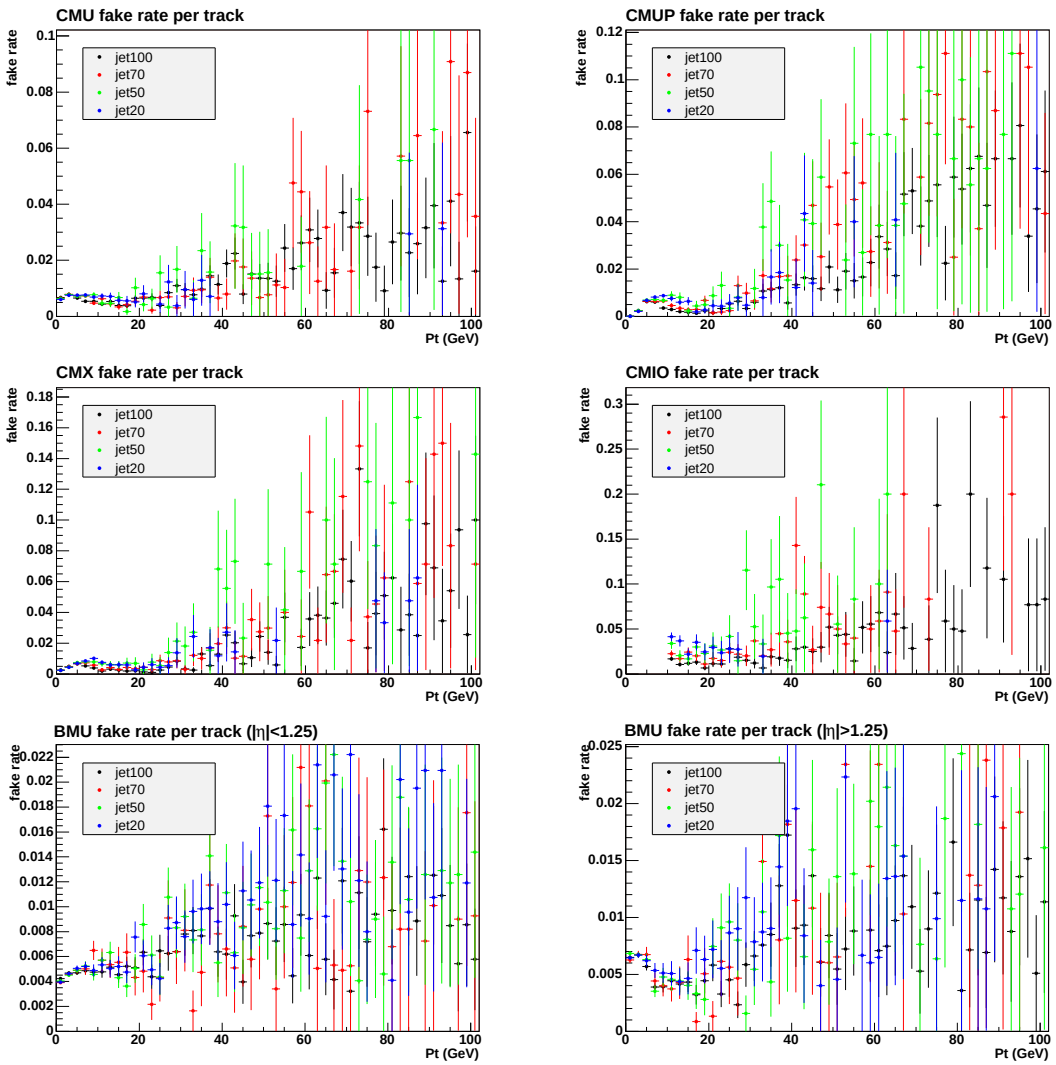

Figure 6.11: Muon fake rates for the jet20, jet50, jet70 and jet100 samples.

The isolation cut on the denominator tracks was introduced to eliminate a sample bias which manifested itself strongly in the jet20 sample, yielding much higher fake rates than other samples. A possible explanation for this effect is that tracks in jet20 have less energy around them than, for example, in jet100. Therefore, tracks in the jet20 sample are often more isolated and therefore more likely to fake isolated muon.

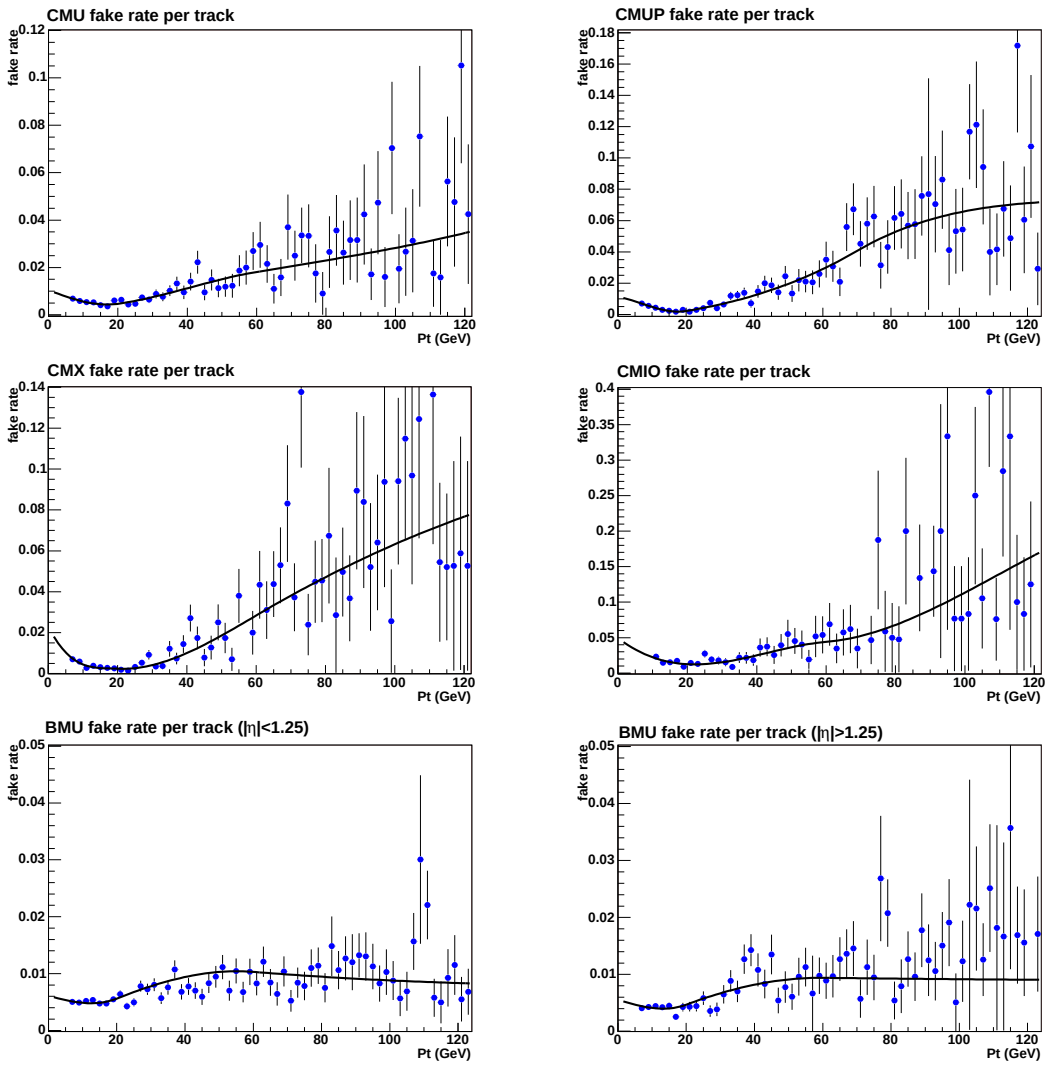

Figure 6.12: Muon fake rates and their fits. The central muon fake rates are the average over the four jet samples. The bottom-left plot shows the rates for BMU using only jet20 which is presumed to be the least biased by the trigger energy threshold.

6.6 Isolated track fake rate

The fake rates of isolated tracks as a function of track p_T are shown in Figure 6.13. Events were selected in high-p_T single lepton triggered datasets (bhelb, bhmub) with an identified Z boson resonance, which constituted the sample for the measurement of the fake rate. Only tracks that cannot be matched to identified leptons in the event are used as numerator and denominator objects.

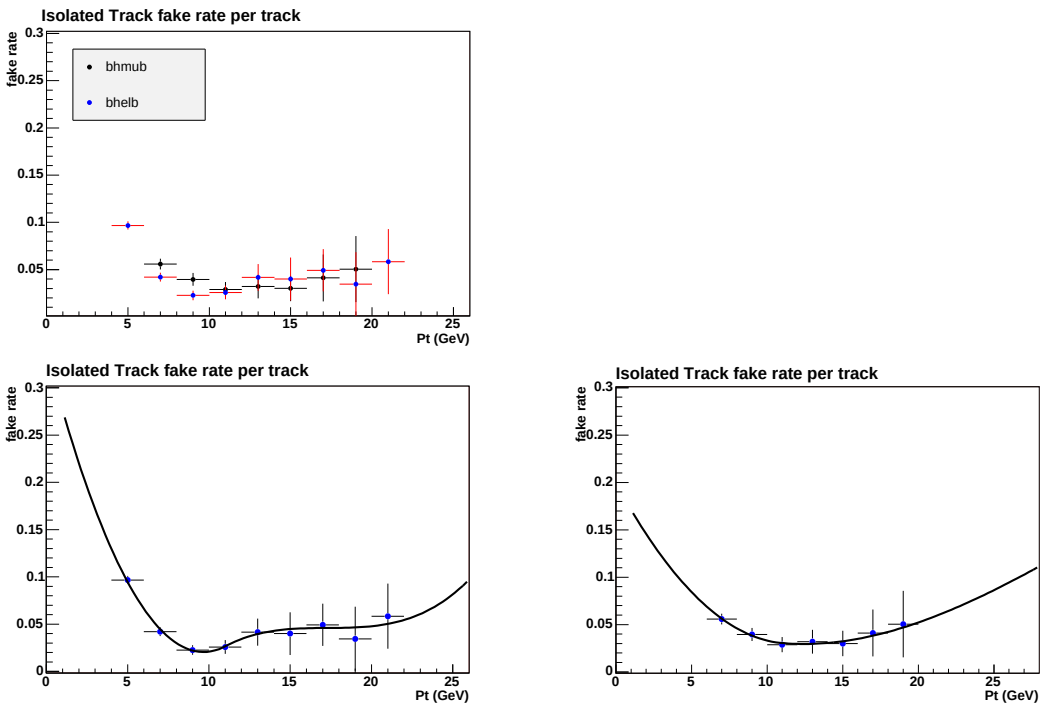

Figure 6.13: Isolated track fake rates measured in high-p_T single lepton triggered datasets bhelb and bhmub. The bottom left plot shows the fake rate measured in dielectron data and its polynomial fit curve. The bottom right plot corresponds to dimuon data.

6.7 Tau Fake Rate and sample bias

The tau fake rate is particularly susceptible to sample bias. Most QCD events in the inclusive jet data have a back-to-back topology with two jets recoiling against each other. However, those events with a jet below the trigger energy threshold must have a third jet present if we assume conservation of transverse momentum. There is a high probability that this third jet comes from the gluon splitting produced by one of the original jets. This splitting leads to two lower energy jets too close in phase space to pass the numerator cuts as fakes, as these cuts are mainly based on isolation requirements. A lower jet to tau fake rate is thus expected for these biased jets as can be observed in Figure 6.15. This results, for example, in a lower fake rate at an energy of 30 GeV measured in a jet50 sample, than the rate at the same energy in a jet20 sample. This can be interpreted as the 30 GeV bin being enriched in denominator jets coming from gluon splitting which are less likely to fake isolated leptons.

In order to reduce this sample bias only those fake rates measured above the trigger energy threshold of a given jet sample are used. The efficiency for a jet with E_T above 25 GeV that passes the identification cuts for a tau denominator to be selected by the Jet20 trigger is of the order of 100%. Likewise, all tau denominator jets with E_T greater than 55, 75 and 105 GeV will be selected by the triggers Jet50, Jet70 and jet100 respectively. If 100% of the denominator jets are selected by these triggers it means that all these jets are unbiased by this trigger selection.

6.7.1 CdfJet denominators for taus

The tau fake rate as a function of jet E_T is shown in Figure 6.14 for different jet samples. The average fake rate is shown in Figure 6.14 as well.

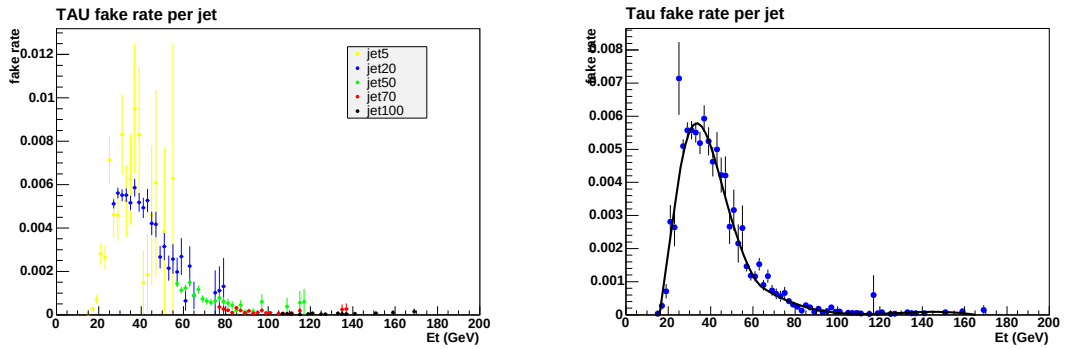

Figure 6.14: Tau fake rates for the jet20, jet50, jet70 and jet100 samples (left), and for their average (right).

6.7.2 CdfTau denominators

The tau fake rate as a function of E_T is shown in Figure 6.15 for different jet samples. The average fake rate is shown in Figure 6.15 as well.

6.8 Systematic Uncertainty

An estimation of the systematic error in the measurement of fake rates from jet data is obtained by observing how the different jet samples distribute relative to one another. Although jets biased by the trigger are excluded from calculations of fake rates, it can be seen in Figure 6.16 that there is still a residual sample bias associated to the sample's trigger energy threshold, with the highest p_T triggered datasets yielding the lowest fake rates particularly below their corresponding trigger energies. As an estimation of this systematic error, "envelop" functions are drawn around the four different fake rate distributions plotted on the same graph. Then, the systematic error at a given E_T (p_T) can be estimated as the ratio between the maximum deviation from the combined fit and the value of the fit at that E_T (p_T).

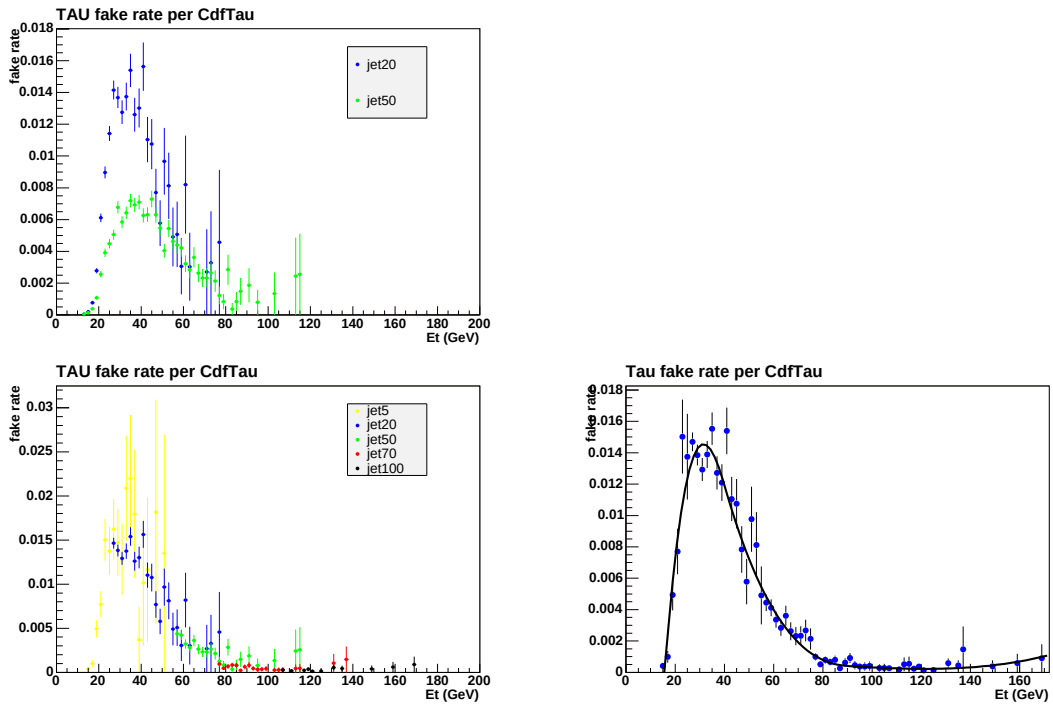

Figure 6.15: Tau fake rates for the jet20, jet50, jet70 and jet100 samples (bottom left), and for their average (top right). The top left plot shows the effect of sample bias in jet50 (blue) where rates below the trigger threshold of 50 GeV are biased by the trigger.

Following this procedure it is observed that for a jet E_T (track p_T) above 20 GeV, the systematic error is approximately 50%, which is the value reported by previous measurements [109]. However, for lower energies the systematic error is of the other of 10 to 20% (Figure 6.16).

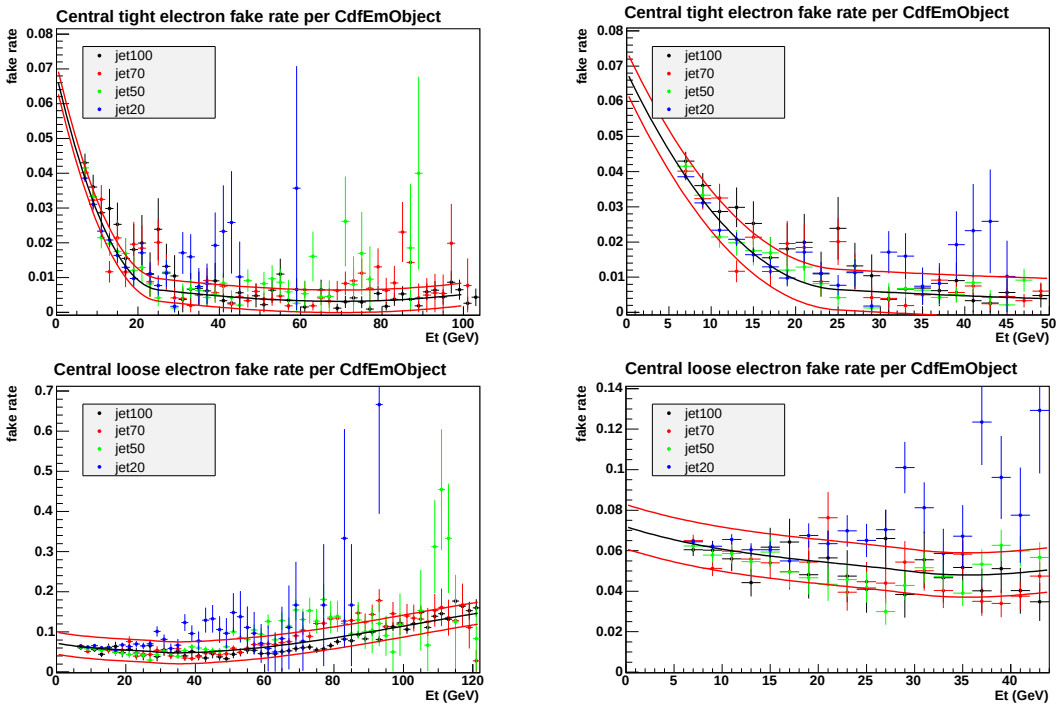

Figure 6.16: Spread of the measurements of different jet samples for tight electrons (top) and loose electrons (bottom). The systematic error is taken to be 50% for high $p_T > 20$ GeV (top left and bottom left) and between 10% to 20% for lower energies (top right and bottom right).

6.9 Consistency check for fake rates

As a way of validating the fake rate infrastructure a self-consistency check was performed. The combined fake rates of Equation (6.2) for each lepton type were applied to the various denominator objects in the jet samples in order to estimate the number of fakes leptons; this estimation was then compared to the observed number of identified leptons. The results of this comparison are shown in Tables 6.2 and 6.3. The errors to the estimated numbers correspond to the systematic uncertainty discussed in section 6.8. A systematic uncertainty of 20% was used for denominators with $p_T < 20$ GeV, and 50% otherwise. The results show good agreement within the expected systematic error.

	gjt1ah		gjt2ah		gjt3ah		gjt4ah	
Central tight	2394	2335 ± 481	732	661 ± 157	676	595 ± 153	638	552 ± 162
Central loose	5237	4927 ± 1096	2329	2164 ± 730	2900	2715 ± 1067	3580	3822 ± 1683
PEM	2371	2413 ± 571	907	903 ± 299	876	804 ± 281	774	653 ± 231
Phoenix	3072	3238±729	1223	1137 ± 342	1051	975 ± 299	942	737 ± 225
Tau	3944	3985 ± 797	590	659 ± 132	135	154 ± 31	27	76 ± 15
CMU	2750	2669 ± 548	1020	1007 ± 210	1243	1204 ± 262	1611	1589 ± 379
CMUP	2068	2179 ± 451	827	818 ± 173	957	969 ± 215	1229	1274 ± 317
CMX	1477	1581 ± 328	593	582 ± 122	668	688 ± 149	829	904 ± 213
CMIO	156	94 ± 47	96	50 ± 25	156	104 ± 52	272	239 ± 119

Table 6.2: Consistency check for jet samples gjt1ah, gjt2ah, gjt3ah, gjt4ah.

	gjt1bj		gjt2bj		gjt3bj		gjt4bj	
BMU	2883	3073 ± 841	952	950 ± 255	1659	1607 ± 426	1855	1694 ± 453

Table 6.3: Consistency check for jet samples gjt1bj, gjt2bj, gjt3bj and gjt4bj.

Chapter 7

Search for chargino-neutralino production in the trilepton signature

This chapter describes a search for chargino-neutralino associated production ($\chi_1^{\pm}\chi_2^0$) at 5.8 fb^{-1}. We look for chargino-neutralino pair production $p\bar{p} \rightarrow \chi_1^{\pm}\chi_2^0$, followed by $\chi_2^0 \rightarrow ll\chi_1^0$ and $\chi_1^{\pm} \rightarrow l\nu\chi_1^0$ ($l = e, \mu$) [118]. The neutralino is taken to be the Lightest Supersymetric particle and R-parity conservation is assumed. Therefore, the signal signature is three isolated leptons and large missing transverse energy. The specific trilepton channels investigated are $\mu\mu + \ell$ and $ee + \ell$, where ℓ can be an electron, muon, hadronic tau or isolated track. With the exception of the hadronic taus, all other objects can have transverse momenta as low as 5 GeV/c. The theoretical motivation is described in Chapter 2, Section 2.2.7. In the following sections, the analysis procedure, techniques, and result are discussed.

7.1 Analysis Strategy

This analysis is a counting experiment where the number of events observed and expected are compared in 64 dilepton/trilepton control regions in the $\not\!\!E_T$ vs dilepton mass $M_{\ell\ell}$ space, with the additional requirement of high or low jet multiplicity. Figure 7.1 graphically presents the dilepton and trilepton control regions. It is also a blind analysis, in the sense that the data remains hidden in the signal region ($M_{\ell\ell} > 20$ GeV/c^2, $\not\!\!E_T > 15$ GeV, $N_j \leq 1$ and exclusion of the Z mass) until all other SM-dominated phase-space regions where we expect to have good agreement between data and expectation are well understood. The low-mass and/or low-$\not\!\!E_T$ control regions are sensitive to the QCD background. The Z-mass control regions are used to understand the contribution of the Drell-Yan (DY) dilepton background and the QCD-originated fake trilepton background. The practice of remaining blind in the signal region has the purpose of avoiding unintentional tuning of the analysis in order to maximize the discrepancy between the observed data and the expectation in this region, where a disagreement is actually desired. By remaining blind, the results are thus statistically unbiased, and the signal region is only unblinded when all control regions are well understood. This analysis pushes the low transverse momenta limit by setting the lower p_T cut for muons, electrons and isolated tracks at 5 GeV, and at 20 GeV for taus.

7.2 The Datasets

The analysis is performed in CDF offline releases 6.1.4 and standard ntuples with tag Stntuple dev 243 corresponding to data collected from February 2002 through February 2010. It consists of two parallel analyses using high-p_T single-muon and single-electron triggers respectively. A dimuon analysis on datasets `bhmucd/h/i/j`

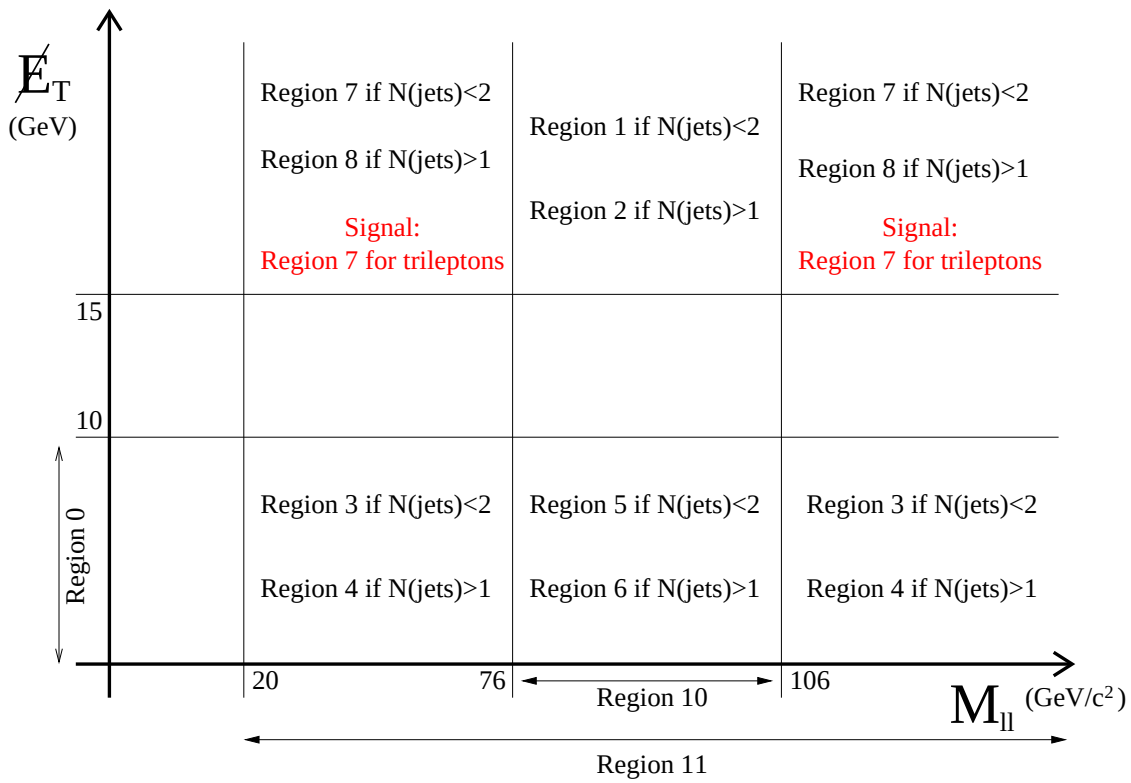

Figure 7.1: The control and signal regions used in this analysis. Since dileptons and trileptons are studied separately for dimuon and dielectron channels, there are a total of 66 control regions.

(datasets updated with latest TStnMuon Stntuple class) and `bhmubk/m` (datasets already updated) collected with a variety of high-p_T single-muon triggers, shown in Table 7.1. And a dielectron analysis conducted on datasets `bhelbd/h/i/j/k/m`, which were collected with the high-p_T single-electron trigger, ELECTRON_CENTRAL_18. A detailed description of the high-p_T triggers can be found in reference [127]. The status of all control regions is presented in this dissertation corresponding to a corrected luminosity of 5.8 fb^{-1} using the good-run list with version 34 and option (1,0,5,1). For events containing Phoenix electrons good silicon runs were required corresponding to a corrected luminosity of 5.6 fb^{-1} using the good-run list with version 34 and option (1,1,5,1). These luminosities are then corrected for a $|Z_v| < 60$

cm vertex cut applied to the data [128].

Single-muon high-p_T triggers
MUON_CMUP18
MUON_CMX18
MUON_CMUP18_L2_LOOSE_LUMI_260
MUON_CMUP18_L2_LOOSE_LUMI_240
MUON_CMUP18_L2_LOOSE_DPS
MUON_CMUP18_L2_PT15
MUON_CMX18_L2_PT15
MUON_CMX18_L2_PT15_LUMI_200
MUON_CMX18_L2_LOOSE_LUMI_200
MUON_CMX18_L2_LOOSE_DPS
MUON_CMX18_LUMI_250
MUON_CMX18_DPS

Table 7.1: The triggers considered in this analysis.

7.3 The Monte Carlo Sets

Several SM processes, produced at Tevatron, have a final state that mimic the signal under study. Events selected in the analysis have as main characteristics: large $\not\!\!E_T$, three isolated leptons, and low jet multiplicity (at most one jet). Dominant SM backgrounds are electroweak diboson production, heavy-flavor production, top-quark pair-production and light-flavor jets falsely reconstructed as identified leptons (mistags). The latter two background contributions are estimated from data.

The PYTHIA event generator is used to estimate the remaining backgrounds. For the event generation the CTEQ5L [129] parton distribution functions were used. Events are passed through the GEANT3-based [130] CDF II detector simulation and weighted by the probability that they would pass the trigger as determined in independent data samples. In order to test the ability to model the backgrounds, and also to compute the data-driven ones, several control regions are define as described in Section 7.9.

The MC samples used, along with the cross sections, K-factors (if any), filter efficiency (if any), and dilepton-mass cut at generator level can be seen on Table 7.2. The good-run-list filter is also applied to the MC datasets, therefore, the MC luminosity is corrected for the number of events that fail this requirement. The background samples generated by the EWK group are described in detail in the group's page [131]

7.4 Event Selection

Events are selected that include two leading muons (or two leading electrons) and a third lepton that can be a muon, electron, tau or an isolated track. All lepton types used in this analysis are defined in Section 5.7, where the cuts for each type are shown in Table 5.1 through Table 5.6. Muons can be of type CMU, CMUP, CMX, CMIO and BMU, with at least one of the leading two muons of type CMUP or CMX. The central electron objects can be tight or loose CEM. If a loose central electron is a third object, its fractional isolation must satisfy: $Iso/E_T < 0.1$. Plug electrons can be PEM or Phoenix. Priority is given to PEM over Phoenix if an electron passes all cuts in both categories. Good silicon run is required in events with at least one Phoenix electron. Hadronic taus and isolated tracks (not overlapping with an identified electron or muon) can only be third objects. In $\mu\mu + X$ events at least one

Process	Monte Carlo dataset	N of events generated	σ (pb)	K-factor (filter eff.)	Mass cut at generation (GeV/c^2)
DY $\to \mu\mu$	dexo5m‡	261 K	175.8	1.4	$70 < M_{\mu\mu} < 100$
DY $\to \mu\mu$	dexo4m‡	1 M	7.7	1.4	$100 < M_{\mu\mu} < 300$
DY $\to \mu\mu$	dexo3m‡	108 K	0.06	1.4	$M_{\mu\mu} > 300$
DY $\to ee$	ze0sdd†	1.7M	355.0	1.4	$M_{ee} > 20$
DY $\to \tau\tau$	ze0sbt†	6.6M	355.0	1.4	$M_{\tau\tau} > 20$
$Z\gamma \to \mu\mu\gamma$	re0s34†	8.5	10.33	1.36	$M_{\mu\mu} > 15$
$Z\gamma \to ee\gamma$	re0s33†	9.4M	10.33	1.36	$M_{ee} > 15$
$Z\gamma \to \tau\tau\gamma$	re0s37†	9.3M	10.33	1.36	$M_{\tau\tau} > 15$
$WZ \to \ell\ell X$	we0scd†	3.6 M	0.365	(0.76)	$M_{\ell\ell} > 20$
$ZZ \to \ell\ell X$	we0sdd†	3.5 M	1.511	(0.23)	$M_{\ell\ell} > 20$
$WW \to \ell\ell$	we0sbd†	3.5 M	1.27	-	$M_{\ell\ell} > 20$
$t\bar{t} \to \ell\ell$	te0s2z†	1.7 M	0.688	-	$M_{\ell\ell} > 20$
$W\gamma \to e\gamma$	re0s28†	0.7M	32.0	1.36	-

Table 7.2: Monte Carlo samples, cross sections, K-factors and filter efficiencies used for this analysis (†: samples produced by the electroweak group; ‡: samples produced by us especially for the multilepton analyses).

CMUP or CMX must have $p_T > 20$ GeV, while in $ee + X$ events at least one central electron must have $p_T > 20$ GeV.

A primary vertex of quality 12 or higher is required. Priority is given to 3-D primary vertices over 1-D vertices. The average of the z-coordinates of the two leading leptons is required to be within 4 cm of the selected primary vertex z-coordinate. The absolute Z position of the primary vertex has to be less than 60 cm. The $|\Delta Z|$ between the leading leptons is required to be within 5 cm. The $|\Delta Z|$ between the third object and the primary vertex is required to be within 5 cm.

The leptons and isolated tracks have to be $\Delta R > 0.4$ away from each-other, the leading dilepton mass has to be greater than 20 GeV/c^2, and the three-dimensional opening angle between the two leading dimuons has to be less that 178 degrees. This latter cut, removes residual cosmic backgrounds from the data, whereas the main cosmic background is removed with the application of standard CDF cosmic filters. Conversions are removed using the stand-alone track collection (not applicable to Phoenix electrons) and a scale factor is applied to MC to account for the difference in conversion removal inefficiency between data and MC [132]. The impact parameter was corrected with respect to a three dimensional primary vertex closest to the two leading leptons, if available, or with respect to the beam if only a one dimensional primary vertex is found.

The tracks of muons, electrons and isolated tracks are beam-constrained if the fit is good and the tracks have no silicon hits. In addition, we apply the "Larry-correction" to account for the COT alignment, with different corrections for COT-only, beam-constrained tracks and COT+SVX tracks. The muon 4-momenta are calculated from the tracker measurements. The energy of electrons is corrected for run-dependent energy scale factors, face and leakage corrections and PPR energy using the methods implemented in the standard ntuples with tag Stntuple dev 243.

In order to clean up the muons from hadronic decays in flight, we apply extra quality tracking cuts. The variables we use are the number of tracking fit residuals transitions from one side of the track to the other (ntrans) and the maximum sequence of residuals on the same side of a track (nmax). Decays in flight give low ntrans and high nmax. After studying the correleation of these variables and unphysical muon momenta and dimuon masses, we apply on our muons the cuts presented in Table 7.3. These cuts are close to 97% efficient for our MC real muons (DY or signal MC).

We count jets in the event if their corrected (level 5, cone size 0.4) energy is greater than 20 GeV, their electromagnetic fraction (e.m.f.) is less than 0.9, their

Kind of muon	NTRANS cut	NMAX cut
CMU or CMUP or CMX	> 20	< 20
CMIO	no cut	< 35
BMU	> 10	< 70

Table 7.3: Muon tracking quality cuts.

detector $|\eta| < 2.5$ and they are $\Delta R > 0.4$ away from the identified electrons and taus in the event.

The missing E_T ($\not\!\!E_T$) in the event is corrected for the presence of muons and isolated tracks, and for electron and jet energy corrections. The jets considered have uncorrected energies greater than 10 GeV, e.m.f < 0.9 and $\Delta R > 0.4$ away from identified leptons in the event. The jet energies are corrected using version `jetCorr18_sl5compat` of JetUser. For muons, the transverse energy depositions in the hadronic and electromagnetic calorimeters are added to the $\not\!\!E_T$; then, the corrected transverse momentum of the muon track is subtracted. For electrons, the raw transverse energy is added to the $\not\!\!E_T$ and then the corrected transverse energy is subtracted. The same is done to account for the jet energy corrections.

In order to reduce false $\not\!\!E_T$ due to jet and electron energy mis-measurements, events are rejected in high-$\not\!\!E_T$ signal (7 and 9) and control (1, 2 and 8) regions if the azimuthal angle between the $\not\!\!E_T$ and any of the identified leptons and jets (with uncorrected energies greater than 10 GeV, e.m.f < 0.9, detector $|\eta| < 2.5$ and $\Delta R > 0.4$ away from the identified electrons and taus in the event) is less than 20° (0.35 radians).

A summary of the event selection cuts used is given below

- Events are selected with two leading electrons, or two leading muons, and a third object, which can be an electron, muon, tau or isolated track. At least one of the leading muons must be of type CMUP or CMX

- Minimum $p_T \geq 5$ for all leptons except for CMIO ($p_T \geq 10$) and hadronic tau ($p_T \geq 20$)

- A primary vertex of quality 12 or higher is required. The average of the z-coordinates of the two leading leptons is required to be within 4 cm of the selected primary vertex z-coordinate. Also, $|Z_{prim}| < 60$ cm

- $m_{\ell\ell} > 20$ GeV

- $|\Delta Z| < 5$ cm between leading leptons

- $|\Delta Z| < 5$ cm between third object and z of primary vertex

- The leptons and isolated tracks have to be $\Delta R > 0.4$ away from each-other

- Conversion veto. $\Delta xy < 0.1$ and $\Delta \cot\theta < 0.02$

- Runs with good silicon required for all events with Phoenix electrons.

- Standard CDF cosmic filters

- The three-dimensional opening angle between the two leading dimuons has to be less that 178 degrees

- The azimuthal angle between the $\not\!\!E_T$ and any of the identified leptons and selected jets must be greater than 20° in signal and control regions of high missing energy ($\not\!\!E_T > 15$ GeV)

7.5 Trigger Efficiencies, lepton ID-reconstruction scale-factors and primary vertex re-weighing

In order to compare the expectation derived from MC simulations to the data, MC events need to be properly weighted to account for the difference in integrated luminosity between the data and the MC samples. Additionally MC events need to be weighted to account for differences in the efficiency of the identification cuts in data and simulation. This is achieved by applying ID-scale factors to the MC, which are defined as ratios of identification efficiencies measured independently in data and MC ($\epsilon_{data}/\epsilon_{MC}$). Finally, the triggering of real events in data must be simulated in MC, which contains many events that would not pass the high-p_T triggers that define the datasets used in this analysis. Therefore, MC events are weighted based on the luminosities of the datasets analyzed. These weights are then multiplied by the trigger efficiency, the lepton ID and reconstruction scale factors, all of which are applied on an event-by-event basis. The run dependent, high-p_T single-muon and single-electron trigger efficiencies, as well as the various high-p_T central lepton identification and reconstruction scale factors, are obtain from the joint-physics class, PerfIdia [127].

Using the values for single-muon (electron) trigger efficiencies, the event trigger efficiency for events with two or more trigger muons (electrons) is calculated as follows: If only two trigger muons (electrons) are found in the event

$$\epsilon_{\text{total}} = \epsilon_1(1-\epsilon_2) + \epsilon_2(1-\epsilon_1) + \epsilon_1\epsilon_2 \tag{7.1}$$

where ϵ_1 and ϵ_2 are the single muon (electron) trigger efficiencies for the two muons (electrons). In case we have 3 trigger muons (electrons) in the event, then the event

trigger efficiency is larger, given by:

$$\epsilon_{\text{total}} = \epsilon_1\epsilon_2\epsilon_3 + \sum_{i\neq j\neq k} \epsilon_i\epsilon_j(1-\epsilon_k) + \sum_{i\neq j\neq k} \epsilon_i(1-\epsilon_j)(1-\epsilon_k)$$

where ϵ_1, ϵ_2, ϵ_3 are the single muon (electron) trigger efficiencies of each muon (electron). Low-p_T lepton ID scale factors are not provided by PerfIdia and were obtained from other sources for muons ([133, 134]) and electrons ([136, 137]).

Since the PEM category consists of plug electrons with stand-alone tracks, the scale factors found in PerfIdia are not applicable because they correspond to electromagnetic clusters with no track requirement. Therefore, the identification and reconstruction (tracking) scale factors for PEM and Phoenix electrons were measured for periods 0 through 28 of data, following closely the method described in [138]. Plug electrons are selected in data and MC from $Z \rightarrow e^+e^-$ events with one electron passing all the tight central electron cuts (Table 5.1 of Chapter 5, Section 5.7) and the other leg in the plug calorimeter. The datasets used were `bhelb` for data and `ze0sdd` for electroweak Drell-Yan MC. The total ID efficiency ϵ_{ID} is defined by the following formula:

$$\epsilon_{ID} = \frac{N_{TP}}{N_{TC}},$$

Where N_{TP} is the number of events with one tight central electron and one plug calorimeter cluster passing all of the PEM or Phoenix ID cuts, while N_{TC} is the number of events with one tight central electron and a plug calorimeter cluster as defined in [138]. The plug cluster efficiency, tracking or reconstruction efficiency ϵ_{PC} is defined by the following formula:

$$\epsilon_{PC} = \frac{N_{TC}}{N_{TE}},$$

Where N_{TC} is the number of events with one tight central electron and one plug calorimeter cluster, while N_{TE} is the number of events with one tight central electron and a plug Em object. The scale factors obtained from calculating the ID and tracking efficiencies for PEM and Phoenix electrons are listed in Table A.1 (Appendix A).

In order to account for the effects of higher instantaneous luminosities (e.g., "pile up"), the DY MC was re-weighted so that the shape of the distribution of primary vertex multiplicity would be the same in data and MC. Histograms of this variable were made in data and DY MC in the region of the Z boson resonance. The histograms were normalized to unity and the contents of each bin were used to calculate a ratio of observation to expectation, thus defining a re-weighing function which depends on the number of vertices in the event. This weight was then applied to the MC sample as w(n) = $\text{obs}_{norm}/\text{exp}_{norm}$, where n is the number of primary vertices (Appendix B).

7.6 Standard Model and Non-physics Background

The possible background processes for the trilepton and missing E_T signature is dependent on the nature of the analysis objects and thus the analysis channel: the background of the dilepton+track channels is fundamentally different from the background of the trilepton channels.

7.6.1 Background in the Trilepton Channels

The background contribution from processes with three genuine leptons, including the processes where one lepton comes from a photon conversion, is estimated with

Monte Carlo. Backgrounds from processes with one faked lepton are estimated independently of the production process for the two real leptons. However, the major contribution is Drell-Yan.

- three genuine leptons from
  - WZ/γ^*
  - $Z/\gamma^*Z/\gamma^*$
  - $t\bar{t}$ with a subsequent semileptonic B decay
- two genuine leptons and a lepton from a photon conversion from
  - WW and a photon conversion
  - Drell-Yan and a photon conversion
- two genuine leptons and a third fake lepton

7.6.2 Background in the Dilepton + Track Channels

The major backgrounds for channels with two genuine leptons and one isolated track are:

- two genuine leptons and on isolated track from a not fully reconstructed lepton from
  - WZ/γ
  - $Z/\gamma^*Z/\gamma^*$
  - $t\bar{t}$ with a subsequent semileptonic B decay
  - WW and a photon conversion

  - Drell-Yan and a photon conversion

- one isolated track from the underlying event or a jet, where one charged particle showers outside the core of the jet, and two genuine leptons from
  - WZ/γ^*
  - WW
  - $Z/\gamma^*Z/\gamma^*$
  - $t\bar{t}$
  - Drell-Yan

7.7 Background estimation

The backgrounds to the dilepton final state can be separated into two main groups: those that correspond to processes that generate two real leptons and those that are characterized by one real lepton and a misidentified lepton (fake lepton). Simarly, the backgrounds to the trilepton final state come from either three real leptons or two leptons accompanied by a fake lepton. To estimate the contribution of the first group, mainly electroweak and top backgrounds, Monte Carlo simulations are used. Processes such as diboson, top-pair and DY, $W + \gamma$, DY+γ are all sources of two or three real leptons.

The second group of background has its origin in QCD processes. A fake lepton is either a track that fakes a muon or a jet that fakes an electron. In the dilepton final state, the real lepton comes mostly (but not necessarily) from a W decay. In the trilepton final state the two real leptons come mostly from the Drell-Yan process. The origin of a fake muon can be a punch-through or a decay-in-flight of kaons and pions. Fake electrons may come from overlaps of π^0's and tracks. This

QCD background is determined with CDF data [139] because Monte Carlo cannot simulate the QCD rates and the misidentification of leptons efficiently. In order to estimate this background, the probability (fake-rate) for an isolated fakeable object (denominator object) to fake an identified lepton (numerator object) is measured. The fake rates are measured using `jet20`, `jet50`, `jet70`, and `jet100` datasets which are rich in fake leptons. A full description of the methodology used to measure fake rates is described in Chapter 6.

7.7.1 Data-estimated backgrounds

For the estimation of the dilepton fakes events with one identified lepton (e/μ) are select from the single-lepton triggered datasets (bhel/bhmu). Then, fake dileptons are constructed from each of these events (possibly more than one pair) by pairing the identified real lepton with each of the fakeable objects found in that event that do not match geometrically to the real lepton. The fake dilepton event is assigned a weight equal to the fake rate associated with the fakeable object and required to satisfy all other kinematic cuts applied to the analysis data. The sum of all weighted fake pairs gives us the dilepton fake estimation. The fakeable objects are different for different leptonic flavors, namely, `CdfEmObjects`, tracks and CdfTaus are used as fakeable electrons, muons and taus respectively. Additional cuts are applied to these basic objects to construct the final fakeable objects (identical to the denominators used in the fake-rate measurements) which are described along with their corresponding leptonic fake rates in Chapter 6.

For the estimation of the trilepton fakes, dilepton events with leptons passing all the ID cuts are identified. Then, trilepton fakes are constructed from each of these dileptons by looping over all fakeable objects in the event (excluding those associated

to the leading leptons) and pairing the two real leptons with the fakeable object. Each fake trilepton event is weighted by the fake rate of the respective fakeable object which is subsequently treated as a real lepton. The sum of all weighted trilepton fakes gives the trilepton fake background. The contribution to the background of events with one real lepton and two fakes is considered to be negligible [140].

7.7.2 MC-estimated backgrounds

As previously mentioned, trilepton backgrounds with three real leptons are estimated with Monte Carlo. As with data, the analysis program is run on the MC samples, this time using the proper luminosity normalization, trigger efficiencies, and lepton-ID and lepton reconstructipn scale factors. Every MC-estimated background has a systematic uncertainty coming from the limited statistics of each sample.

The Monte Carlo events are weighted on an event-by-event basis with the following weight:

$$\text{weight} = \frac{\mathcal{L}_{\text{data}}}{\mathcal{L}_{\text{MC}}} \text{SF}_{\text{ID,1}} \text{SF}_{\text{ID,2}} \cdots \text{SF}_{\text{ID,N}} \epsilon_{\text{trig}},$$

where $\text{SF}_{\text{ID,i}}$ are the ID-scale factors for the N leptons identified in the event, ϵ_{trig} is the event trigger efficiency, $\mathcal{L}_{\text{data}}$ is the data luminosity and $\mathcal{L}_{\text{MC}}$ is the luminosity of the MC defined as:

$$\mathcal{L}_{\text{MC}} = \frac{N_{\text{gen}}}{\sigma K \epsilon_{\text{filter}}},$$

where N_{gen} are the MC events generated, σ is the SM leading-order cross section (usually given by Pythia), K is a factor that corrects the cross-section for next-to-leading order effects, and ϵ_{filter} is the post-generation filter efficiency. The values for some of these quantities are given in Table 7.2. The scale factors and trigger efficiencies are period-dependent and are given by PerfIdia for high-p_T muons, electrons and taus and in [133, 134, 135, 136, 137] for low-p_T muons and electrons. The track

identification scale factor is taken to be 1.0 [141]. Because some of the triggers are dynamically pre-scaled (DPS), the lifetime of the triggers and their overlaps are used in the determination of the event trigger efficiency. The lifetime of the DPS triggers is determined from an analytic list of luminosities per trigger per run, for all triggers and all runs considered in this analysis.

7.8 Systematics

Systematic errors are the main source of uncertainty in this search. The sources of systematic uncertainty for the MC-estimated backgrounds are:

- The luminosity uncertainty (a 6% effect),
- The lepton-ID and isolation scale factors (a 2% effect [142]),
- Trigger efficiency uncertainty (a 0.5 % effect [142]),
- Parton Distribution Functons systematic (a 2% [142], [140]),
- Cross sections theory systematic (8% for both SM and signal, [140]).
- Jet Energy Scale. A systematic error in the calorimeter energy scale affect the total transverse energy of the jets. The jet-energy systematic uncertainty affects both the jet counting, and the missing transverse energy (which is corrected for the jet energy). As a result, the effect of this systematic uncertainty migrates events across the control/signal regions and also affects the $\not\!\!E_T$ distribution. We measured the effect of this uncertainty to be $< 0.2\%$ in the signal region, so we ignore it.

Overall the MC signal or SM systematic is 10 %. The systematic uncertainty associated to the fake estimation is determined from the spread in the measurements

of the fake probabilities using different jet-rich CDF datasets triggered by different jet-energy thresholds. Due to a large reduction of sample bias achieved in the measurement of the fake rates, the fakes-estimation systematic uncertainty was reduced to $\sim 20\%$ for low-energy (< 20 GeV) fakeable leptons, at high energies the systematic remains close to 50 % [139].

7.9 Control Regions

To avoid potential biases when searching for new physics we perfom a "blind search." To be sure about our predictions' reliability, we test the various background contributions in distinct control regions that are defined a priori, and in which the expectation for signal is negligible when compared to the background. As previously mentioned, the control regions are defined in the $\not\!\!E_T$ vs dilepton mass $M_{\ell\ell}$ space, with the additional requirement of high or low jet multiplicity. As shown in Figure 7.2, different control regions are useful for validating specific kinds of backgrounds. The central region in dilepton masses between 76 GeV and 106 GeV (for high and low $\not\!\!E_T$) validates electroweak backgrounds, specifically the Z boson resonance. In dilepton channels, this region is particularly useful for validating the overall normalization of the MC, which is the result of the application of several weights: ID-scale factors, trigger efficiencies, luminosity scales, etc. In trileptons channels, this region is useful for validating the fake rate of muons, electrons, taus and isolated tracks. Control regions of high $\not\!\!E_T$ and high jet multiplicity have large contributions of top backgrounds where $t\bar{t}$ is clearly visible in dilepton channels. On the other hand, high $\not\!\!E_T$ and low jet multiplicity regions are rich in diboson backgrounds as can be appreciated in trilepton kinematic plots.

By allowing for a gap in the $\not\!\!E_T$ considered, the presence of SUSY signal in the control regions is minimized. SM event-yield predictions are compared with observed

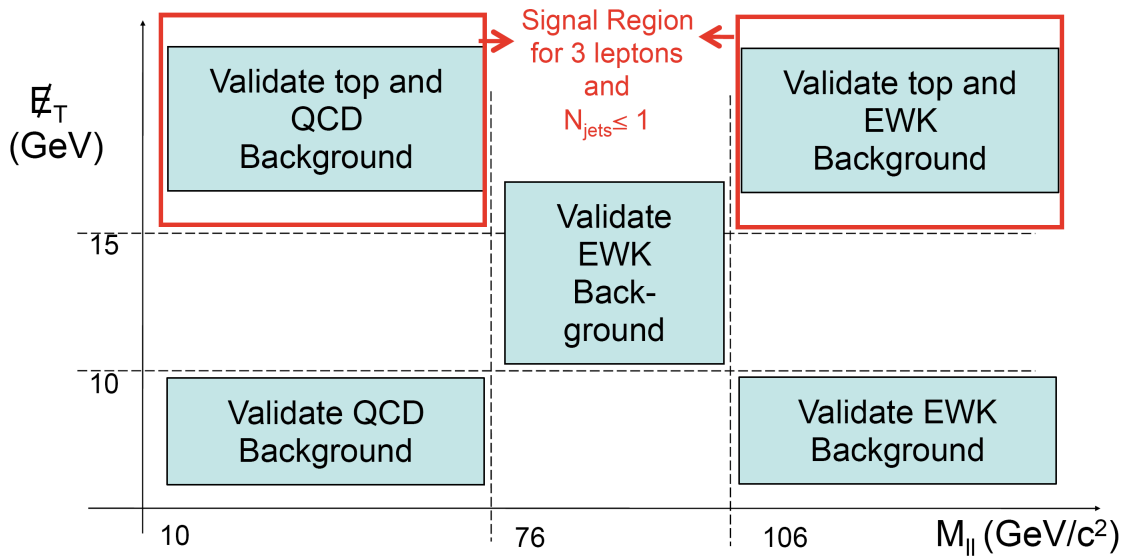

Figure 7.2: Control regions and background validation.

events in the control regions (along with kinematic plots), whereas the signal regions remain blind until the very end of the analysis. Tables of yields and kinematic plots for all dilepton and trilepton control regions can found in Appendices C and D respectively.

In total, 66 phase-space regions are defined (58 control regions and 8 signal regions):

- 11 ee, 9 ee+lepton, 9 ee+track control regions,
- 11 $\mu\mu$, 9 $\mu\mu$+lepton, 9 $\mu\mu$+track control regions,
- 2 ee+lepton, 2 ee+track, 2 $\mu\mu$+lepton, 2 $\mu\mu$+track singal regions.

7.9.1 Trilepton Control Regions

Control Region 0

In this region, we simply require $\not{E}_T < 10$ GeV.

Table of $\mu\mu$+X yields						
	Drell-Yan+γ	Fakes	Diboson	Top	Total SM	Observed
$\mu\mu$+lepton	115 ± 12	126 ± 35	3.1 ± 0.3	0.019 ± 0.007	244 ± 37	**254**
$\mu\mu$+IsoTrack	27 ± 3	695 ± 140	1.5 ± 0.1	0.016 ± 0.006	723 ± 140	**641**

Table 7.4: Trilepton events for data and SM prediction in region 0.

Table of ee+X yields							
	Drell-Yan+γ	Fakes	Diboson	Wγ	Top	Total SM	Observed
ee+lepton	174 ± 17	226 ± 63	5.2 ± 0.5	0 ± 0	0.041 ± 0.009	406 ± 65	**434**
ee+IsoTrack	39 ± 4	1380 ± 277	1.7 ± 0.2	0 ± 0	0.019 ± 0.006	1420 ± 277	**1321**

Table 7.5: Trilepton events for data and SM prediction in region 0.

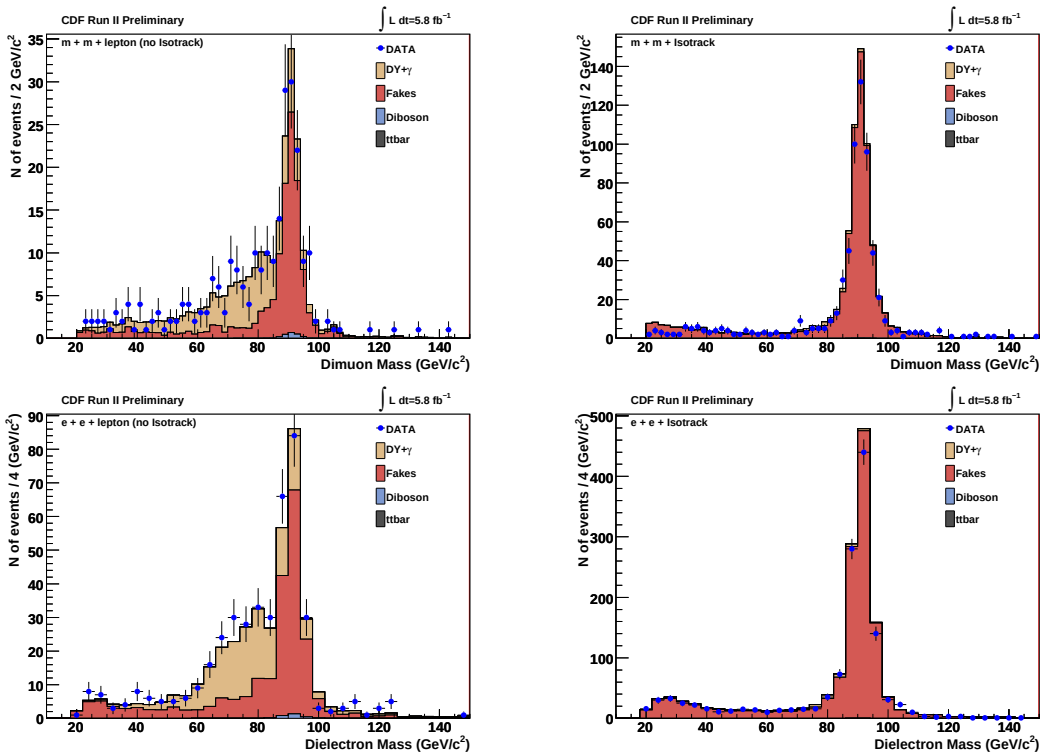

Figure 7.3: Dilepton mass of trilepton events for data and SM prediction in region 0.

Control Region 1

In this region, we require $\not{E}_T > 15$ GeV, dilepton mass within the Z region and low jet multiplicity (at most one jet).

Table of $\mu\mu$+X yields						
	Drell-Yan+γ	Fakes	Diboson	Top	Total SM	Observed
$\mu\mu$+lepton	2.8 ± 0.3	19 ± 6	8.8 ± 0.9	0.043 ± 0.01	30 ± 6	**26**
$\mu\mu$+IsoTrack	1.6 ± 0.2	169 ± 38	3.3 ± 0.3	0.033 ± 0.009	174 ± 38	**183**

Table 7.6: Trilepton events for data and SM prediction in region 1.

Table of ee+X yields							
	Drell-Yan+γ	Fakes	Diboson	Wγ	Top	Total SM	Observed
ee+lepton	2.4 ± 0.3	21 ± 7	13 ± 1	0.2 ± 0.2	0.13 ± 0.02	37 ± 7	**35**
ee+IsoTrack	6.6 ± 0.7	249 ± 57	5.8 ± 0.6	0.4 ± 0.2	0.08 ± 0.01	262 ± 57	**285**

Table 7.7: Trilepton events for data and SM prediction in region 1.

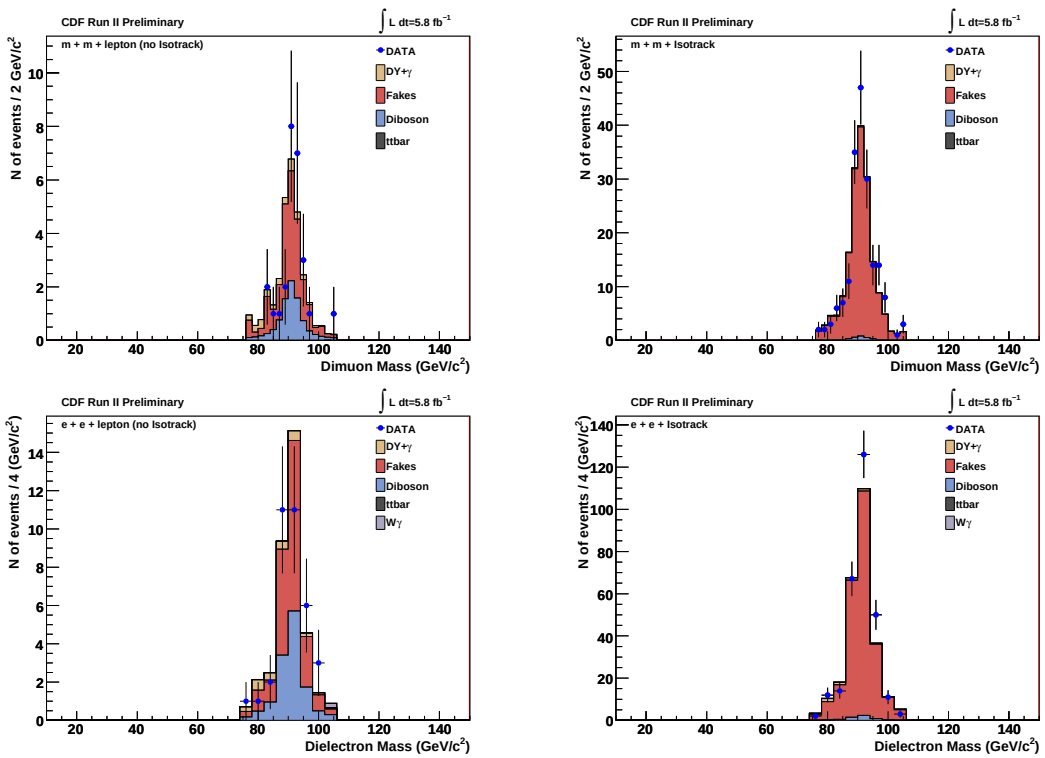

Figure 7.4: Dilepton mass of trilepton events for data and SM prediction in region 1.

Control Region 2

In this region, we require $\not{E}_T > 15$ GeV, dilepton mass within the Z region and high jet multiplicity (more than one jet).

Table of $\mu\mu$+X yields						
	Drell-Yan+γ	Fakes	Diboson	Top	Total SM	Observed
$\mu\mu$+lepton	0.08 ± 0.02	1 ± 0.4	0.18 ± 0.02	0.035 ± 0.009	1.3 ± 0.4	**3**
$\mu\mu$+IsoTrack	0.03 ± 0.01	12 ± 3	0.28 ± 0.03	0.14 ± 0.02	12 ± 3	**16**

Table 7.8: Trilepton events for data and SM prediction in region 2.

Table of ee+X yields							
	Drell-Yan+γ	Fakes	Diboson	Wγ	Top	Total SM	Observed
ee+lepton	0.13 ± 0.03	1.4 ± 0.5	0.26 ± 0.03	0 ± 0	0.06 ± 0.01	1.8 ± 0.5	**4**
ee+IsoTrack	0.25 ± 0.04	18 ± 4	0.59 ± 0.06	0 ± 0	0.2 ± 0.03	19 ± 4	**25**

Table 7.9: Trilepton events for data and SM prediction in region 2.

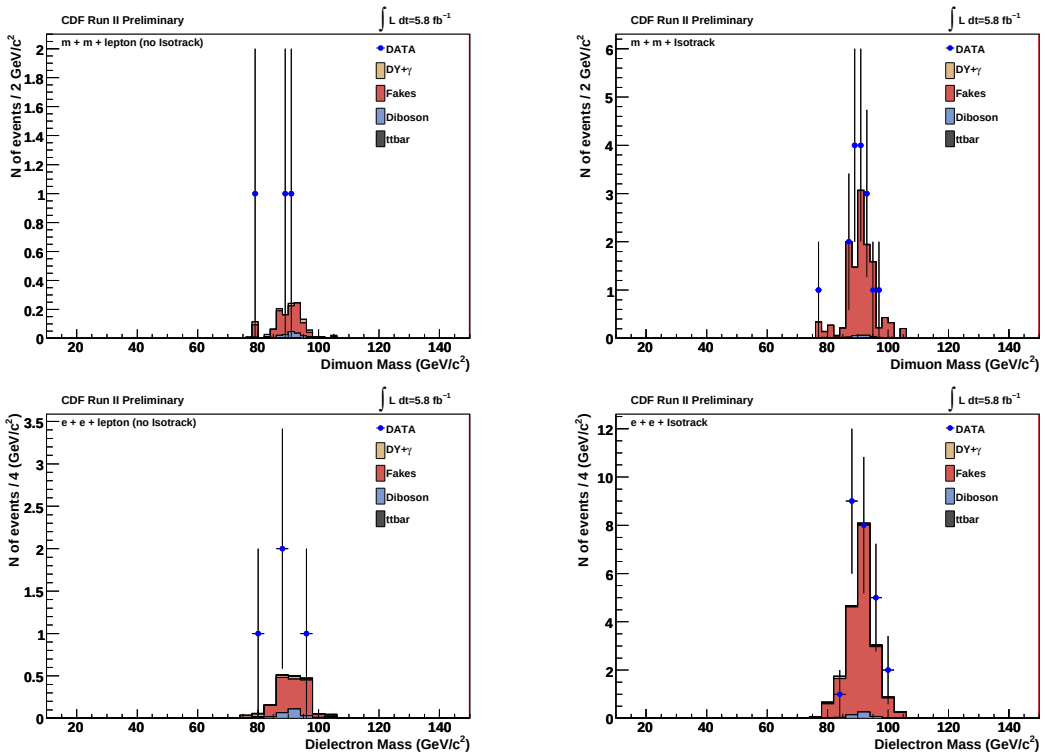

Figure 7.5: Dilepton mass of trilepton events for data and SM prediction in region 2.

Control Region 3

In this region, we require $\not{E}_T < 10$ GeV, exclusion of the Z mass region and low jet multiplicity (at most one jet).

Table of $\mu\mu$+X yields						
	Drell-Yan+γ	Fakes	Diboson	Top	Total SM	Observed
$\mu\mu$+lepton	58 ± 6	26 ± 8	0.64 ± 0.07	0.015 ± 0.006	85 ± 10	**94**
$\mu\mu$+IsoTrack	10 ± 1	128 ± 26	0.16 ± 0.02	0.005 ± 0.003	139 ± 26	**116**

Table 7.10: Trilepton events for data and SM prediction in region 3.

Table of ee+X yields							
	Drell-Yan+γ	Fakes	Diboson	Wγ	Top	Total SM	Observed
ee+lepton	86 ± 9	59 ± 18	1.9 ± 0.2	0 ± 0	0.026 ± 0.007	147 ± 20	**165**
ee+IsoTrack	15 ± 2	290 ± 58	0.27 ± 0.03	0 ± 0	0.004 ± 0.003	306 ± 58	**270**

Table 7.11: Trilepton events for data and SM prediction in region 3.

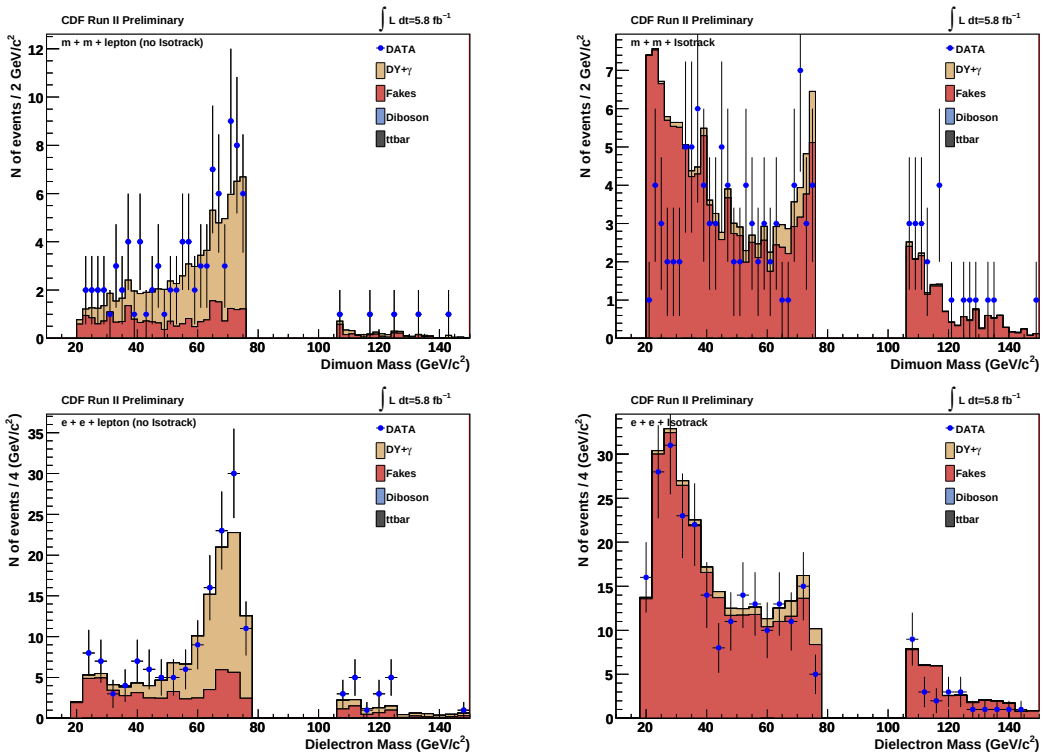

Figure 7.6: Dilepton mass of trilepton events for data and SM prediction in region 3.

Control Region 4

In this region, we require $\not{E}_T < 10$ GeV, exclusion of the Z mass region and high jet multiplicity (more than one jet).

Table of $\mu\mu$+X yields						
	Drell-Yan+γ	Fakes	Diboson	Top	Total SM	Observed
$\mu\mu$+lepton	0.37 ± 0.07	0.5 ± 0.2	0.027 ± 0.004	0.004 ± 0.003	0.9 ± 0.2	**0**
$\mu\mu$+IsoTrack	0.17 ± 0.04	5 ± 1	0.059 ± 0.008	0.009 ± 0.004	6 ± 1	**8**

Table 7.12: Trilepton events for data and SM prediction in region 4.

Table of ee+X yields							
	Drell-Yan+γ	Fakes	Diboson	Wγ	Top	Total SM	Observed
ee+lepton	0.51 ± 0.07	1.2 ± 0.4	0.075 ± 0.009	0 ± 0	0.008 ± 0.004	1.8 ± 0.4	**4**
ee+IsoTrack	0.28 ± 0.05	15 ± 3	0.065 ± 0.008	0 ± 0	0.013 ± 0.005	15 ± 3	**18**

Table 7.13: Trilepton events for data and SM prediction in region 4.

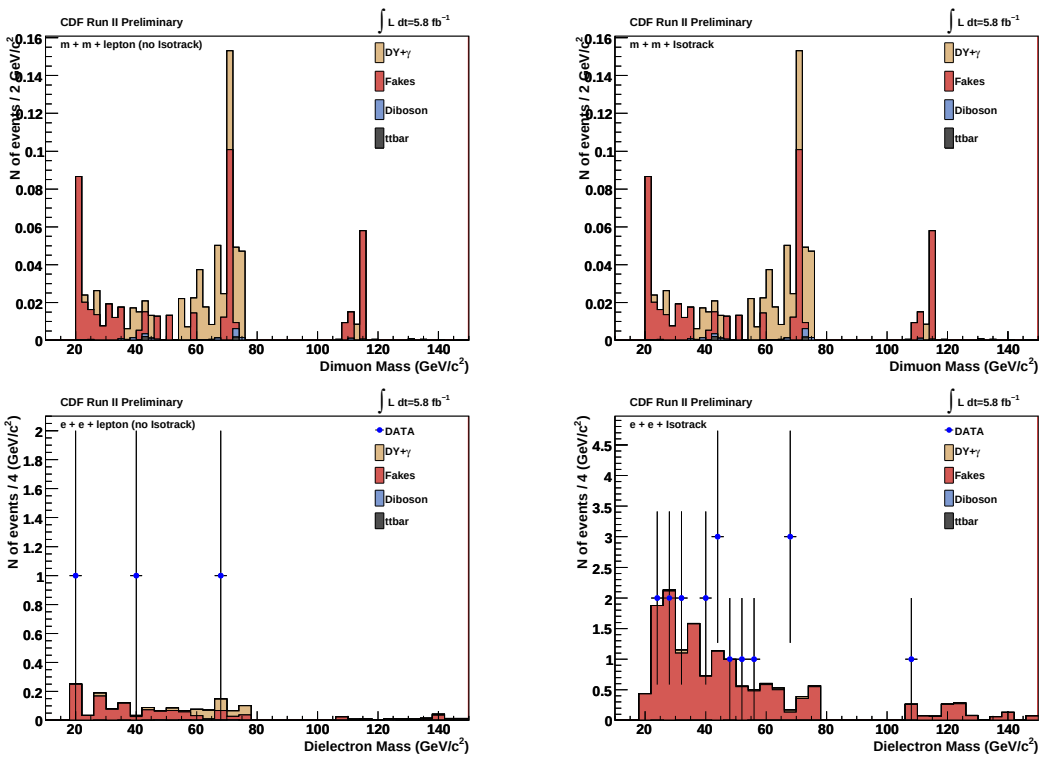

Figure 7.7: Dilepton mass of trilepton events for data and SM prediction in region 4.

Control Region 5

In this region, we require $\not{E}_T < 10$ GeV, dilepton mass in the Z region and low jet multiplicity (at most one jet).

Table of $\mu\mu$+X yields						
	Drell-Yan+γ	Fakes	Diboson	Top	Total SM	Observed
$\mu\mu$+lepton	56 ± 6	98 ± 26	2.4 ± 0.2	0 ± 0	156 ± 27	**156**
$\mu\mu$+IsoTrack	17 ± 2	540 ± 109	0.68 ± 0.07	0 ± 0	557 ± 109	**498**

Table 7.14: Trilepton events for data and SM prediction in region 5.

Table of ee+X yields							
	Drell-Yan+γ	Fakes	Diboson	Wγ	Top	Total SM	Observed
ee+lepton	87 ± 9	161 ± 43	3.1 ± 0.3	0 ± 0	0.002 ± 0.002	251 ± 44	**257**
ee+IsoTrack	23 ± 2	1035 ± 208	0.77 ± 0.08	0 ± 0	0.002 ± 0.002	1058 ± 208	**1002**

Table 7.15: Trilepton events for data and SM prediction in region 5.

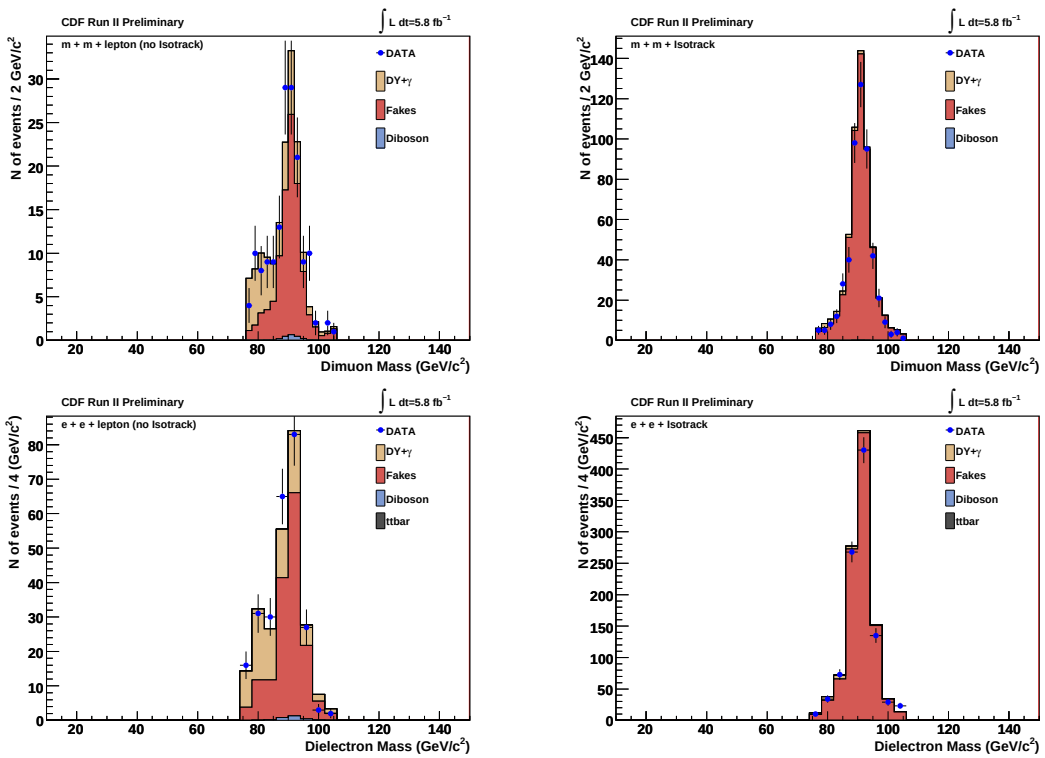

Figure 7.8: Dilepton mass of trilepton events for data and SM prediction in region 5.

Control Region 6

In this region, we require $\not{E}_T < 10$ GeV, dilepton mass in the Z region and high jet multiplicity (more than one jet).

Table of $\mu\mu$+X yields						
	Drell-Yan+γ	Fakes	Diboson	Top	Total SM	Observed
$\mu\mu$+lepton	0.56 ± 0.09	2.3 ± 0.7	0.11 ± 0.01	0 ± 0	3 ± 0.7	**4**
$\mu\mu$+IsoTrack	0.32 ± 0.06	21 ± 4	0.55 ± 0.06	0.002 ± 0.002	22 ± 4	**19**

Table 7.16: Trilepton events for data and SM prediction in region 6.

Table of ee+X yields							
	Drell-Yan+γ	Fakes	Diboson	Wγ	Top	Total SM	Observed
ee+lepton	0.77 ± 0.1	5 ± 1	0.15 ± 0.02	0 ± 0	0.005 ± 0.003	6 ± 1	**8**
ee+IsoTrack	0.35 ± 0.06	40 ± 8	0.59 ± 0.06	0 ± 0	0 ± 0	41 ± 8	**31**

Table 7.17: Trilepton events for data and SM prediction in region 6.

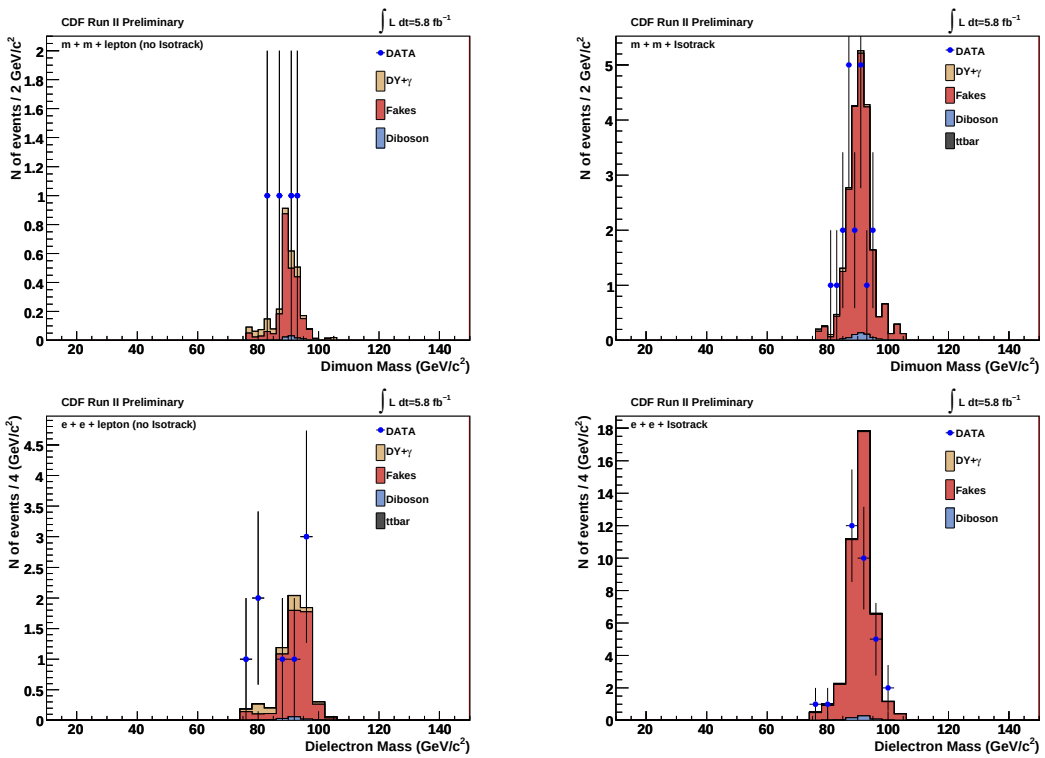

Figure 7.9: Dilepton mass of trilepton events for data and SM prediction in region 6.

Control Region 8

In the control region SIG_A2, we require $\not\!\!E_T > 15$ GeV, exclusion of the Z mass region and high jet multiplicity (more than one jet).

Table of $\mu\mu$+X yields						
	Drell-Yan+γ	Fakes	Diboson	Top	Total SM	Observed
$\mu\mu$+lepton	0.1 ± 0.03	0.4 ± 0.1	0.08 ± 0.01	0.14 ± 0.02	0.7 ± 0.1	**0**
$\mu\mu$+IsoTrack	0.06 ± 0.02	5 ± 1	0.1 ± 0.01	0.47 ± 0.06	5 ± 1	**2**

Table 7.18: Trilepton events for data and SM prediction in region 8.

Table of ee+X yields							
	Drell-Yan+γ	Fakes	Diboson	Wγ	Top	Total SM	Observed
ee+lepton	0.09 ± 0.02	0.9 ± 0.3	0.12 ± 0.01	0 ± 0	0.25 ± 0.03	1.3 ± 0.3	**3**
ee+IsoTrack	0.62 ± 0.08	13 ± 3	0.24 ± 0.03	0 ± 0	0.65 ± 0.07	14 ± 3	**8**

Table 7.19: Trilepton events for data and SM prediction in region 8.

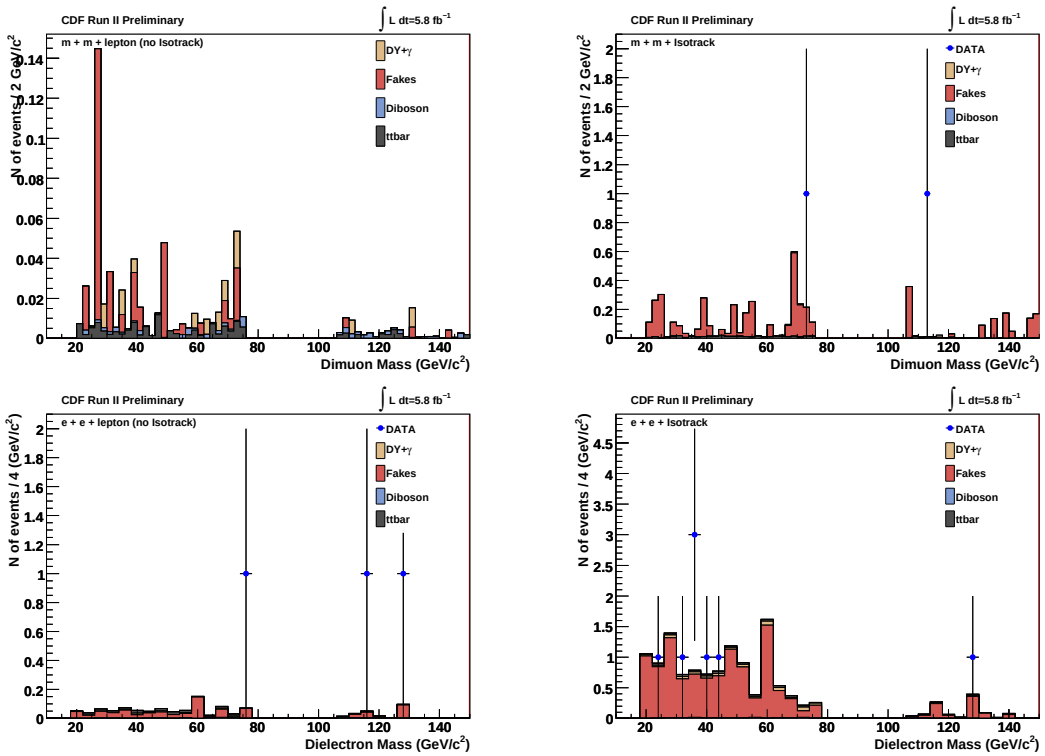

Figure 7.10: Dilepton mass of trilepton events for data and SM prediction in region 8.

Control Region 10

In this region, we require opposite sign for the dileptons, and dilepton mass between 76 and 106 GeV.

Table of $\mu\mu$+X yields						
	Drell-Yan+γ	Fakes	Diboson	Top	Total SM	Observed
$\mu\mu$+lepton	77 ± 8	170 ± 49	15 ± 2	0.09 ± 0.02	262 ± 49	**274**
$\mu\mu$+IsoTrack	25 ± 3	1151 ± 238	7.3 ± 0.7	0.24 ± 0.03	1184 ± 238	**1221**

Table 7.20: Trilepton events for data and SM prediction in region 10.

Table of $ee + X$ yields							
	Drell-Yan+γ	Fakes	Diboson	Wγ	Top	Total SM	Observed
ee+lepton	94 ± 9	243 ± 69	20 ± 2	0.2 ± 0.2	0.21 ± 0.03	358 ± 70	**385**
ee+IsoTrack	42 ± 4	1890 ± 390	11 ± 1	0 ± 0	0.36 ± 0.04	1942 ± 390	**1964**

Table 7.21: Trilepton events for data and SM prediction in region 10.

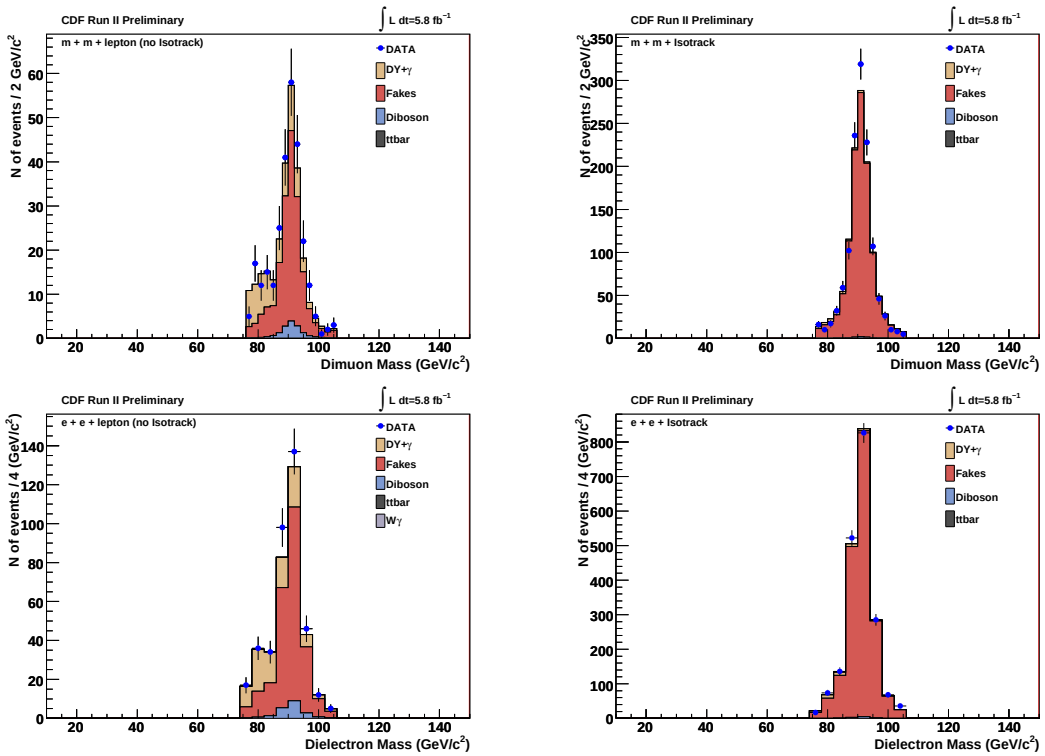

Figure 7.11: Dilepton mass of trilepton events for data and SM prediction in region 10.

Control Region 11

In this region we apply none of the cuts that define the previous control regions.

Table of $\mu\mu$+X yields						
	Drell-Yan+γ	Fakes	Diboson	Top	Total SM	Observed
$\mu\mu$+lepton	156 ± 16	224 ± 65	22 ± 2	0.66 ± 0.07	402 ± 67	**435**
$\mu\mu$+IsoTrack	43 ± 4	1463 ± 303	12 ± 1	1.2 ± 0.1	1518 ± 303	**1560**

Table 7.22: Trilepton events for data and SM prediction in region 11.

Table of $ee + X$ yields							
	Drell-Yan+γ	Fakes	Diboson	Wγ	Top	Total SM	Observed
ee+lepton	215 ± 22	371 ± 108	34 ± 3	0.7 ± 0.4	1.3 ± 0.1	621 ± 111	**687**
ee+IsoTrack	114 ± 11	2707 ± 560	18 ± 2	4 ± 0.9	1.9 ± 0.2	2845 ± 560	**2843**

Table 7.23: Trilepton events for data and SM prediction in region 11.

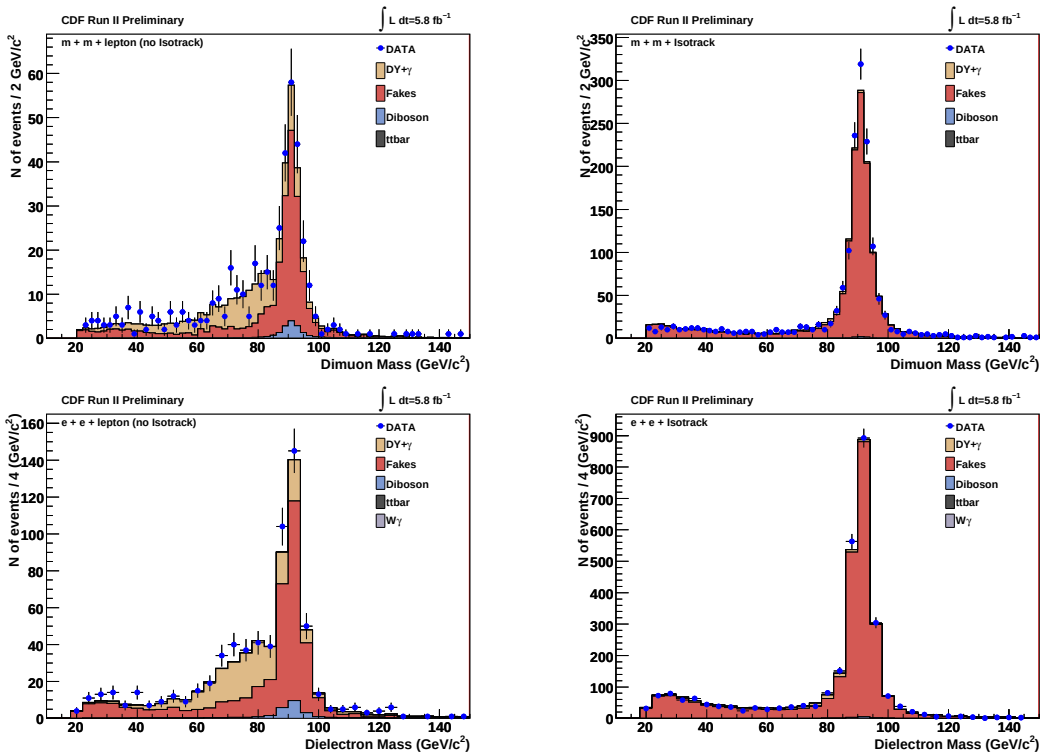

Figure 7.12: Dilepton mass of trilepton events for data and SM prediction in region 11.

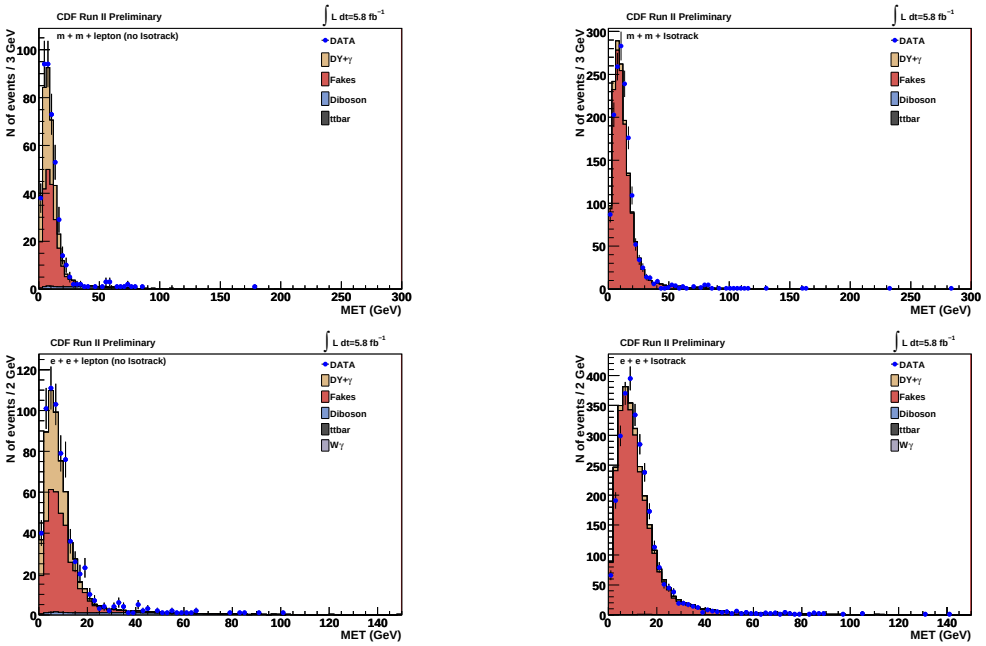

Figure 7.13: Missing energy of trilepton events for data and SM prediction in region 11 (inclusive).

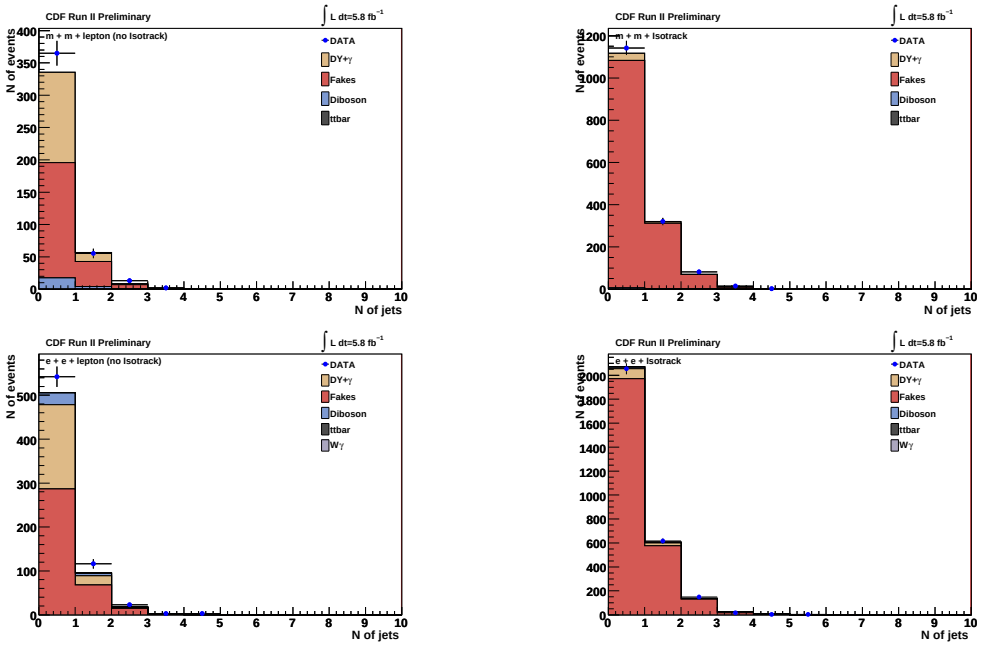

Figure 7.14: Jet multiplicity of trilepton events for data and SM prediction in region 11 (inclusive).

7.10 Signal Region results

The signal region is characterized by 3 leptons, large $\not\!\!E_T$, exclusion of the Z peak region and low jet multiplicity (for the elimination of the $t\bar{t}$ background). Two distinct "signal" regions were investigated, SIG_UNM (with $\not\!\!E_T > 20$ GeV, exclusion of the Z region and $M_{\ell\ell} > 20$ GeV/c^2) and the SIG_A (with $\not\!\!E_T > 15$ GeV, exclusion of the Z region and $M_{\ell\ell} > 20$ GeV/c^2). The signal acceptance in these two regions is comparable, and the same is true for the background estimation. However, SIG_A was chosen as the canonical signal region for consistency with previous CDF analyses.

After observing very good agreement between observation and SM expectation in both event yields and kinematics in the 58 control regions, the data was unblinded in the signal regions.

7.10.1 Signal Region 7

In the signal region, we require $\not{E}_T > 15$ GeV, exclusion of the Z mass region and low jet multiplicity (at most one jet).

Table of $\mu\mu$+X yields						
	Drell-Yan+γ	Fakes	Diboson	Top	Total SM	Observed
$\mu\mu$+lepton	2.8 ± 0.3	7 ± 2	3.4 ± 0.3	0.24 ± 0.03	13 ± 2	**20**
$\mu\mu$+IsoTrack	1 ± 0.1	65 ± 15	2.2 ± 0.2	0.19 ± 0.03	68 ± 15	**62**

Table 7.24: Trilepton events for data and SM prediction in region 7.

Table of ee+X yields							
	Drell-Yan+γ	Fakes	Diboson	Wγ	Top	Total SM	Observed
ee+lepton	3.1 ± 0.3	10 ± 4	5.9 ± 0.6	0.1 ± 0.1	0.44 ± 0.05	20 ± 4	**34**
ee+IsoTrack	26 ± 3	124 ± 27	4 ± 0.4	2.4 ± 0.7	0.27 ± 0.04	157 ± 28	**146**

Table 7.25: Trilepton events for data and SM prediction in region 7.

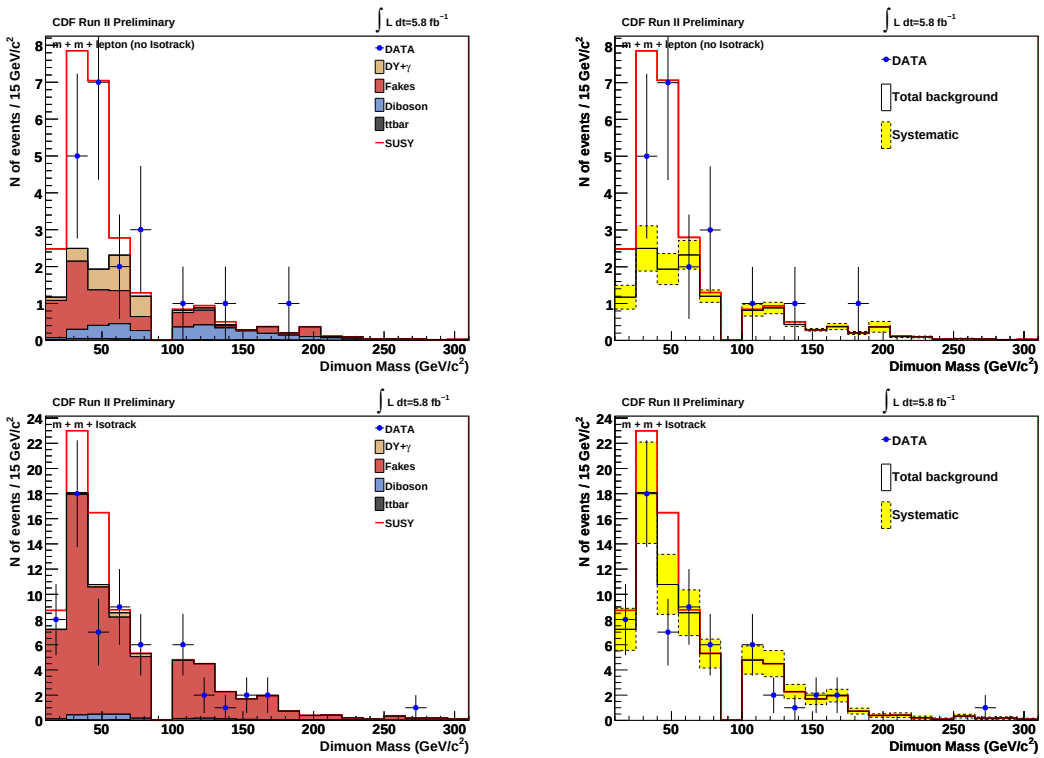

Figure 7.15: Dimuon mass of trilepton events for data and SM prediction in region 7.

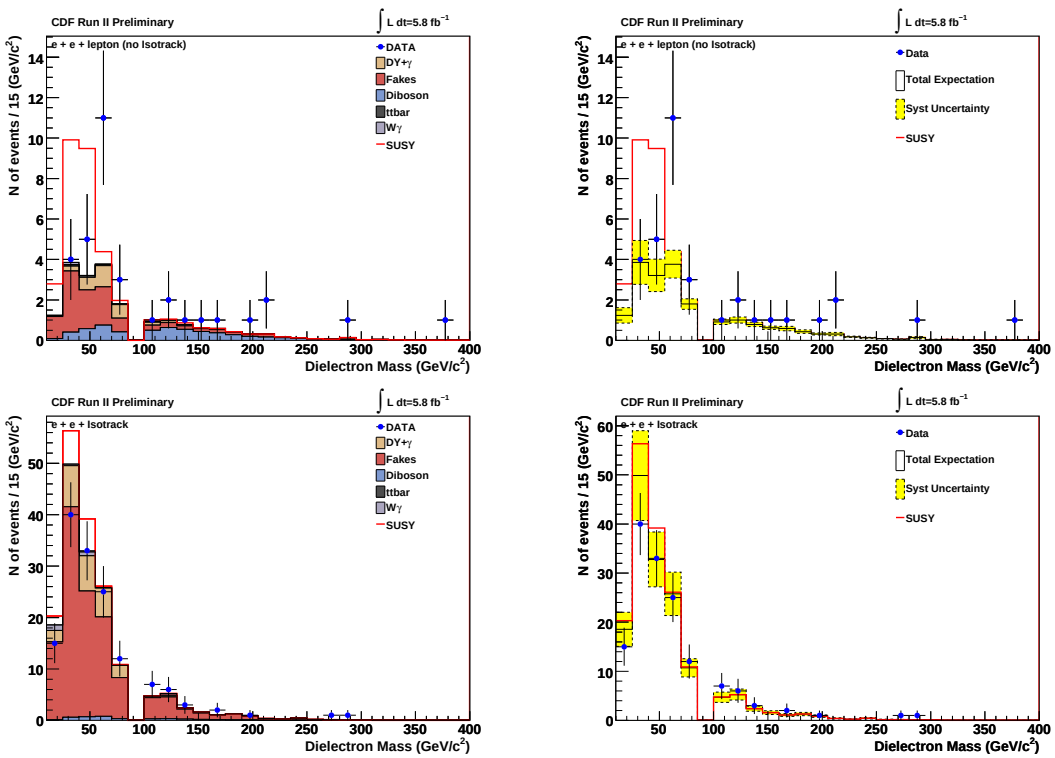

Figure 7.16: Dielectron mass of trilepton events for data and SM prediction in region 7.

7.10.2 Signal Region 9

In the signal region SIG_UNM, we require $\not{E}_T > 20$ GeV.

Table of $\mu\mu$+X yields						
	Drell-Yan+γ	Fakes	Diboson	Top	Total SM	Observed
$\mu\mu$+lepton	0.7 ± 0.1	4 ± 1	3.2 ± 0.3	0.37 ± 0.05	9 ± 1	**7**
$\mu\mu$+IsoTrack	0.36 ± 0.06	45 ± 10	2.2 ± 0.2	0.64 ± 0.07	48 ± 10	**38**

Table 7.26: Trilepton events for data and SM prediction in region 9.

Table of ee+X yields							
	Drell-Yan+γ	Fakes	Diboson	Wγ	Top	Total SM	Observed
ee+lepton	0.9 ± 0.1	7 ± 3	5.5 ± 0.6	0.1 ± 0.1	0.66 ± 0.07	14 ± 3	**24**
ee+IsoTrack	21 ± 2	83 ± 19	4 ± 0.4	2.4 ± 0.7	0.91 ± 0.1	111 ± 19	**99**

Table 7.27: Trilepton events for data and SM prediction in region 9.

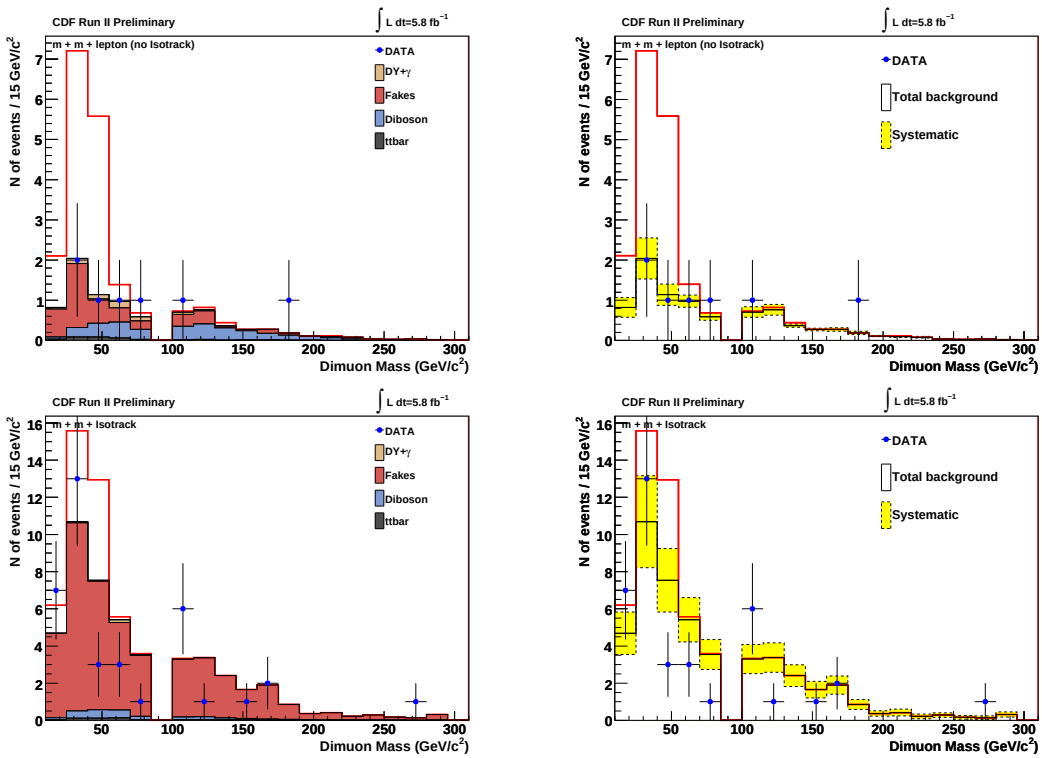

Figure 7.17: Dimuon mass of trilepton events for data and SM prediction in region 9.

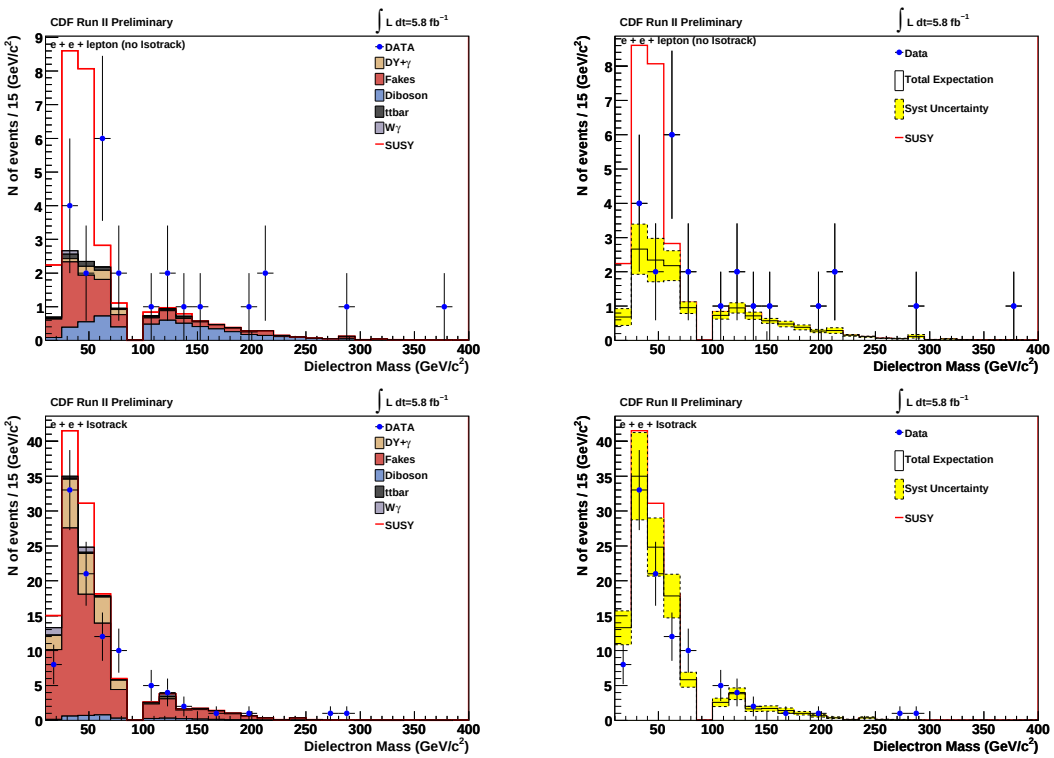

Figure 7.18: Dielectron mass of trilepton events for data and SM prediction in region 9.

7.11 Results

Tables 7.24 and 7.24 show the expected number of background and signal events for $\mu\mu + X$ and $ee + X$ channels respectively. After the signal box was opened, there were 20 events in the $\mu\mu$+lepton channel, 62 events in the $\mu\mu$+IsoTrack channel, 34 events in the ee+lepton channel and 146 events in the ee+IsoTrack channel. The trilepton signal results are interpreted in the mSUGRA model. To determine the acceptance, signal MC was generated in the same way as background and normalized to the PROSPINO [144] NLO production cross section of chargino-neutralino, for both charges of chargino. The branching ratio (BR) to trileptons is determined by using the Les-Houches formatted (SOFTSUSY/SDECAY) [145, 146] spectrum (and BR) generators. This procedure was repeated for all signal MC samples generated for the mSUGRA parameters $m_0 = 60$ GeV/c^2, $\tan\beta = 3$, $A_0 = 0$, and $M_{1/2} = 162 - 280$ GeV/c^2[21], which correspond to lightest chargino masses $M_{\tilde{\chi}_1^\pm} = 97 - 200$ GeV/c^2 and lightest neutralino masses $M_{\tilde{\chi}_1^0} = 55 - 108$ GeV/c^2.

The selection in the variables $M_{\ell\ell}$, $\not\!\!E_T$, and transverse-momenta was optimized individually for each of the above values of $M_{1/2}$ (or $M_{\tilde{\chi}_1^\pm}$ and $M_{\tilde{\chi}_1^0}$). For example, kinematically, a cut-off is expected in the dilepton mass at about $M_{\ell\ell} = M_{\tilde{\chi}_1^\pm} - M_{\tilde{\chi}_1^0}$. Also, the expected signal $\not\!\!E_T$ increases as this difference increases (since it will give higher momentum to the missing LSP). The optimization figure of merit was the ratio of expected signal over expected background. In addition, extra cuts were applied on the lepton transverse momenta and on the other two combinations of dilepton masses; the latter cuts reduce the diboson background. Table 7.28 shows the optimization cuts and table 7.29 shows the expected background, expected chargino-neutralino

[1]Fifteen signal MC samples were generated with the mSUGRA parameters $m_0 = 60$ GeV/c^2, $\tan\beta = 3$, $A_0 = 0$, and $M_{1/2} = 162, 166, 170, 180, 190, 200, 210, 215, 220, 230, 240, 250, 260, 270, 280$. These samples or points were used in the calculation of the limit on the chargino mass.

signal, and observed events in the signal region for the benchmark point ($m_0 = 60$ GeV/c^2, $\tan\beta = 3$, $A_0 = 0$, and $M_{1/2} = 190$ GeV/c^2) for ee+lepton, ee+track, $\mu\mu$+lepton, and $\mu\mu$+track.

Optimization cuts	
$M_{\ell_1\ell_2}$	$> M_{\tilde{\chi}_1^\pm} - M_{\tilde{\chi}_1^0}$
$M_{\ell_1\ell_3}$	< 75 GeV/c^2
$M_{\ell_2\ell_3}$	< 75 GeV/c^2
$\not\!\!E_T$	> 25 GeV
$p_{T,2}$	$(> 8$ and $< 36 - 65)$ GeV/c
$p_{T,3}$	> 8 GeV/c

Table 7.28: The optimization cuts on the three dilepton-mass combinations, $\not\!\!E_T$, and lepton transverse momenta. The leading dilepton mass cut-off cut and second-leading transverse momentum cut are mSUGRA-point dependent.

Optimized Trilepton Yields for Benchmark			
Channel	**SM background**	**SUSY signal**	**Observation**
ee+lepton	1.5 ± 0.4	8.0 ± 0.8	**3**
ee+track	11.6 ± 1.7	7.6 ± 0.8	**13**
$\mu\mu$+lepton	0.5 ± 0.1	6.7 ± 0.7	**0**
$\mu\mu$+track	3.6 ± 1.0	6.2 ± 0.6	**3**

Table 7.29: The optimized trilepton yields in the signal region. The chargino-neutralino signal corresponds to the mSUGRA parameters $m_0 = 60$ GeV/c^2, $\tan\beta = 3$, $A_0 = 0$, and $M_{1/2} = 190$ GeV/c^2

The limit on the chargino mass is determined using a modified frequentist approach (CL_s method) [147, 148] and by treating all the channels independently.

Figure 7.19 shows our upper cross-section 95% CL limit as a function of the chargino mass. Intersection with the NLO theoretical curve gives us the lower chargino mass limit. At 95% CL, we exclude $\sigma(\tilde{\chi}_1^{\pm}\tilde{\chi}_2^0) \times \mathrm{BR}(\ell\ell\ell)$ above 0.1 fb and chargino masses below 168 GeV/c^2 for the mSUGRA parameters $m_0 = 60$ GeV/c^2, $\tan\beta = 3$, $A_0 = 0$.

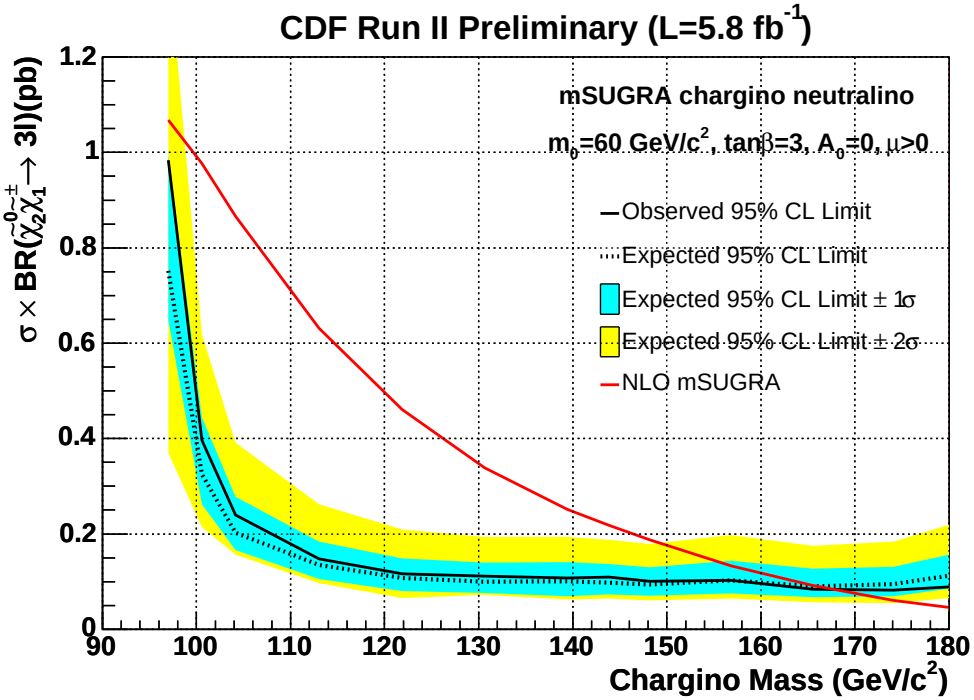

Figure 7.19: Expected and observed limits for the mSUGRA model. The red curve shows the theory cross-section×branching ratio. The black dashed curve shows the expected limit from this analysis with the 1 σ error on the expected limit in cyan and 2 σ in yellow. The solid black curve shows the observed limit. We exclude chargino masses below approximately 168 GeV/c^2 in this specific model.

7.12 Conclusions

Events with multiple, isolated leptons are predicted in many models of physics beyond the Standard Model. In many of these models the leptons are predicted to be produced with low p_T. The "golden" search channel for mSUGRA is the $\chi^{\pm}{}_1\chi^0_2 \to 3\ell$ (three leptons) channel.

We performed a 5.8 fb^{-1} trilepton+$\not\!\!E_T$ search for new physics, the golden Tevatron channel for SUSY searches. The direct LEP2 limit on chargino mass $M_{\chi^{\pm}_1} > 95$ GeV implies that gluinos and most squarks should have masses typically greater than 300 GeV, therefore, strong sparticle production at the Tevatron is expected to be suppressed. On the other hand, $\chi^{\pm}{}_1\chi^0_2$ production is expected to be one of the dominant sparticle production mechanisms, offering a reasonable signal $\sigma \times BR$ to trileptons in the mSUGRA framework, with very small contributions from Standard Model backgrounds.

We used data collected at CDF II from February 2002 through February 2010. Two high-p_T, single-lepton (e/μ) triggered datasets were used to collect mutually exclusive $ee + X$ and $\mu\mu + X$ channels, where X can be an electron, muon, hadronic tau or isolated track. Pursuing our goal of performing a general search for new physics, we expanded our leptonic acceptance geometrically by including the forward parts of the detector, increasing the number of trilepton events by about 50%. We further increased our acceptance kinematically by going as low in p_T as possible ($p_T >$ 5 GeV for most leptons) and by the inclusion of tau leptons decaying hadronically. Although inspired by SUSY, we did not optimize our selection specifically for this theory in order to maximize our discovery potential.

We tested the various background predictions in distinct control regions where the expectation for the signal is negligible relative to the background. These control regions are defined in the $\not\!\!E_T$ vs dilepton mass $M_{\ell\ell}$ space, with the additional re-

quirement of high or low jet multiplicity. The signal region is characterized by three isolated leptons, $\not\!\!E_T > 15$ GeV and at most one high energy jet ($p_T > 20$ GeV). The dominant background at low transverse momentum and invariant mass is the contribution of fake leptons. This background alone comprised roughly between 50% to nearly 100% of the total background expectation in the trilepton control and signal regions. One of the greatest challenges of this analysis was the accurate measurement of lepton fake rates from jet data. We were able to reduce the systematic uncertainty commonly associated with fake lepton estimation from 50% to 20% for low p_T leptons.

After achieving a good understanding of the SM backgrounds in 24 dilepton and 40 trilepton control regions, we observed signal-region results with a slight excess not incompatible with expectation. We interpreted the results in the mSUGRA model, and we set a limit in the chargino-neutralino production cross-section with subsequent decay to trileptons. At 95% CL, we exclude $\sigma(\tilde{\chi}_1^{\pm}\tilde{\chi}_2^0) \times \mathrm{BR}(\ell\ell\ell)$ above 0.1 fb and chargino masses below 168 GeV/c^2.

The conquest of the Terascale will be lead by the LHC, which will be the biggest challenge in the coming years. The work presented in this thesis had two mayor goals: exploring the Tevatron's energy frontier searching for new physics, and the development of analysis techniques which will prove useful to future searches at the LHC. Both goals have been realized in the present work, setting best world exclusion limits and successfully developing and implementing analysis techniques.

References

[1] Mary K. Gaillard, Paul D. Grannis, and Frank J. Sciulli. The standard model of particle physics. Rev. Mod. Phys., 71:S96S111, 1999.

[2] A.D.Martin F. Halzen. Quarks and Leptons: An Introductory Course in Modern Particle Physics. Wiley Text Books, 1984.

[3] David Griffiths. Introduction to Elementary Particles. Wiley, 1987.

[4] K.G. Wilson, Phys. Rev. D10:2445-2459 (1974); G. Altarelli and G. Parisi, Nucl. Phys. B126:298 (1977).

[5] S.L. Glashow, Nucl. Phys. 22, 579-588, 1961; S. Weinberg, Phys. Rev. Lett. 19, 1264-66, 1967; A. Salam, in Elementary Particle Theory, N. Svartholm, ed. (Stockholm: Almquist and Wiksell, 1968).

[6] S. Weinberg, The Quantum Theory of Fields, Vol. II, Cambridge (1995).

[7] C. Quigg, Gauge Theories of the Strong, Weak, and Electromagnetic Interactions, The Benjamin-Cummings Publishing Co., Inc. Canada (1983).

[8] C. Athanassopoulos et al. Evidence for $\nu_\mu \rightarrow \nu_e$ Neutrino oscillations from LSND, Phys. Rev. Lett. 81, 1774-1777 (1998).

[9] W. M. Yao et al. Review of particle physics. J. Phys., G33:11232, 2006.

[10] CDF and D Collaborations. Combination of cdf and D results on the mass of the top quark. hep-ex/0903.2503, 2009.

[11] D. A. Krakauer and R. L. Talaga, Limit on flavor-changing neutral currents from a measurement of neutrino-electron elastic scattering, Phys. Rev. D 45, 975977 (1992).

[12] M. Kobayashi and T. Maskawa, CP Violation in the renormalizable theory of weak interaction, Progr. Theor. Phys. 49, 652-657 (1973).

[13] J. Christenson, J. Cronin, V. Fitch, and R. Turlay Evidence for the 2π decay of the K_2^0 meson Phys. Rev. Lett. 13, 138-140 (1964).

[14] Brian Hatfield Quantum Field Theory of Point Particles and Fields Addison-Weslet, Reading, MA (1992).

[15] R. P. Feynman. Mathematical formulation of the quantum theory of electromagnetic interaction. Phys. Rev., 80:440457, 1950.

[16] Stephen P. Martin A SUPERSYMMETRY PRIMER. hep-ph 9709356 (1999).

[17] UA1 Collaboration, G. Arnison et al., Phys. Lett., B122, 103 (1983).

[18] UA2 Collaboration, M. Banner et al., Phys. Lett., B122, 476 (1983).

[19] R. Keith Ellis, W. James Stirling, and B. R. Webber. Qcd and collider physics. Camb. Monogr. Part. Phys. Nucl. Phys. Cosmol., 8:1435, 1996.

[20] G. Dissertori, I. G. Knowles, and M. Schmelling. High energy experiments and theory. Oxford, UK: Clarendon (2003) 538 p.

[21] P. W. Higgs, Phys. Lett. 12, 132 (1964).

[22] Brian Hatfield Quantum Field Theory of Point Particles and Fields Addison-Weslet, Reading, MA (1992).

[23] Leonard Susskind. Dynamics of spontaneous symmetry breaking in the weinberg- salam theory. Phys. Rev., D20:26192625, 1979.

[24] Hitoshi Murayama. Supersymmetry phenomenology. 2000.

[25] Rudolf Haag, Jan T. Lopuszanski, and Martin Sohnius. All possible generators of supersymmetries of the s matrix. Nucl. Phys., B88:257, 1975.

[26] Robert Nyden Hill and Edward H. Kerner. Unique canonical representation of the inhomogeneous lorentz group in relativistic particle dynamics. Phys. Rev. Lett., 17:1156, 1966.

[27] Joseph Polchinski and Leonard Susskind. Breaking of supersymmetry at intermediate energy. Phys. Rev., D26:3661, 1982.

[28] H. E. Haber, (ed.) Harvey, Jeffrey A., and (ed.) Polchinski, J. Recent directions in particle theory: From superstrings and black holes to the standard model. proceedings, theoretical advanced study institute in elementary particle physics, boulder, usa, june 1-26, 1992. pages 589686. Singapore, Singapore: World Scientific (1993) 827 p.

[29] Edward Witten. Dynamical breaking of supersymmetry. Nucl. Phys., B188:513, 1981.

[30] Romesh K. Kaul. Gauge hierarchy in a supersymmetric model. Phys. Lett., B109:19, 1982.

[31] S. Dawson. The mssm and why it works. 1997.

[32] Savas Dimopoulos and Howard Georgi. Softly broken supersymmetry and SU(5). Nucl. Phys., B193:150, 1981.

[33] N. Sakai. Naturalness in supersymmetric guts. Zeit. Phys., C11:153, 1981.

[34] P. Fayet. Spontaneously broken supersymmetric theories of weak, electromagnetic and strong interactions. Phys. Lett., B69:489, 1977.

[35] Pierre Fayet. Relations between the masses of the superpartners of leptons and quarks, the goldstino couplings and the neutral currents. Phys. Lett., B84:416, 1979.

[36] Steven Weinberg. Supersymmetry at ordinary energies. 1. masses and conservation laws. Phys. Rev., D26:287, 1982.

[37] N. Sakai and Tsutomu Yanagida. Proton decay in a class of supersymmetric grand unified models. Nucl. Phys., B197:533, 1982.

[38] Savas Dimopoulos, Stuart Raby, and Frank Wilczek. Proton decay in supersymmetric models. Phys. Lett., B112:133, 1982.

[39] John R. Ellis, Dimitri V. Nanopoulos, and Serge Rudaz. Nucl. Phys., B202:43, 1982.

[40] F. Zwirner. Observable delta b=2 transitions without nucleon decay in a minimal supersymmetric extension of the standard model. Phys. Lett., B132:103106, 1983.

[41] Gautam Bhattacharyya. R-parity-violating supersymmetric yukawa couplings: A minireview. Nucl. Phys. Proc. Suppl., 52A:8388, 1997.

[42] G. 't Hooft, Phys. Rev. Lett. **37**, 8 (1976).

[43] Glennys R. Farrar and Pierre Fayet. Phenomenology of the production, decay, and detection of new hadronic states associated with supersymmetry. Phys. Lett., B76:575579, 1978.

[44] Lawrence J. Hall and Mahiko Suzuki. Explicit r-parity breaking in supersymmetric models. Nucl. Phys., B231:419, 1984.

[45] John R. Ellis, G. Gelmini, C. Jarlskog, Graham G. Ross, and J.W. F. Valle. Phenomenology of supersymmetry with broken r-parity. Phys. Lett., B150:142, 1985.

[46] Graham G. Ross and J.W. F. Valle. Supersymmetric models without r-parity. Phys. Lett., B151:375, 1985.

[47] Sally Dawson. R-parity breaking in supersymmetric theories. Nucl. Phys., B261:297, 1985.

[48] Savas Dimopoulos and Lawrence J. Hall. Lepton and baryon number violating collider signatures from supersymmetry. Phys. Lett., B207:210, 1988.

[49] H. Goldberg, Phys. Rev. Lett. **50**, 1419 (1983); J. Ellis, J. Hagelin, D.V. Nanopoulos, K. Olive, and M. Srednicki, Nucl. Phys. B **238**, 453 (1984).

[50] Carl E. Carlson, Probir Roy, and Marc Sher. New bounds on r-parity violating couplings. Phys. Lett., B357:99104, 1995.

[51] L. Girardello and M.T. Grisaru Nucl. Phys. B **194**, 65 (1982).

[52] S. Dimopoulos and D. Sutter, Nucl. Phys. B **452**, 496 (1995) [hep-ph/9504415].

[53] J. Ellis and D.V. Nanopoulos, Phys. Lett. B **110**, 44 (1982); R. Barbieri and R. Gatto, Phys. Lett. B **110**, 211 (1982); B.A. Campbell, Phys. Rev. D **28**, 209 (1983).

[54] M. Ciuchini, E. Franco, A. Masiero and L. Silvestrini, Phys. Rev. D **67**, 075016 (2003) [Erratum-ibid. D **68**, 079901 (2003)] [hep-ph/0212397].

[55] P. Langacker, "Precision Tests Of The Standard Model," in Proceedings of the PASCOS90 Symposium, (World Scientific, 1990); J. Ellis, S. Kelley, and D. Nanopoulos, Phys. Lett. B **260**, 131 (1991); U. Amaldi, W. de Boer, and H. Furstenau, Phys. Lett. B **260**, 447 (1991); P. Langacker and M. Luo, Phys. Rev. D **44**, 817 (1991); C. Giunti, C.W. Kim and U.W. Lee, Mod. Phys. Lett. A **6**, 1745 (1991).

[56] M. Dine and W. Fischler, Phys. Lett. B **110**, 227 (1982); C.R. Nappi and B.A. Ovrut, Phys. Lett. B **113**, 175 (1982); L. Alvarez-Gaumé, M. Claudson and M. B. Wise, Nucl. Phys. B **207**, 96 (1982).

[57] M. Dine, A. E. Nelson, Phys. Rev. D **48**, 1277 (1993) [hep-ph/9303230]; M. Dine, A.E. Nelson, Y. Shirman, Phys. Rev. D **51**, 1362 (1995) [hep-ph/9408384]; M. Dine, A.E. Nelson, Y. Nir, Y. Shirman, Phys. Rev. D **53**, 2658 (1996) [hep-ph/9507378].

[58] M. Drees, R. M. Godbole, and P. Roy, Theory and Phenomenology of Sparticles. World Scientific, 2004.

[59] A. Chamseddine, R. Arnowitt, and P. Nath, Phys. Rev. Lett. 49 (1982) 970; R. Barbieri, S. Ferrara, and C. Savoy, Phys. Lett. B 119 (1982) 343; L. J. Hall, J. Lykken, and S. Weinberg, Phys. Rev. D 27 (1983) 2359; for a review, see H. P. Nilles, Phys. Rept. 110 (1984) 1.

[60] K. Fujii, D. J. Miller, and A. Soni, eds., Linear Collider Physics in the new Millenium. World Scientific, 2005.

[61] K. Inoue, A. Kakuto, H. Komatsu and S. Takeshita, Prog. Theor. Phys. 67, 1889 (1982); R.A.Flores and M. Sher, Annals Phys. 148, 95 (1983).

[62] See e.g. E. Lancon, ALEPH Status report talk given at CERN LEPC meeting, November, 1998.

[63] H. Baer, K. Hagiwara, and X. Tata, Phys. Rev. Lett. 57, 294 (1986); Phys. Rev. D 35, 1598 (1987); R. Arnowitt and P. Nath, Mod. Phys. Lett. A 2, 331 (1987); R. Barbieri, F. Caravaglios, M. Frigeni, and M. Mangano, Nucl. Phys. B367, 28 (1991); H. Baer and X. Tata, Phys. Rev. D 47, 2739 (1993); J. Lopez, D. Nanopoulos, X. Wang, and A. Zichichi, ibid. 48, 2062 (1993) H. Baer, C. Kao, and X. Tata, ibid. 48, 5175 (1993); S. Mrenna, G. Kane, G. D. Kribs, and J. D. Wells, ibid. 53, 1168 (1996).

[64] H. Baer, C. H. Chen, C. Kao, and X. Tata, Phys. Rev. D 52, 1565 (1995).

[65] H. Baer, C. H. Chen, F. Paige, and X. Tata, Phys. Rev. D 54, 5866 (1996).

[66] baer:1998) H. Baer, C. H. Chen, M. Drees, F. Paige, and X. Tata, Phys. Rev. Lett. 79, 986 (1997); Phys. Rev. D 58, 075008 (1998).

[67] V. Barger, C. Kao, and T. Li, Phys. Lett. B 433, 328 (1998).

[68] V. Barger and C. Kao, Phys. Rev. D 60, 115015 (1999).

[69] J. Lykken and K. Matchev, Phys. Rev. D 61, 015001 (2000); K. Matchev and D. Pierce, ibid. 60, 075004 (1999).

[70] H. Baer, M. Drees, F. Paige, P. Quintana and X. Tata, Phys. Rev. D 61 (2000) 095007.

[71] A. Bartl, H. Fraas and W. Majerotto, Nucl. Phys. B **278**, 1 (1986); Z. Phys. C **30**, 441 (1986); Z. Phys. C **41**, 475 (1988); A. Bartl, H. Fraas, W. Majerotto and B. Mösslacher, Z. Phys. C **55**, 257 (1992). For large $\tan\beta$ results, see H. Baer, C.-h. Chen, M. Drees, F. Paige and X. Tata, Phys. Rev. Lett. **79**, 986 (1997) [hep-ph/9704457].

[72] H.E. Haber and D. Wyler, Nucl. Phys. B **323**, 267 (1989); S. Ambrosanio and B. Mele, Phys. Rev. D **55**, 1399 (1997) [Erratum-ibid. D **56**, 3157 (1997)] [hep-ph/9609212]; S. Ambrosanio et al., Phys. Rev. D **55**, 1372 (1997) [hep-ph/9607414].

[73] H. Baer, K. Hagiwara, and X. Tata, Phys. Rev. Lett. 57, 294 (1986).

[74] Fermilab Beams Division, Run II Handbook.

[75] Fermilab Beams Division, Fermilab Linac Upgrade. Conceptual Design.

[76] Fermilab Beams Division, The Booster rookie book.

[77] Fermilab Beams Division, The Main Injector rookie book.

[78] Fermilab Beams Division, Recycler design report. FERMILAB-TM-1991.

[79] Fermilab Beams Division, The antiproton source rookie book.

[80] Fermilab Beams Division, Another antiproton source rookie book.

[81] Fermilab Beams Division, The Tevatron rookie book.

[82] Fermilab Beam Division. Run II Handbook.
http://www-bd.fnal.gov/runII/index.html.

[83] CDF Collaboration, The CDF II detector. Technical design report. FERMILAB-Pub-96/390-E, (1996).

[84] J. Bjorken and E. Paschos, Inelastic $e-p$ and $\gamma-p$ scattering and the structure of the nucleon. Phys. Rev. 175(1975).

[85] D. Amidei et al, The Silicon Vertex Detector of the Collider Detector at Fermilab. NIMPR A350,73 (1994).

[86] Chris Hays, et al, The COT Pattern Recognition Algorithm and Offline Code. CDF note 6992.

[87] F. Abe at al. Phys. Rev. D50 (1994) 2296.

[88] G. Acolli et al. The CDF central muon detector. Nucl. Instr. & Meth., Volume A, 268, 63-67 (1988).

[89] CDF Collaboration, The 1992 CDF muon system upgrade. CDF Note 2858 (1994).

[90] J.D. Jackson Classical Electrodynamics. John Wiley and Sons, 1999, pg. 715.

[91] CDF Collaboration Proposal for Enhancement of the CDFII Detector: An Inner Silicon Layer and A Time of Flight Detector. http://www-cdf.fnal.gov/upgrades/PAC/p909.ps.

[92] CDF Collaboration Update to Proposal P-909: Physics Performance of the CDFII Detector with An Inner Silicon Layer and A Time of Flight Detector. http://www-cdf.fnal.gov/upgrades/btb update jan99.ps.

[93] CDF Collaboration Luminosity Monitor Based on Cherenkov Counters for P Anti-P Colliders. Nucl. Instr. & Meth., Volume A, 441, 366-373 (2000).

[94] CDF Collaboration The CDF Run II Luminosity Monitor. Nucl. Instr. & Meth., Volume A, 461, 540-544 (2001).

[95] D. Acosta et al. The performance of the CDF luminosity monitor. Nucl. Instrum. Meth., A 494:5762, 2002.

[96] F. Abe et al. Measurement of the pp total cross-section at $\sqrt{s} = 546$ GeV and 1800 GeV. Phys. Rev., D50:55505561, 1994.

[97] S. Klimenko, J. Konigsberg, and Tony M. Liss. Averaging of the inelastic cross sections measured by the CDF and the E811 experiments. FERMILAB-FN-0741.

[98] S. Jundariani et al. Luminosity uncertainty for Run II up until August 2004. CDF/ANA/7446, 2005.

[99] M. Shimojima et al. CONSUMER-SERVER/LOGGER SYSTEM FOR THE CDF EXPERIMENT. IEEE Trans. Nucl. Sci. Vol 47, page 236 (2000).

[100] H. Frisch et al. Conceptual Design of a Deadtimeless Trigger for the CDF Trigger Upgrade. CDF Note 2034 (1994).

[101] K. Anikeev et al. Event Builder and Level-3 for aces. CDF Note 5793, (2001).

[102] The Trigger and Datasets Working Group. Run II trigger table and datasets plan. CDF/PHYS/TRIGGER/CDFR/4718, 2001.

[103] PerfIDia, http://ncdf70.fnal.gov:8001/PerfIDia/PerfIDia.html.

[104] J. Goldstein et al., Silicon Tracking for Plug Electrons. CDF Note 5970 (2002).

[105] Andrew G. Ivanov, Search for Anomalous Kinematics of Top Dilepton Events in $p\bar{p}$ Collisions at $\sqrt{s} = 1.96$ TeV. Ph.D. thesis. University of Rochester (2004).

[106] A. Anastassov et al., Search for neutral MSSM Higgs boson(s) in the $\tau\tau$ decay channel. CDF Note 7622 (2005).

[107] A. Anastassov, Non-isolated π^0/γ reconstruction. CDF Note 6688 (2003).

[108] C.DeBenedetti, P.Murat, Y.Tu, Identication of the hadronic tau decays: improved electron rejection. CDF internal note 9002.

[109] Martin Griffiths, Beate Heinemann, Giulia Manca. Measurement of the Fake Rate of Electrons and Muons. CDF internal note 7470.

[110] Yanjun Tu, Pavel Murat. Monte Carlo modelling of the jet$\rightarrow \tau_h$ fake rates. CDF internal note 8809.

[111] P. Totaro, M. Rossi, A.M. Zanetti. A new Tau Identification Algorithm Based on a Boosted Decision Tree Method. CDF internal note 9667.

[112] Shih-Chieh Hsu, Elliot Lipeles, Kevin McCarthy, Mark Neubauer, Frank Wurthwein. Lepton ID and Fake Rates for the WW and WZ Analyses. CDF internal note 8093.

[113] Mircea Coca, Andrew Ivanov, Ricardo Eusebi, Eva Halkiadakis. An Alternate Determination of the Fake Lepton Background for the Summer 2003 Top Dilepton Cross Section Analysis. CDF internal note 6742.

[114] Shan-Huei S.Chuang, Mircea Coca, Mark Kruse. Lepton Fake Estimate Using 320 pb^{-1} CDF Run II Data. CDF internal note 7497.

[115] P. Murat. W $\rightarrow \tau\nu$ Cross Section Measurement: parametrization of the jet $\rightarrow \tau$ fake rates. CDF internal note 6887.

[116] Anton Anastassov, John Conway, Dongwook Jang, Amit Lath, Fedor Ratnikov, Zongru Wan. Tau Reconstruction Efficiency and QCD Fake Rate for Run 2. CDF internal note 6308.

[117] Toru Okusawa, Yoshihiro Seiya, Takayuki Wakisaka and Kazuhiro Yamamoto. Study of Fake-Lepton Rates for the High-P_T Like-Sign Dilepton Analysis to Search for the Wh Production. CDF internal note 9239.

[118] H. Baer, M. Drees, F. Paige, P. Quintana and X. Tata, Phys. Rev. D 61 (2000) 095007.

[119] G. R. Farrar and P. Fayet, Phys. Lett. B 76, 575 (1978).

[120] Report of the SUGRA working group for run II of the Tevatron, arXiv:hep-ph/0003154.

[121] J. Ellis, S. Kelley, and D. Nanopoulos, Phys. Lett. B 260 (1991)131; P. Langacker and M. Luo, Phys. Rev. D 44 (1991) 817; U. Amaldi,W. deBoer, and H. Furstenau, Phys. Lett. B 260(1991) 447; M. Carena, S. Pokorski, and C. Wagner, Nucl. Phys. B 406 (1993) 59; P. Langacker and N. Polonsky, Phys. Rev. D 47 (1993) 4028.

[122] Report of the SUGRA working group for run II of the Tevatron, arXiv:hep-ph/0003154.

[123] Searching for R-parity violation at Run-II of the Tevatron, arXiv:hep-ph/9906224.

[124] CDF Collaboration, Phys. Rev. Lett. **99**, 191806 (2007).

[125] CDF Collaboration, Phys. Rev. Lett. **101**, 251801 (2008).

[126] CDF public note 9817 (2009).

[127] PerfIDia, http://ncdf70.fnal.gov:8001/PerfIDia/PerfIDia.html.

[128] Efficiency of the Z-vertex cut of 60 cm for data, http://www-cdf.fnal.gov/internal/physics/joint_physics/instructions/zvertex-efficiency.html.

[129] H. L. Lai et al. Global QCD analysis of parton structure of the nucleon: CTEQ5 parton distributions. Eur. Phys. J., C12:375392, 2000.

[130] R. Brun et al. GEANT 3 manual, CERN Program Library Long Writeup. 1994.

[131] http://www-cdf.fnal.gov/internal/physics/ewk/ewkII.html.

[132] A. Attal, A. Canepa, hoton Conversion Removal Efficiency, CDF 8073.

[133] M. Gold, V. Rekovic, Low p_T Muon Isolation Efficiency and Scale Factors, CDF 7432.

[134] M. Gold, V. Rekovic, Low p_T Muon ID efficiencies and Scale Factors for Exotics Searches, CDF 7210.

[135] M. Gold, V. Rekovic, J. Strologas, Low p_T Muon ID Efficiencies in gen6 Data for Exotic Searches, CDF 8307.

[136] S. Dube, J. Zhou, S. Somalwar, Low E_T electron ID efficiency and scale-factors using J/Ψ, CDF 7379.

[137] S. Dube, J. Zhou, S. Somalwar, Medium ET electron identification efficiency and scale-factors, CDF 8321.

[138] A. Attal, ID Efficiencies for Medium E_T Plug Electrons, CDF 7345.

[139] M. Gold, J. Strologas, M. Vogel, Measurement of fake rates for electrons, muons and tau leptons, CDF 10413.

[140] G. Manca, M. Griffiths, B. Heinemann, Searches for Chargino and Neutralino in the e+e/μ+e/μ with 1 fb^{-1} of data, CDF 8389.

[141] S. Dube, J. Glatzer, A. Sood, S. Somalwar, CDF 9097, Unified Search for Chargino-Neutralino Production with 2 fb^{-1}.

[142] CDF Collaboration, Phys. Rev. D **79**, 052004 (2009).

[143] CDF Collaboration, Phys. Rev. Lett. **102**, 031801 (2009).

[144] W. Beenakker *et al.* Phys. Rev. Lett. 83, 3780 (1999).

[145] B. C. Allanach, Comput. Phys. Commun. 143, 305 (2002), arXiv:hep-ph/0104145.

[146] M. Muhlleitner, A. Djouadi, Y. Mambrini, Comput. Phys. Commun. 168, 46 (2005), arXiv:hep-ph/0311167.

[147] T. Junk, Nucl. Instrum. Methods, Volume A 434, 435 (1999).

[148] A. Read, J. Phys. G, 28, 2693 (2002).

[149] P. Fayet and J. Iliopoulos, Phys. Lett. B **51**, 461 (1974); P. Fayet, Nucl. Phys. B **90**, 104 (1975).

[150] L. O'Raifeartaigh, Nucl. Phys. B **96**, 331 (1975).

[151] J. Wess and B. Zumino, Nucl. Phys. B **70** (1974) 39.

[152] P. Nath and R. Arnowitt, Phys. Lett. B **56**, 177 (1975); R. Arnowitt, P. Nath and B. Zumino, Phys. Lett. B **56**, 81 (1975); S. Ferrara, D.Z. Freedman and P. van Nieuwenhuizen, Phys. Rev. D **13**, 3214 (1976); S. Deser and B. Zumino, Phys. Lett. B **62**, 335 (1976); D.Z. Freedman and P. van Nieuwenhuizen, Phys. Rev. D **14**, 912 (1976); E. Cremmer et al., Nucl. Phys. B **147**, 105 (1979); J. Bagger, Nucl. Phys. B **211**, 302 (1983).

[153] E. Cremmer, S. Ferrara, L. Girardello, and A. van Proeyen, Nucl. Phys. B **212**, 413 (1983).

[154] A.H. Chamseddine, R. Arnowitt and P. Nath, Phys. Rev. Lett. **49**, 970 (1982); R. Barbieri, S. Ferrara and C. A. Savoy, Phys. Lett. B **119**, 343 (1982); L.E. Ibáñez, Phys. Lett. B **118**, 73 (1982); L.J. Hall, J.D. Lykken and S. Weinberg, Phys. Rev. D **27**, 2359 (1983); N. Ohta, Prog. Theor. Phys. **70**, 542 (1983).

[155] J. Ellis, D.V. Nanopoulos and K. Tamvakis, Phys. Lett. B **121**, 123 (1983); L. Alvarez-Gaumé, J. Polchinski, and M. Wise, Nucl. Phys. B **221**, 495 (1983).

[156] J. Glatzer. Probing mSUGRA with a Search for Chargino-Neutralino Production using Trileptons. FERMILAB-MASTERS-2008.

[157] ALEPH, DELPHI, L3, OPAL Collaborations, G. Abbiendi, et al., (The LEP Working Group for Higgs Boson Searches), Phys. Lett. B 565, 61 (2003).

[158] K. Nakamura et al. [Particle Data Group], J. Phys. G 37, 075021 (2010).

[159] E. Komatsu et al. [WMAP Collaboration], Astrophys. J. Suppl. 192, 18 (2011).[arXiv:1001.4538 [astro-ph.CO]].

[160] K. Abe et al. (Belle Collaboration), Phys. Lett. B 511 (2001) 151.

[161] D. Cronin-Hennessy et al. (Cleo Collaboration), Phys. Rev. Lett. 87 (2001) 251808.

[162] R. Barate et al. (Aleph Collaboration), Phys. Lett. B 429 (1998) 169.

[163] A. Ali and C. Greub, Phys. Lett. B 259, 182 (1991); Z. Phys. C 60, 433 (1993); A. Buras et al. , Nucl. Phys. B370, 69 (1992); B375, 501 (1992); B400, 37 (1993); B400 75 (1993); M. Ciuchini et a/. , Phys. Lett. B 301, 263 (1993); Nucl. Phys. B415, 403 (1994).

[164] Final report of the E821 muon anomalous magnetic moment measurement at BNL. Phys. Rev. D 73, 072003 (2006).

[165] Jegerlehner F, Nyffeler A. Phys. Rept., 2009, 477: 1.

[166] Davier M et al. arXiv:0908.4300.

[167] Davier M. These proceedings, arXiv:1001.2243.

[168] Davier M et al. arXiv:0906.5443.

[169] Update of g-2 of the muon and Delta alpha. T. Teubner, K. Hagiwara, R. Liao, A. D. Martin, Daisuke Nomura. arXiv:1001.5401.

[170] $B_s \to \mu^+\mu^-$in Supersymmetric Grand Unified Theories. Bhaskar Dutta, (Texas A-M) , Yukihiro Mimura, Yudi Santoso, (Taiwan, Natl. Taiwan U.) . MIFPA-11-30, Jul 2011. 15pp. e-Print: arXiv:1107.3020 [hep-ph].

[171] G. Buchalla and A. J. Buras, Nucl. Phys. B 400, 225 (1993); A. J. Buras, Phys. Lett. B 566, 115 (2003) [hep-ph/0303060].

[172] E. Gamiz, C. T. H. Davies, G. P. Lepage, J. Shigemitsu and M. Wingate [HPQCD Collaboration], Phys. Rev. D 80, 014503 (2009) [arXiv:0902.1815 [hep-lat]].

[173] CDF Collaboration, arXiv:1107.2304 [hep-ex].

[174] Collider, direct and indirect detection of supersymmetric dark matter. Howard Baer, (Oklahoma U.), Eun-Kyung Park, (Bonn U.), Xerxes Tata, (Hawaii U.). Mar 2009. 28pp. New J.Phys.11:105024,2009. e-Print: arXiv:0903.0555 [hep-ph].

[175] H. Goldberg, Phys. Rev. Lett. 50 (1983) 1419; J. Ellis et al. Nucl. Phys. B 238 (1984) 453; P. Nath and R. Arnowitt, Phys. Rev. Lett. 70 (1993) 3696; H. Baer and M. Brhlik, Phys. Rev. D 53 (1996) 597; V. Barger and C. Kao, Phys. Rev. D 57 (1998) 3131.

[176] J. Ellis, T. Falk and K. Olive, Phys. Lett. B 444 (1998) 367; J. Ellis, T. Falk, K. Olive and M. Srednicki, Astropart. Phys. 13 (2000) 181; M.E. Gomez, G. Lazarides and C. Pallis, Phys. Rev. D 61 (2000) 123512 and Phys. Lett. B 487 (2000) 313; A. Lahanas, D. V. Nanopoulos and V. Spanos, Phys. Rev. D 62 (2000) 023515; R. Arnowitt, B. Dutta and Y. Santoso, Nucl. Phys. B 606 (2001) 59.

[177] K. L. Chan, U. Chattopadhyay and P. Nath, Phys. Rev. D 58 (1998) 096004; J. Feng, K. Matchev and T. Moroi, Phys. Rev. Lett. 84 (2000) 2322 and Phys. Rev. D 61 (2000) 075005; see also H. Baer, C. H. Chen, F. Paige and X. Tata, Phys. Rev. D 52 (1995) 2746 and Phys. Rev. D 53 (1996) 6241; H. Baer, C. H. Chen, M. Drees, F. Paige and X. Tata, Phys. Rev. D 59 (1999) 055014; for a model-independent approach, see H. Baer, T. Krupovnickas, S. Profumo and P. Ullio, J. High Energy Phys. 0510 (2005) 020.

[178] M. Drees and M. Nojiri, Phys. Rev. D 47 (1993) 376; H. Baer and M. Brhlik, Phys. Rev. D 57 (1998) 567; H. Baer, M. Brhlik, M. Diaz, J. Ferrandis, P. Mercadante, P. Quintana and X. Tata, Phys. Rev. D 63 (2001) 015007; J. Ellis, T. Falk, G. Ganis, K. Olive and M. Srednicki, Phys. Lett. B 510 (2001) 236; L. Roszkowski, R. Ruiz de Austri and T. Nihei, J. High Energy Phys. 0108 (2001) 024; A. Djouadi, M. Drees and J. L. Kneur, J. High Energy Phys. 0108 (2001) 055; A. Lahanas and V. Spanos, Eur. Phys. J. C 23 (2002) 185.

[179] R. Arnowitt and P. Nath, Phys. Rev. Lett. 70 (1993) 3696; H. Baer and M. Brhlik, Ref. [175]; A. Djouadi, M. Drees and J. Kneur, Phys. Lett. B 624 (2005) 60.

[180] C. Böhm, A. Djouadi and M. Drees, Phys. Rev. D 62 (2000) 035012; J. R. Ellis, K. A. Olive and Y. Santoso, Astropart. Phys. 18 (2003) 395; J. Edsjö, et al., JCAP 0304 (2003) 001.

Appendices

Appendix A

Plug electron ID and tracking scale factors

We measured our own identification and reconstruction (tracking) scale factors for PEM and Phoenix electrons for periods 0 through 28 of data. Plug electrons are selected in data and MC from $Z \rightarrow e^+e^-$ events with one electron passing all the tight central cuts of Table 5.1 and the other electron in the plug calorimeter. The datasets used were bhelb for data and the electroweak DY sample ze0sdd. The total ID efficiency ϵ_{ID} is defined by the following formula:

$$\epsilon_{ID} = \frac{N_{TP}}{N_{TC}},$$

Where N_{TP} is the number of events with one tight central electron and one plug calorimeter cluster passing all of the PEM or Phoenix ID cuts, while N_{TC} is the number of events with one tight central electron and a plug calorimeter cluster as defined in [138]. The plug cluster efficiency, tracking or reconstruction efficiency ϵ_{PC} is defined by the following formula:

$$\epsilon_{PC} = \frac{N_{TC}}{N_{TE}},$$

Where N_{TC} is the number of events with one tight central electron and one plug calorimeter cluster, while N_{TE} is the number of events with one tight central electron and a plug Em object. The scale factors obtained from calculating the ID and tracking efficiencies for PEM and Phoenix electrons are listed in Table A.1.

	PEM		PHOENIX	
Period	ID	Tracking	ID	Tracking
0	0.949339	0.950057	0.961569	0.958429
1	0.961944	0.948618	0.969894	0.981503
2	0.968893	0.944098	0.940459	0.982515
3	0.966833	0.929439	0.936875	0.933489
4	0.958369	0.9285	0.94435	0.976958
5	0.963365	0.937965	0.932989	1.02725
6	0.942301	0.926863	0.932334	0.981212
7	0.95391	0.958012	0.937148	0.999186
8	0.950263	0.906984	0.934381	0.980638
9	0.937532	0.906779	0.944052	0.99648
10	0.935623	0.883392	0.905517	0.981089
11	0.92178	0.866638	0.916955	0.957246
12	0.944192	0.881895	0.941645	0.973274
13	0.903183	0.683259	0.983855	1.06912
14	0.975906	0.866162	0.951307	1.00134
15	0.917181	0.859814	0.90127	1.00162
16	0.932798	0.852184	0.877883	1.00731
17	0.906677	0.802496	0.902006	0.960109
18	0.922454	0.76756	0.888944	1.03043
19	0.913418	0.773467	0.880839	1.0097
20	0.908271	0.766429	0.896297	1.04706
21	0.917358	0.739998	0.885852	1.04574
22	0.92478	0.739998	0.874887	1.01541
23	0.92203	0.744559	0.890275	1.05092
24	0.898782	0.713172	0.862861	1.02758
25	0.91039	0.726104	0.884546	1.02136
26	0.919729	0.750415	0.876021	1.01757
27	0.920694	0.737913	0.883611	1.01598
28	0.914205	0.762673	0.885247	1.02165

Table A.1: ID and tracking scale factor for PEM electrons.

Appendix B

Primary vertex multiplicity and re-weighted Drell-Yan MC

In order to account for the effects of higher instantaneous luminosities (e.g., "pile up"), the DY MC was re-weighted so that the shape of the distribution of primary vertex multiplicity would be the same in data and MC. Histograms of this variable were made in data and DY MC in the region of the Z boson resonance. The histograms were normalized to unity and the contents of each bin were used to calculate a ratio of observation to expectation, thus defining a re-weighing function which depends on the number of vertices in the event. This weight was then applied to the MC sample as $\mathrm{w(n)} = \mathrm{obs}_{norm}/\mathrm{exp}_{norm}$, where n is the number of primary vertices.

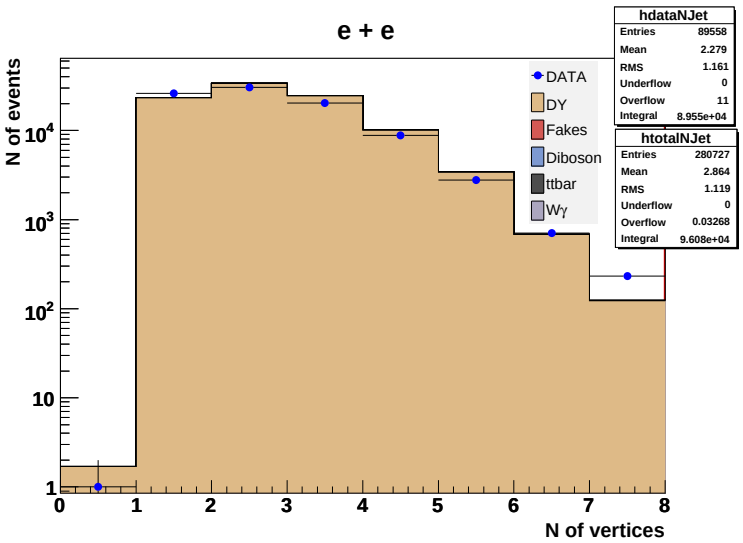

Figure B.1: DY MC is re-weighted such that the distributions of primary vertex multiplicity of data and MC have the same shape in the Z peak.

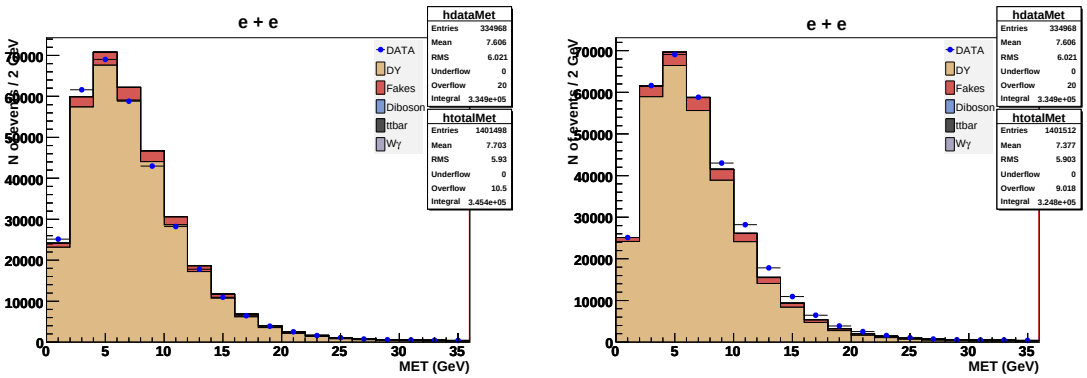

Figure B.2: Dielectron $\not\!\!E_T$ distribution. Left plot: DY is scaled according to the number of primary vertices in the event. Right plot: DY is not scaled.

Appendix C

Tables of Yields

The expected and observed yields for all control regions are summarized in Tables C.1 through C.6. Tables C.1 and C.4 correspond to dimuon and dielectron events respectively. Trileptons are separated into four groups: $\mu\mu(ee) + \ell$, where $\ell = \mu, e$ or τ (Tables C.2,C.5), and $\mu\mu(ee)$ + isolated track (Tables C.3, C.6). The error in the expectation corresponds to the total systematic uncertainty in the background estimation, which is calculated using the values listed in section 7.8. Figures C.1 through C.6 show the ratio of the observation over the expectation for each control region, which is calculated using the yields listed in the corresponding tables. The error bars for each point represent the statistical and systematic uncertainty in the background estimation added in quadrature.

Table of dimuon yields						
	Drell-Yan	**Fakes**	**Diboson**	**Top**	**Total SM**	**Observed**
Region0	114498 ± 11454	226 ± 113	75 ± 8	1.8 ± 0.2	114802 ± 11455	**115884**
Region1	7926 ± 802	38 ± 19	72 ± 7	3.6 ± 0.4	8039 ± 802	**7272**
Region2	319 ± 40	1.6 ± 0.8	8.8 ± 0.9	12 ± 1	341 ± 40	**308**
Region3	12171 ± 1218	70 ± 35	9.7 ± 1	0.33 ± 0.04	12251 ± 1218	**12729**
Region4	170 ± 18	2 ± 1	3.4 ± 0.3	1.1 ± 0.1	177 ± 18	**199**
Region5	100913 ± 10100	152 ± 76	30 ± 3	0.08 ± 0.01	101095 ± 10100	**101740**
Region6	1244 ± 132	3 ± 1	32 ± 3	0.31 ± 0.04	1279 ± 132	**1216**
Region7	1170 ± 118	273 ± 136	118 ± 12	14 ± 1	1575 ± 181	**1610**
Region8	36 ± 4	9 ± 5	3.7 ± 0.4	41 ± 4	89 ± 7	**125**
Region9	366 ± 37	258 ± 129	113 ± 11	53 ± 5	790 ± 135	**808**
Region10	145635 ± 14572	245 ± 123	202 ± 20	21 ± 2	146103 ± 14573	**142386**
Region11	163932 ± 16397	728 ± 364	364 ± 36	98 ± 10	165122 ± 16401	**162127**

Table C.1: Dilepton Control Regions: $\mu\mu$ (all signs)

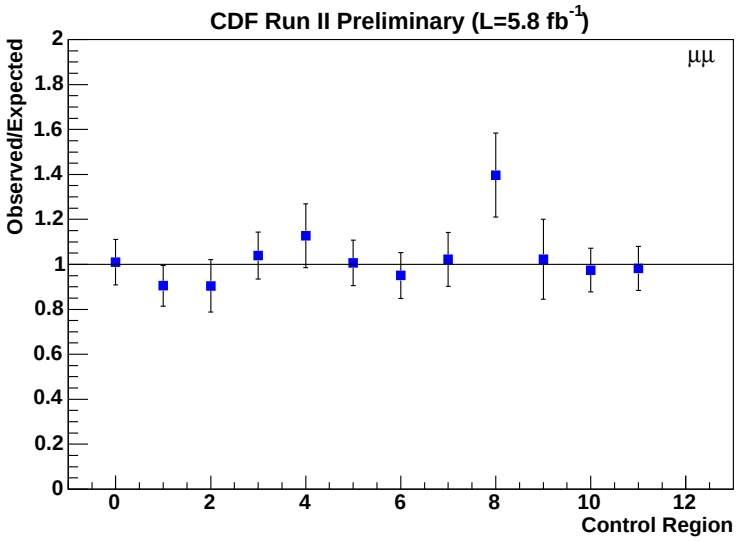

Figure C.1: Summary of control regions: Observation/Expectation for dimuon events. The error bars represent the statistical and systematic uncertainty in the background estimation added in quadrature.

Table of $\mu\mu$+lepton yields						
	Drell-Yan	**Fakes**	**Diboson**	**Top**	**Total SM**	**Observed**
Region0	115 ± 12	126 ± 35	3.1 ± 0.3	0.019 ± 0.007	244 ± 37	**254**
Region1	2.8 ± 0.3	19 ± 6	8.8 ± 0.9	0.043 ± 0.01	30 ± 6	**26**
Region2	0.08 ± 0.02	1 ± 0.4	0.18 ± 0.02	0.035 ± 0.009	1.3 ± 0.4	**3**
Region3	58 ± 6	26 ± 8	0.64 ± 0.07	0.015 ± 0.006	85 ± 10	**94**
Region4	0.37 ± 0.07	0.5 ± 0.2	0.027 ± 0.004	0.004 ± 0.003	0.9 ± 0.2	**0**
Region5	56 ± 6	98 ± 26	2.4 ± 0.2	0 ± 0	156 ± 27	**156**
Region6	0.56 ± 0.09	2.3 ± 0.7	0.11 ± 0.01	0 ± 0	3 ± 0.7	**4**
Region7	2.8 ± 0.3	7 ± 2	3.4 ± 0.3	0.24 ± 0.03	13 ± 2	**20**
Region8	0.1 ± 0.03	0.4 ± 0.1	0.08 ± 0.01	0.14 ± 0.02	0.7 ± 0.1	**0**
Region9	0.7 ± 0.1	4 ± 1	3.2 ± 0.3	0.37 ± 0.05	9 ± 1	**7**
Region10	77 ± 8	170 ± 49	15 ± 2	0.09 ± 0.02	262 ± 49	**274**
Region11	156 ± 16	224 ± 65	22 ± 2	0.66 ± 0.07	402 ± 67	**435**

Table C.2: Trilepton Control Regions: $\mu\mu + \ell$(no isolated tracks)

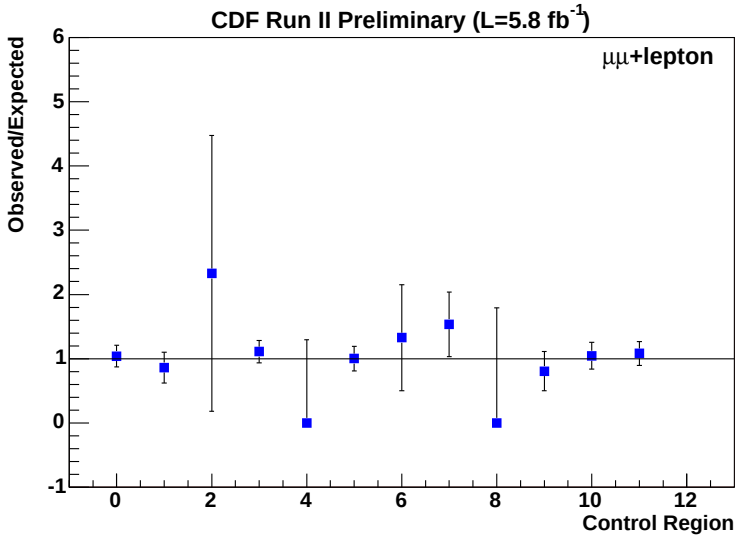

Figure C.2: Summary of control regions: Observation/Expectation for $\mu\mu + \ell$(no isolated tracks). The error bars represent the statistical and systematic uncertainty in the background estimation added in quadrature.

Table of $\mu\mu$+IsoTrack yields						
	Drell-Yan	Fakes	Diboson	Top	Total SM	Observed
Region0	27 ± 3	695 ± 140	1.5 ± 0.1	0.016 ± 0.006	723 ± 140	**641**
Region1	1.6 ± 0.2	169 ± 38	3.3 ± 0.3	0.033 ± 0.009	174 ± 38	**183**
Region2	0.03 ± 0.01	12 ± 3	0.28 ± 0.03	0.14 ± 0.02	12 ± 3	**16**
Region3	10 ± 1	128 ± 26	0.16 ± 0.02	0.005 ± 0.003	139 ± 26	**116**
Region4	0.17 ± 0.04	5 ± 1	0.059 ± 0.008	0.009 ± 0.004	6 ± 1	**8**
Region5	17 ± 2	540 ± 109	0.68 ± 0.07	0 ± 0	557 ± 109	**498**
Region6	0.32 ± 0.06	21 ± 4	0.55 ± 0.06	0.002 ± 0.002	22 ± 4	**19**
Region7	1 ± 0.1	65 ± 15	2.2 ± 0.2	0.19 ± 0.03	68 ± 15	**62**
Region8	0.06 ± 0.02	5 ± 1	0.1 ± 0.01	0.47 ± 0.06	5 ± 1	**2**
Region9	0.36 ± 0.06	45 ± 10	2.2 ± 0.2	0.64 ± 0.07	48 ± 10	**38**
Region10	25 ± 3	1151 ± 238	7.3 ± 0.7	0.24 ± 0.03	1184 ± 238	**1221**
Region11	43 ± 4	1463 ± 303	12 ± 1	1.2 ± 0.1	1518 ± 303	**1560**

Table C.3: Trilepton Control Regions: $\mu\mu$ + isolated track

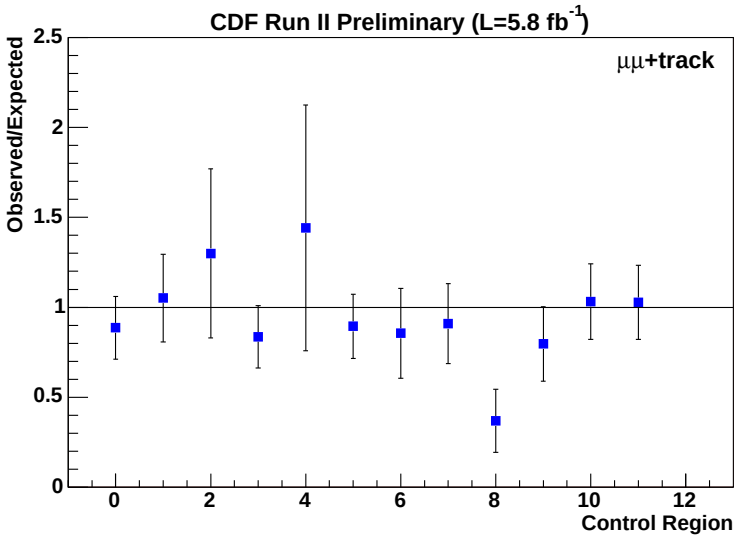

Figure C.3: Summary of control regions: Observation/Expectation for $\mu\mu$ + isolated track. The error bars represent the statistical and systematic uncertainty in the background estimation added in quadrature.

Table of dielectron yields							
	Drell-Yan	**Fakes**	**Diboson**	**Wγ**	**Top**	**Total SM**	**Observed**
Region0	251266 ± 25133	12261 ± 4234	124 ± 12	12 ± 2	2.6 ± 0.3	263666 ± 25500	**257588**
Region1	9942 ± 1004	387 ± 172	103 ± 10	35 ± 5	5.2 ± 0.5	10472 ± 1033	**10077**
Region2	359 ± 43	22 ± 9	11 ± 1	0.7 ± 0.5	16 ± 2	407 ± 46	**506**
Region3	29663 ± 2969	7711 ± 2139	16 ± 2	11 ± 2	0.49 ± 0.06	37401 ± 3661	**36538**
Region4	396 ± 45	285 ± 80	5.5 ± 0.5	0 ± 0	1.5 ± 0.2	688 ± 92	**727**
Region5	218481 ± 21856	4191 ± 1985	49 ± 5	0.9 ± 0.5	0.13 ± 0.02	222722 ± 21950	**217846**
Region6	2726 ± 280	74 ± 30	54 ± 5	0 ± 0	0.45 ± 0.05	2855 ± 287	**2477**
Region7	2203 ± 226	2152 ± 524	165 ± 16	360 ± 37	19 ± 2	4898 ± 594	**4909**
Region8	66 ± 11	136 ± 38	4.9 ± 0.5	3.2 ± 0.9	56 ± 6	265 ± 42	**338**
Region9	764 ± 83	1620 ± 382	157 ± 16	339 ± 35	72 ± 7	2952 ± 406	**3270**
Region10	263448 ± 26353	4891 ± 2309	282 ± 28	20 ± 3	28 ± 3	268670 ± 26486	**260010**
Region11	324059 ± 32412	20218 ± 6638	527 ± 53	472 ± 48	134 ± 13	345410 ± 33196	**334968**

Table C.4: Dilepton Control Regions: *ee* (all signs)

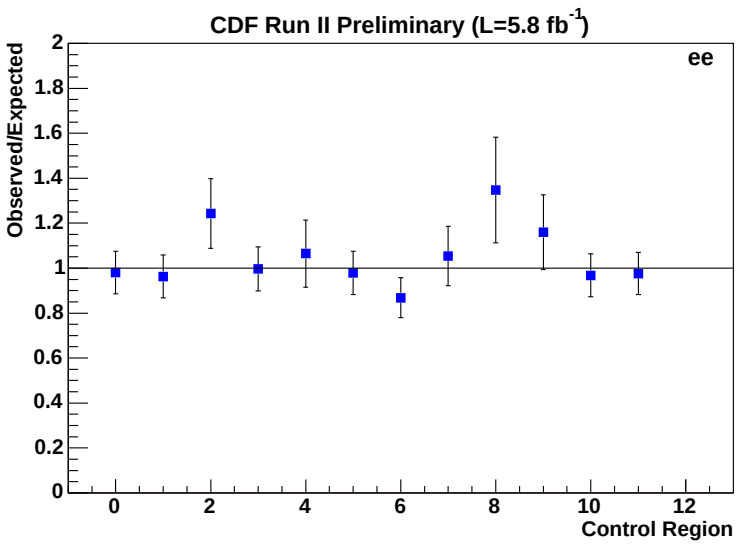

Figure C.4: Summary of control regions: Observation/Expectation for *ee* (all signs). The error bars represent the statistical and systematic uncertainty in the background estimation added in quadrature.

Table of ee+lepton yields							
	Drell-Yan+γ	Fakes	Diboson	Wγ	Top	Total SM	Observed
Region0	174 ± 17	226 ± 63	5.2 ± 0.5	0 ± 0	0.041 ± 0.009	406 ± 65	**434**
Region1	2.4 ± 0.3	21 ± 7	13 ± 1	0.2 ± 0.2	0.13 ± 0.02	37 ± 7	**35**
Region2	0.13 ± 0.03	1.4 ± 0.5	0.26 ± 0.03	0 ± 0	0.06 ± 0.01	1.8 ± 0.5	**4**
Region3	86 ± 9	59 ± 18	1.9 ± 0.2	0 ± 0	0.026 ± 0.007	147 ± 20	**165**
Region4	0.51 ± 0.07	1.2 ± 0.4	0.075 ± 0.009	0 ± 0	0.008 ± 0.004	1.8 ± 0.4	**4**
Region5	87 ± 9	161 ± 43	3.1 ± 0.3	0 ± 0	0.002 ± 0.002	251 ± 44	**257**
Region6	0.77 ± 0.1	5 ± 1	0.15 ± 0.02	0 ± 0	0.005 ± 0.003	6 ± 1	**8**
Region7	3.1 ± 0.3	10 ± 4	5.9 ± 0.6	0.1 ± 0.1	0.44 ± 0.05	20 ± 4	**34**
Region8	0.09 ± 0.02	0.9 ± 0.3	0.12 ± 0.01	0 ± 0	0.25 ± 0.03	1.3 ± 0.3	**3**
Region9	0.9 ± 0.1	7 ± 3	5.5 ± 0.6	0.1 ± 0.1	0.66 ± 0.07	14 ± 3	**24**
Region10	94 ± 9	243 ± 69	20 ± 2	0.2 ± 0.2	0.21 ± 0.03	358 ± 70	**385**
Region11	215 ± 22	371 ± 108	34 ± 3	0.7 ± 0.4	1.3 ± 0.1	621 ± 111	**687**

Table C.5: Trilepton Control Regions: $ee + \ell$(no isolated tracks)

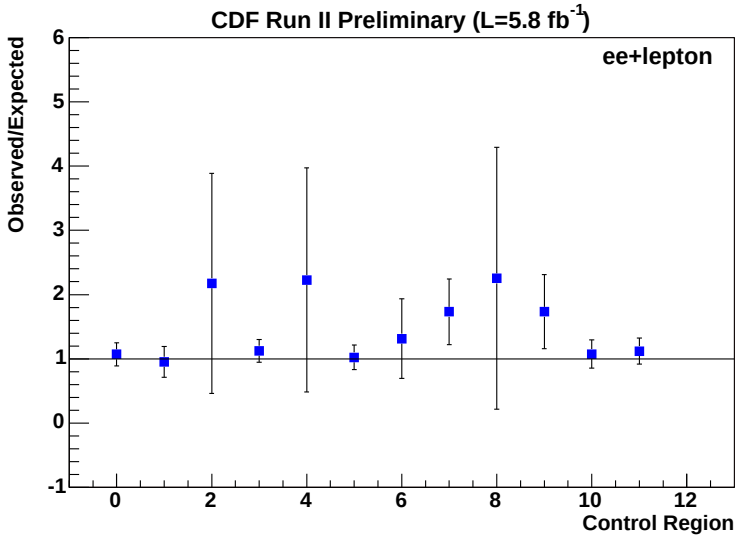

Figure C.5: Summary of control regions: Observation/Expectation for $ee + \ell$(no isolated tracks). The error bars represent the statistical and systematic uncertainty in the background estimation added in quadrature.

Table of ee+isoTracks yields							
	Drell-Yan+γ	Fakes	Diboson	Wγ	Top	Total SM	Observed
Region0	39 ± 4	1380 ± 277	1.7 ± 0.2	0 ± 0	0.019 ± 0.006	1420 ± 277	**1321**
Region1	6.6 ± 0.7	249 ± 57	5.8 ± 0.6	0.4 ± 0.2	0.08 ± 0.01	262 ± 57	**285**
Region2	0.25 ± 0.04	18 ± 4	0.59 ± 0.06	0 ± 0	0.2 ± 0.03	19 ± 4	**25**
Region3	15 ± 2	290 ± 58	0.27 ± 0.03	0 ± 0	0.004 ± 0.003	306 ± 58	**270**
Region4	0.28 ± 0.05	15 ± 3	0.065 ± 0.008	0 ± 0	0.013 ± 0.005	15 ± 3	**18**
Region5	23 ± 2	1035 ± 208	0.77 ± 0.08	0 ± 0	0.002 ± 0.002	1058 ± 208	**1002**
Region6	0.35 ± 0.06	40 ± 8	0.59 ± 0.06	0 ± 0	0 ± 0	41 ± 8	**31**
Region7	26 ± 3	124 ± 27	4 ± 0.4	2.4 ± 0.7	0.27 ± 0.04	157 ± 28	**146**
Region8	0.62 ± 0.08	13 ± 3	0.24 ± 0.03	0 ± 0	0.65 ± 0.07	14 ± 3	**8**
Region9	21 ± 2	83 ± 19	4 ± 0.4	2.4 ± 0.7	0.91 ± 0.1	111 ± 19	**99**
Region10	42 ± 4	1890 ± 390	11 ± 1	0 ± 0	0.36 ± 0.04	1942 ± 390	**1964**
Region11	114 ± 11	2707 ± 560	18 ± 2	4 ± 0.9	1.9 ± 0.2	2845 ± 560	**2843**

Table C.6: Trilepton Control Regions: *ee* + isolated track

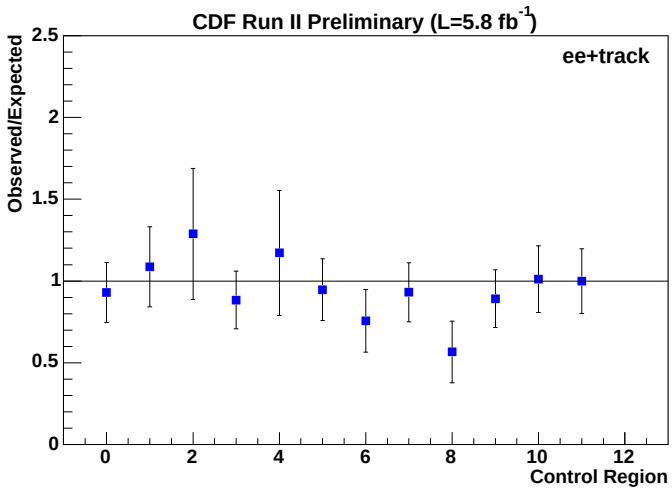

Figure C.6: Summary of control regions: Observation/Expectation for *ee* + isolated track. The error bars represent the statistical and systematic uncertainty in the background estimation added in quadrature.

Appendix D

Kinematic Variables per Control Region

We test the various background contributions in distinct control regions where the signal expectation is negligible compared to the background. The control regions are defined in the $\not{E}_T$ vs dilepton mass $M_{\ell\ell}$ space, with the additional requirement of high or low jet multiplicity. As shown in Figure D.1, different control regions are useful for validating specific kinds of backgrounds. The central region in dilepton masses between 76 GeV and 106 GeV (for high and low $\not{E}_T$) validates electroweak backgrounds, specifically the Z boson resonance. In dilepton channels, this region is particularly useful for validating the overall normalization of the MC, which is the result of the application of several weights: ID-scale factors, trigger efficiencies, luminosity scales, etc. In trileptons channels, this region is useful for validating the fake rate of muons, electrons, taus and isolated tracks. Control regions of high $\not{E}_T$ and high jet multiplicity have large contributions of top backgrounds where $t\bar{t}$ is clearly visible in dilepton channels. On the other hand, high $\not{E}_T$ and low jet multiplicity regions are rich in diboson backgrounds as can be appreciated in the trilepton kinematic plots. The yields for for data and expectation can be found in

Appendix C.

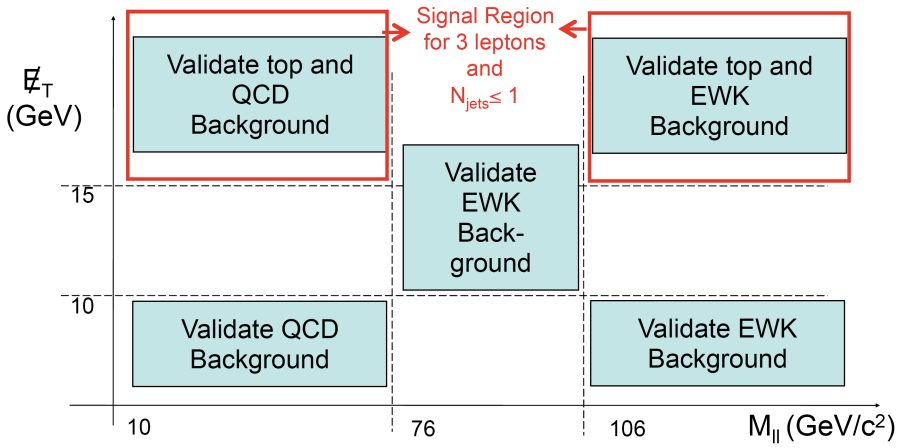

Figure D.1: Control regions and background validation.

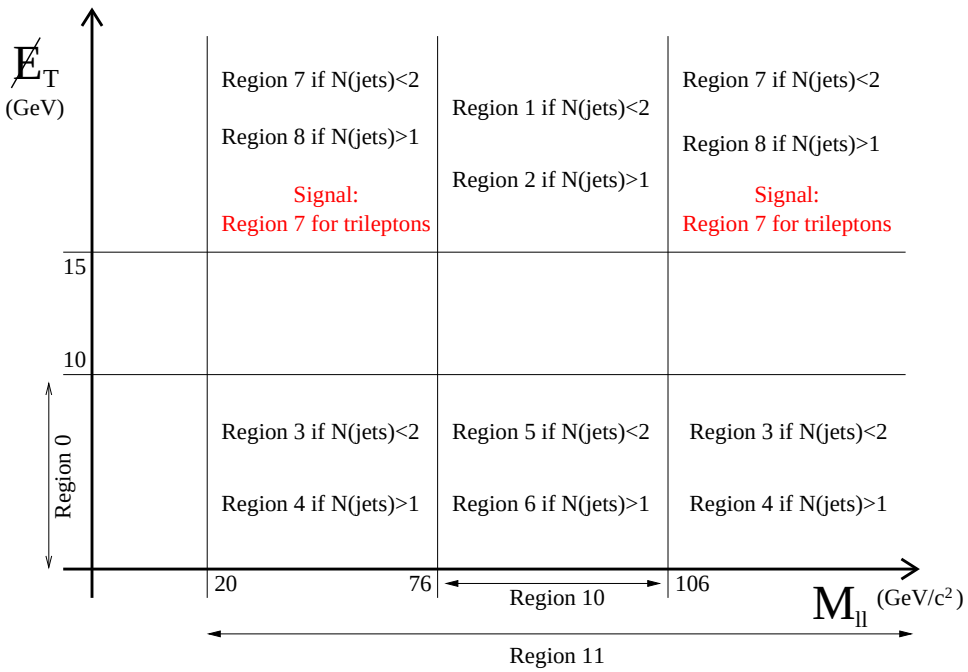

Figure D.2: The control and signal regions used in this analysis. Since dileptons and trileptons are studied separately for dimuon and dielectron channels, there are a total of 66 control regions.

D.1 Kinematic Variables for Region 0

In this section we show the invariant mass, $\not\!\!E_T$ and jet multiplicity in the control region defined by: $\not\!\!E_T < 10$.

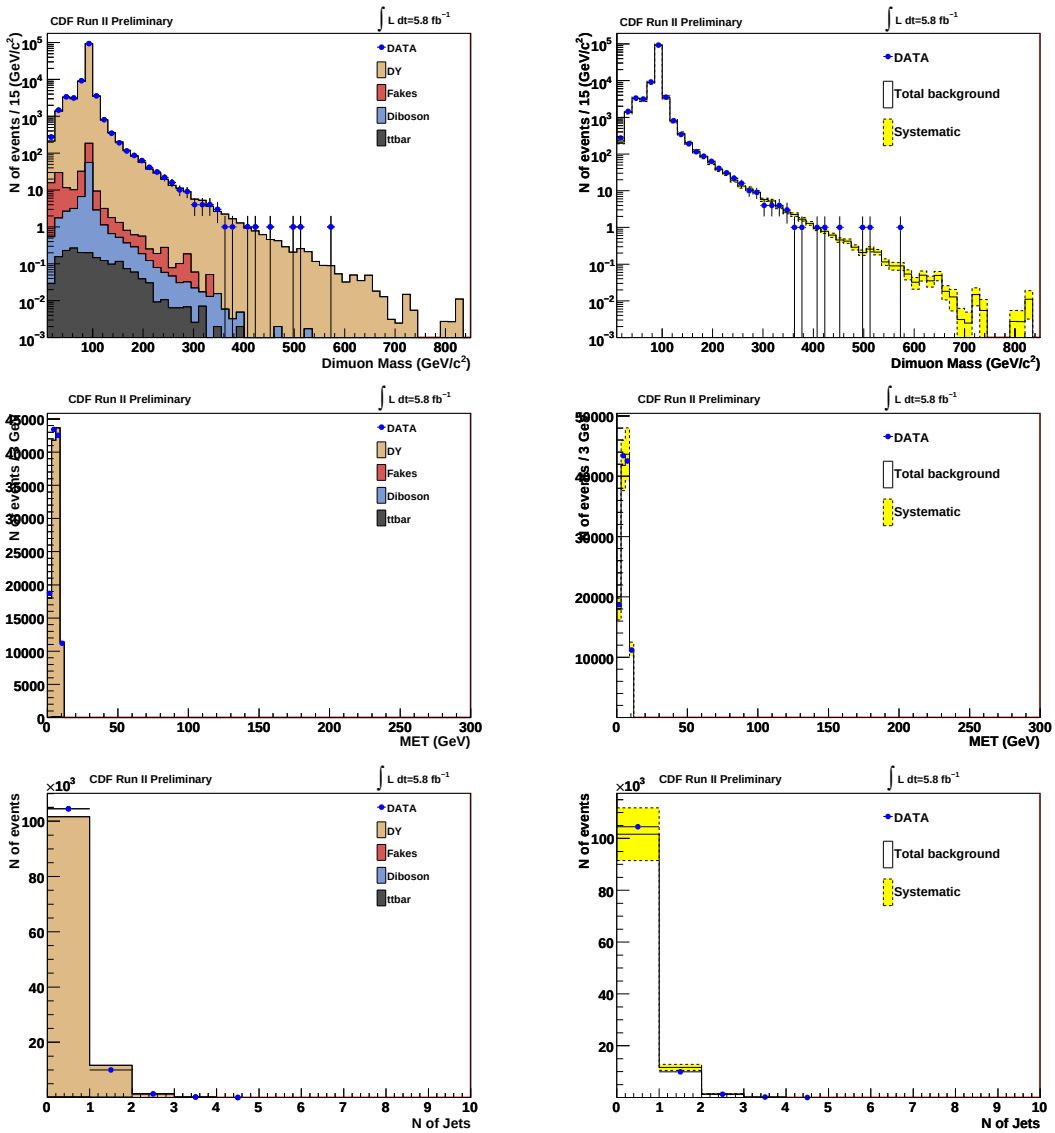

Figure D.3: Dimuon mass, $\not\!\!E_T$ and jet multiplicity for data and SM prediction in region 0 ($\not\!\!E_T < 10$). Plots on the right show the total systematic uncertainty in the expectation (yellow band).

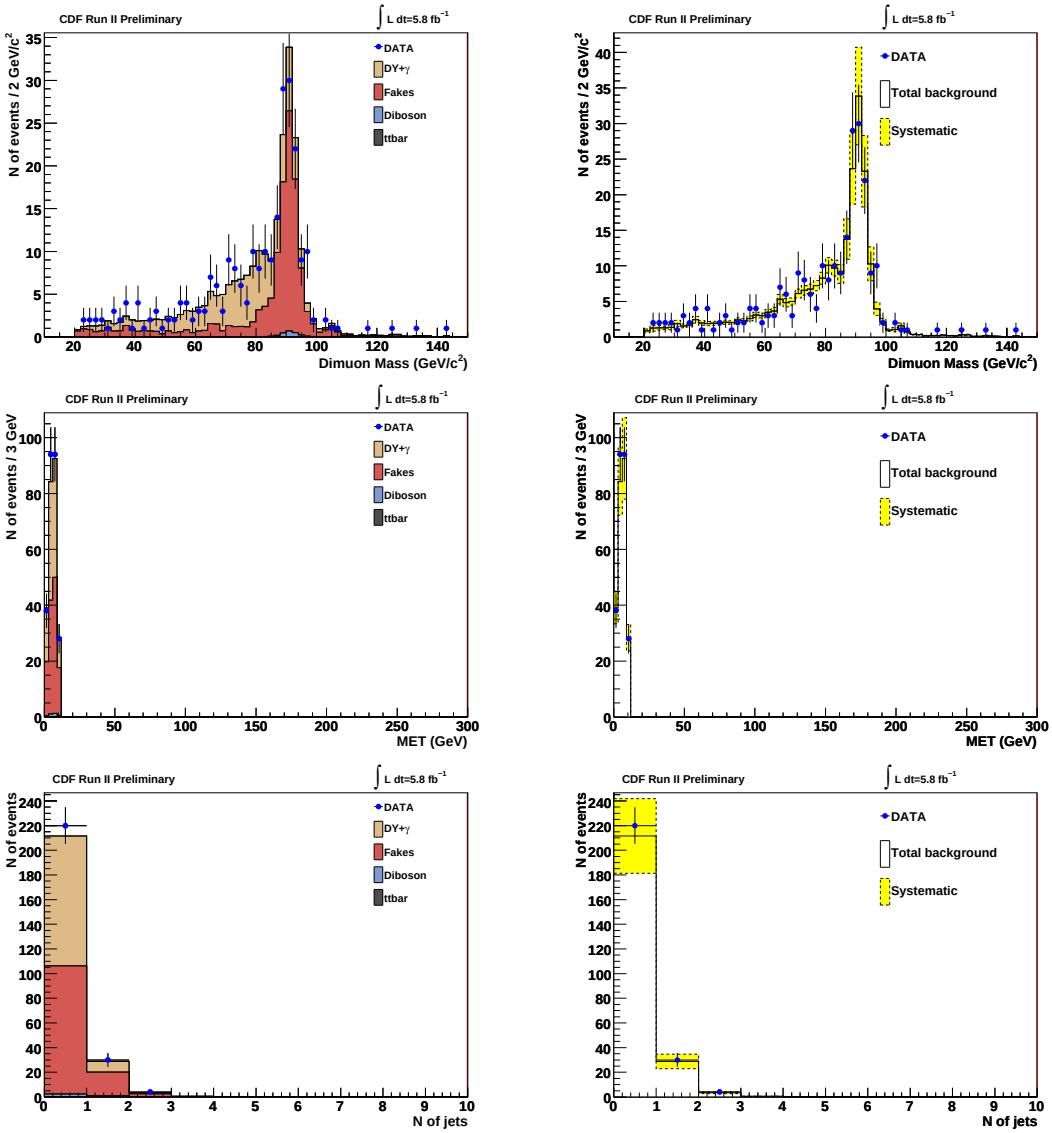

Figure D.4: Dimuon mass, $\not\!\!E_T$ and jet multiplicity of $\mu\mu$+lepton(e,μ,τ) events for data and SM prediction in region 0. Plots on the right show the total systematic uncertainty in the expectation (yellow band).

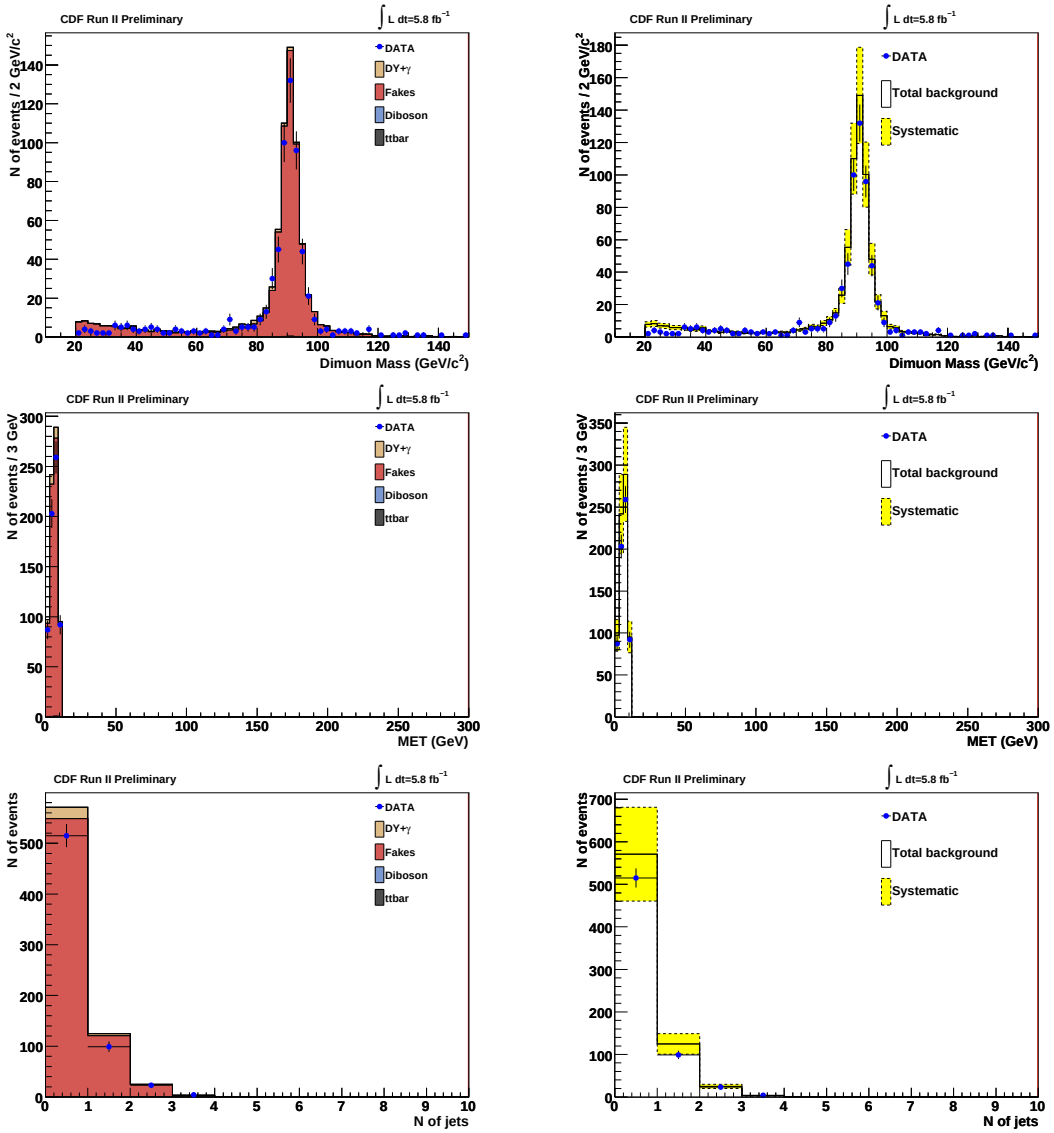

Figure D.5: Dimuon mass, $\not\!\!E_T$ and jet multiplicity of $\mu\mu$+isotrack events for data and SM prediction in region 0. Plots on the right show the total systematic uncertainty in the expectation (yellow band).

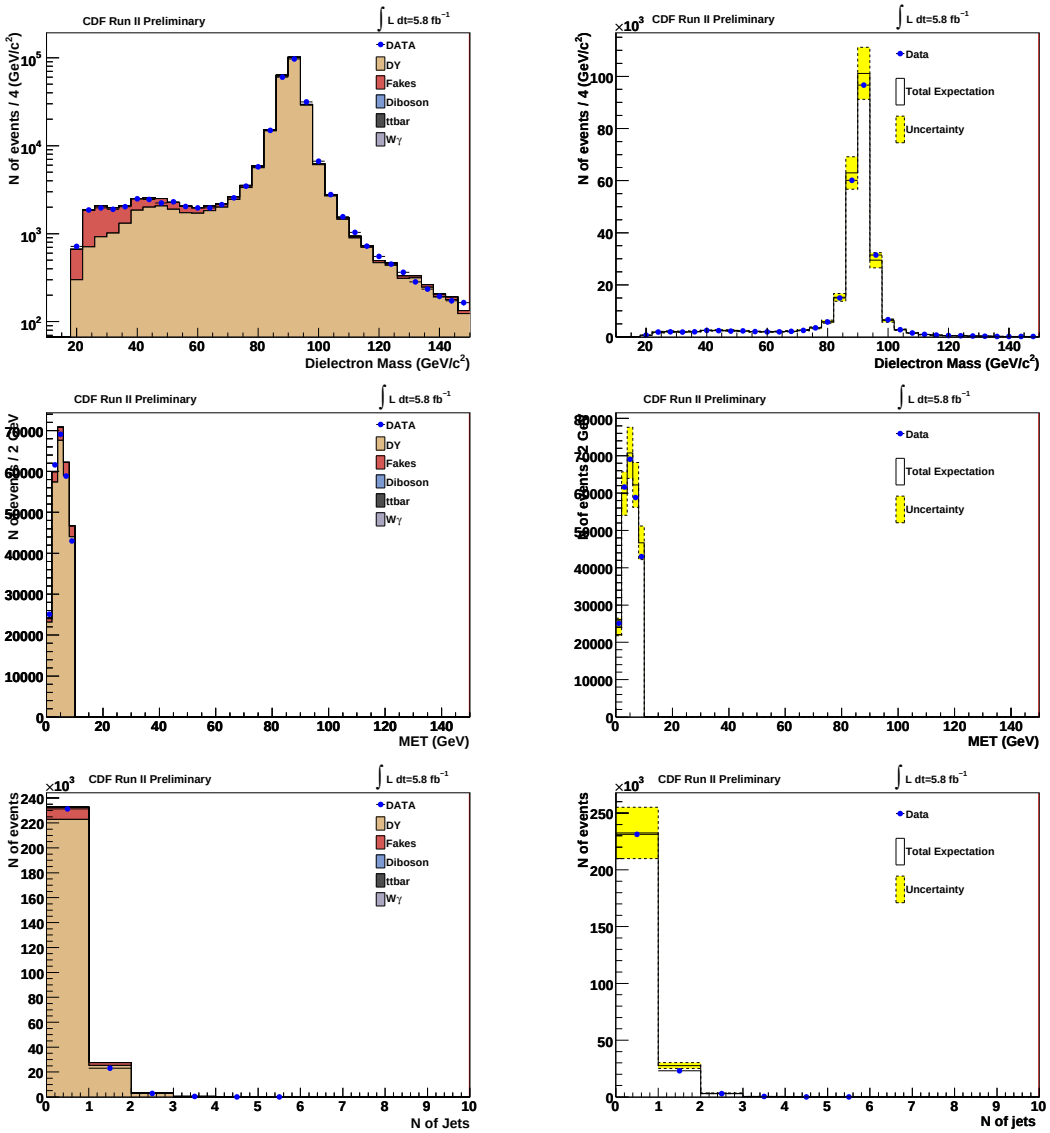

Figure D.6: Dielectron mass, $\not\!\!E_T$ and jet multiplicity for data and SM prediction in region 0. Plots on the right show the total systematic uncertainty in the expectation (yellow band).

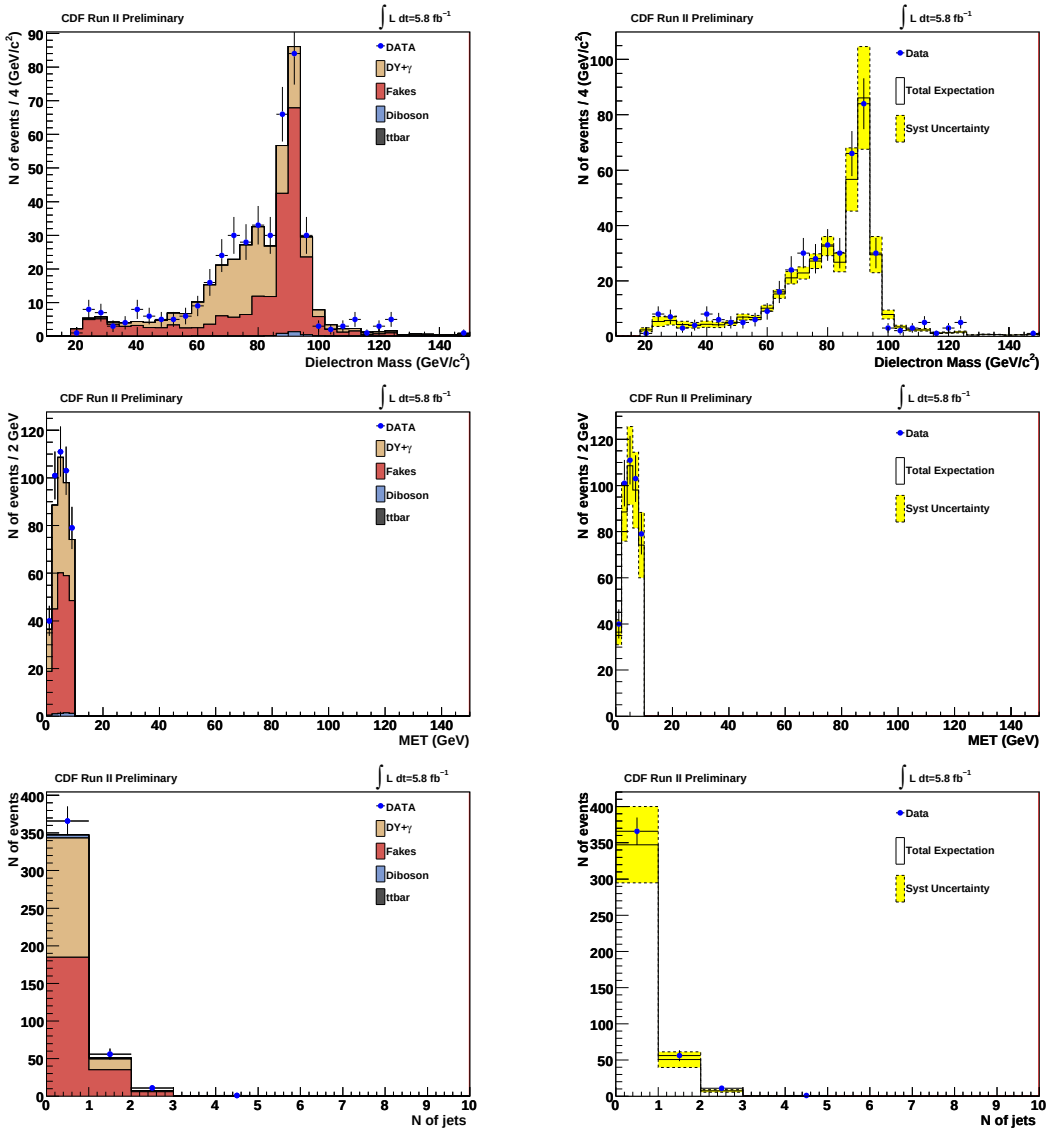

Figure D.7: Dielectron mass, $\not\!\!E_T$ and jet multiplicity of the ee+lepton(e,μ,τ) events for data and SM prediction in region 0. Plots on the right show the total systematic uncertainty in the expectation (yellow band).

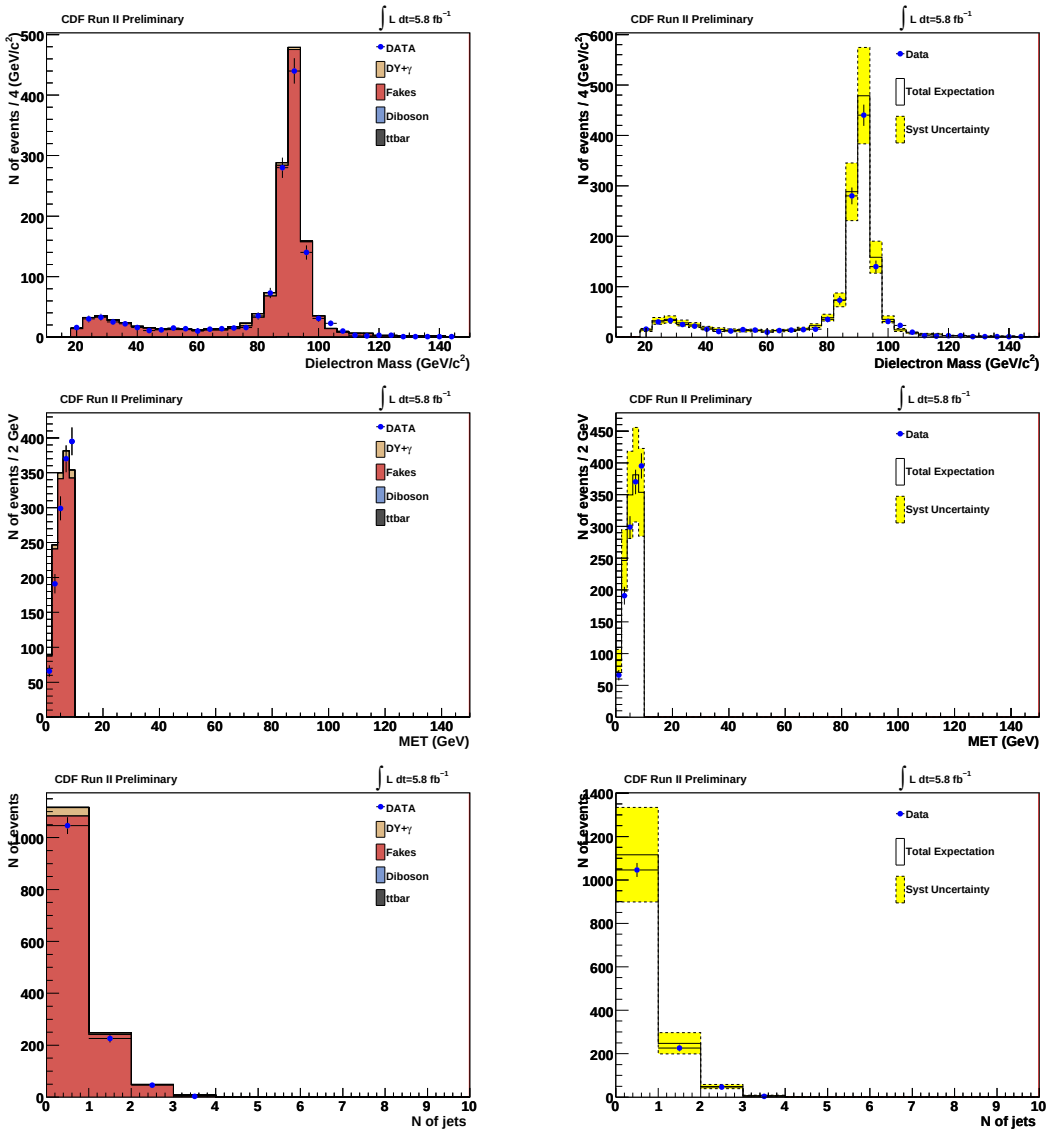

Figure D.8: Dielectron mass, $\not\!\!E_T$ and jet multiplicity of the ee+isotrack events for data and SM prediction in region 0. Plots on the right show the total systematic uncertainty in the expectation (yellow band).

D.2 Kinematic Variables for Region 1

In this section we show the invariant mass, $\not\!\!E_T$ and jet multiplicity in the control region defined by: $\not\!\!E_T > 15, N_{\text{jet}} \leq 1, Z$

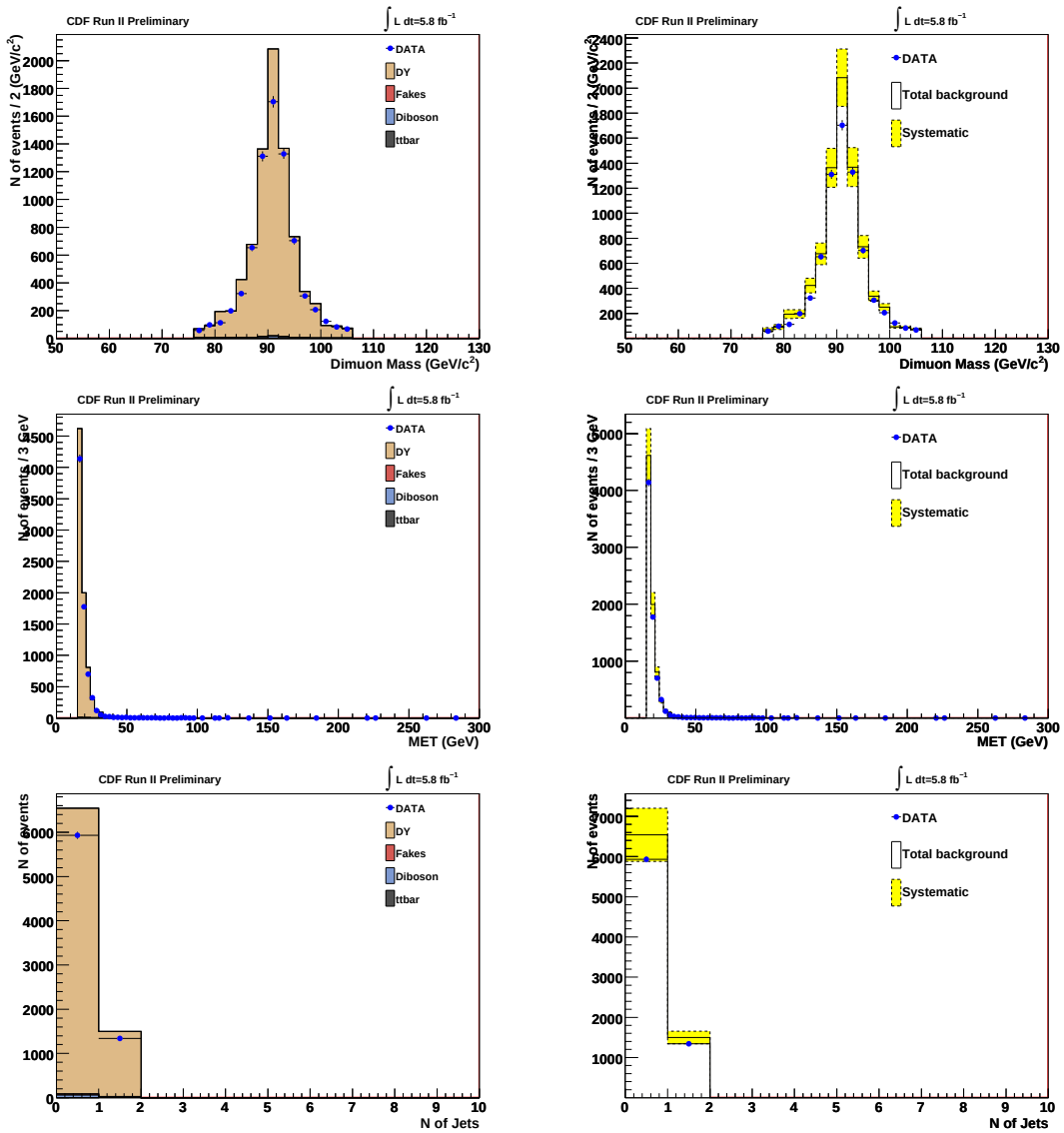

Figure D.9: Dimuon mass, $\not\!\!E_T$ and jet multiplicity for data and SM prediction in region 1 ($\not\!\!E_T > 15, N_{\text{jet}} \leq 1, Z$). Plots on the right show the total systematic uncertainty in the expectation (yellow band).

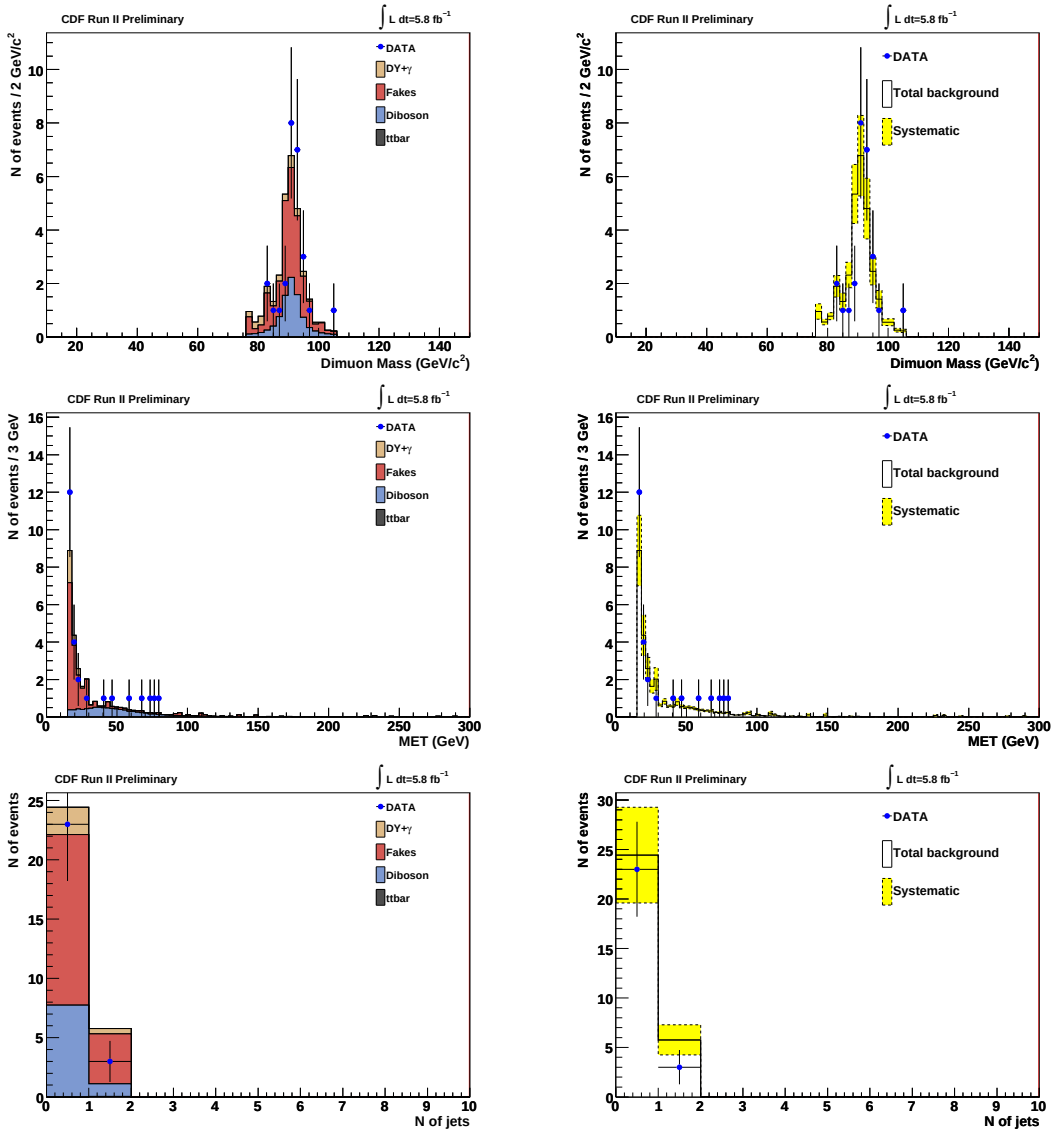

Figure D.10: Dimuon mass, $\not\!\!E_T$ and jet multiplicity of $\mu\mu$+lepton(e,μ,τ) events for data and SM prediction in region 1 ($\not\!\!E_T > 15, N_{\text{jet}} \leq 1, Z$). Plots on the right show the total systematic uncertainty in the expectation (yellow band).

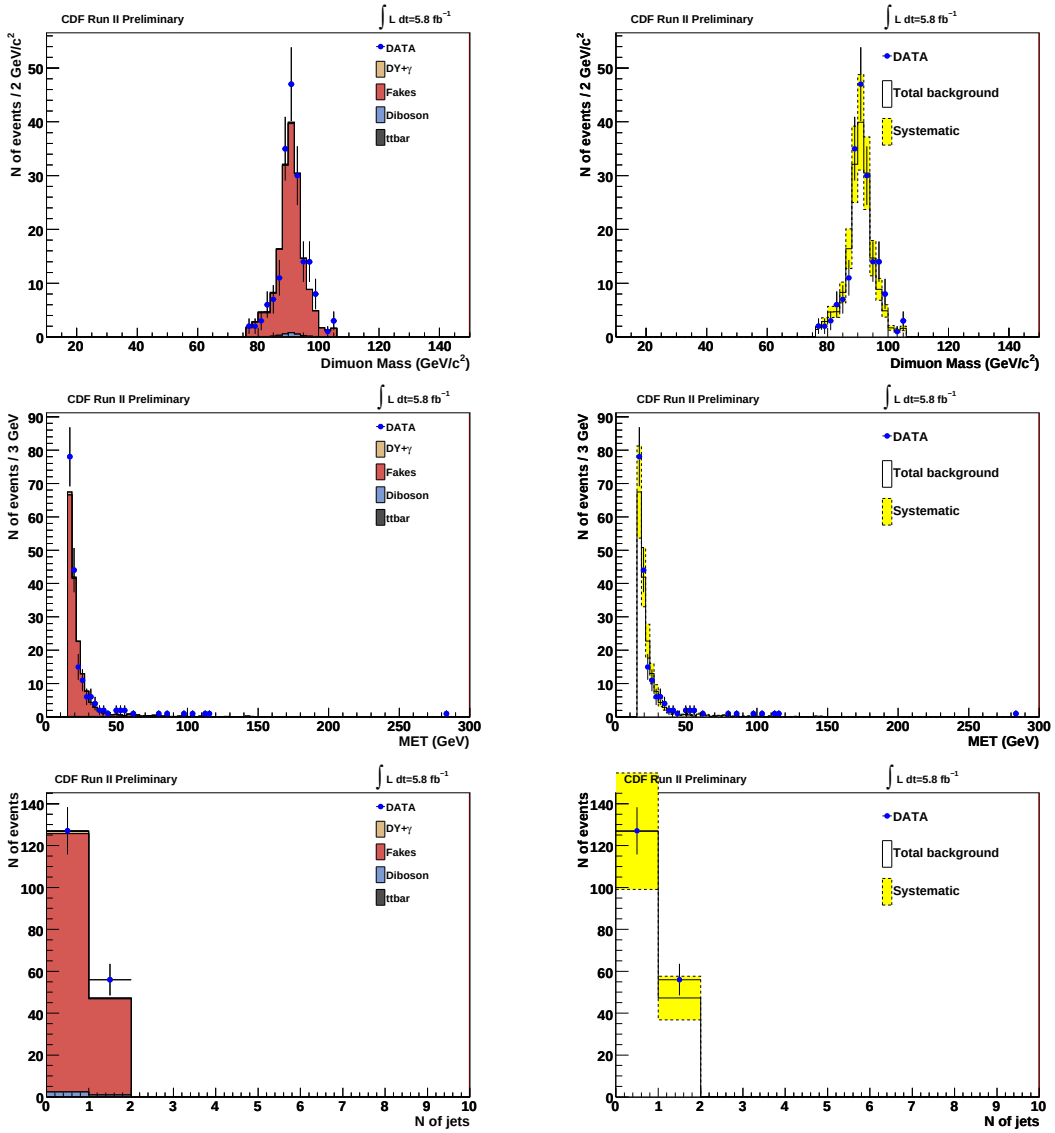

Figure D.11: Dimuon mass, $\not\!\!E_T$ and jet multiplicity of $\mu\mu$+isotrack events for data and SM prediction in region 1 ($\not\!\!E_T > 15, N_{\text{jet}} \leq 1, Z$). Plots on the right show the total systematic uncertainty in the expectation (yellow band).

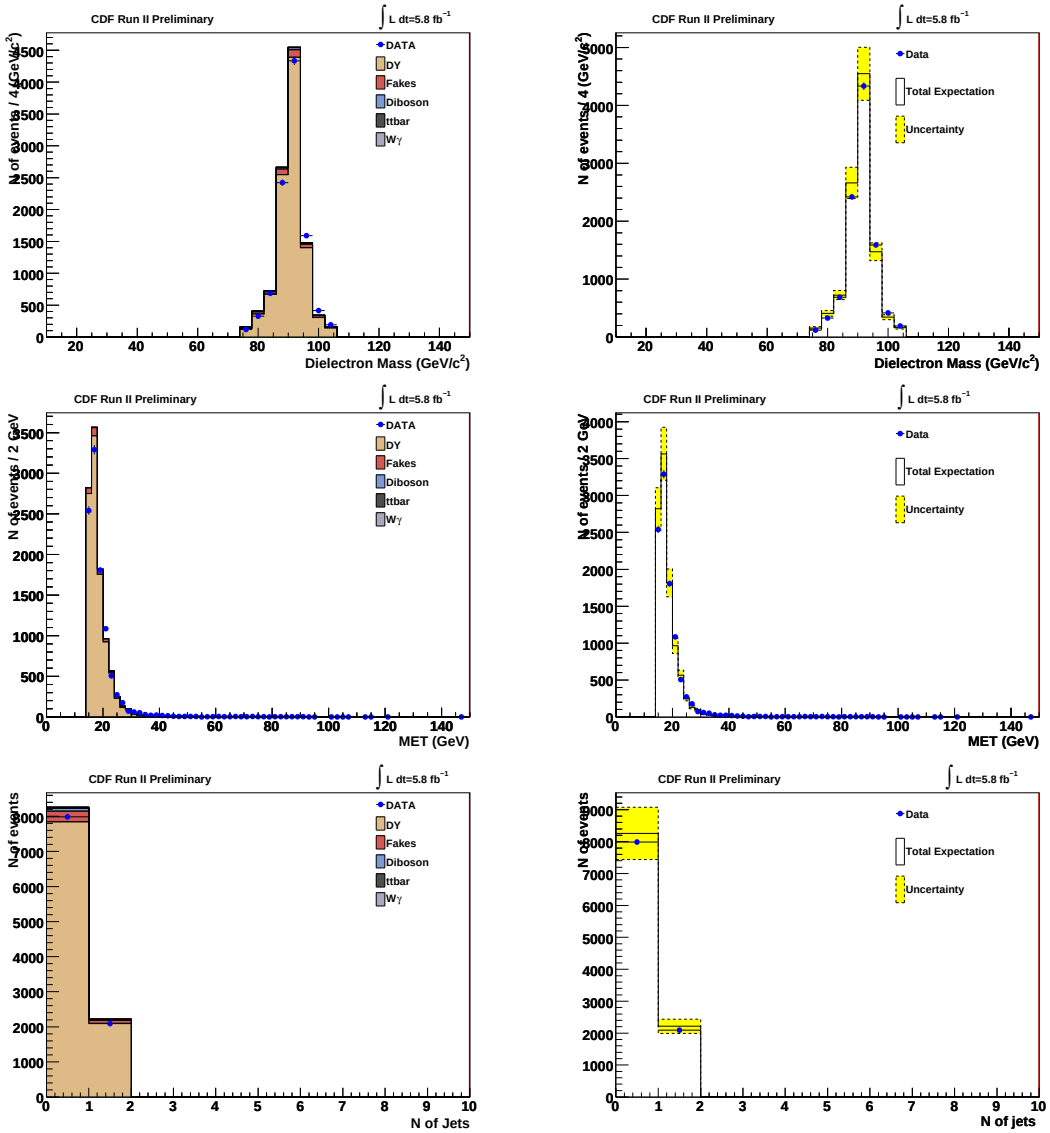

Figure D.12: Dielectron mass, $\not\!\!E_T$ and jet multiplicity for data and SM prediction in region 1 ($\not\!\!E_T > 15, N_{\text{jet}} \leq 1, Z$). Plots on the right show the total systematic uncertainty in the expectation (yellow band).

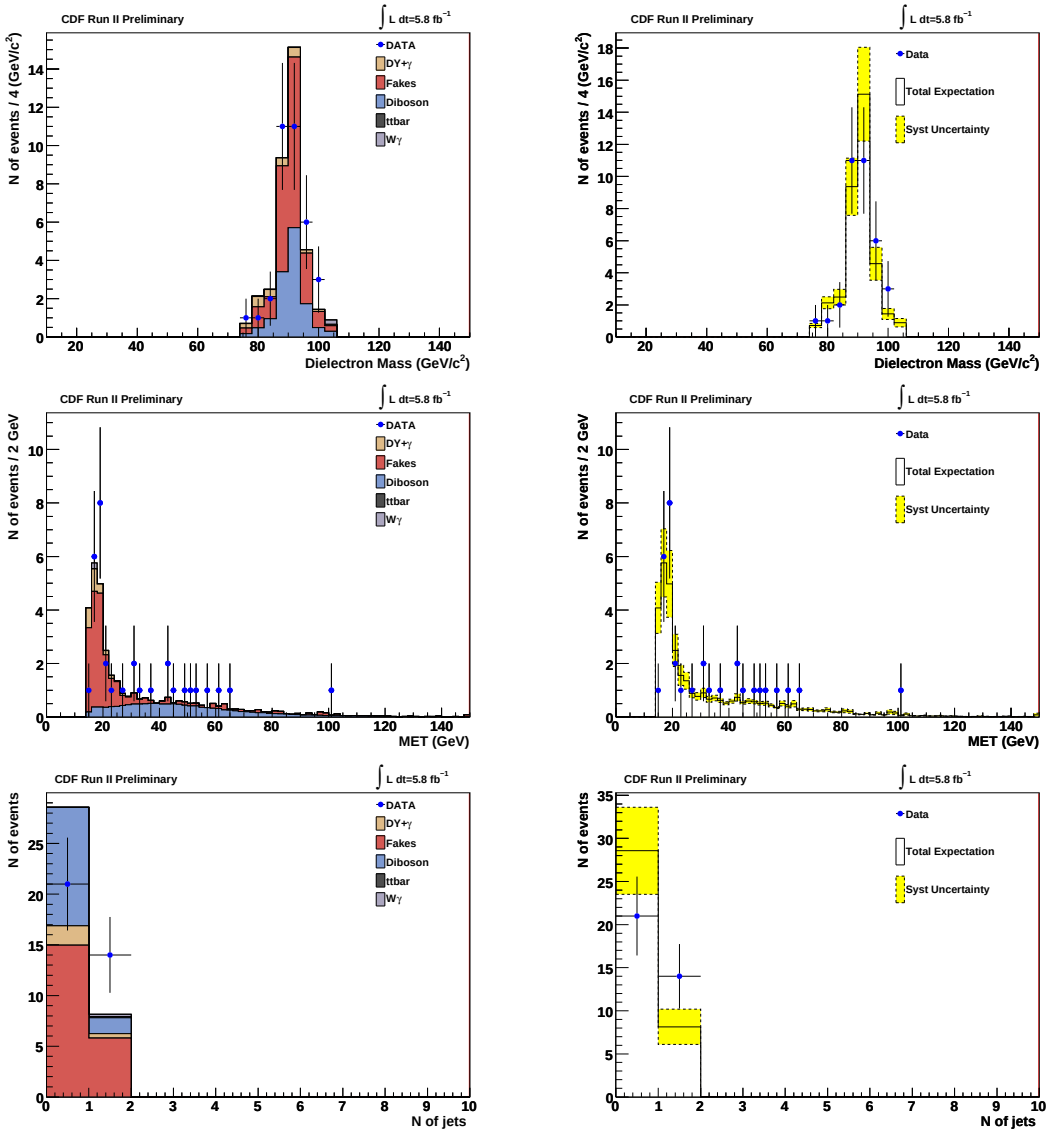

Figure D.13: Dielectron mass, $\not\!\!E_T$ and jet multiplicity of the ee+lepton(e,μ,τ) events for data and SM prediction in region 1 ($\not\!\!E_T > 15, N_{\text{jet}} \leq 1, Z$). Plots on the right show the total systematic uncertainty in the expectation (yellow band).

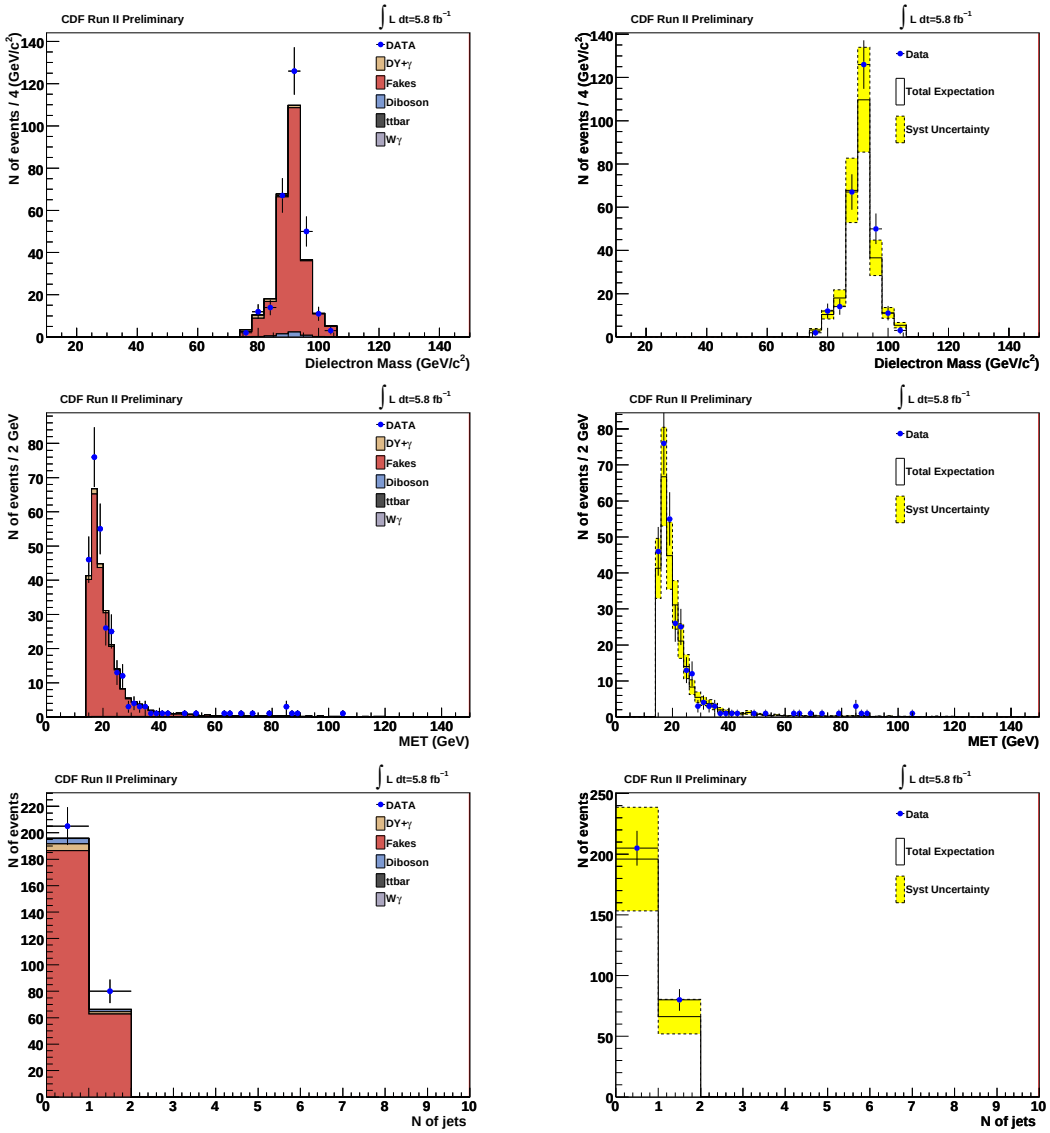

Figure D.14: Dielectron mass, $\not\!\!E_T$ and jet multiplicity of the ee+isotrack events for data and SM prediction in region 1 ($\not\!\!E_T > 15, N_{\text{jet}} \leq 1, Z$). Plots on the right show the total systematic uncertainty in the expectation (yellow band).

D.3 Kinematic Variables for Region 2

In this section we show the invariant mass, $\not\!\!E_T$ and jet multiplicity in the control region defined by: $\not\!\!E_T > 15, N_{\text{jet}} \geq 2, Z$

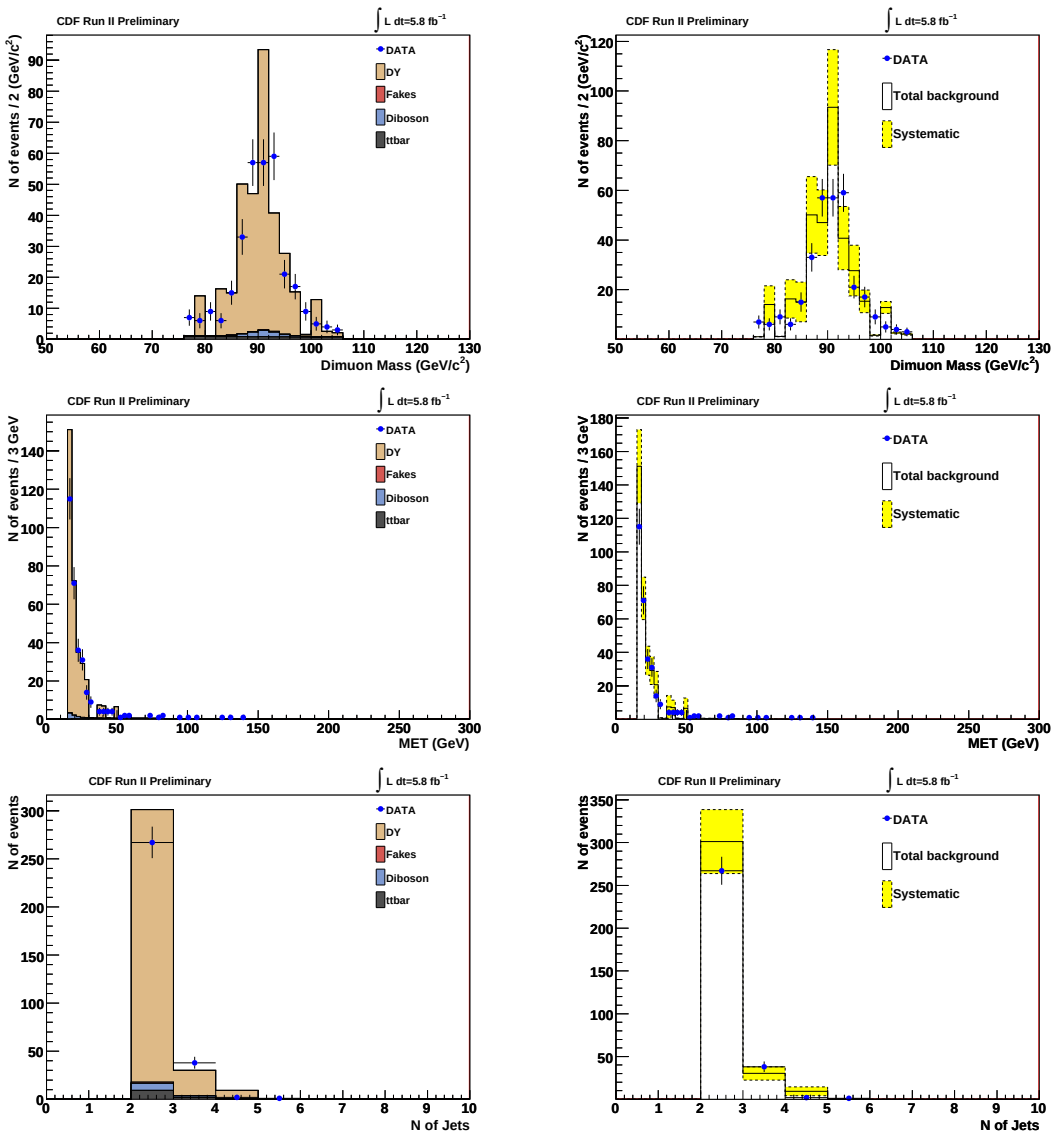

Figure D.15: Dimuon mass, $\not\!\!E_T$ and jet multiplicity for data and SM prediction in region 2 ($\not\!\!E_T > 15, N_{\text{jet}} \geq 2, Z$). Plots on the right show the total systematic uncertainty in the expectation (yellow band).

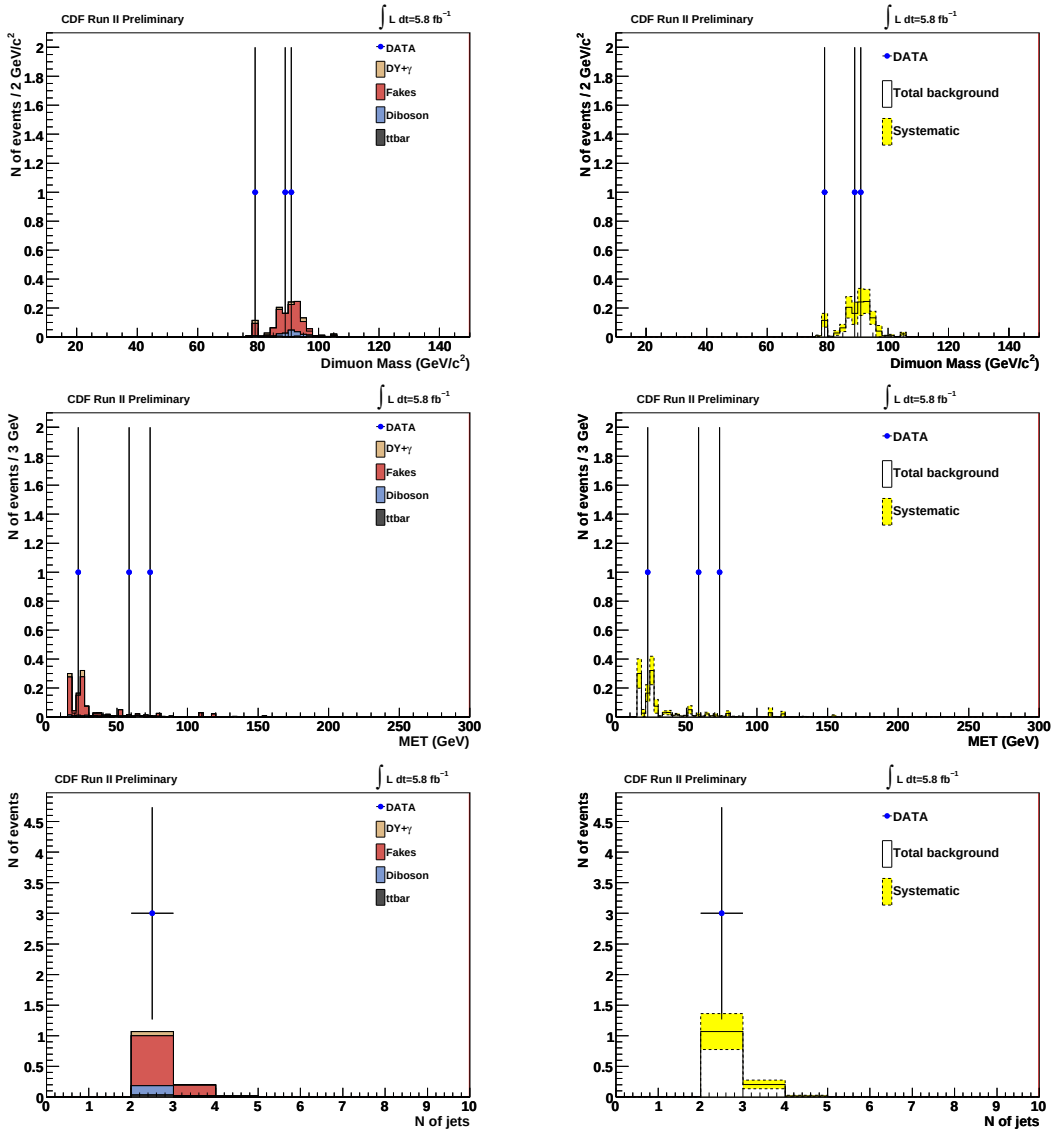

Figure D.16: Dimuon mass, $\not\!\!E_T$ and jet multiplicity of $\mu\mu$+lepton(e,μ,τ) events for data and SM prediction in region 2 ($\not\!\!E_T > 15, N_{\text{jet}} \geq 2, Z$). Plots on the right show the total systematic uncertainty in the expectation (yellow band).

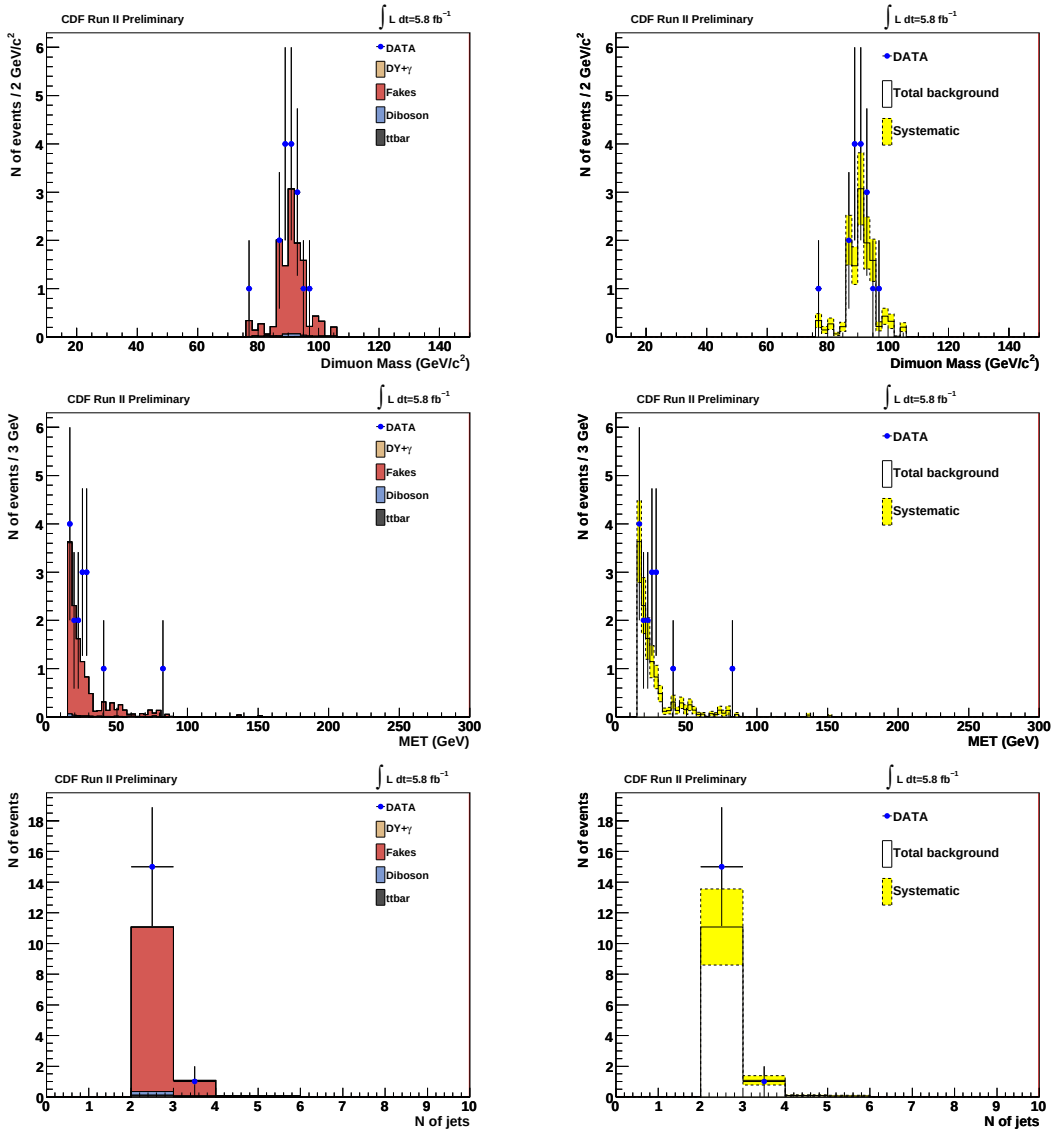

Figure D.17: Dimuon mass, $\not\!\!E_T$ and jet multiplicity of $\mu\mu$+isotrack events for data and SM prediction in region 2 ($\not\!\!E_T > 15, N_{\text{jet}} \geq 2, Z$). Plots on the right show the total systematic uncertainty in the expectation (yellow band).

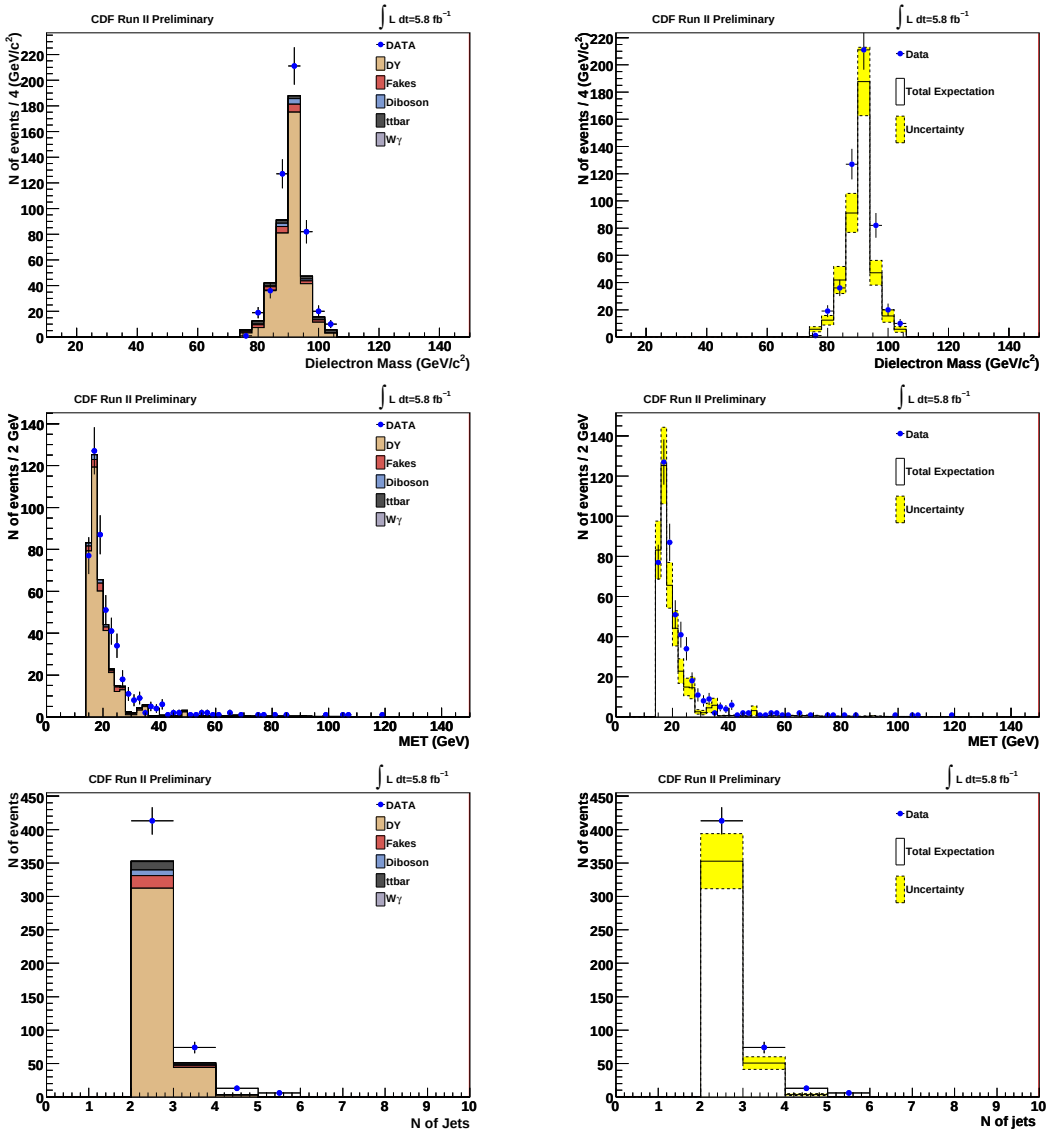

Figure D.18: Dielectron mass, $\not\!\!E_T$ and jet multiplicity for data and SM prediction in region 2 ($\not\!\!E_T > 15, N_{\text{jet}} \geq 2, Z$). Plots on the right show the total systematic uncertainty in the expectation (yellow band).

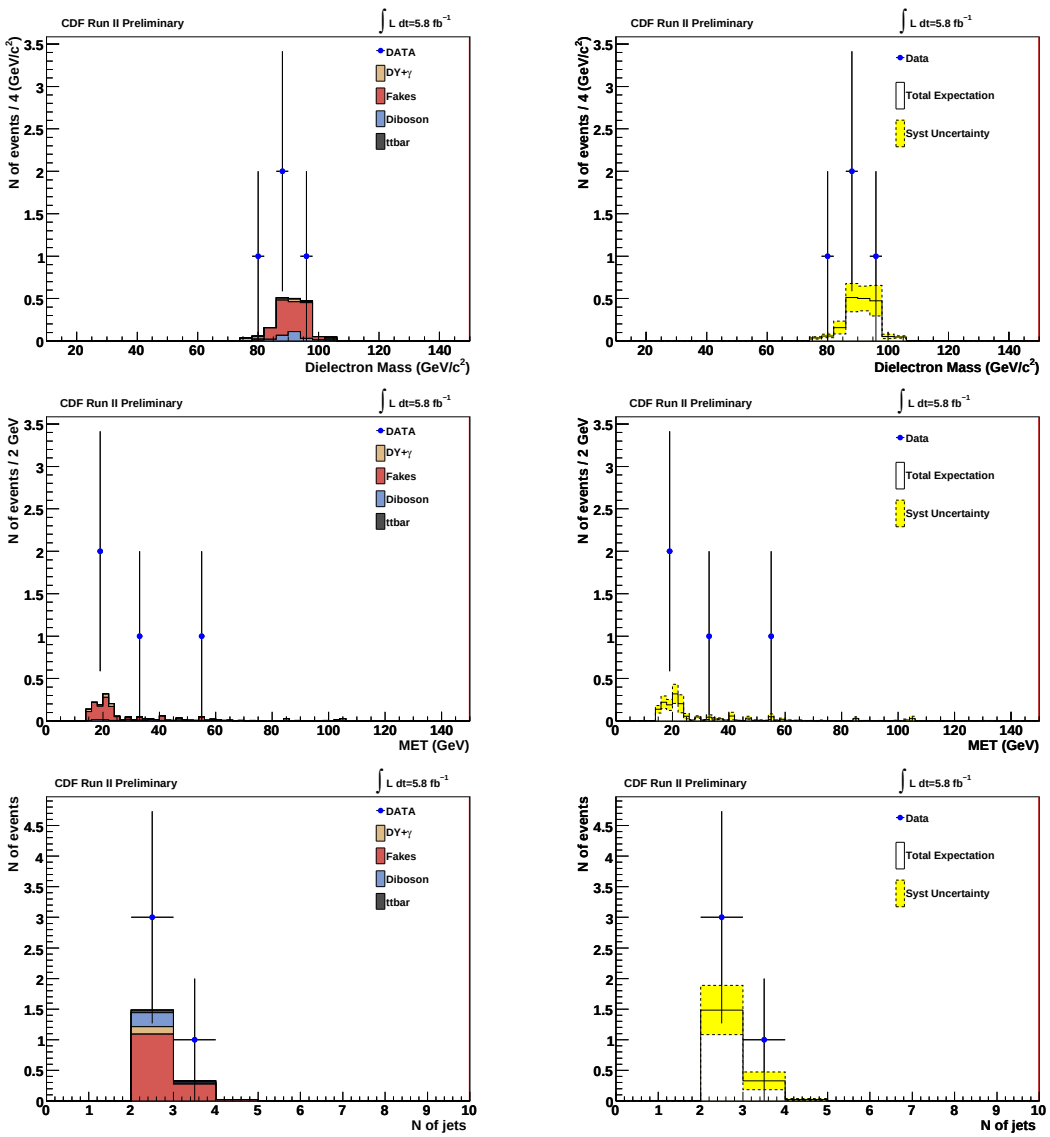

Figure D.19: Dielectron mass, $\not\!\!E_T$ and jet multiplicity of the ee+lepton(e,μ,τ) events for data and SM prediction in region 2 ($\not\!\!E_T > 15, N_{\text{jet}} \geq 2, Z$). Plots on the right show the total systematic uncertainty in the expectation (yellow band).

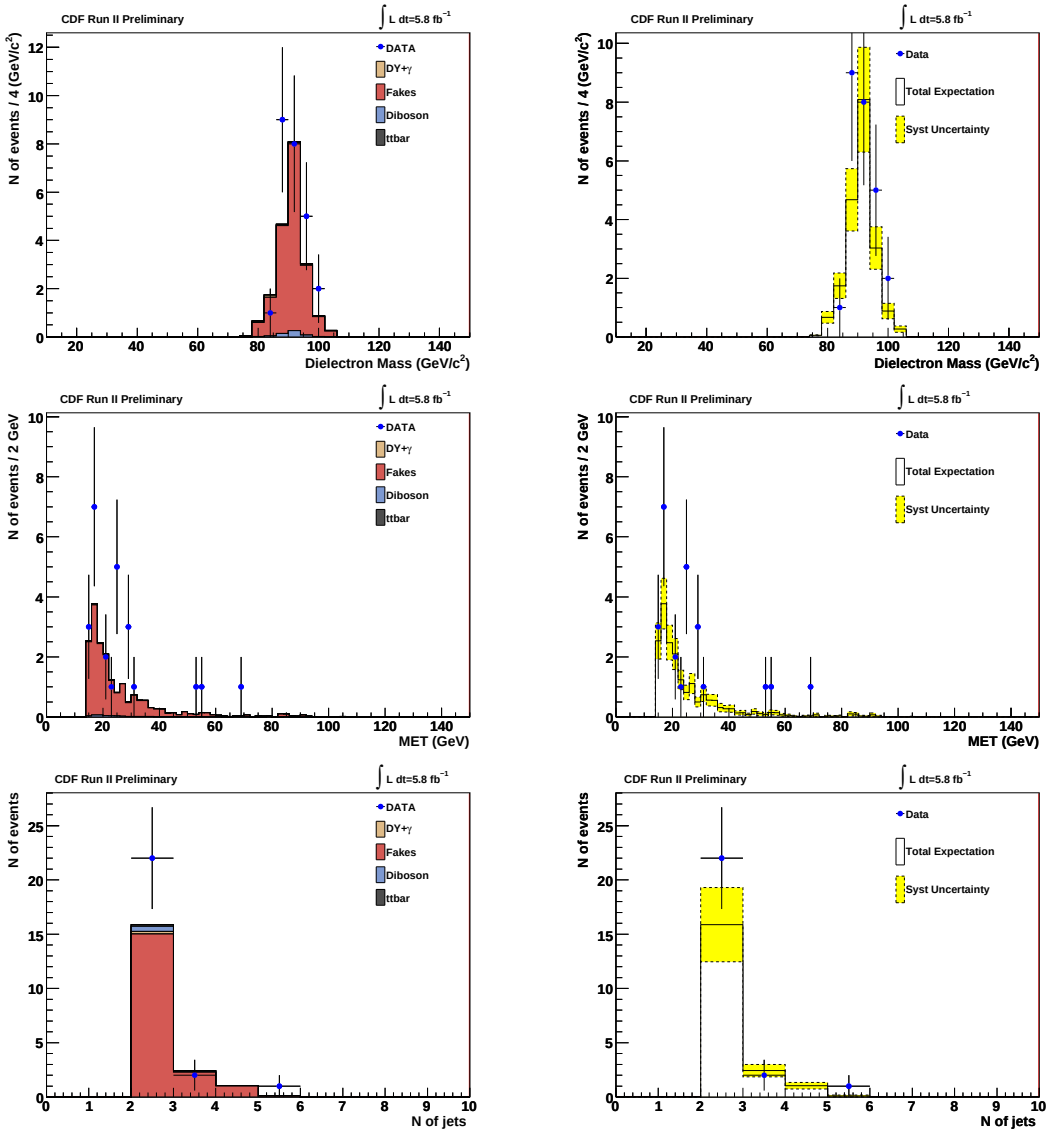

Figure D.20: Dielectron mass, $\not\!\!E_T$ and jet multiplicity of the ee+isotrack events for data and SM prediction in region 2 ($\not\!\!E_T > 15, N_{\text{jet}} \geq 2, Z$). Plots on the right show the total systematic uncertainty in the expectation (yellow band).

D.4 Kinematic Variables for Region 3

In this section we show the invariant mass, $\not\!\!E_T$ and jet multiplicity in the control region defined by: $\not\!\!E_T < 10, N_{\text{jet}} \leq 1, !Z$

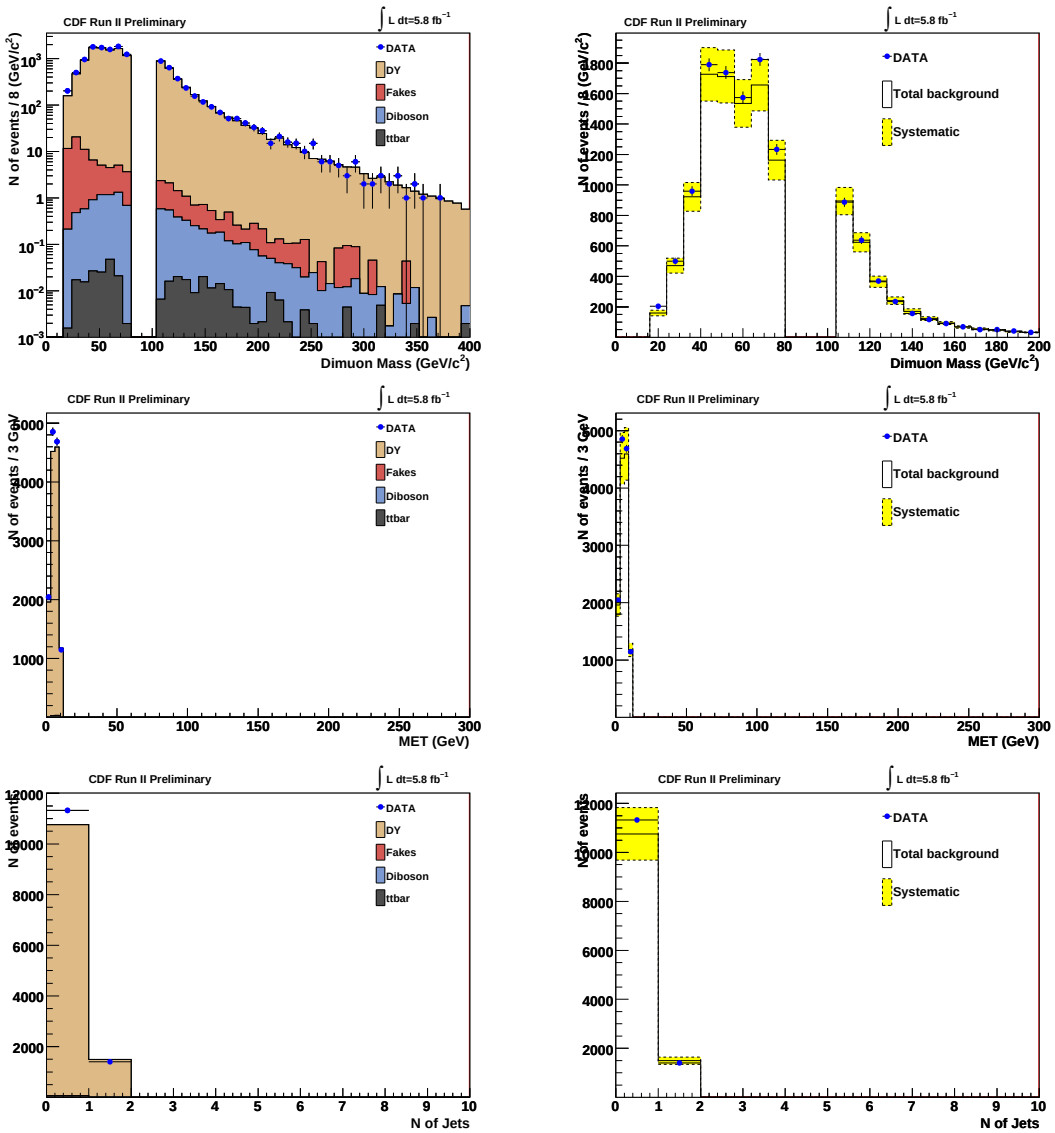

Figure D.21: Dimuon mass, $\not\!\!E_T$ and jet multiplicity for data and SM prediction in region 3 ($\not\!\!E_T < 10, N_{\text{jet}} \leq 1, !Z$). Plots on the right show the total systematic uncertainty in the expectation (yellow band).

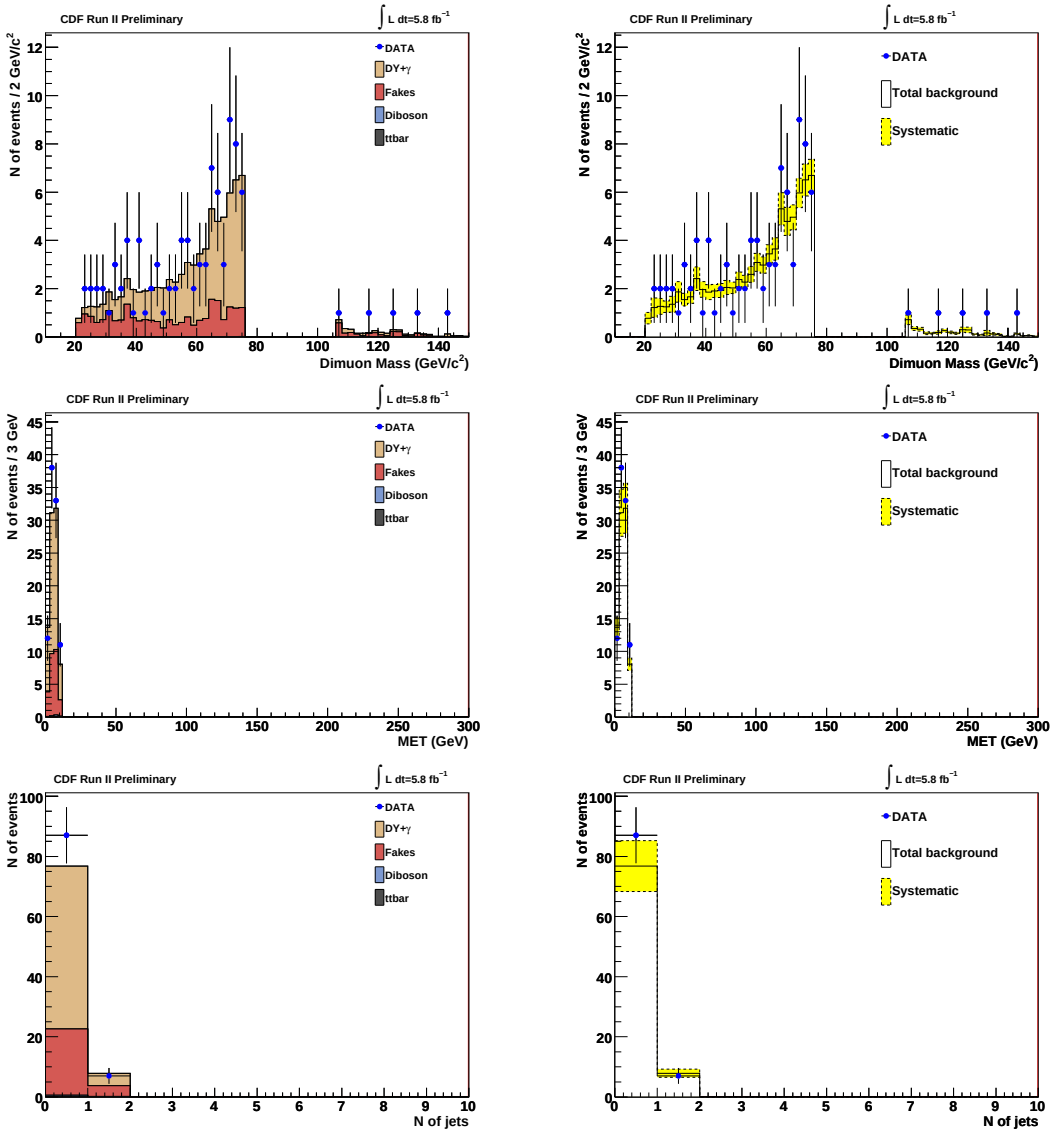

Figure D.22: Dimuon mass, $\not\!\!E_T$ and jet multiplicity of $\mu\mu$+lepton(e,μ,τ) events for data and SM prediction in region 3 ($\not\!\!E_T < 10, N_{\text{jet}} \leq 1, !Z$). Plots on the right show the total systematic uncertainty in the expectation (yellow band).

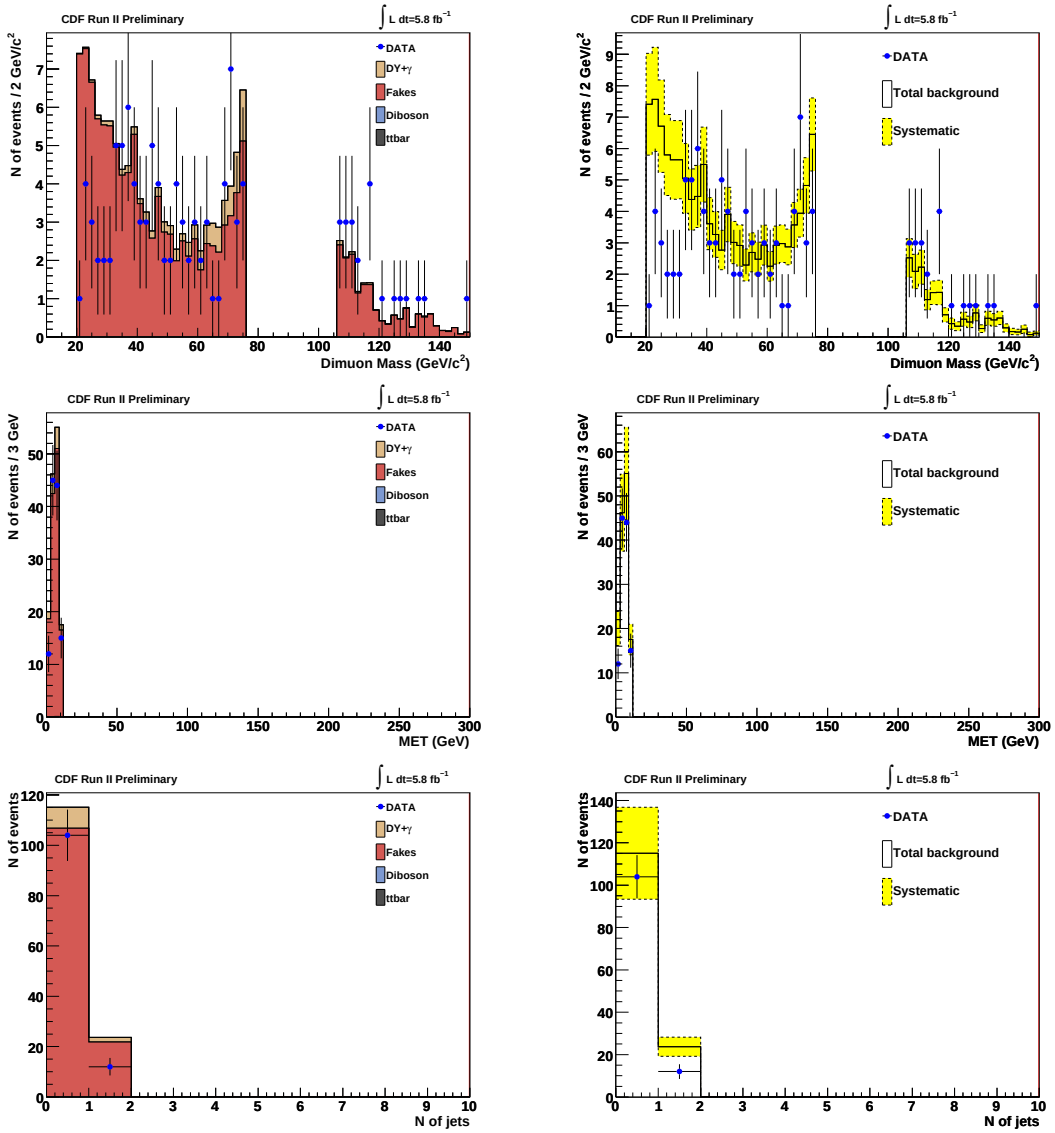

Figure D.23: Dimuon mass, $\not\!\!E_T$ and jet multiplicity of $\mu\mu$+isotrack events for data and SM prediction in region 3 ($\not\!\!E_T < 10, N_{\text{jet}} \leq 1, !Z$). Plots on the right show the total systematic uncertainty in the expectation (yellow band).

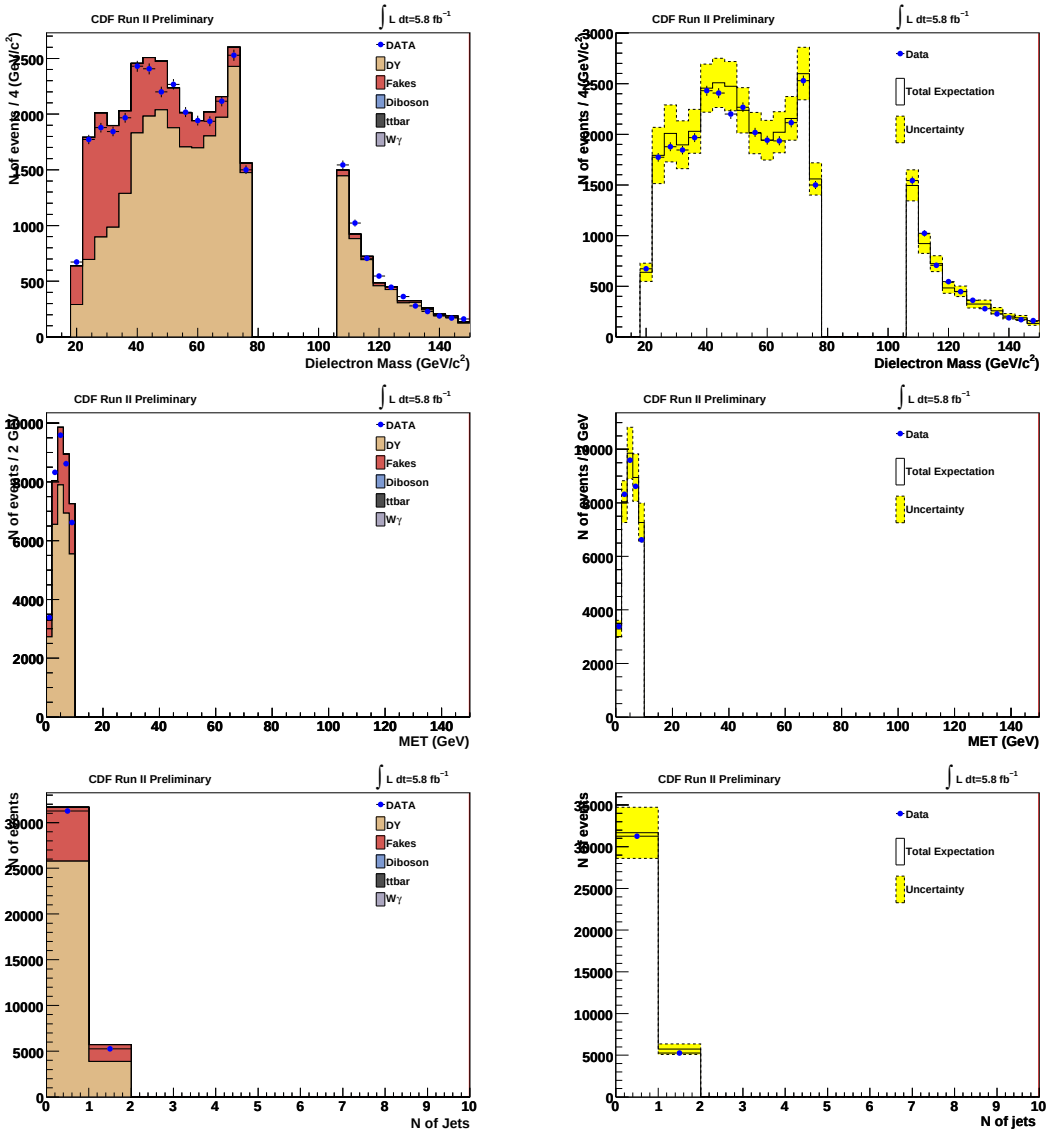

Figure D.24: Dielectron mass, $\not\!\!E_T$ and jet multiplicity for data and SM prediction in region 3 ($\not\!\!E_T < 10, N_{\text{jet}} \leq 1, !Z$). Plots on the right show the total systematic uncertainty in the expectation (yellow band).

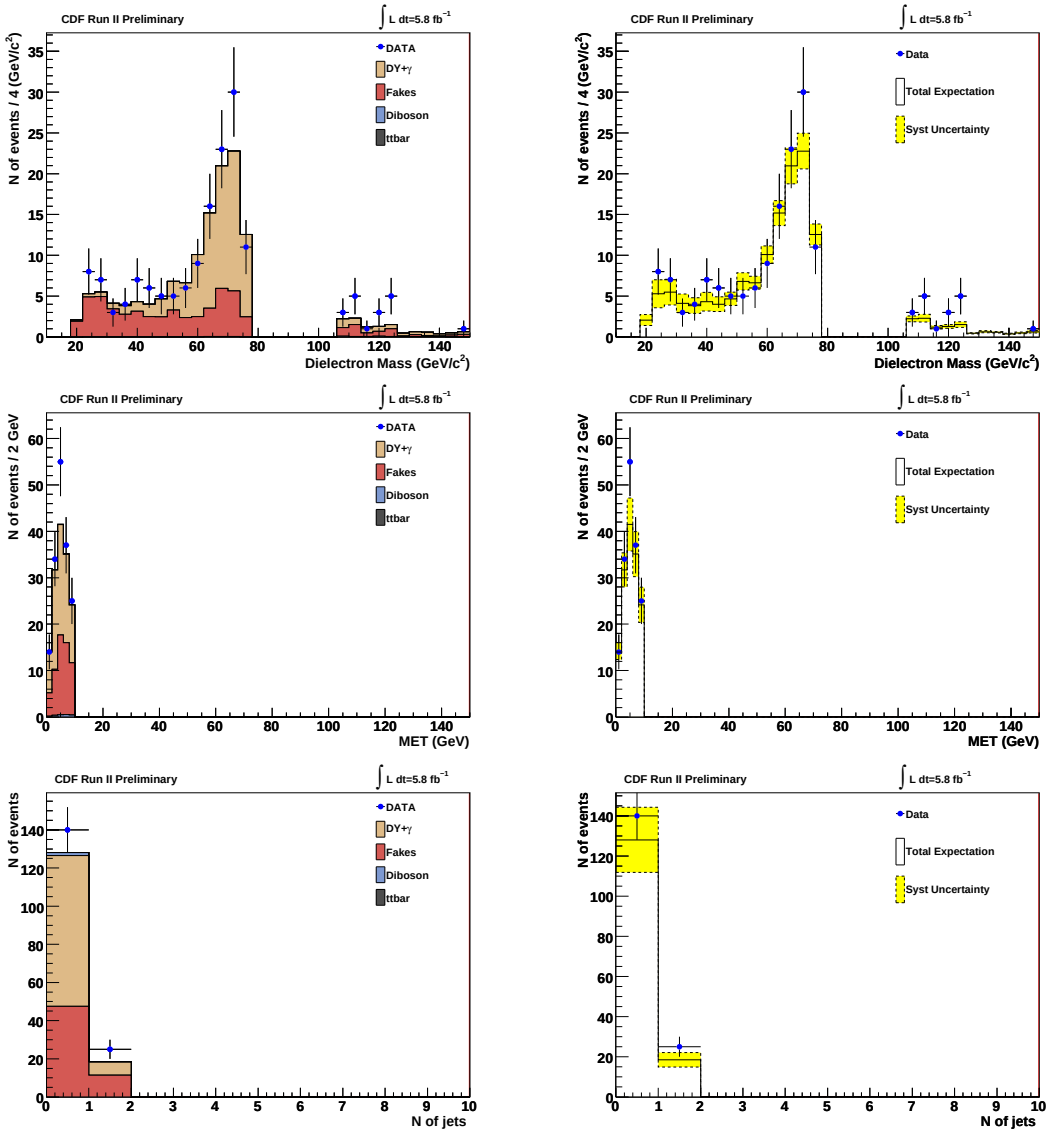

Figure D.25: Dielectron mass, $\not\!\!E_T$ and jet multiplicity of the ee+lepton(e,μ,τ) events for data and SM prediction in region 3 ($\not\!\!E_T < 10, N_{\text{jet}} \leq 1, !Z$). Plots on the right show the total systematic uncertainty in the expectation (yellow band).

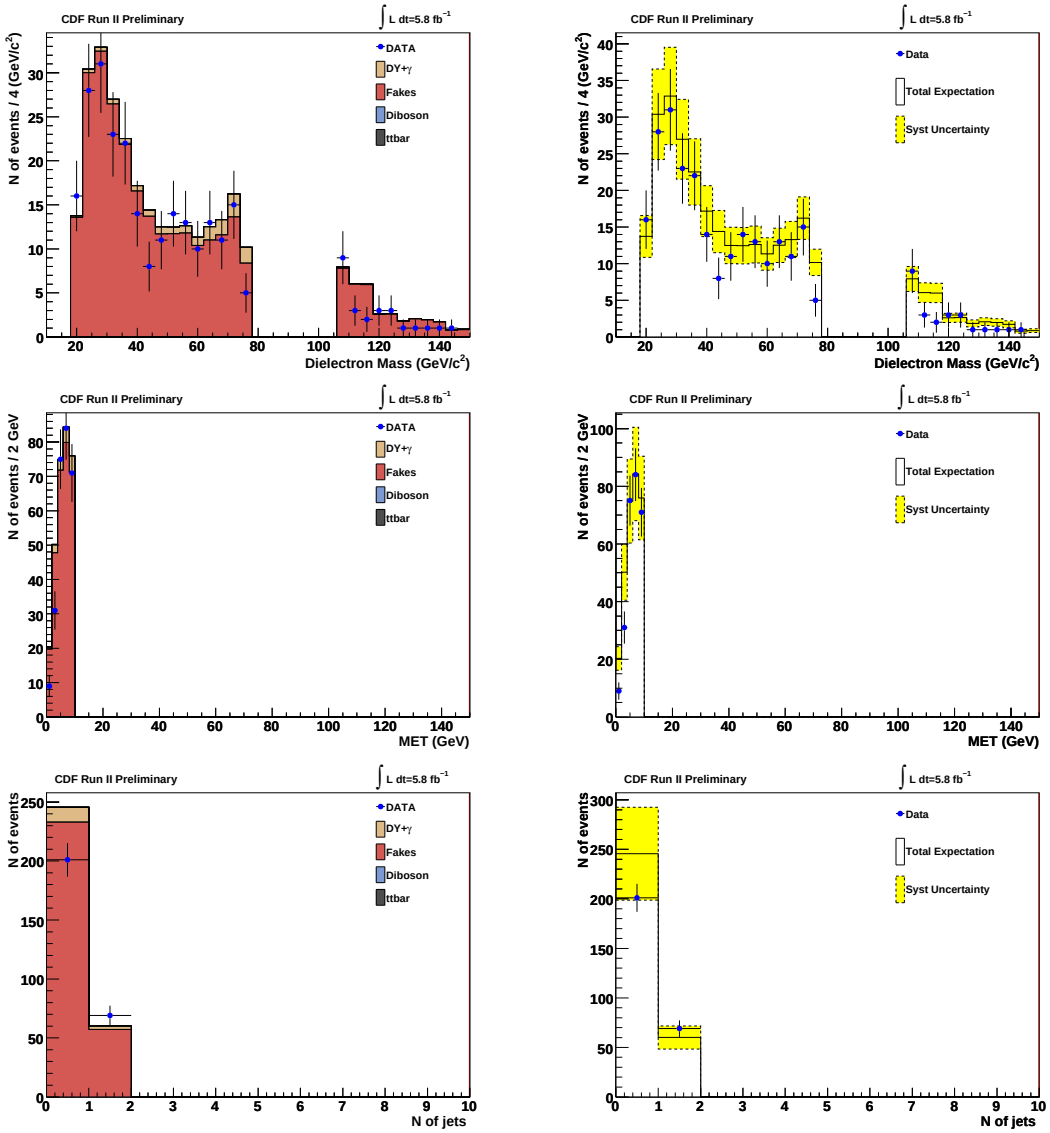

Figure D.26: Dielectron mass, $\not\!\!E_T$ and jet multiplicity of the ee+isotrack events for data and SM prediction in region 3 ($\not\!\!E_T < 10, N_{\text{jet}} \leq 1, !Z$). Plots on the right show the total systematic uncertainty in the expectation (yellow band).

D.5 Kinematic Variables for Region 4

In this section we show the invariant mass, $\not\!\!E_T$ and jet multiplicity in the control region defined by: $\not\!\!E_T < 10, N_{\text{jet}} \geq 2, !Z$

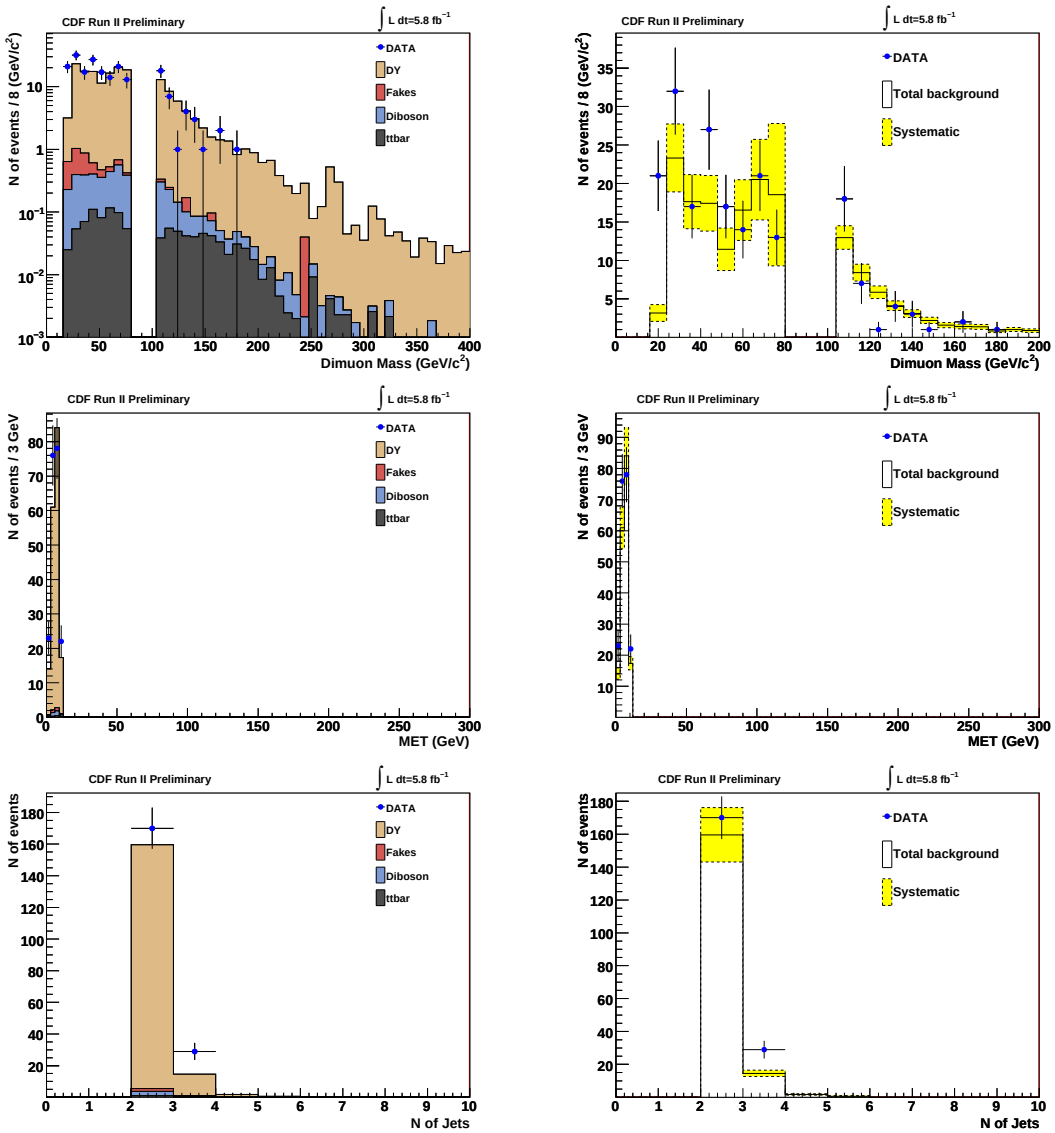

Figure D.27: Dimuon mass, $\not\!\!E_T$ and jet multiplicity for data and SM prediction in region 4 ($\not\!\!E_T < 10, N_{\text{jet}} \geq 2, !Z$). Plots on the right show the total systematic uncertainty in the expectation (yellow band).

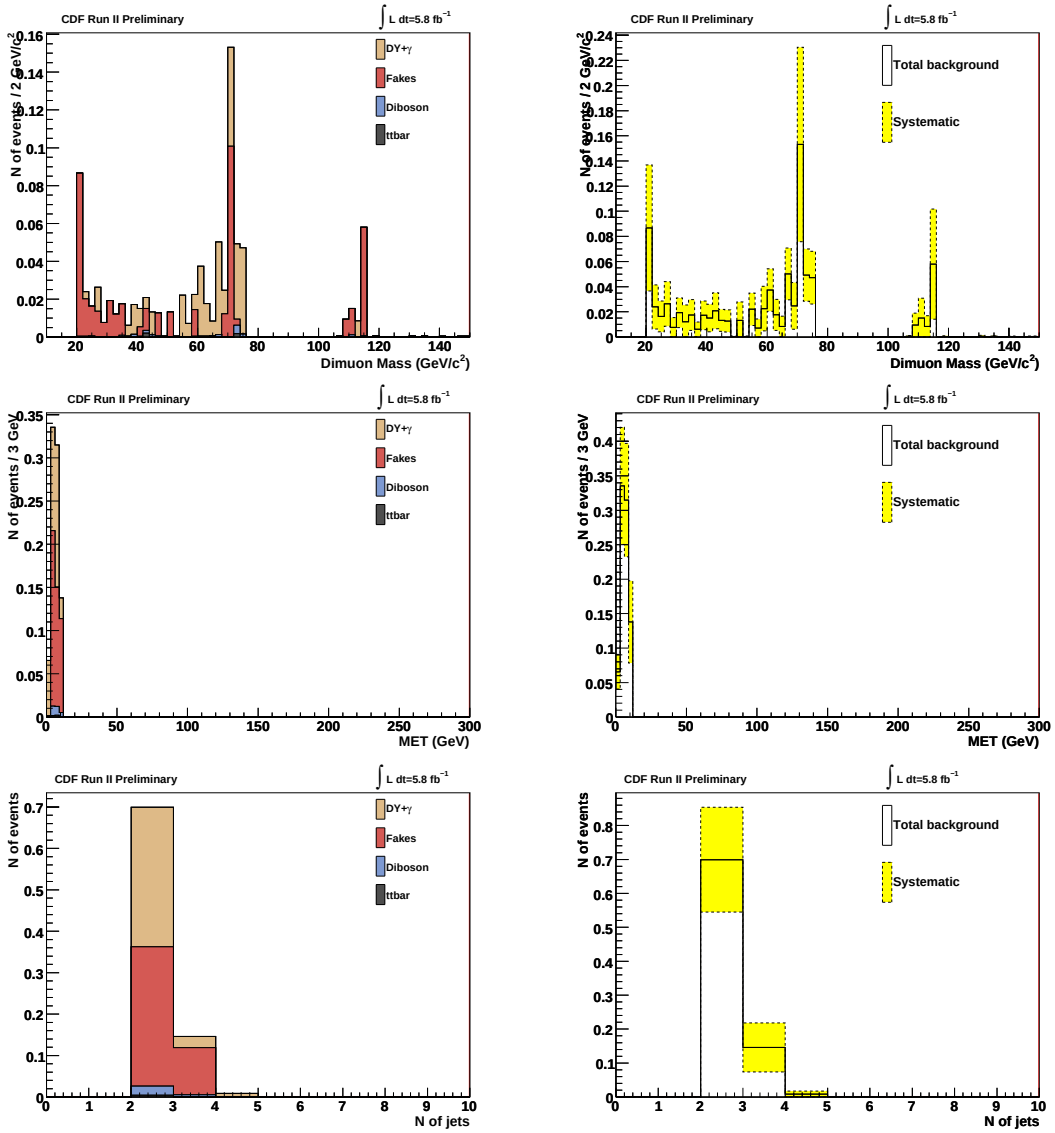

Figure D.28: Dimuon mass, $\not\!\!E_T$ and jet multiplicity of $\mu\mu$+lepton(e,μ,τ) events for data and SM prediction in region 4 ($\not\!\!E_T < 10, N_{\rm jet} \geq 2, !Z$). Plots on the right show the total systematic uncertainty in the expectation (yellow band).

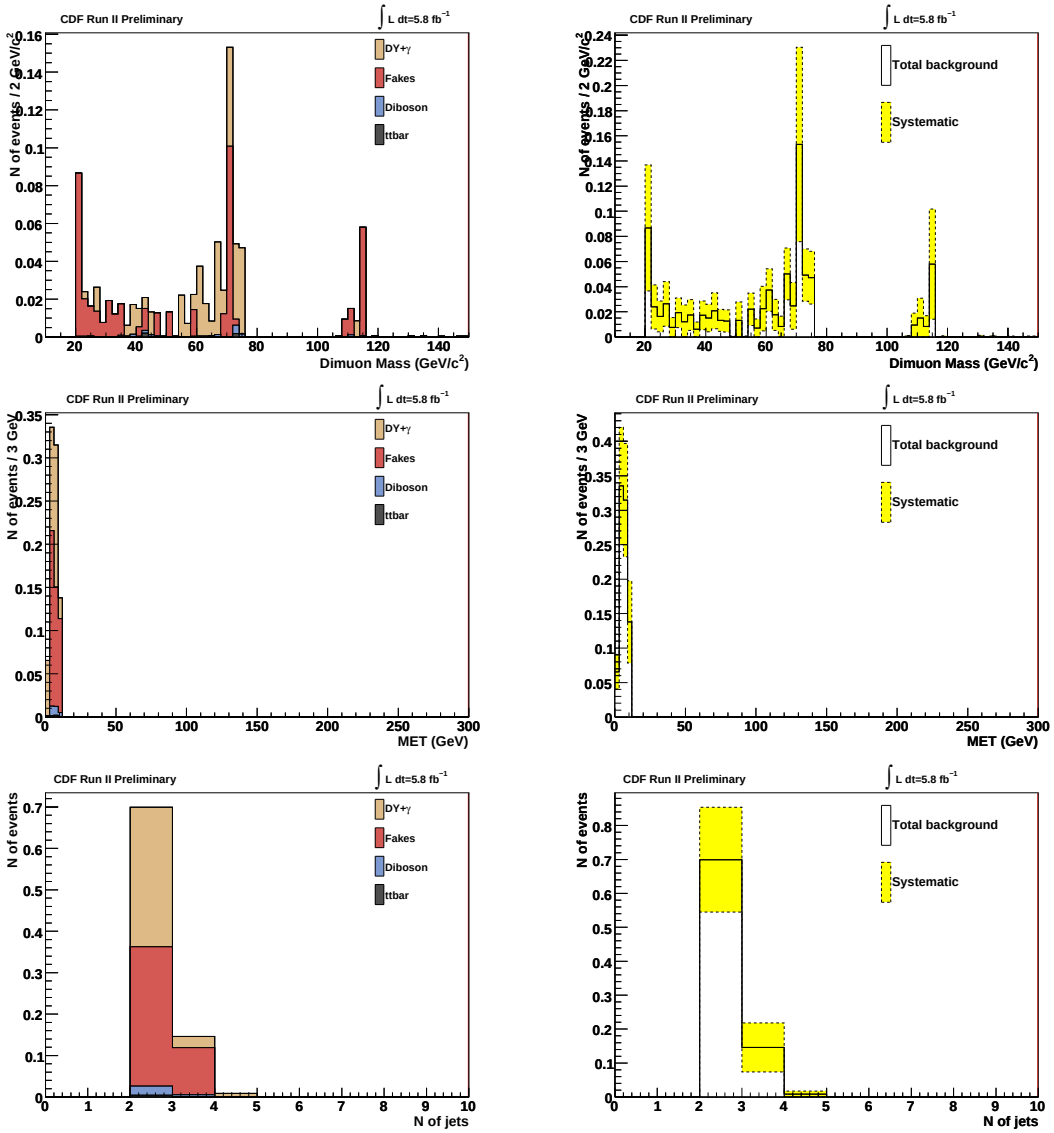

Figure D.29: Dimuon mass, $\not\!\!E_T$ and jet multiplicity of $\mu\mu$+isotrack events for data and SM prediction in region 4 ($\not\!\!E_T < 10, N_{\text{jet}} \geq 2, !Z$). Plots on the right show the total systematic uncertainty in the expectation (yellow band).

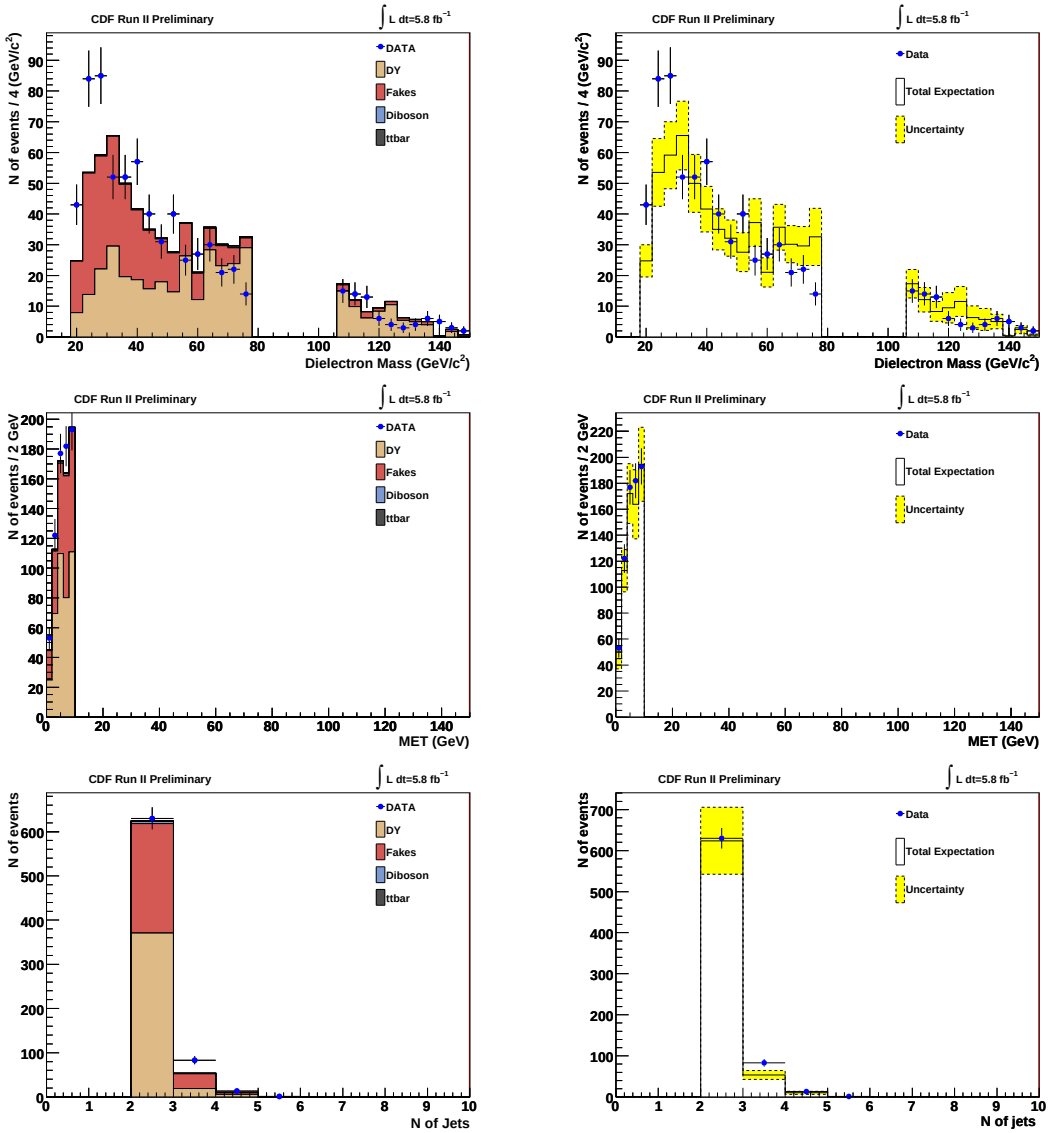

Figure D.30: Dielectron mass, $\not\!\!E_T$ and jet multiplicity for data and SM prediction in region 4 ($\not\!\!E_T < 10, N_{\text{jet}} \geq 2, !Z$). Plots on the right show the total systematic uncertainty in the expectation (yellow band).

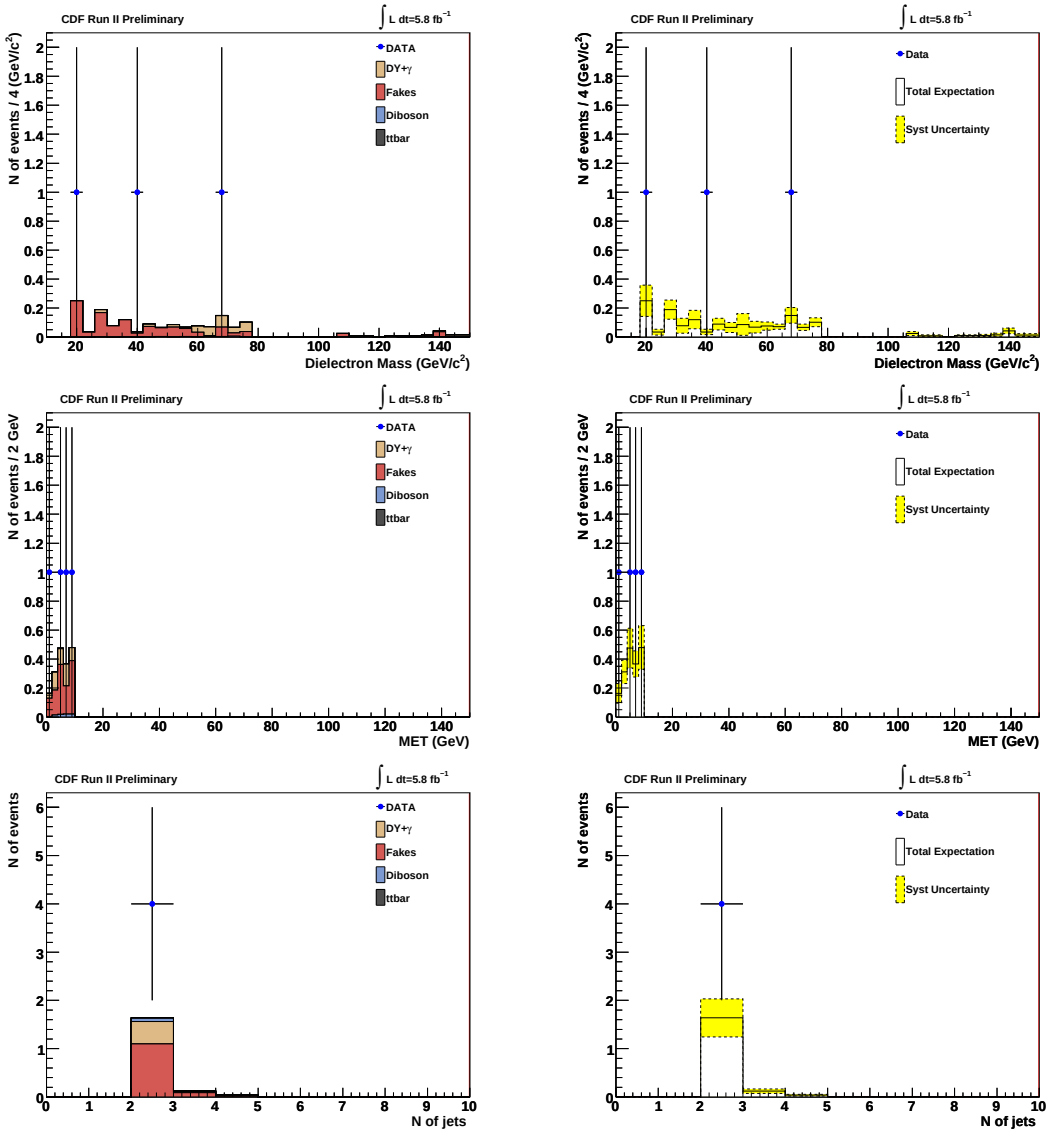

Figure D.31: Dielectron mass, $\not\!\!E_T$ and jet multiplicity of the ee+lepton(e,μ,τ) events for data and SM prediction in region 4 ($\not\!\!E_T < 10, N_{\text{jet}} \geq 2, !Z$). Plots on the right show the total systematic uncertainty in the expectation (yellow band).

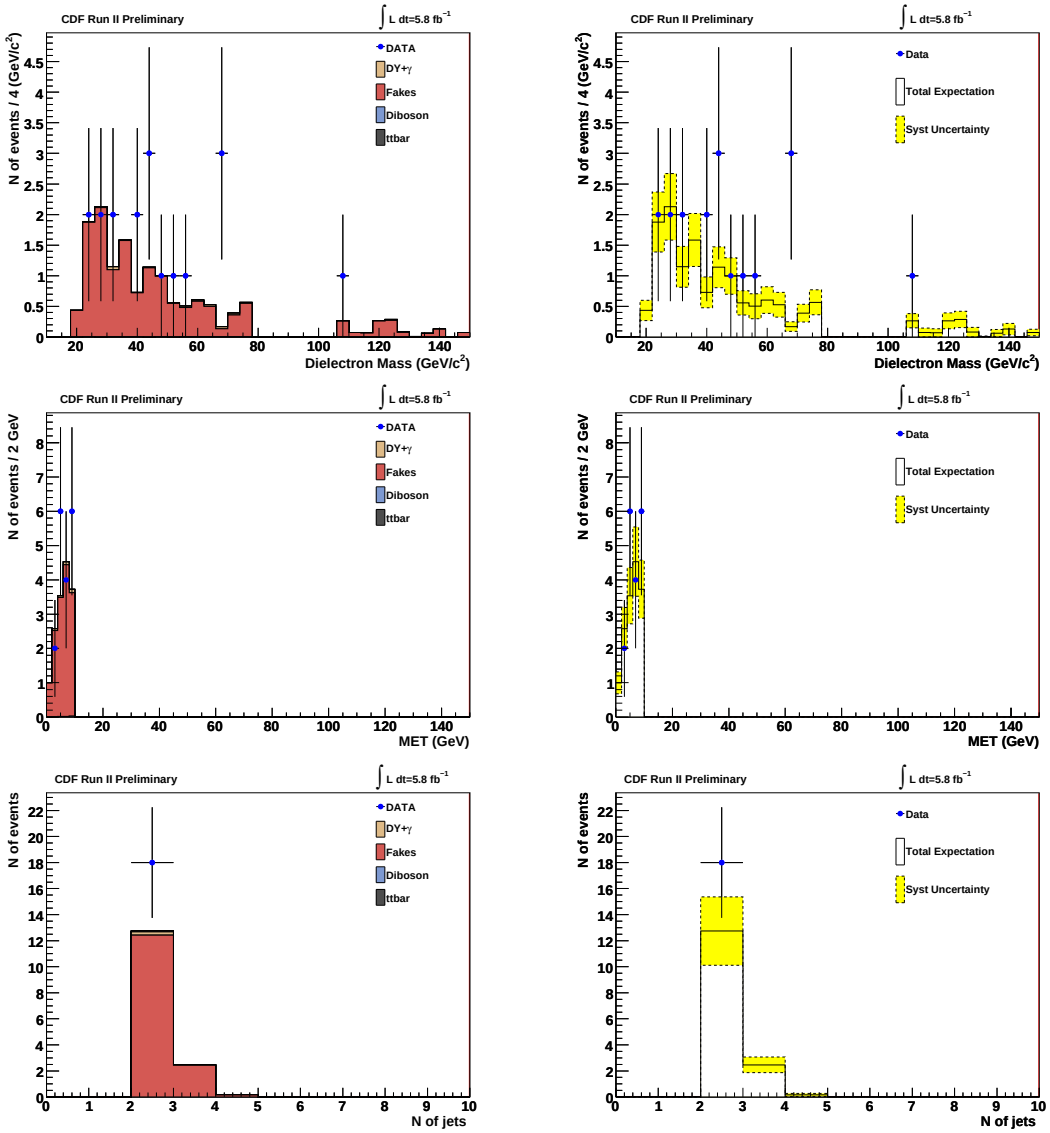

Figure D.32: Dielectron mass, $\not\!\!E_T$ and jet multiplicity of the ee+isotrack events for data and SM prediction in region 4 ($\not\!\!E_T < 10, N_{\text{jet}} \geq 2, !Z$). Plots on the right show the total systematic uncertainty in the expectation (yellow band).

D.6 Kinematic Variables for Region 5

In this section we show the invariant mass, $\not\!\!E_T$ and jet multiplicity in the control region defined by: $\not\!\!E_T < 10, N_{\text{jet}} \leq 1, Z$

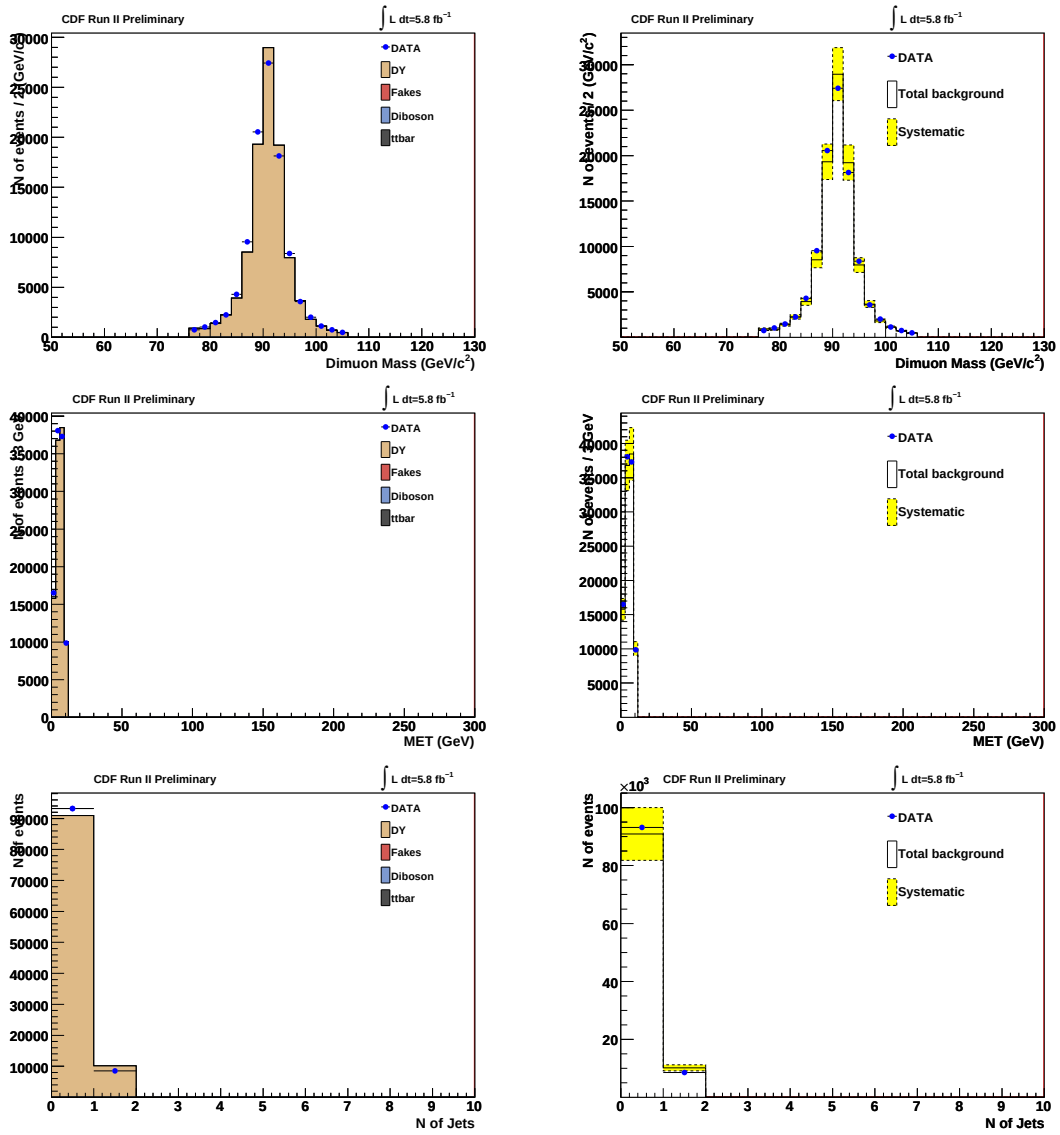

Figure D.33: Dimuon mass, $\not\!\!E_T$ and jet multiplicity for data and SM prediction in region 5 ($\not\!\!E_T < 10, N_{\text{jet}} \leq 1, Z$). Plots on the right show the total systematic uncertainty in the expectation (yellow band).

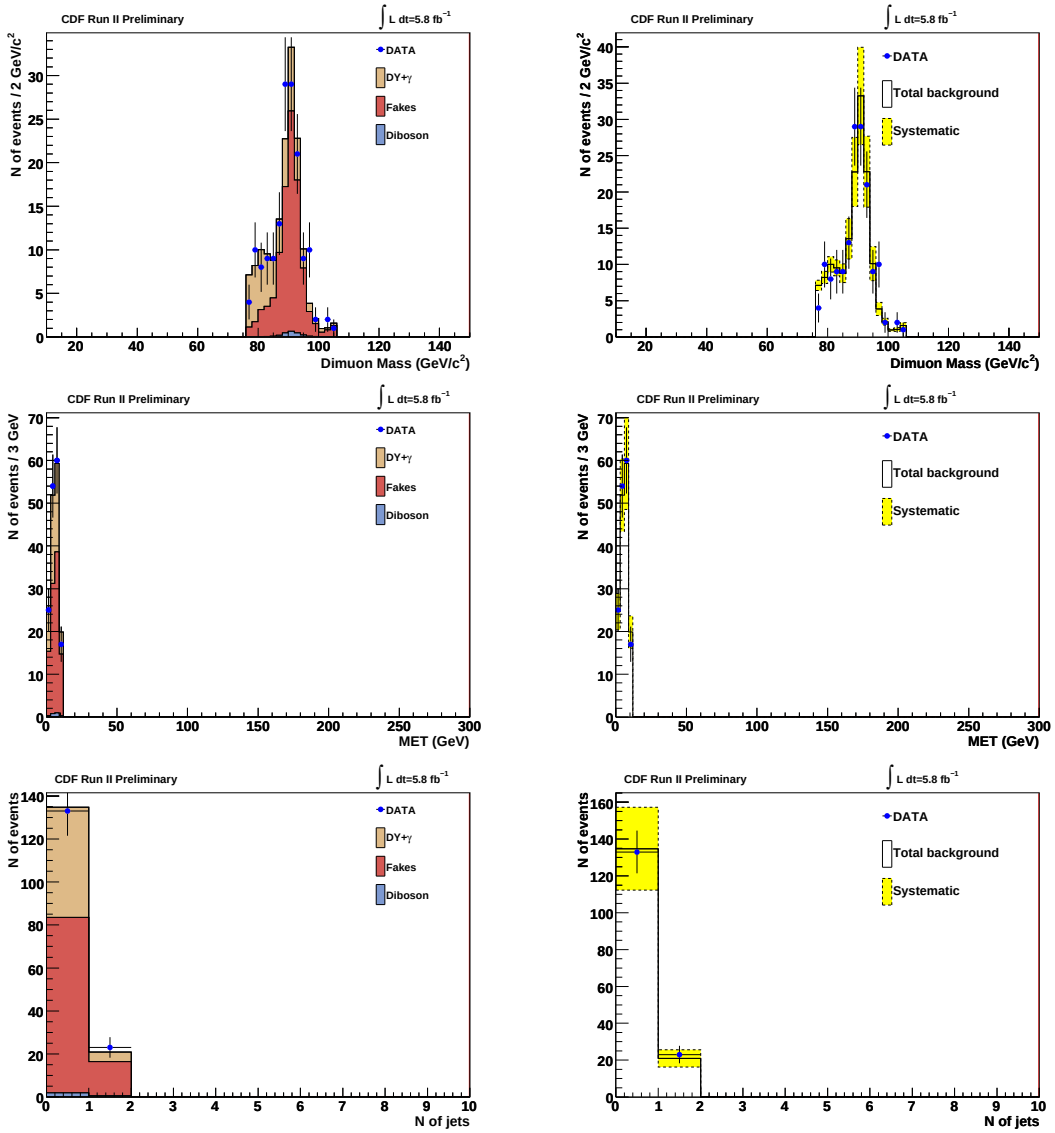

Figure D.34: Dimuon mass, $\not\!\!E_T$ and jet multiplicity of $\mu\mu$+lepton(e,μ,τ) events for data and SM prediction in region 5 ($\not\!\!E_T < 10, N_{\text{jet}} \leq 1, Z$). Plots on the right show the total systematic uncertainty in the expectation (yellow band).

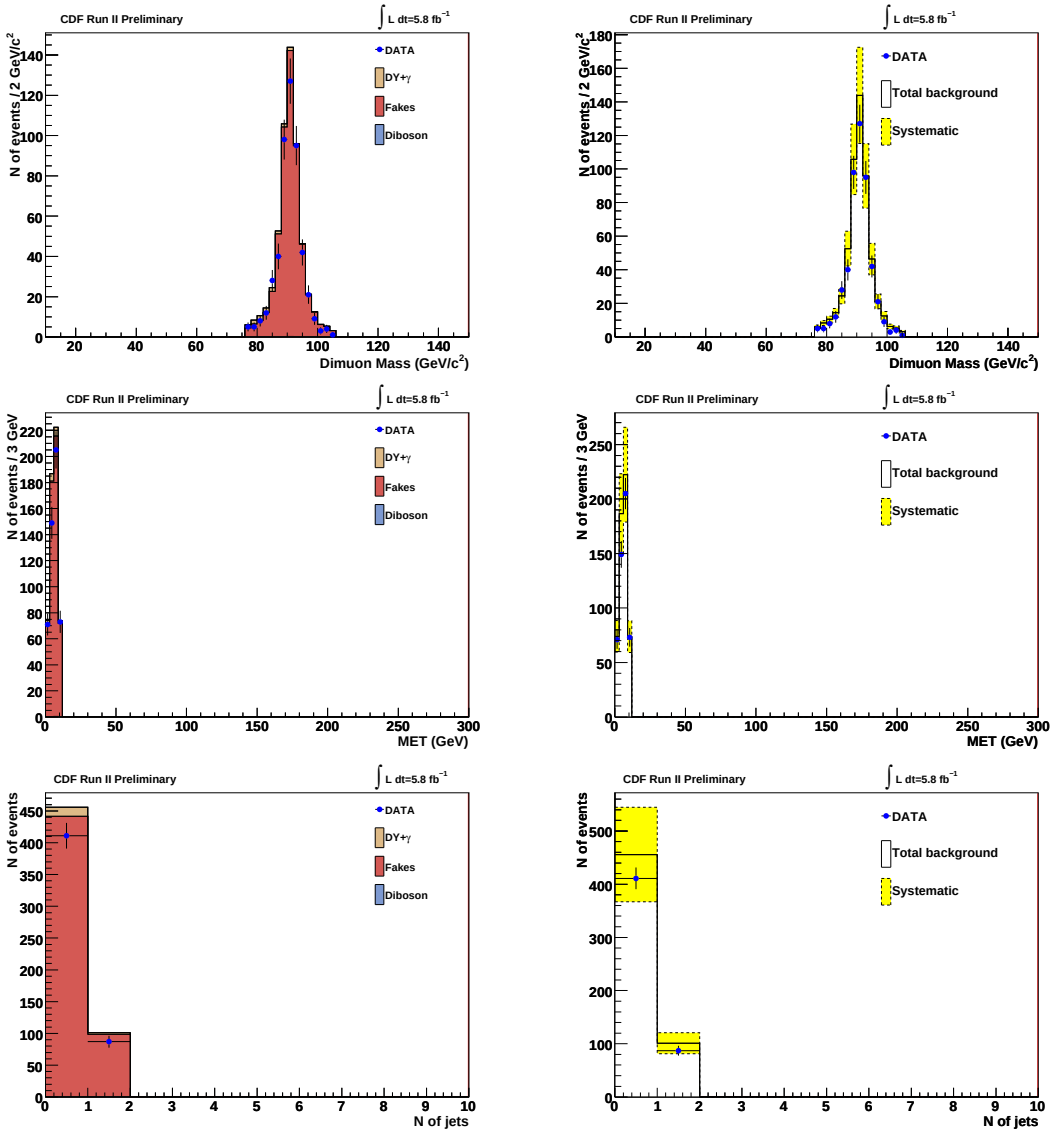

Figure D.35: Dimuon mass, $\not\!\!E_T$ and jet multiplicity of $\mu\mu$+isotrack events for data and SM prediction in region 5 ($\not\!\!E_T < 10, N_{\text{jet}} \leq 1, Z$). Plots on the right show the total systematic uncertainty in the expectation (yellow band).

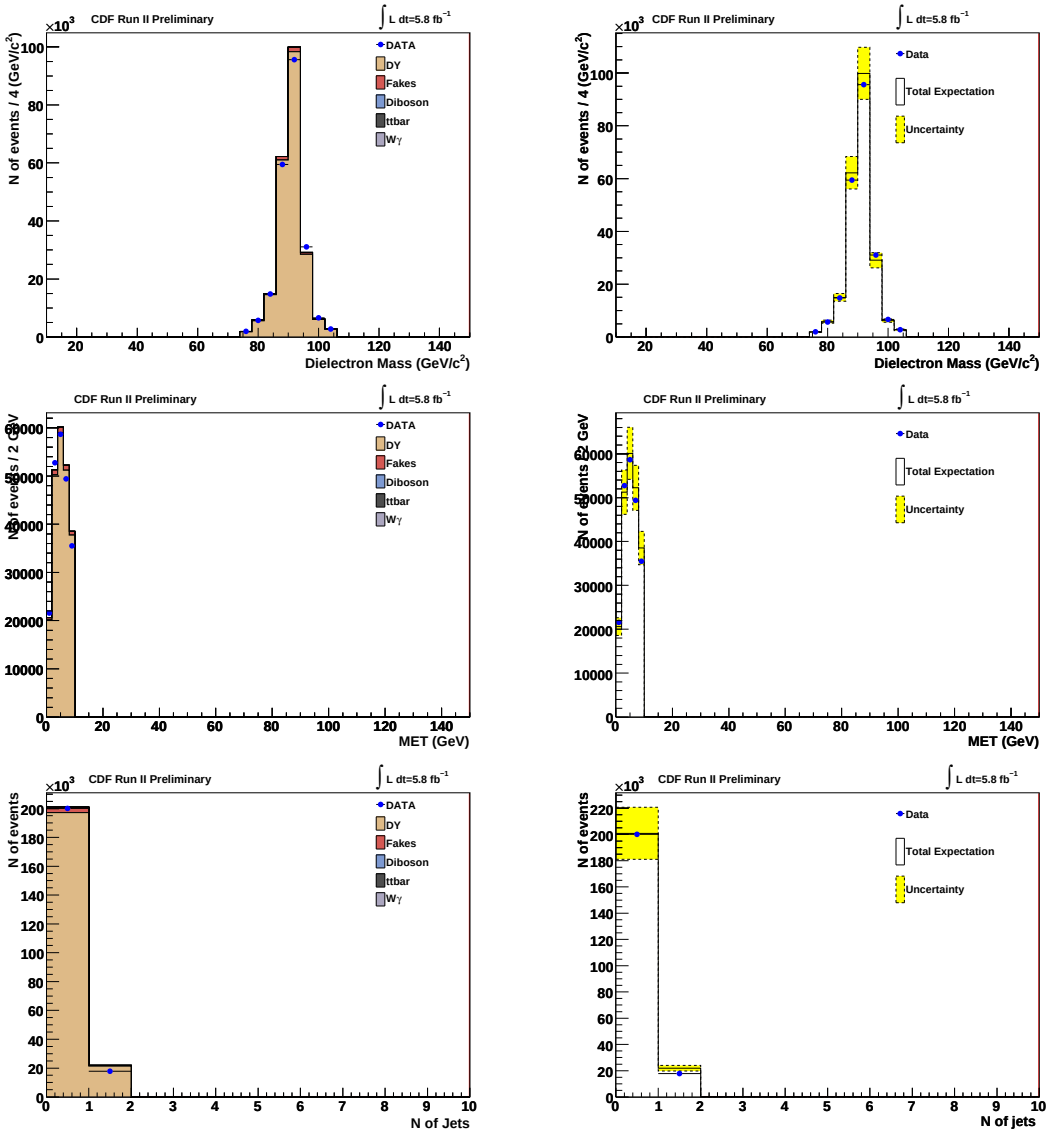

Figure D.36: Dielectron mass, $\not\!\!E_T$ and jet multiplicity for data and SM prediction in region 5 ($\not\!\!E_T < 10, N_{\text{jet}} \leq 1, Z$). Plots on the right show the total systematic uncertainty in the expectation (yellow band).

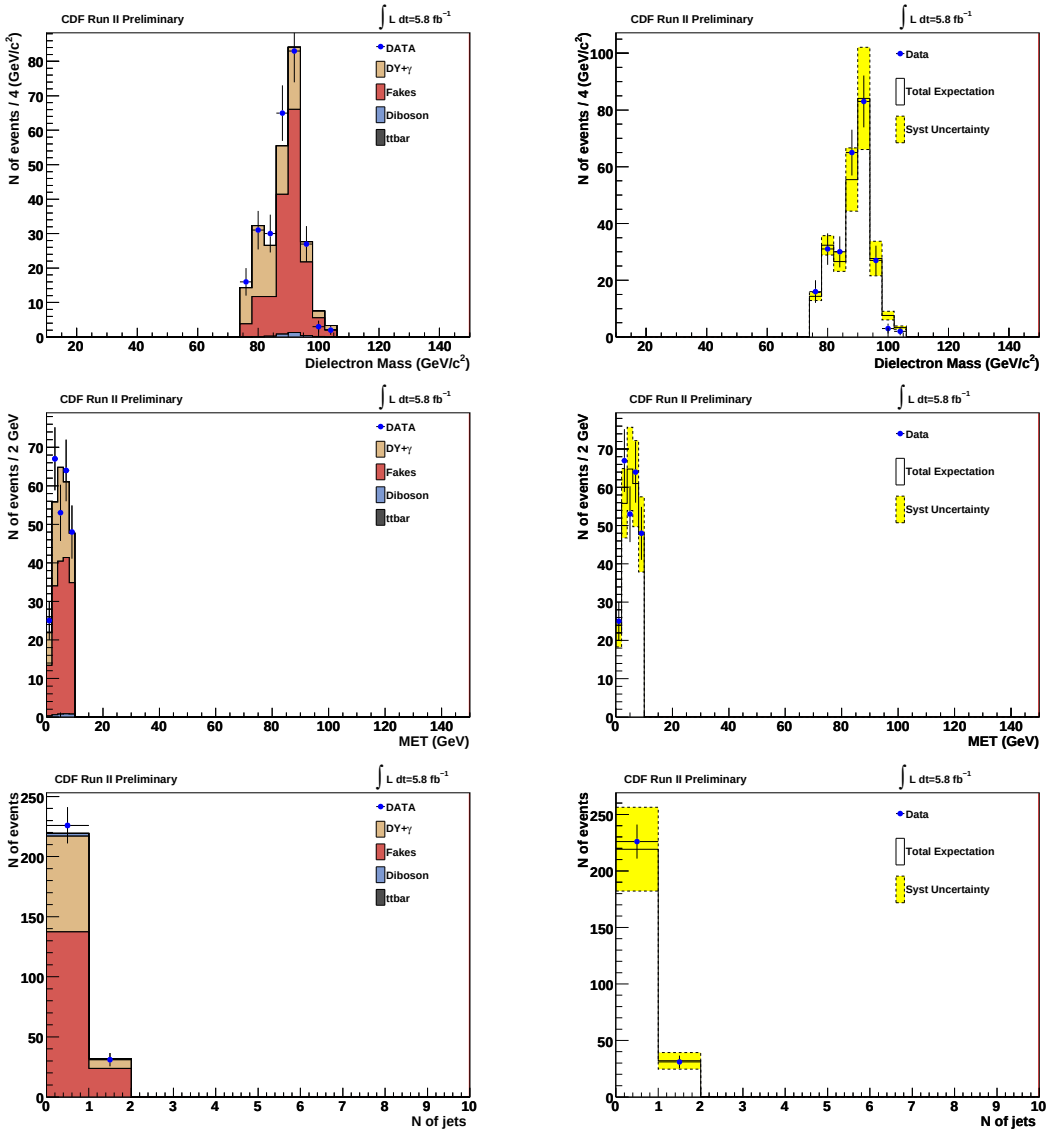

Figure D.37: Dielectron mass, $\not\!\!E_T$ and jet multiplicity of the ee+lepton(e,μ,τ) events for data and SM prediction in region 5 ($\not\!\!E_T < 10, N_{\text{jet}} \leq 1, Z$). Plots on the right show the total systematic uncertainty in the expectation (yellow band).

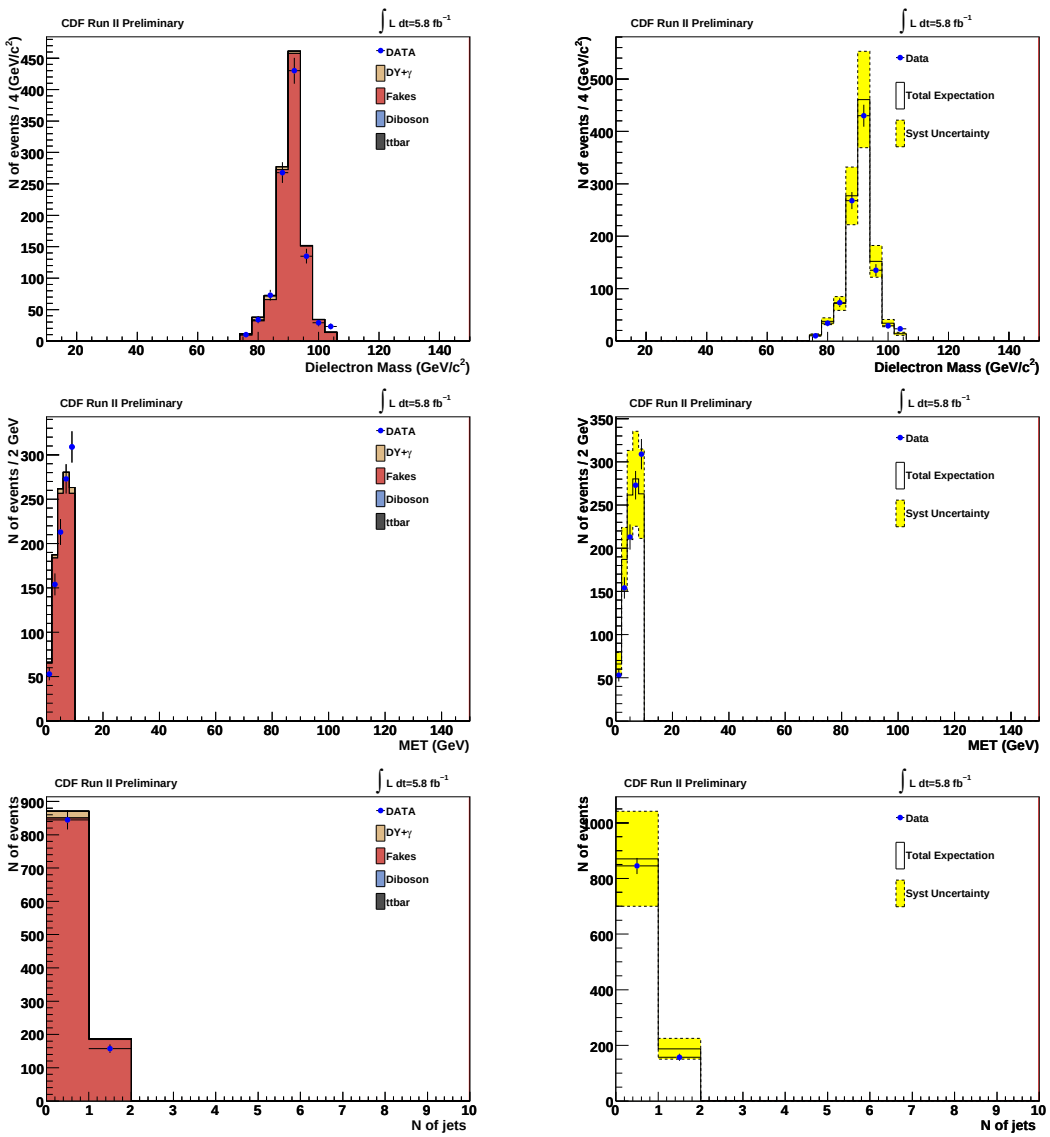

Figure D.38: Dielectron mass, $\not\!\!E_T$ and jet multiplicity of the ee+isotrack events for data and SM prediction in region 5 ($\not\!\!E_T < 10, N_{\text{jet}} \leq 1, Z$). Plots on the right show the total systematic uncertainty in the expectation (yellow band).

D.7 Kinematic Variables for Region 6

In this section we show the invariant mass, $\not\!\!E_T$ and jet multiplicity in the control region defined by: $\not\!\!E_T < 10, N_{\text{jet}} \geq 2, Z$

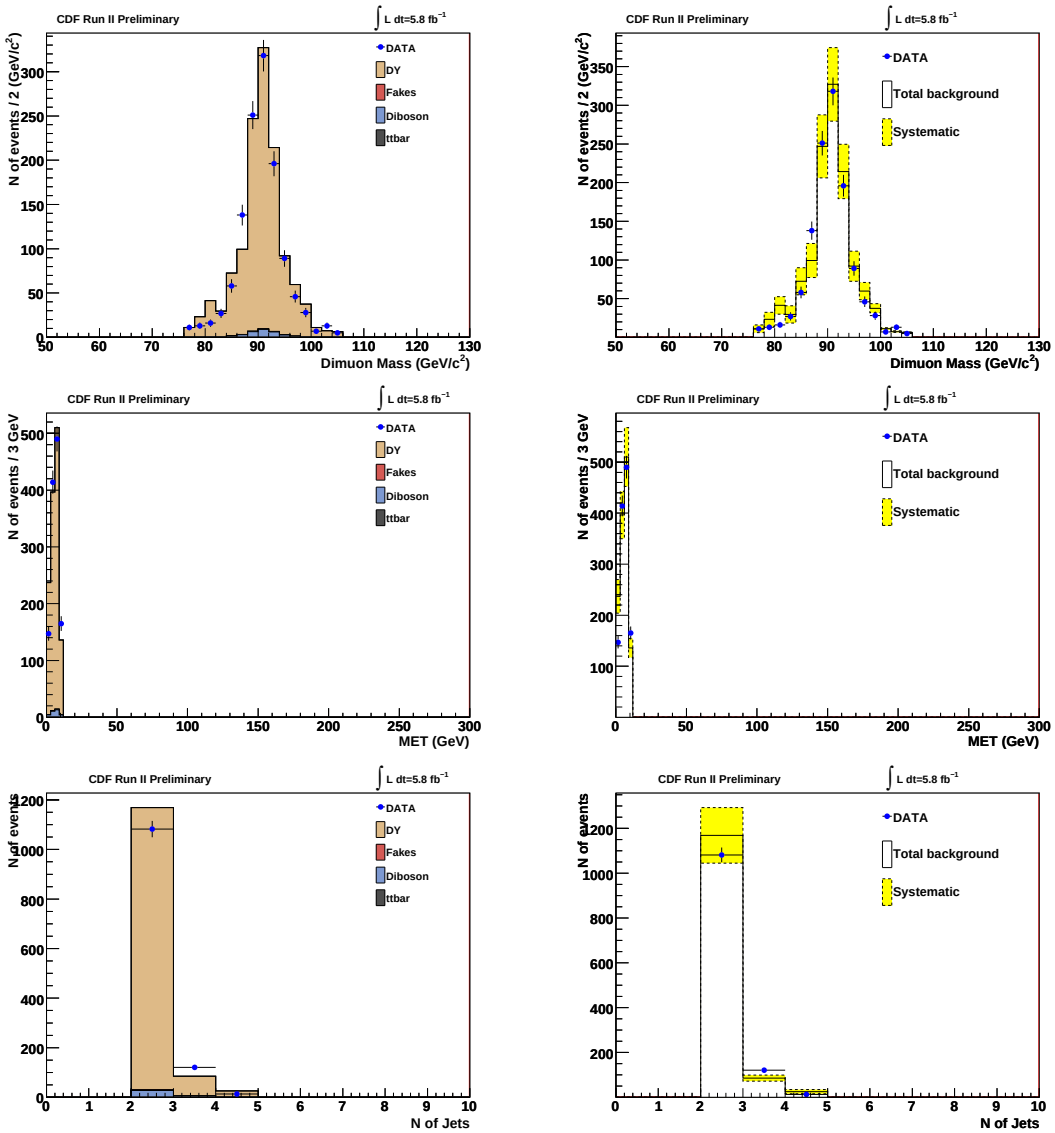

Figure D.39: Dimuon mass, $\not\!\!E_T$ and jet multiplicity for data and SM prediction in region 6 ($\not\!\!E_T < 10, N_{\text{jet}} \geq 2, Z$). Plots on the right show the total systematic uncertainty in the expectation (yellow band).

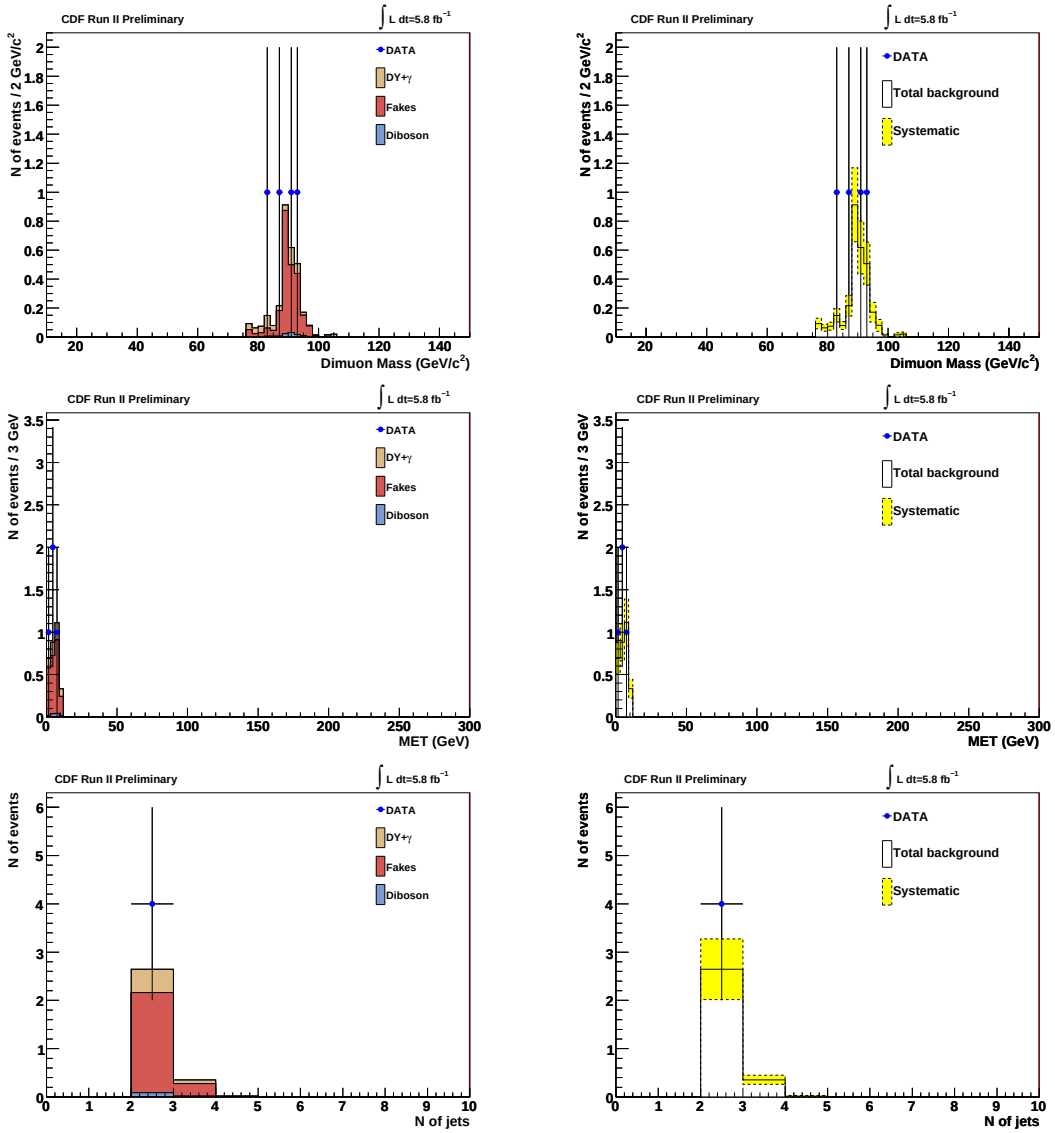

Figure D.40: Dimuon mass, $\not\!\!E_T$ and jet multiplicity of $\mu\mu$+lepton(e,μ,τ) events for data and SM prediction in region 6 ($\not\!\!E_T < 10, N_{\text{jet}} \geq 2, Z$). Plots on the right show the total systematic uncertainty in the expectation (yellow band).

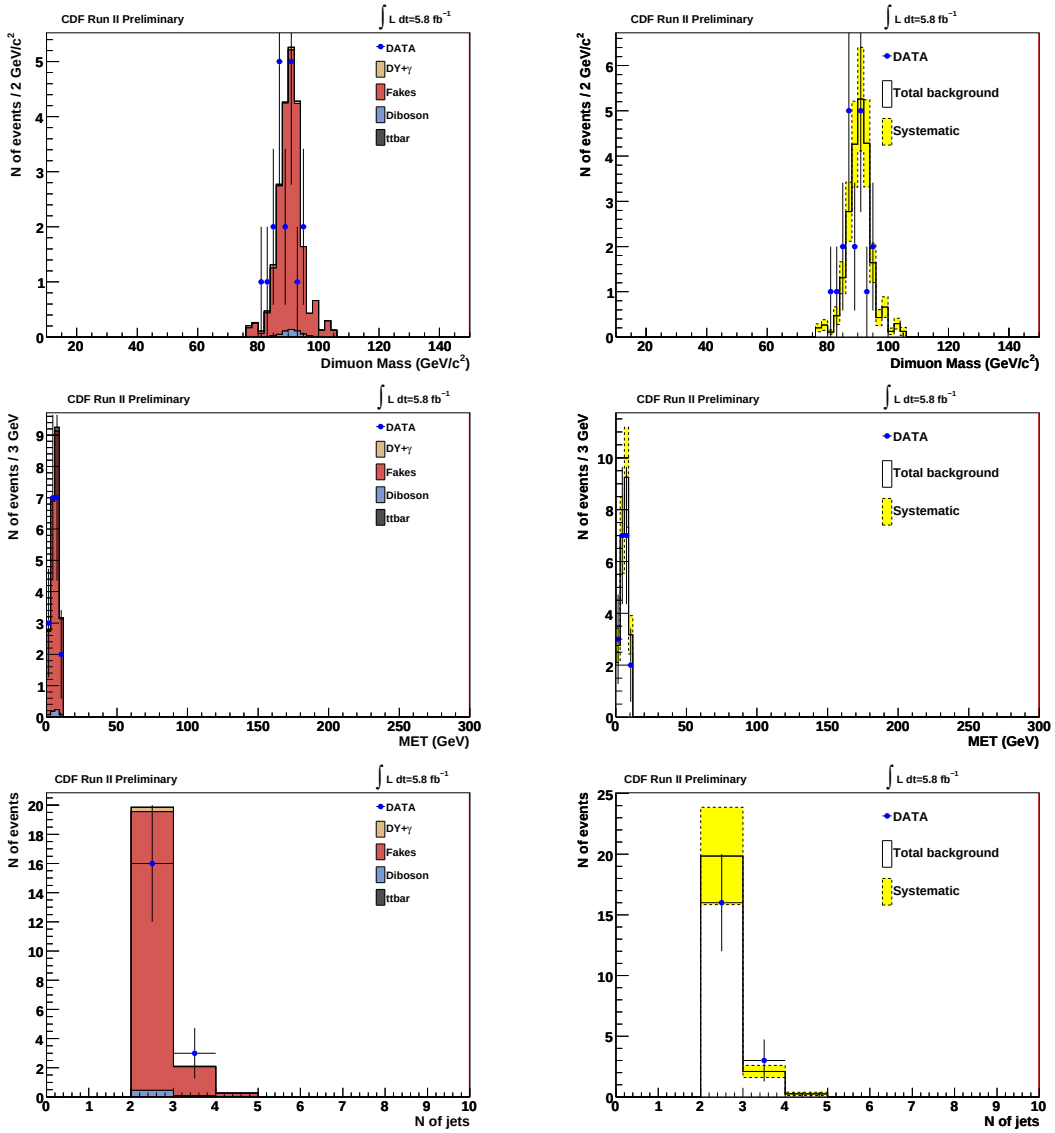

Figure D.41: Dimuon mass, $\not\!\!E_T$ and jet multiplicity of $\mu\mu$+isotrack events for data and SM prediction in region 6 ($\not\!\!E_T < 10, N_{\text{jet}} \geq 2, Z$). Plots on the right show the total systematic uncertainty in the expectation (yellow band).

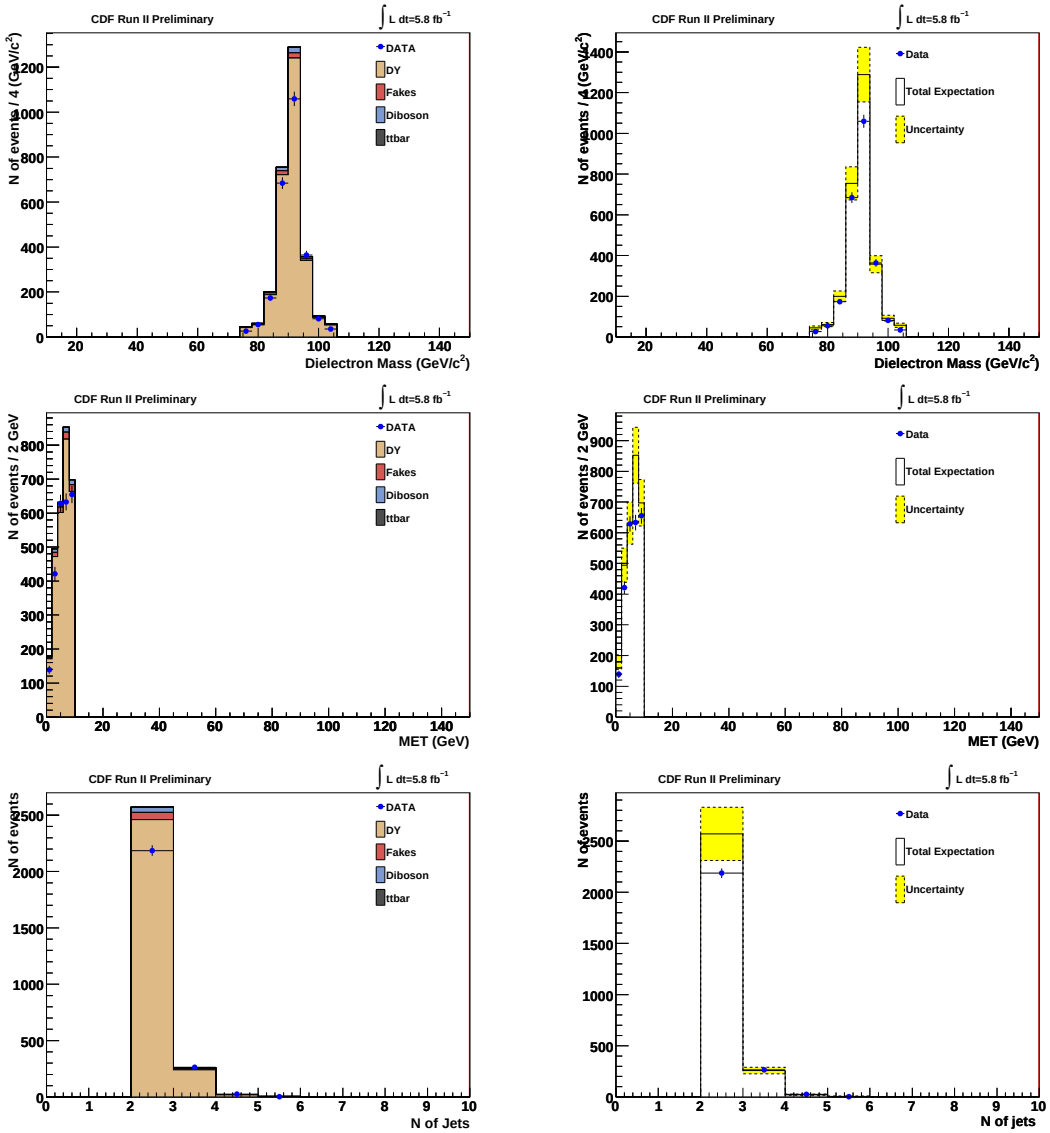

Figure D.42: Dielectron mass, $\not\!\!E_T$ and jet multiplicity for data and SM prediction in region 6 ($\not\!\!E_T < 10, N_{\text{jet}} \geq 2, Z$). Plots on the right show the total systematic uncertainty in the expectation (yellow band).

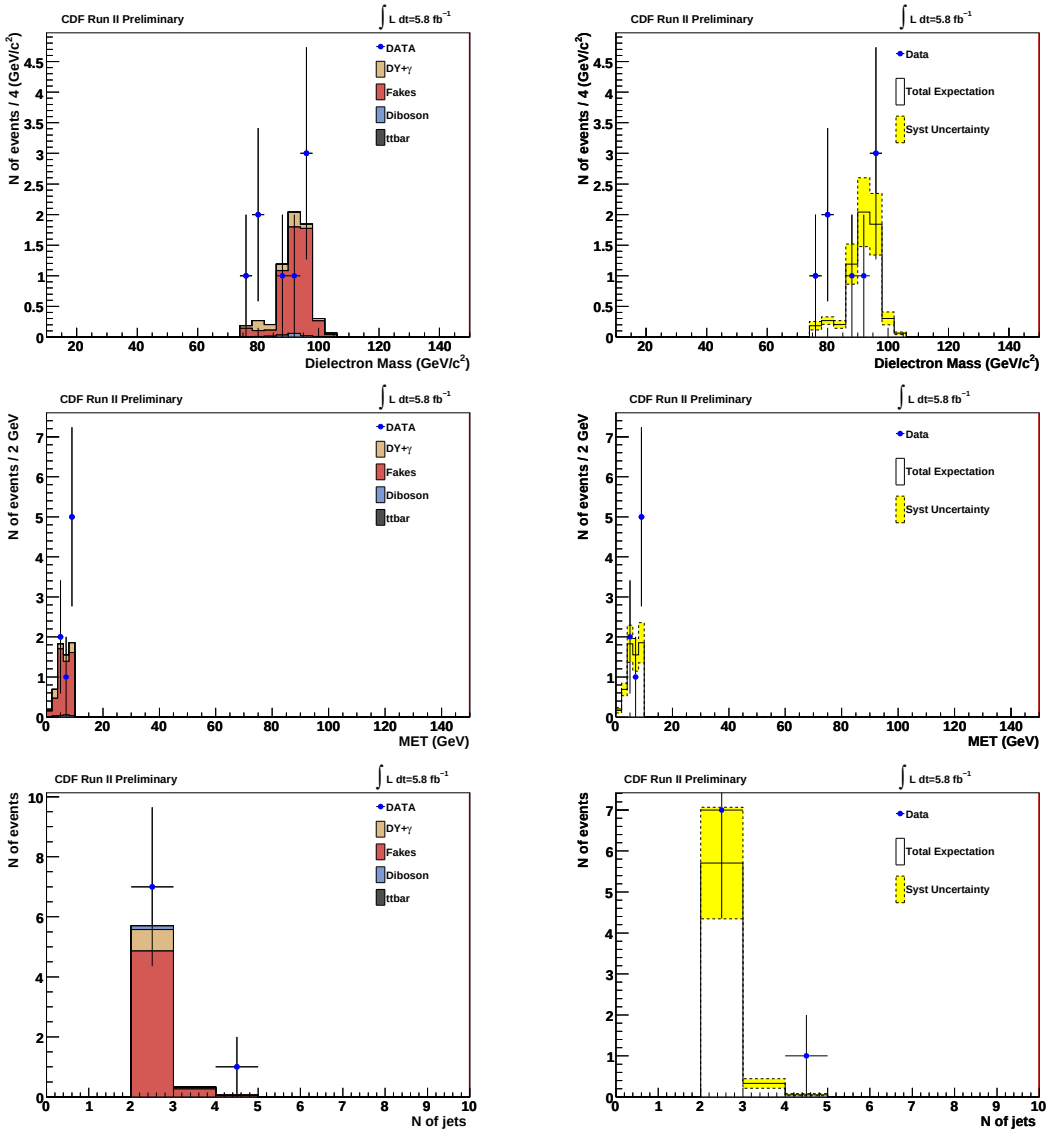

Figure D.43: Dielectron mass, $\not\!\!E_T$ and jet multiplicity of the ee+lepton(e,μ,τ) events for data and SM prediction in region 6 ($\not\!\!E_T < 10, N_{\text{jet}} \geq 2, Z$). Plots on the right show the total systematic uncertainty in the expectation (yellow band).

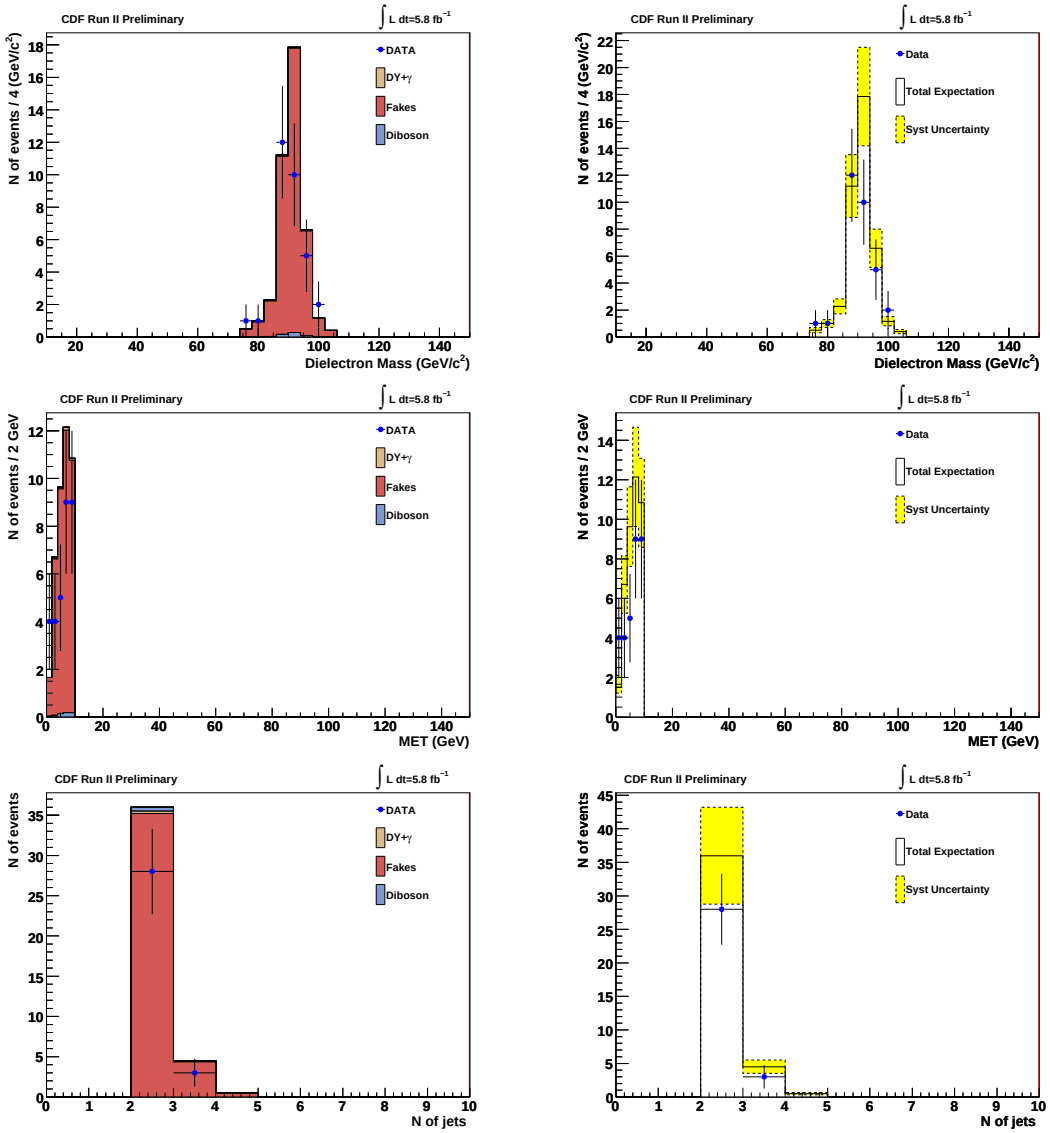

Figure D.44: Dielectron mass, $\not\!\!E_T$ and jet multiplicity of the ee+isotrack events for data and SM prediction in region 6 ($\not\!\!E_T < 10, N_{\text{jet}} \geq 2, Z$). Plots on the right show the total systematic uncertainty in the expectation (yellow band).

D.8 Kinematic Variables for Region 7

In this section we show the invariant mass, $\not\!\!E_T$ and jet multiplicity in the control region defined by: $\not\!\!E_T > 15, N_{\text{jet}} \leq 1, !Z$

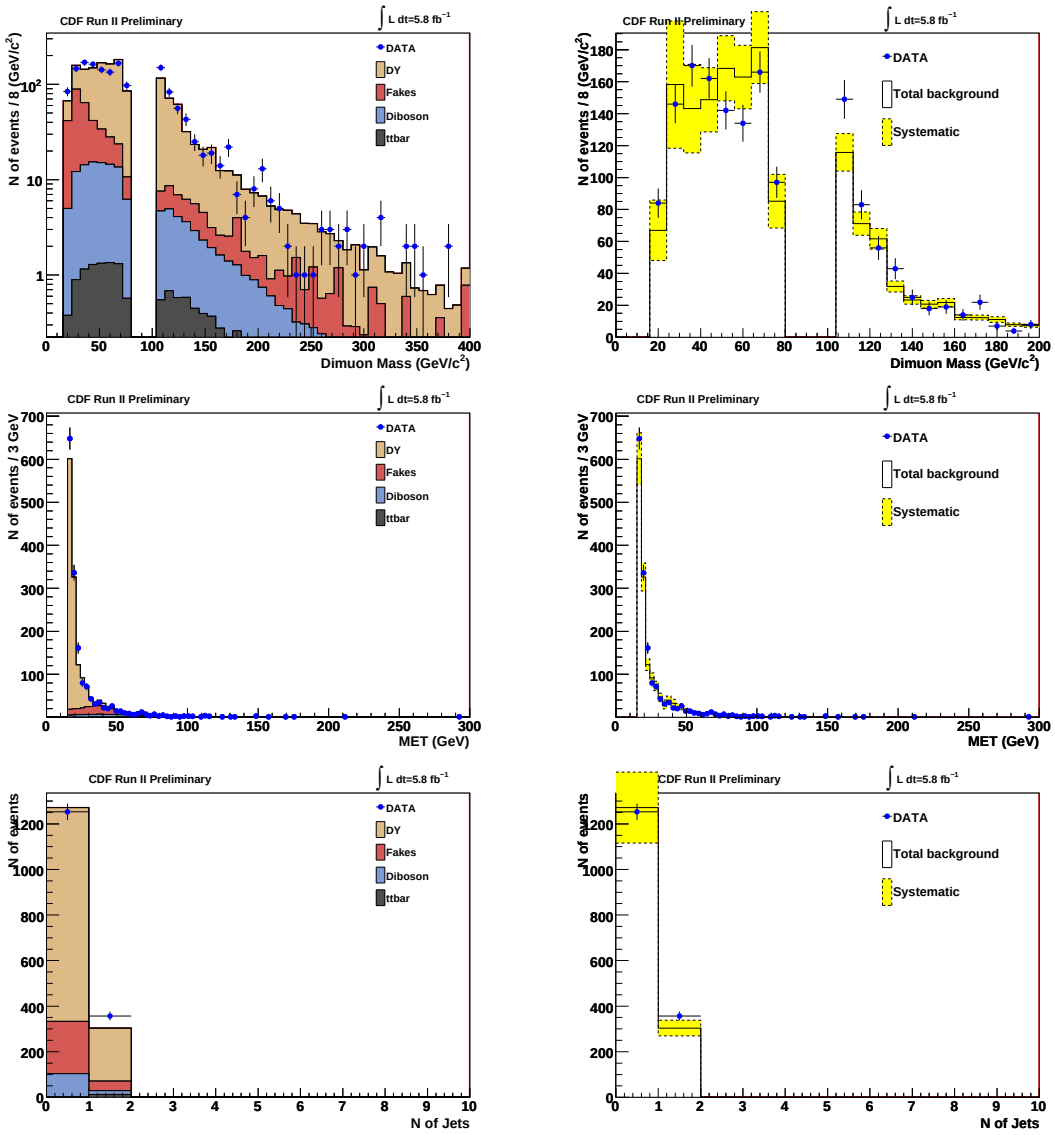

Figure D.45: Dimuon mass, $\not\!\!E_T$ and jet multiplicity for data and SM prediction in region 7 ($\not\!\!E_T > 15, N_{\text{jet}} \leq 1, !Z$). Plots on the right show the total systematic uncertainty in the expectation (yellow band).

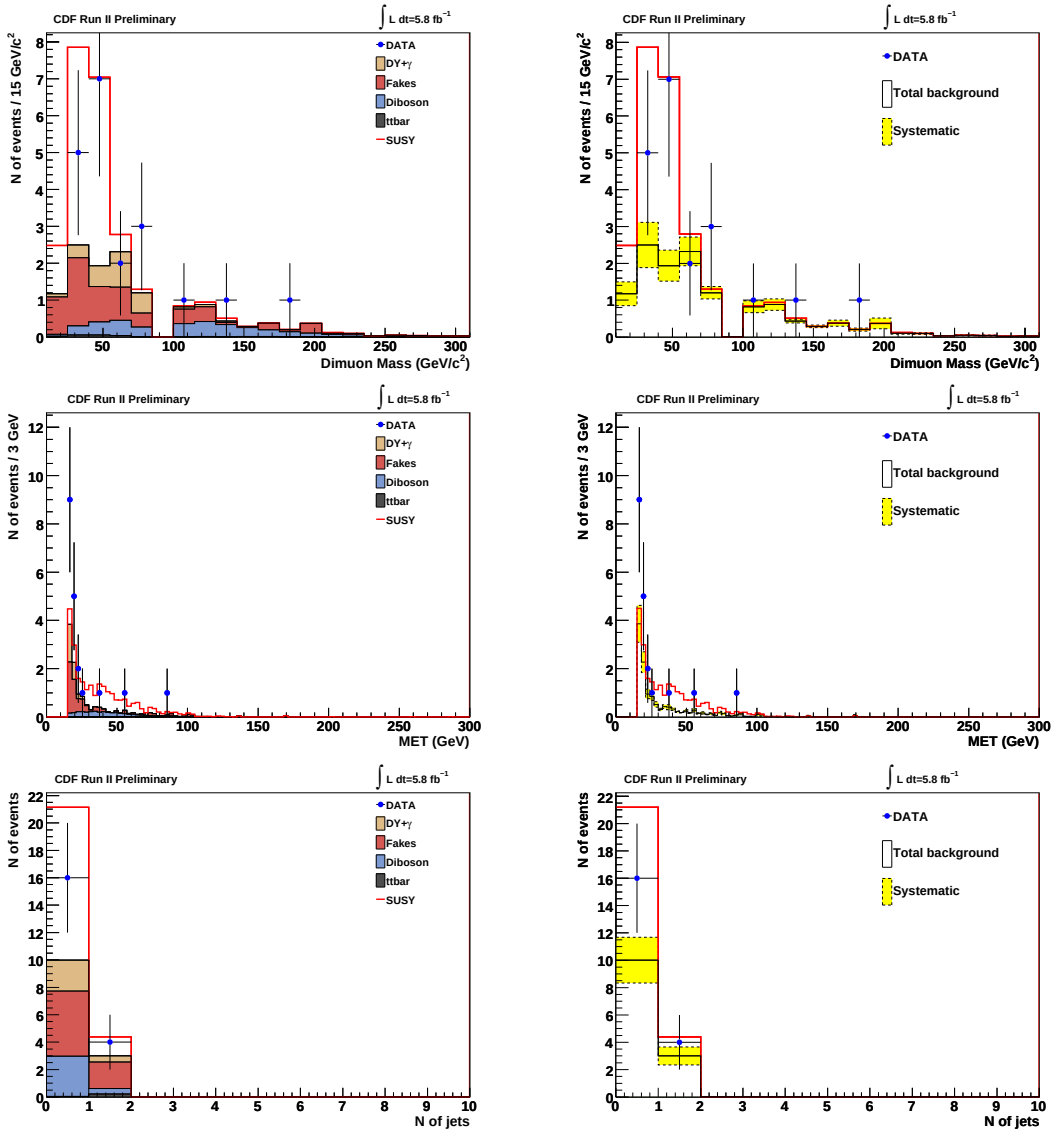

Figure D.46: Dimuon mass, $\not\!\!E_T$ and jet multiplicity of $\mu\mu$+lepton(e,μ,τ) events for data and SM prediction in region 7 ($\not\!\!E_T > 15, N_{\text{jet}} \leq 1, !Z$). Plots on the right show the total systematic uncertainty in the expectation (yellow band).

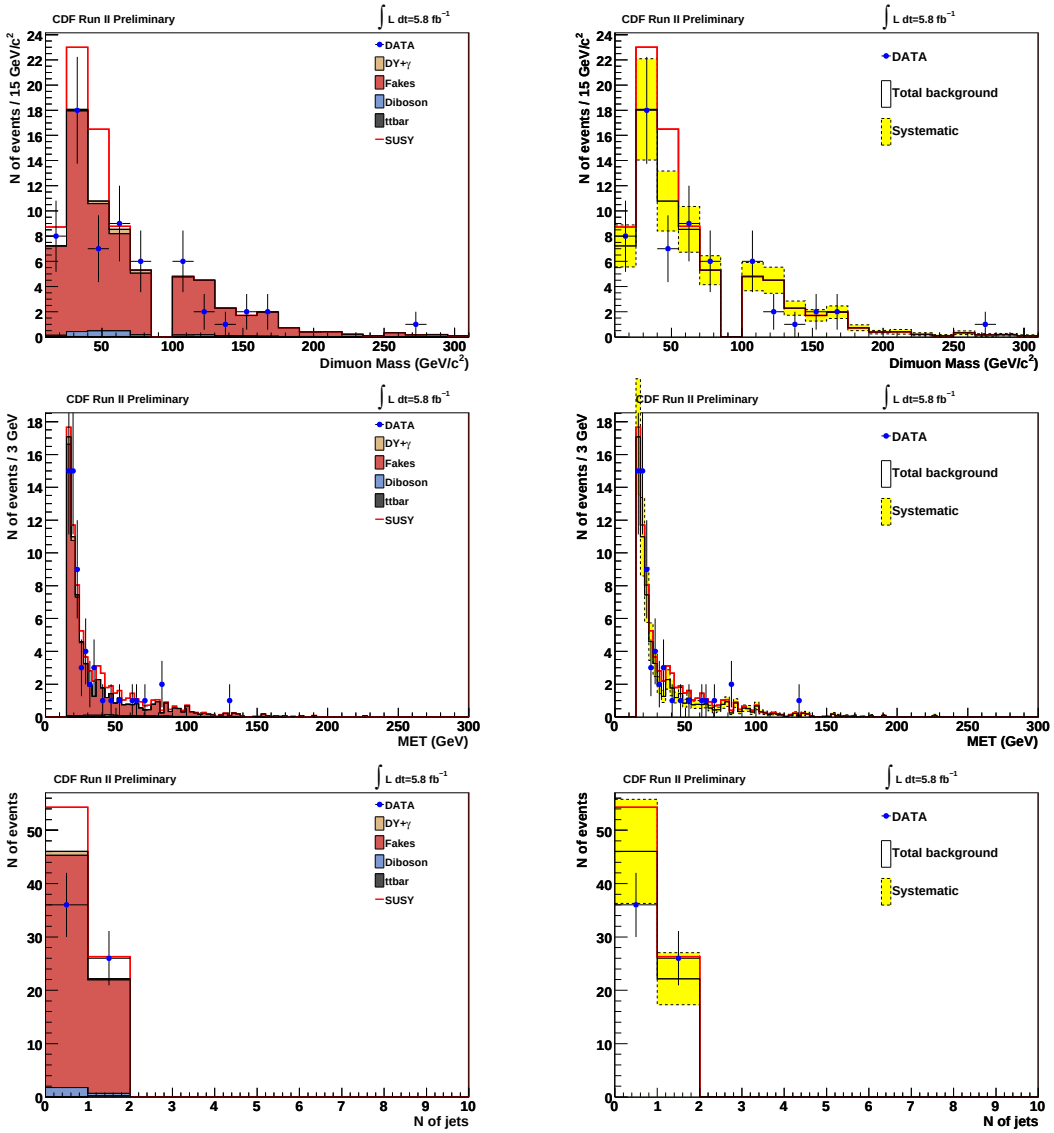

Figure D.47: Dimuon mass, $\not\!\!E_T$ and jet multiplicity of $\mu\mu$+isotrack events for data and SM prediction in region 7 ($\not\!\!E_T > 15, N_{\text{jet}} \leq 1, !Z$). Plots on the right show the total systematic uncertainty in the expectation (yellow band).

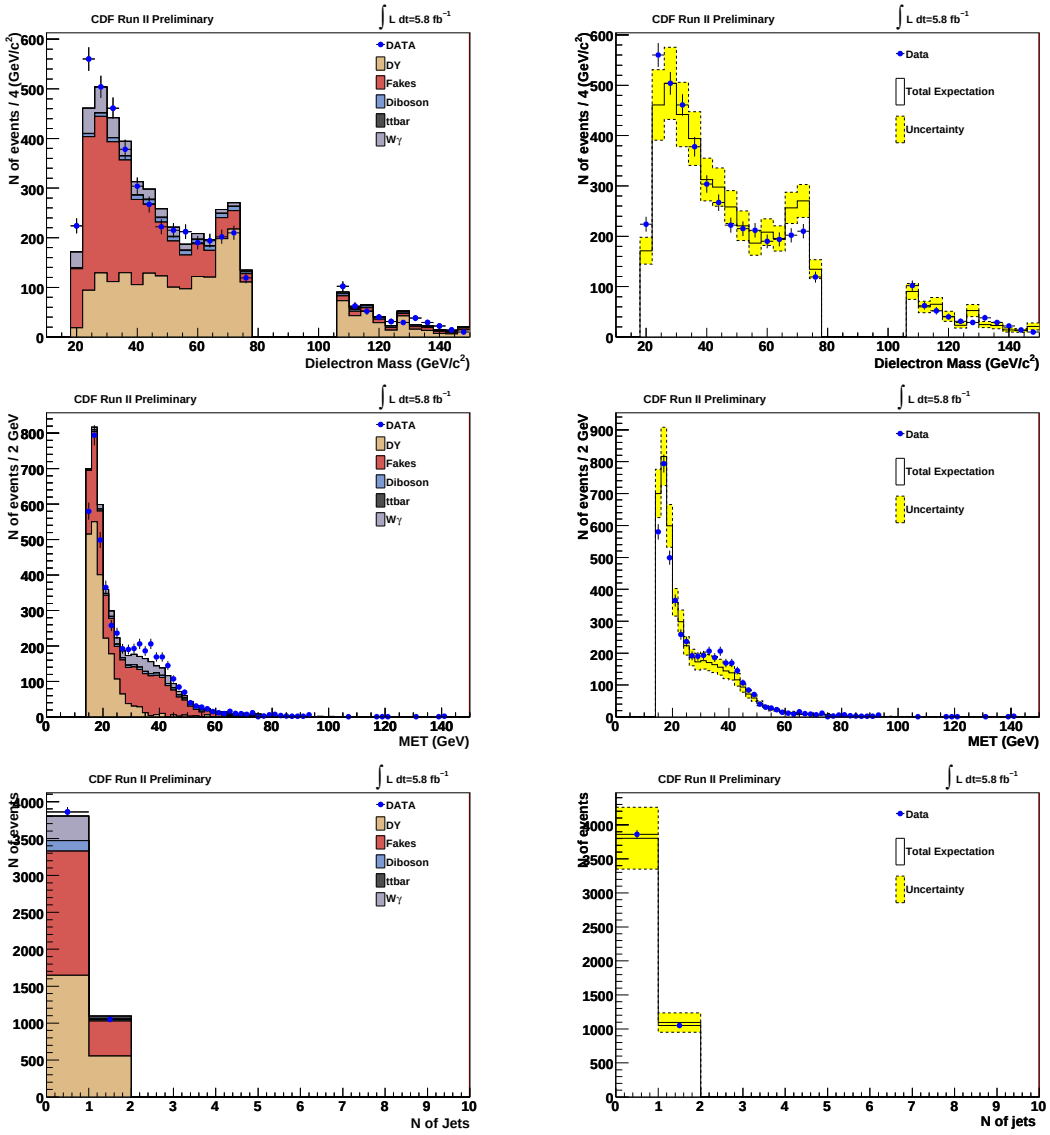

Figure D.48: Dielectron mass, $\not\!\!E_T$ and jet multiplicity for data and SM prediction in region 7 ($\not\!\!E_T > 15, N_{\text{jet}} \leq 1, !Z$). Plots on the right show the total systematic uncertainty in the expectation (yellow band).

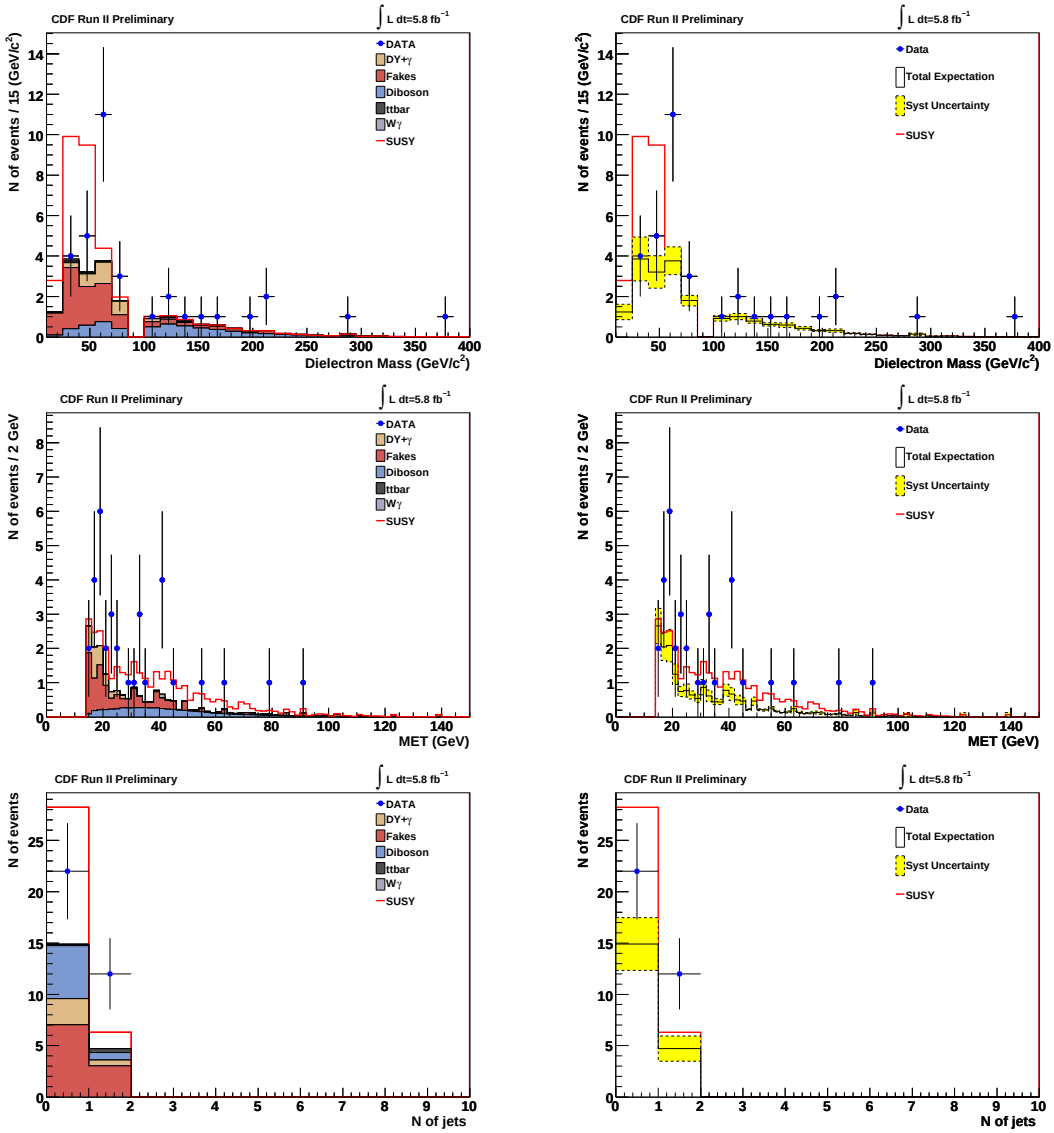

Figure D.49: Dielectron mass, $\not\!\!E_T$ and jet multiplicity of the ee+lepton(e,μ,τ) events for data and SM prediction in region 7 ($\not\!\!E_T > 15, N_{\text{jet}} \leq 1, !Z$). Plots on the right show the total systematic uncertainty in the expectation (yellow band).

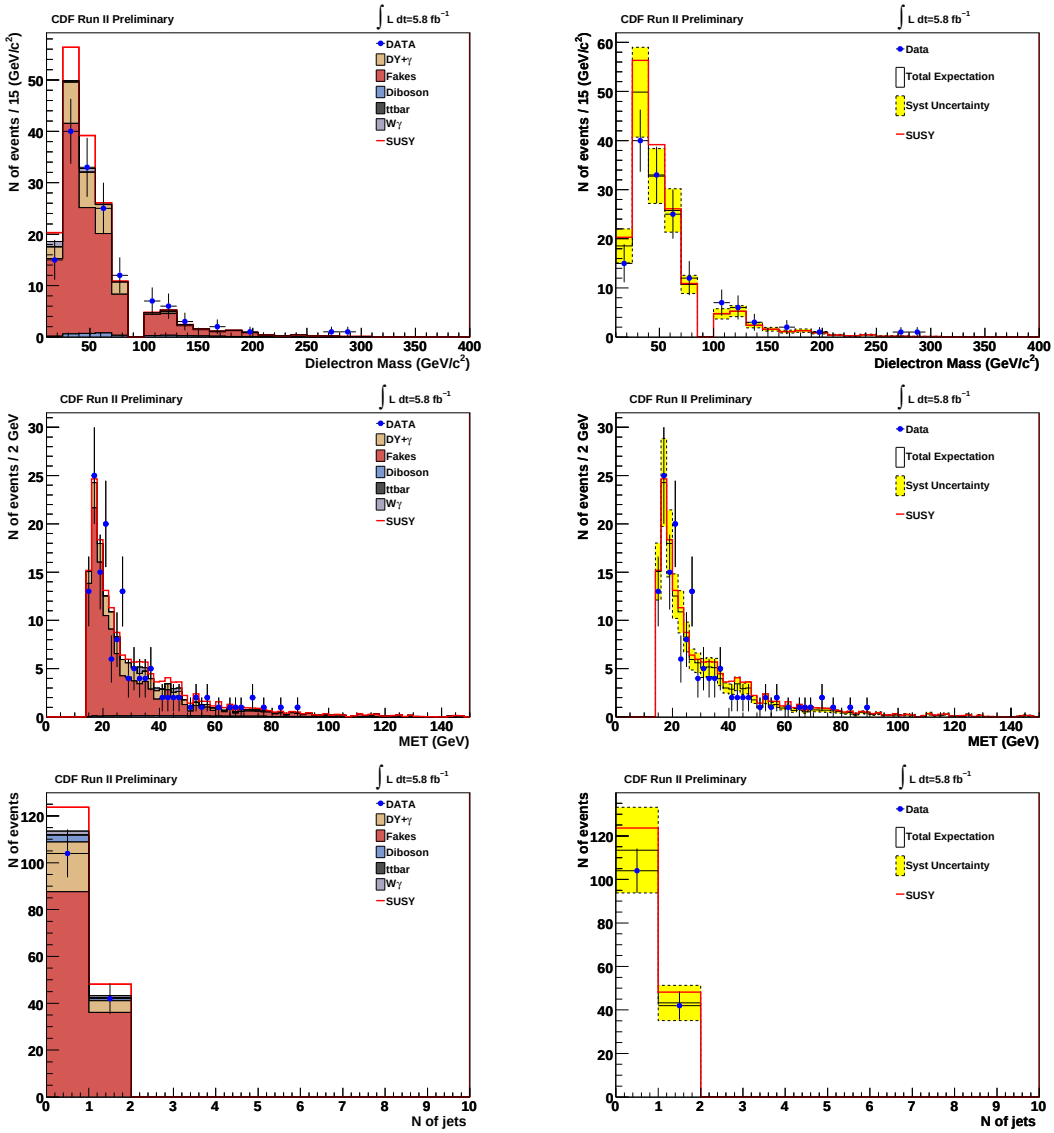

Figure D.50: Dielectron mass, $\not\!\!E_T$ and jet multiplicity of the ee+isotrack events for data and SM prediction in region 7 ($\not\!\!E_T > 15, N_{\text{jet}} \leq 1, !Z$). Plots on the right show the total systematic uncertainty in the expectation (yellow band).

D.9 Kinematic Variables for Region 8

In this section we show the invariant mass, $\not\!\!E_T$ and jet multiplicity in the control region defined by: $\not\!\!E_T > 15, N_{\text{jet}} \geq 2, !Z$

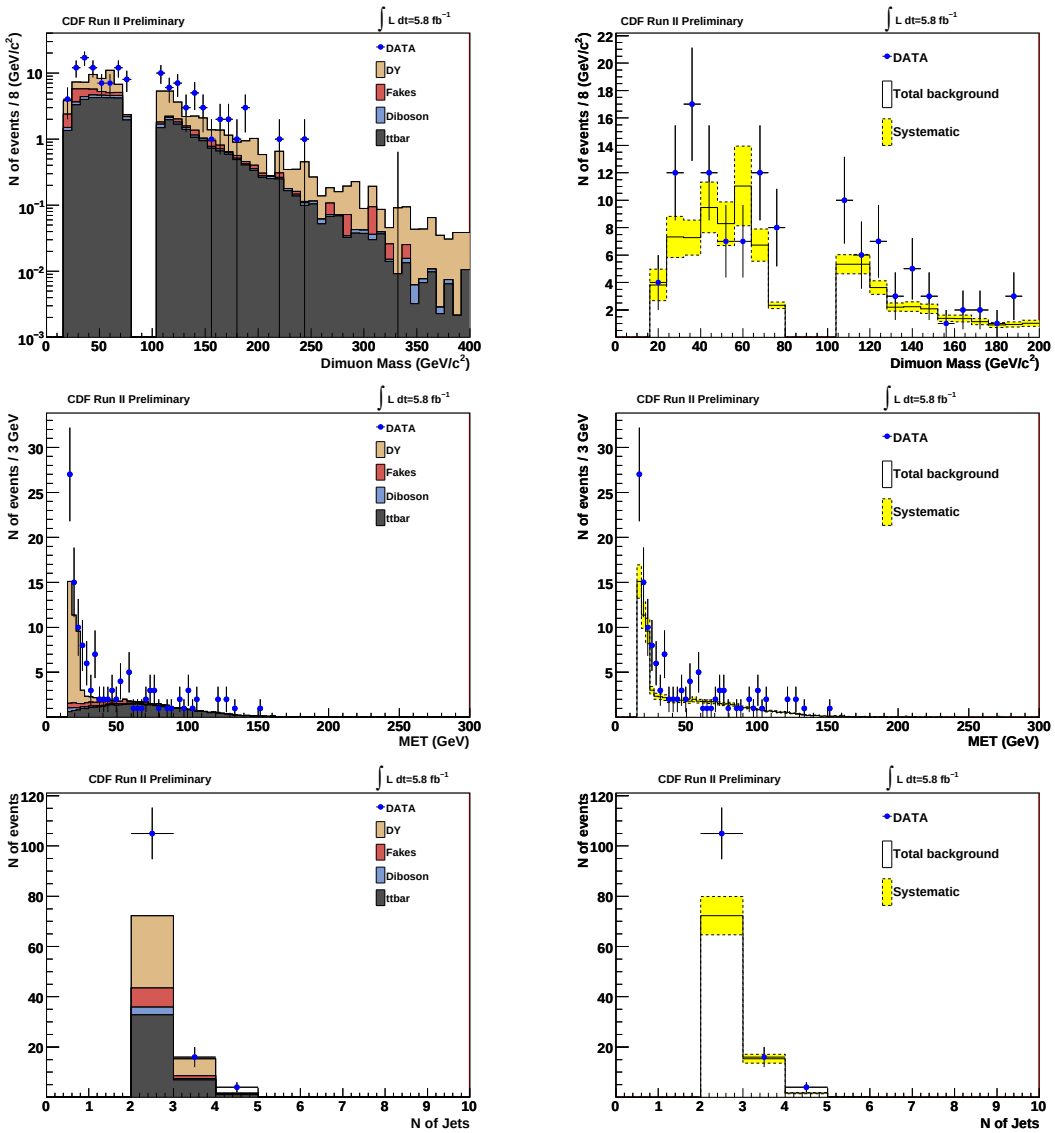

Figure D.51: Dimuon mass, $\not\!\!E_T$ and jet multiplicity for data and SM prediction in region 8 ($\not\!\!E_T > 15, N_{\text{jet}} \geq 2, !Z$). Plots on the right show the total systematic uncertainty in the expectation (yellow band).

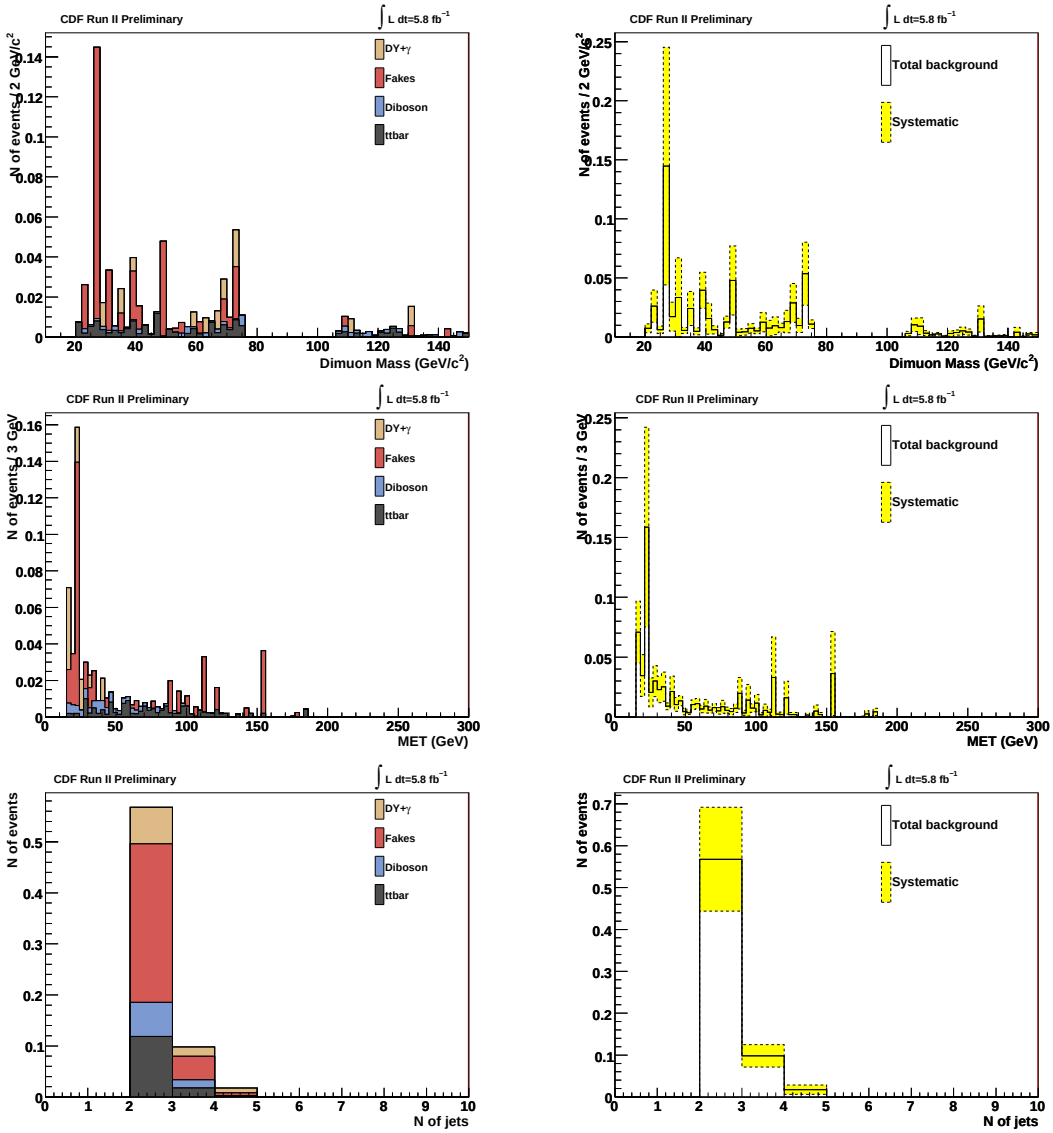

Figure D.52: Dimuon mass, $\not\!\!E_T$ and jet multiplicity of $\mu\mu$+lepton(e,μ,τ) events for data and SM prediction in region 8 ($\not\!\!E_T > 15, N_{\text{jet}} \geq 2, !Z$). Plots on the right show the total systematic uncertainty in the expectation (yellow band).

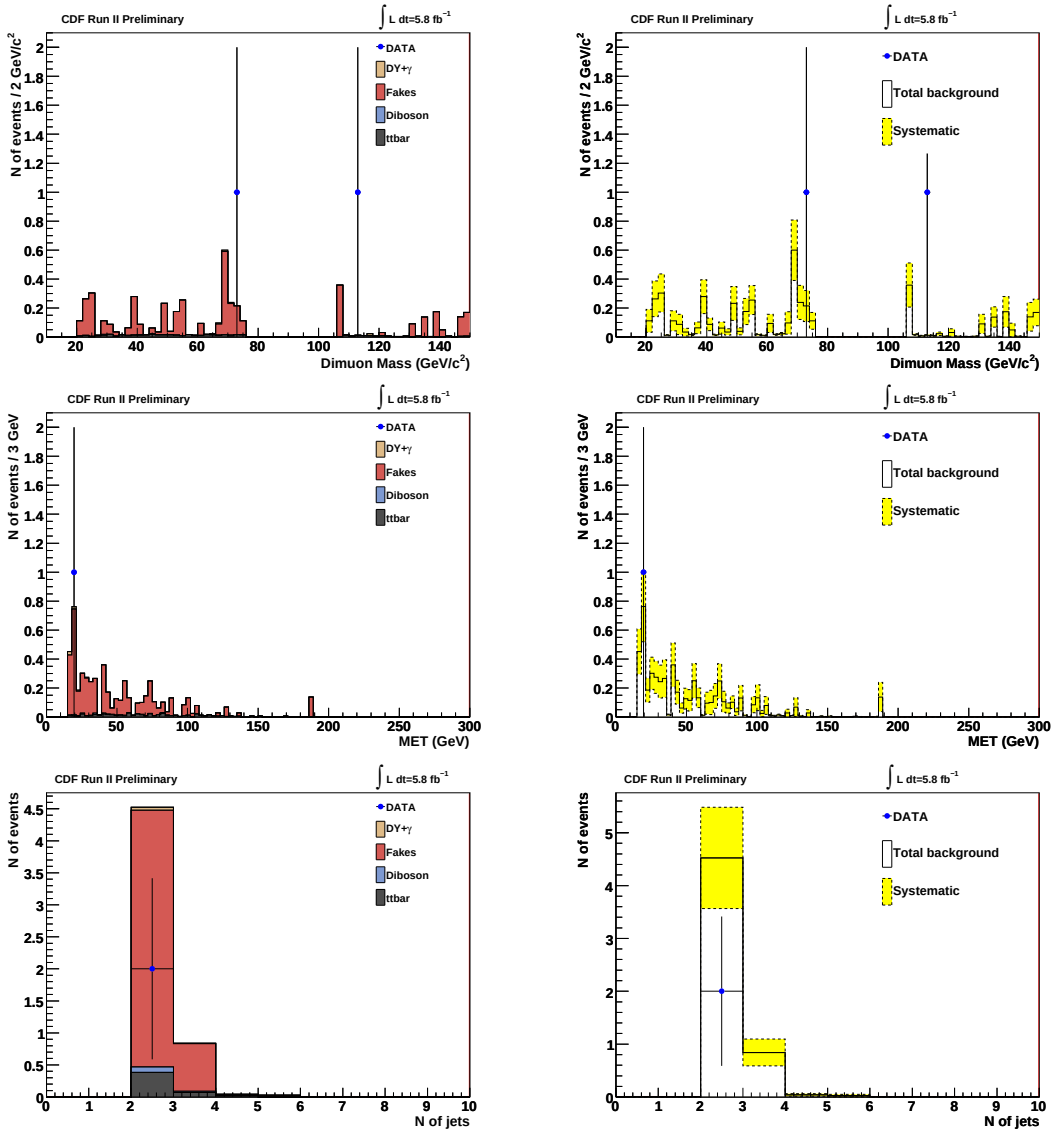

Figure D.53: Dimuon mass, $\not\!\!E_T$ and jet multiplicity of $\mu\mu$+isotrack events for data and SM prediction in region 8 ($\not\!\!E_T > 15, N_{\text{jet}} \geq 2, !Z$). Plots on the right show the total systematic uncertainty in the expectation (yellow band).

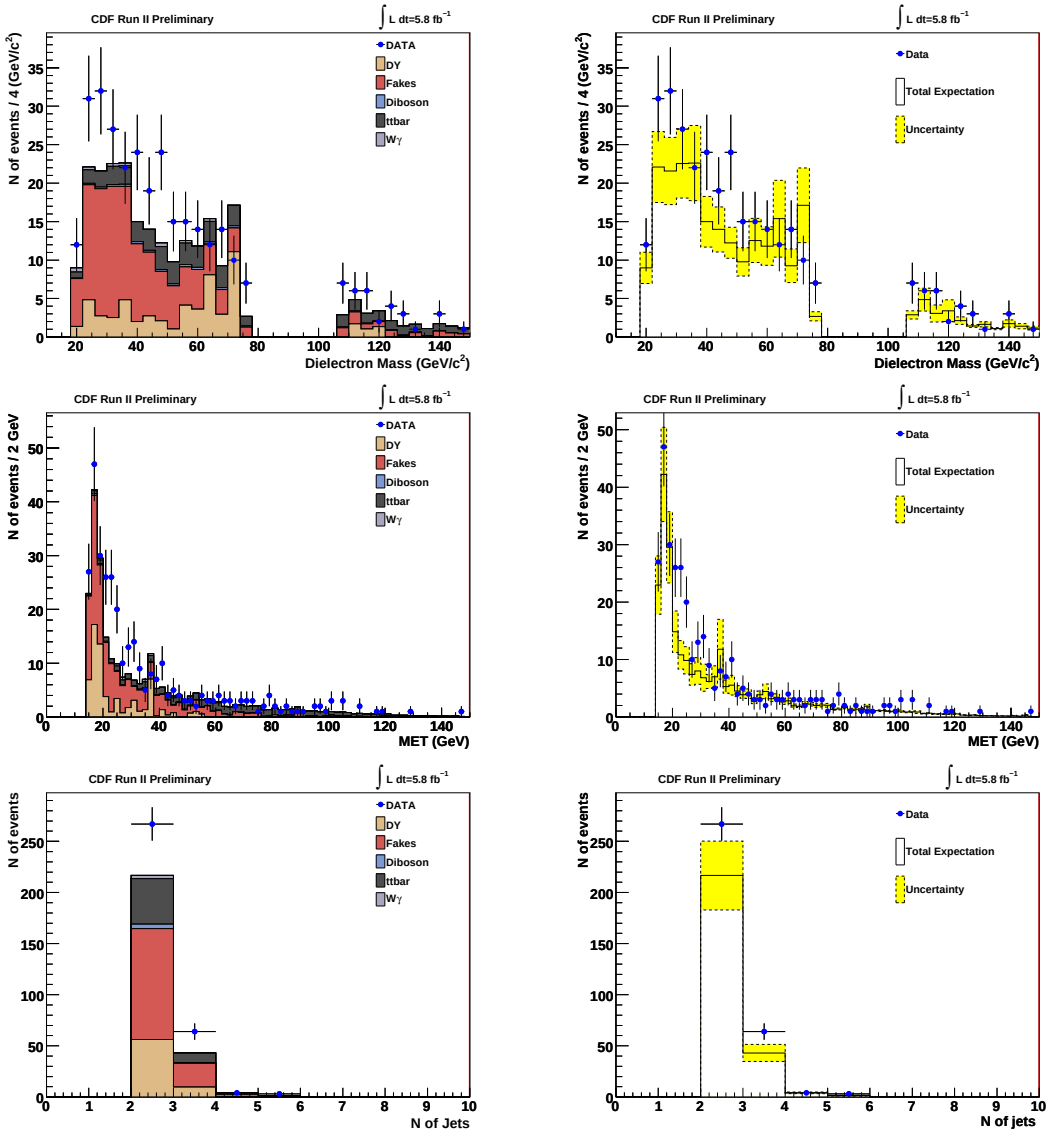

Figure D.54: Dielectron mass, $\not\!\!E_T$ and jet multiplicity for data and SM prediction in region 8 ($\not\!\!E_T > 15, N_{\text{jet}} \geq 2, !Z$). Plots on the right show the total systematic uncertainty in the expectation (yellow band).

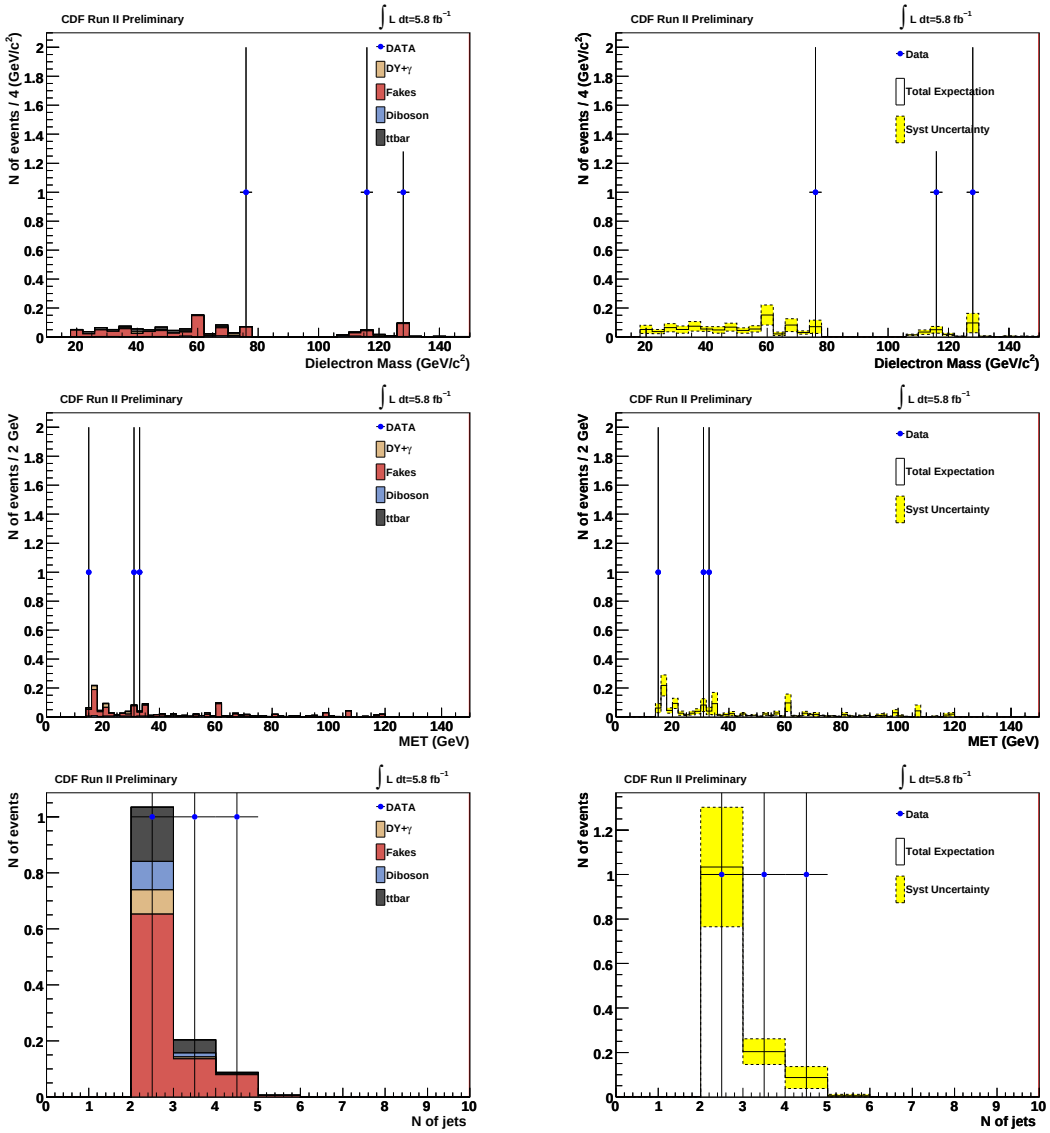

Figure D.55: Dielectron mass, $\not\!\!E_T$ and jet multiplicity of the ee+lepton(e,μ,τ) events for data and SM prediction in region 8 ($\not\!\!E_T > 15, N_{\rm jet} \geq 2, !Z$). Plots on the right show the total systematic uncertainty in the expectation (yellow band).

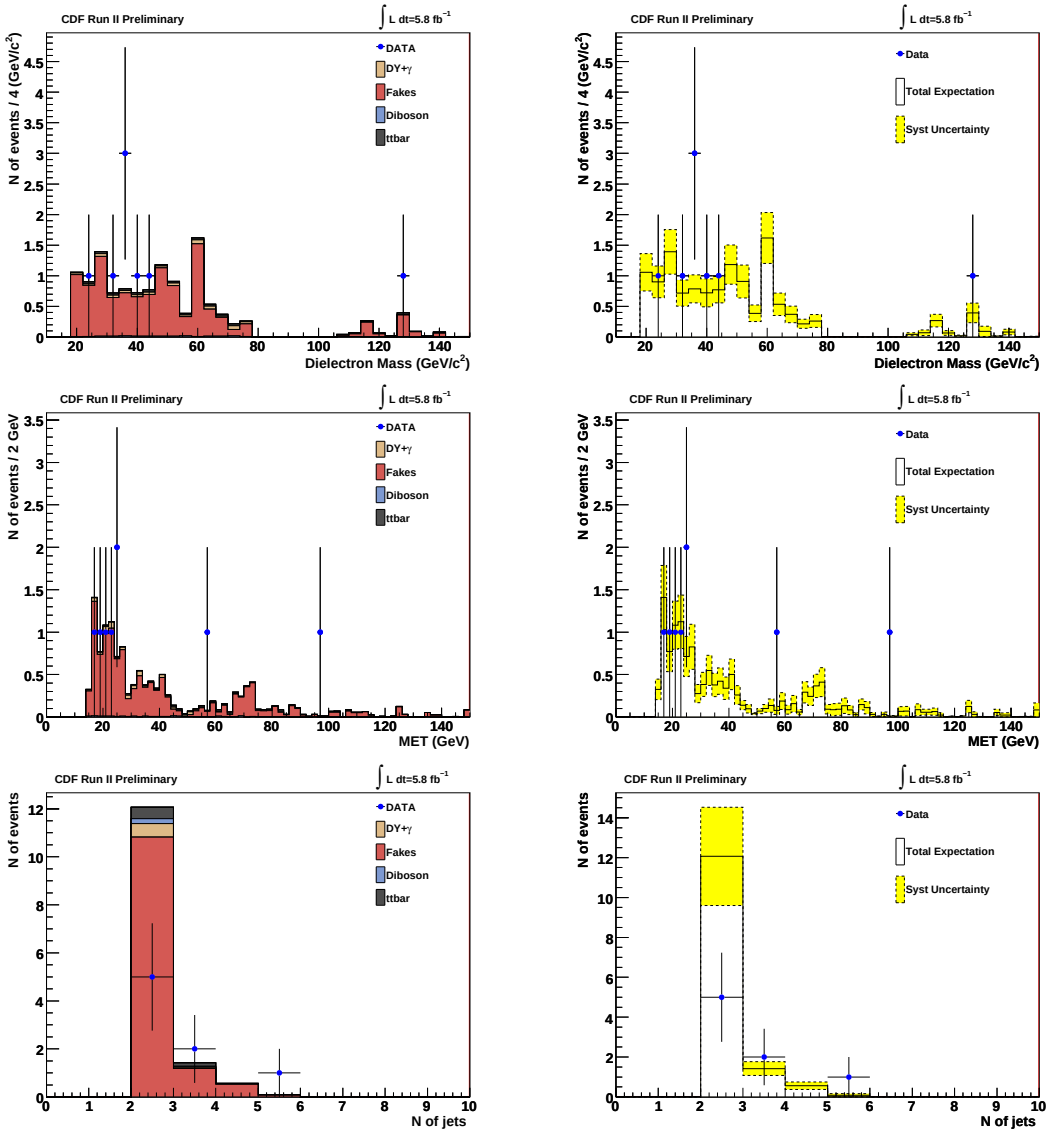

Figure D.56: Dielectron mass, $\not\!\!E_T$ and jet multiplicity of the ee+isotrack events for data and SM prediction in region 8 ($\not\!\!E_T > 15, N_{\text{jet}} \geq 2, !Z$). Plots on the right show the total systematic uncertainty in the expectation (yellow band).

D.10 Kinematic Variables for Region 9

In this section we show the invariant mass, $\not\!\!E_T$ and jet multiplicity in the control region defined by: $\not\!\!E_T > 20, !Z$

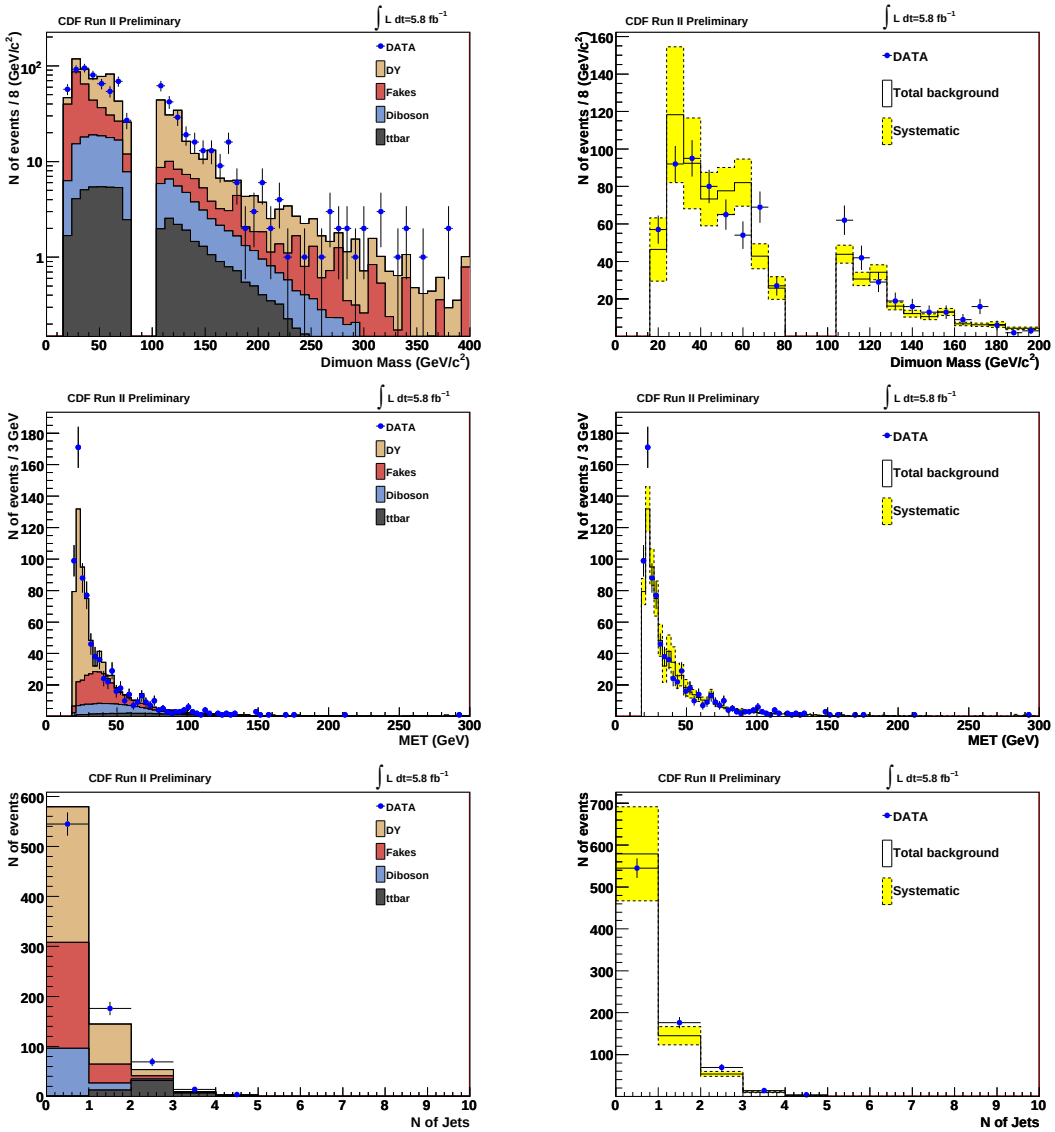

Figure D.57: Dimuon mass, $\not\!\!E_T$ and jet multiplicity for data and SM prediction in region 9 ($\not\!\!E_T > 20, !Z$). Plots on the right show the total systematic uncertainty in the expectation (yellow band).

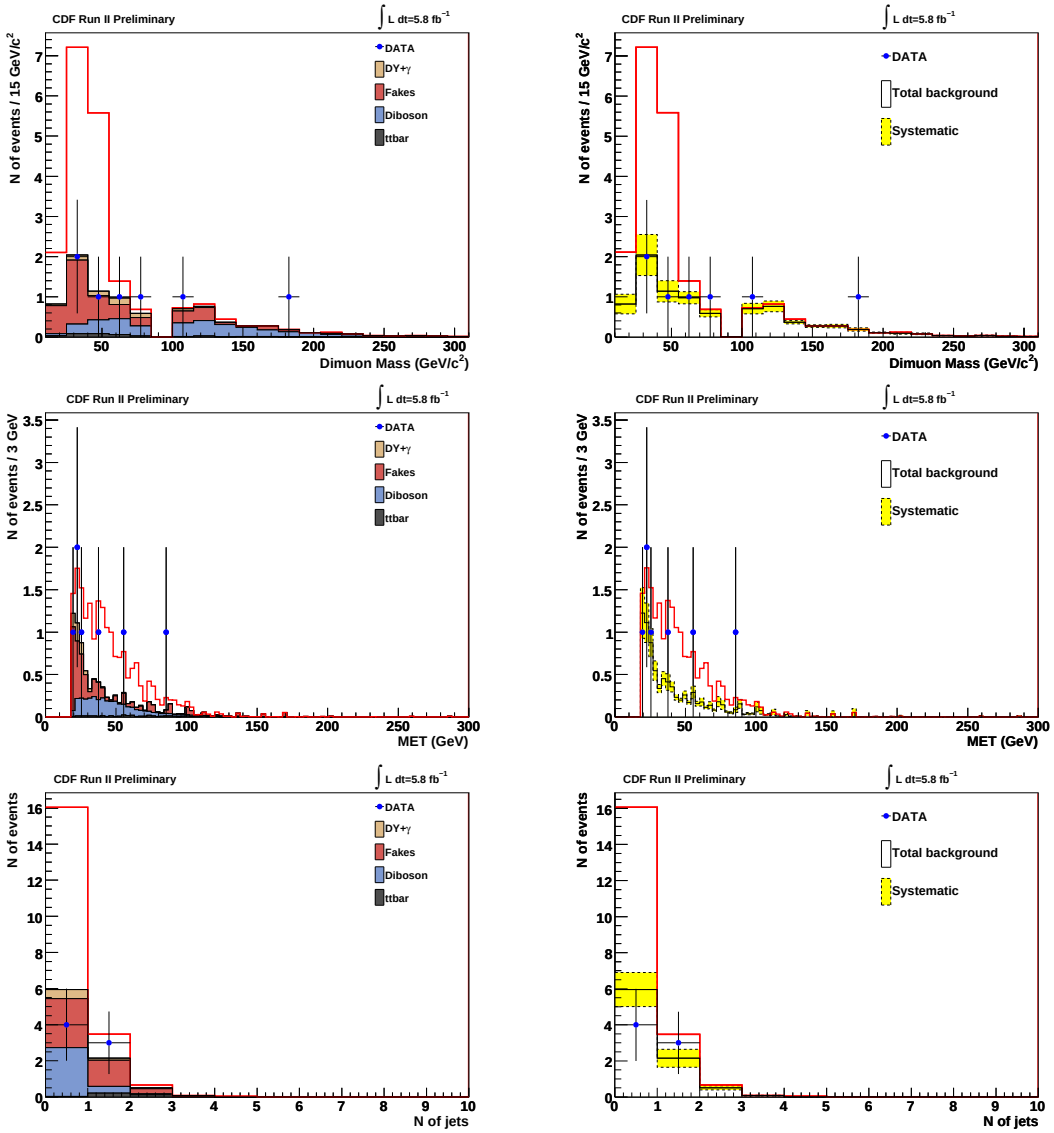

Figure D.58: Dimuon mass, $\not\!\!E_T$ and jet multiplicity of $\mu\mu$+lepton(e,μ,τ) events for data and SM prediction in region 9 ($\not\!\!E_T > 20, !Z$). Plots on the right show the total systematic uncertainty in the expectation (yellow band).

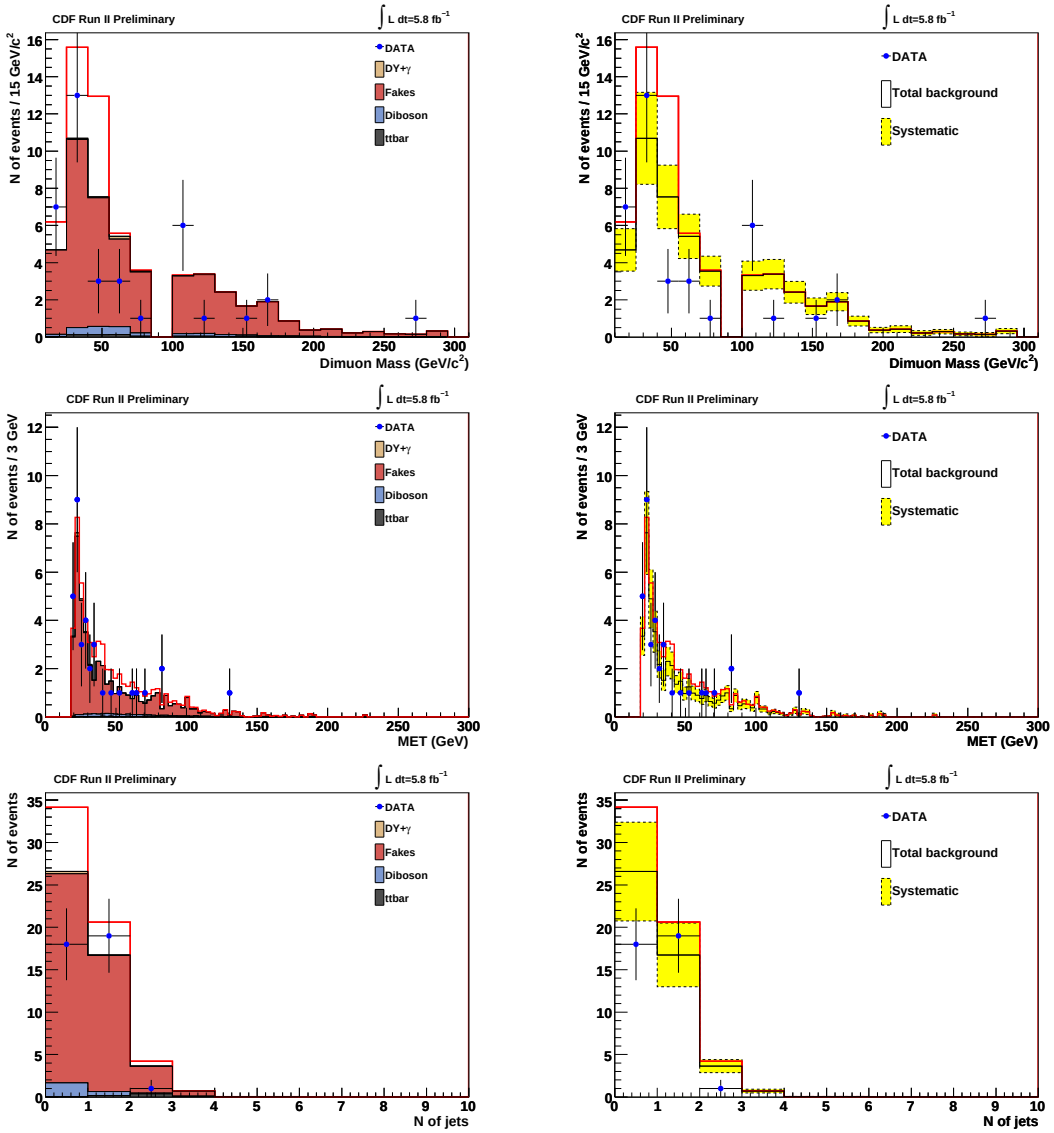

Figure D.59: Dimuon mass, $\not\!\!E_T$ and jet multiplicity of $\mu\mu$+isotrack events for data and SM prediction in region 9 ($\not\!\!E_T > 20, !Z$). Plots on the right show the total systematic uncertainty in the expectation (yellow band).

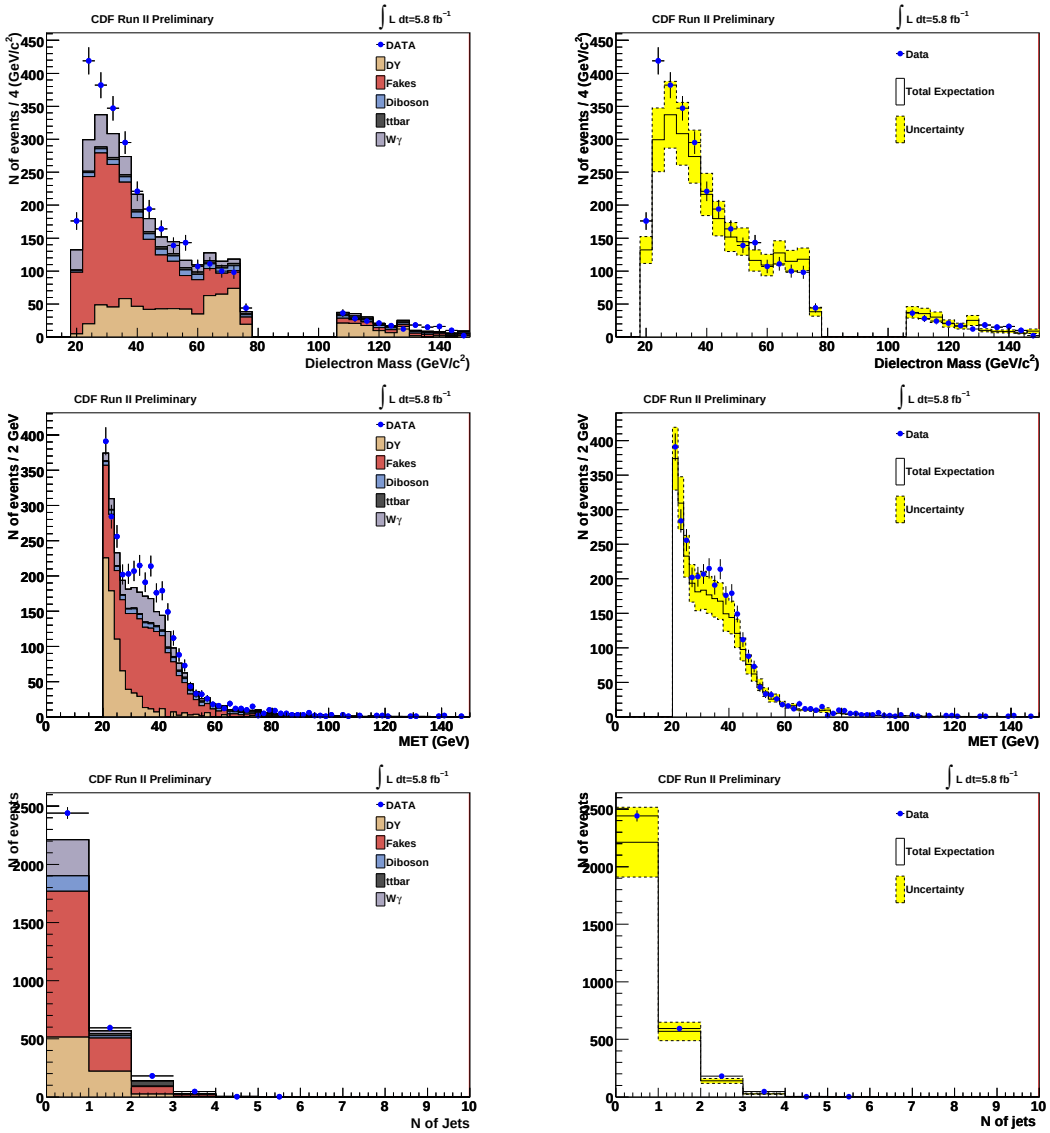

Figure D.60: Dielectron mass, $\not\!\!E_T$ and jet multiplicity for data and SM prediction in region 9 ($\not\!\!E_T > 20, !Z$). Plots on the right show the total systematic uncertainty in the expectation (yellow band).

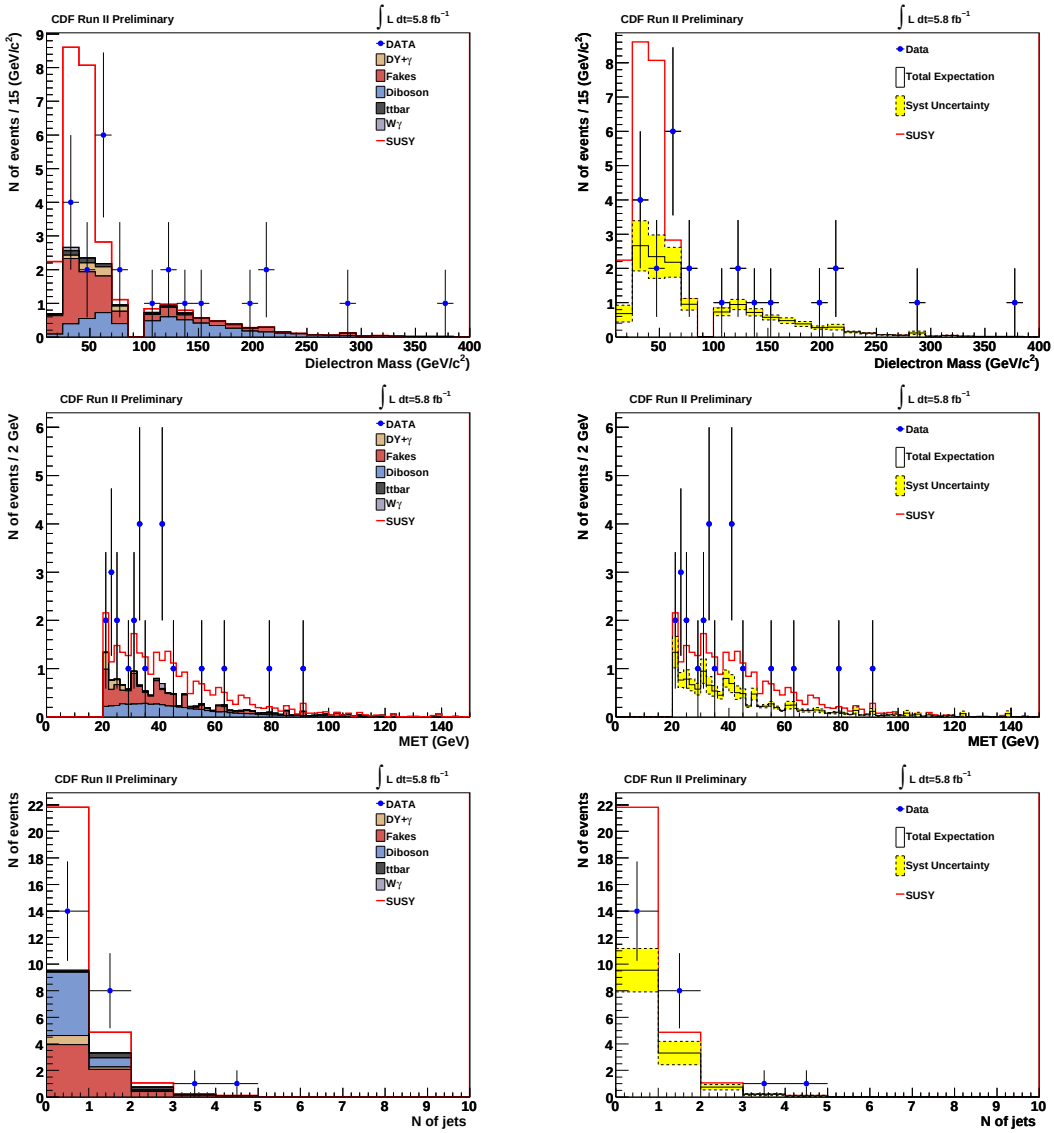

Figure D.61: Dielectron mass, $\not\!\!E_T$ and jet multiplicity of the ee+lepton(e,μ,τ) events for data and SM prediction in region 9 ($\not\!\!E_T > 20, !Z$). Plots on the right show the total systematic uncertainty in the expectation (yellow band).

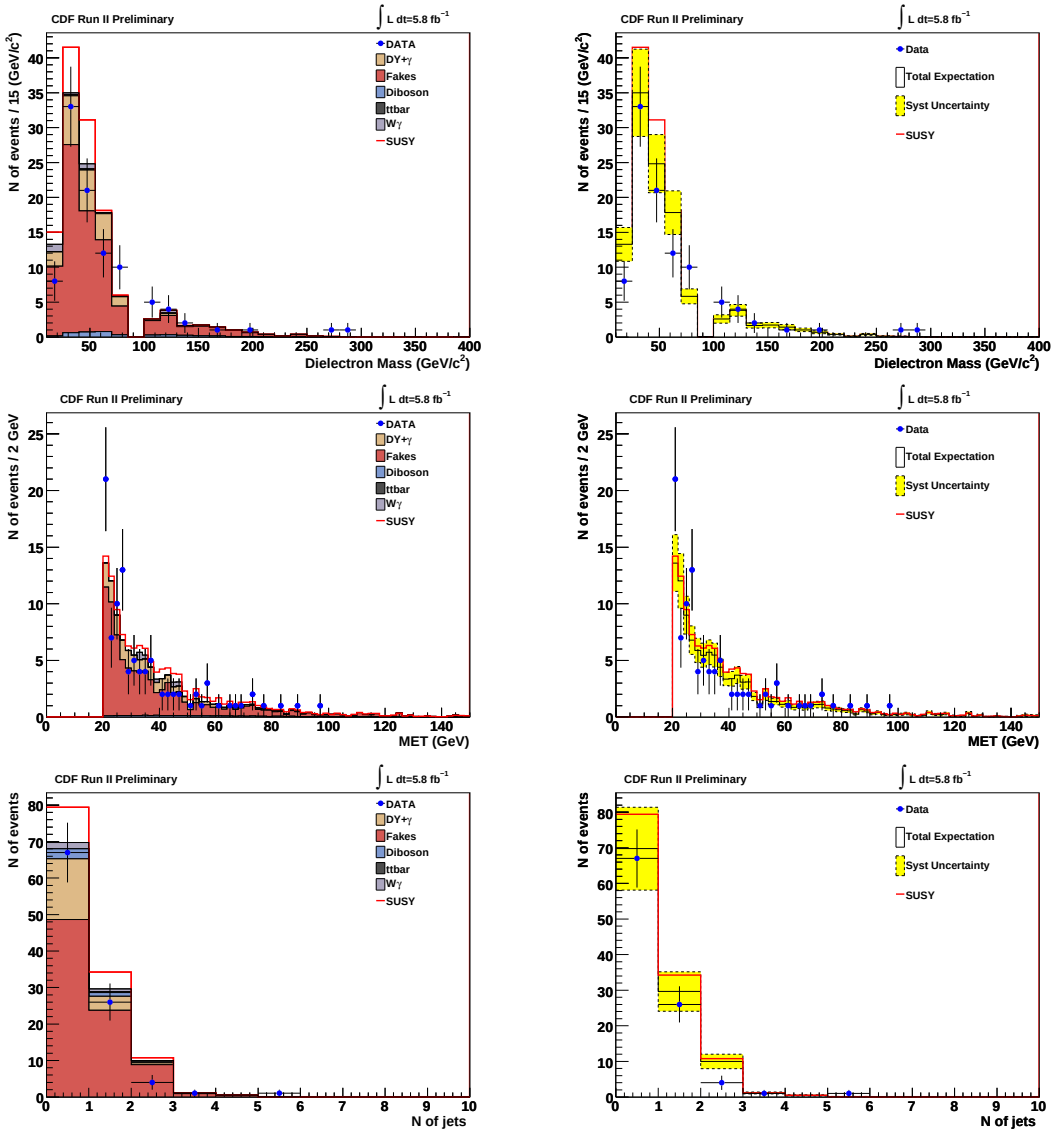

Figure D.62: Dielectron mass, $\not\!\!E_T$ and jet multiplicity of the ee+isotrack events for data and SM prediction in region 9 ($\not\!\!E_T > 20, !Z$). Plots on the right show the total systematic uncertainty in the expectation (yellow band).

D.11 Kinematic Variables for Region 10

In this section we show the invariant mass, $\not\!\!E_T$ and jet multiplicity in the control region defined by: $Z(OS)$

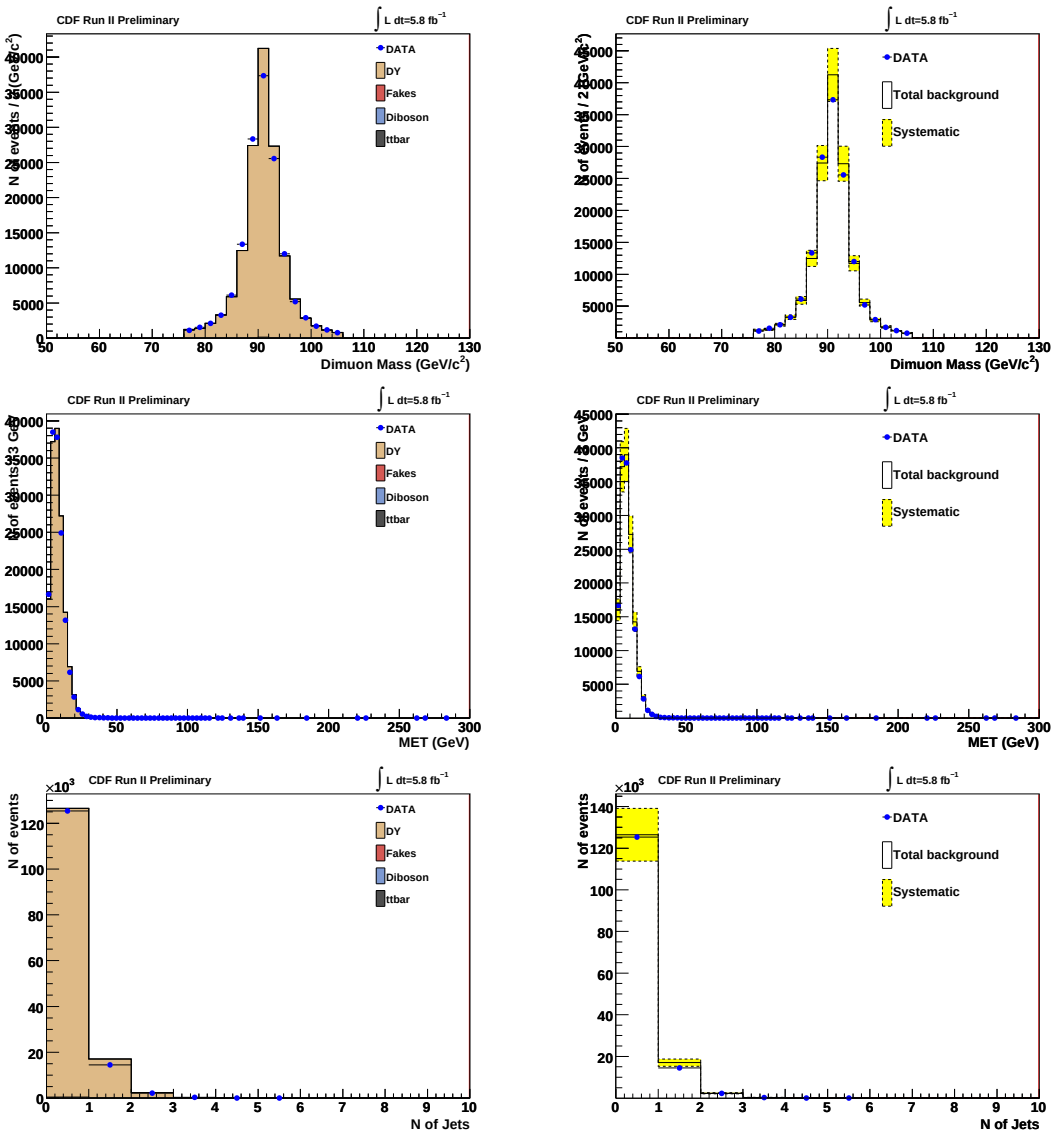

Figure D.63: Dimuon mass, $\not\!\!E_T$ and jet multiplicity for data and SM prediction in region 10 ($Z(OS)$). Plots on the right show the total systematic uncertainty in the expectation (yellow band).

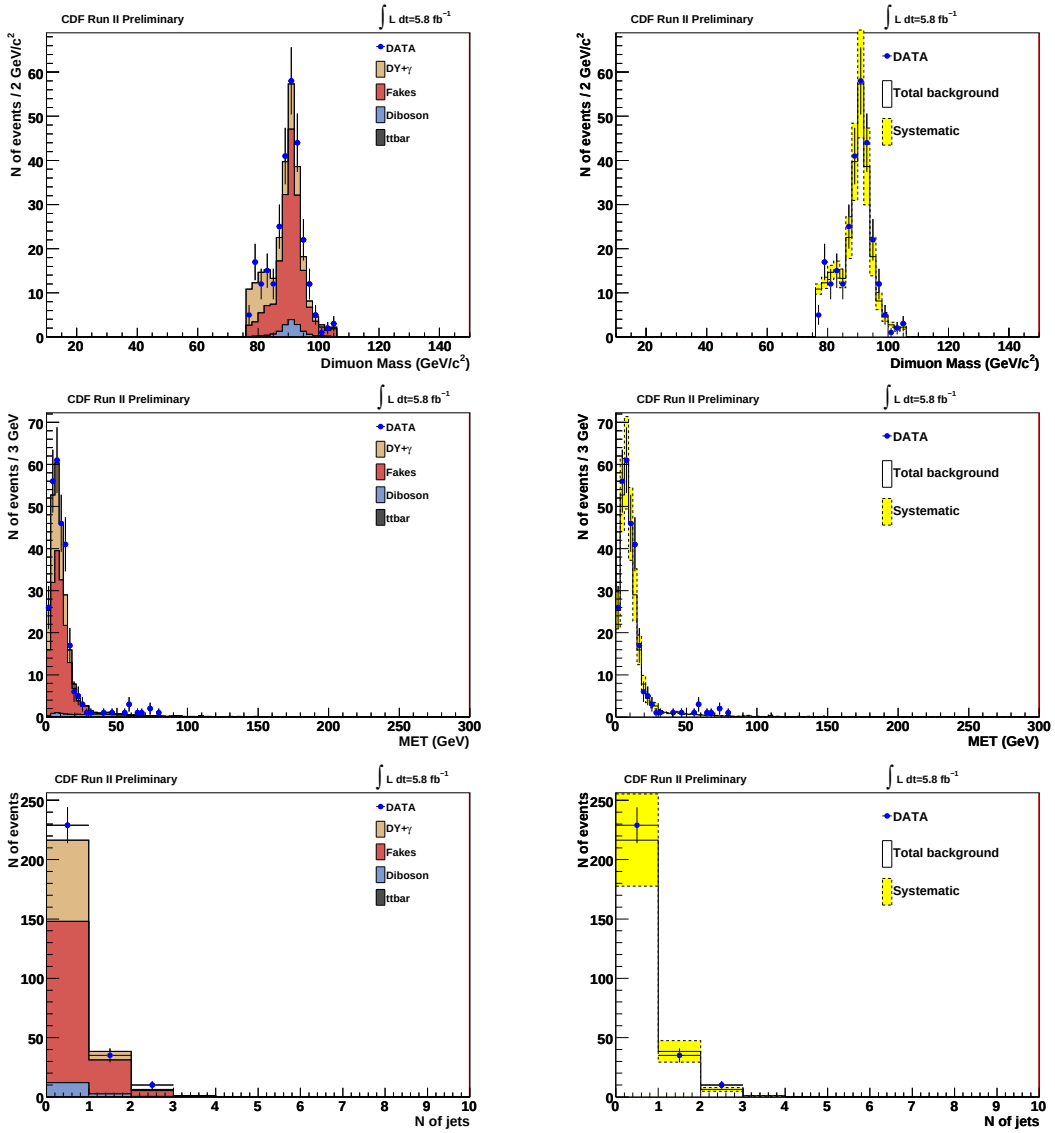

Figure D.64: Dimuon mass, $\not\!\!E_T$ and jet multiplicity of $\mu\mu$+lepton(e,μ,τ) events for data and SM prediction in region 10 ($Z(OS)$). Plots on the right show the total systematic uncertainty in the expectation (yellow band).

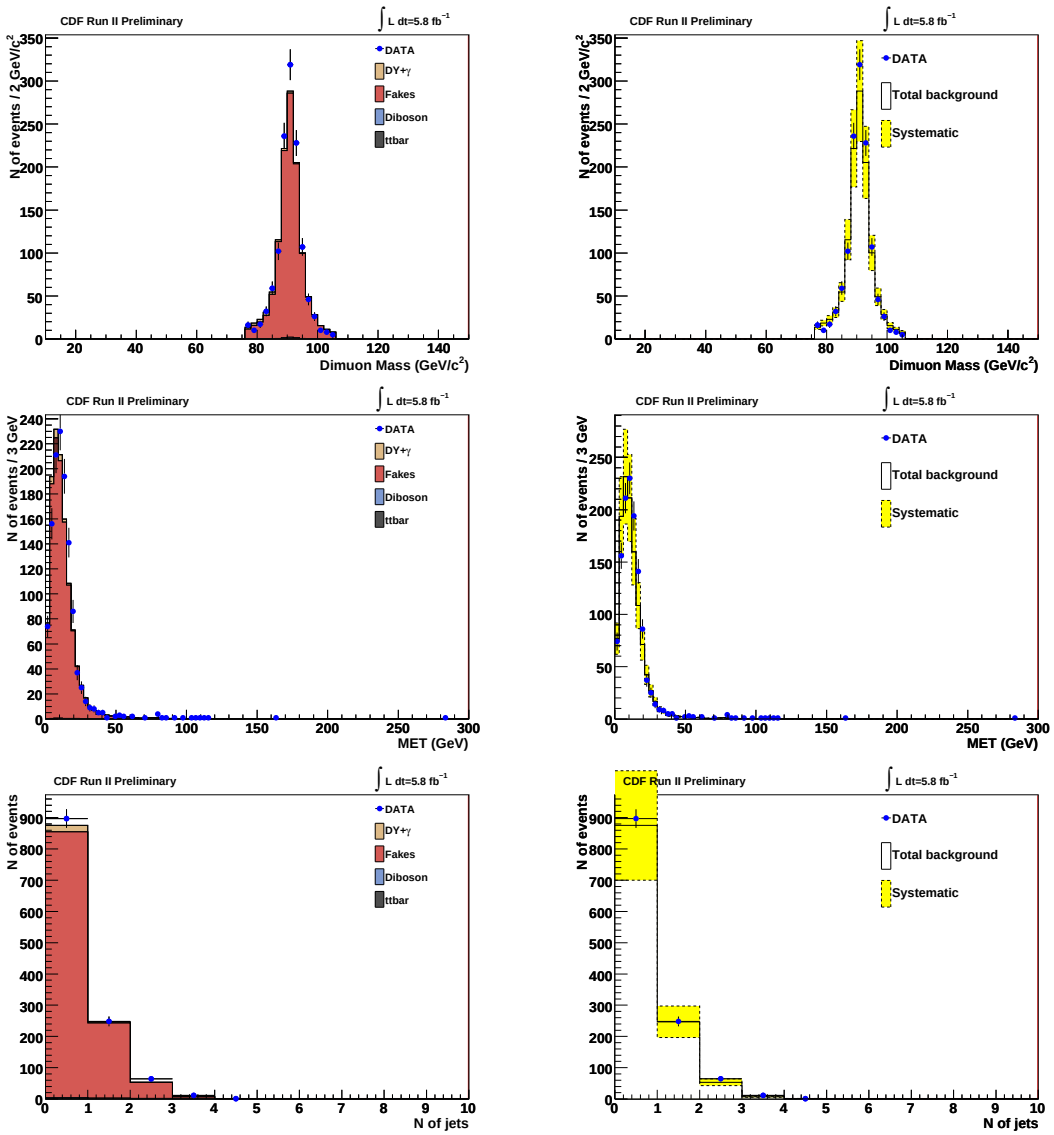

Figure D.65: Dimuon mass, $\not\!\!E_T$ and jet multiplicity of $\mu\mu$+isotrack events for data and SM prediction in region 10 ($Z(OS)$). Plots on the right show the total systematic uncertainty in the expectation (yellow band).

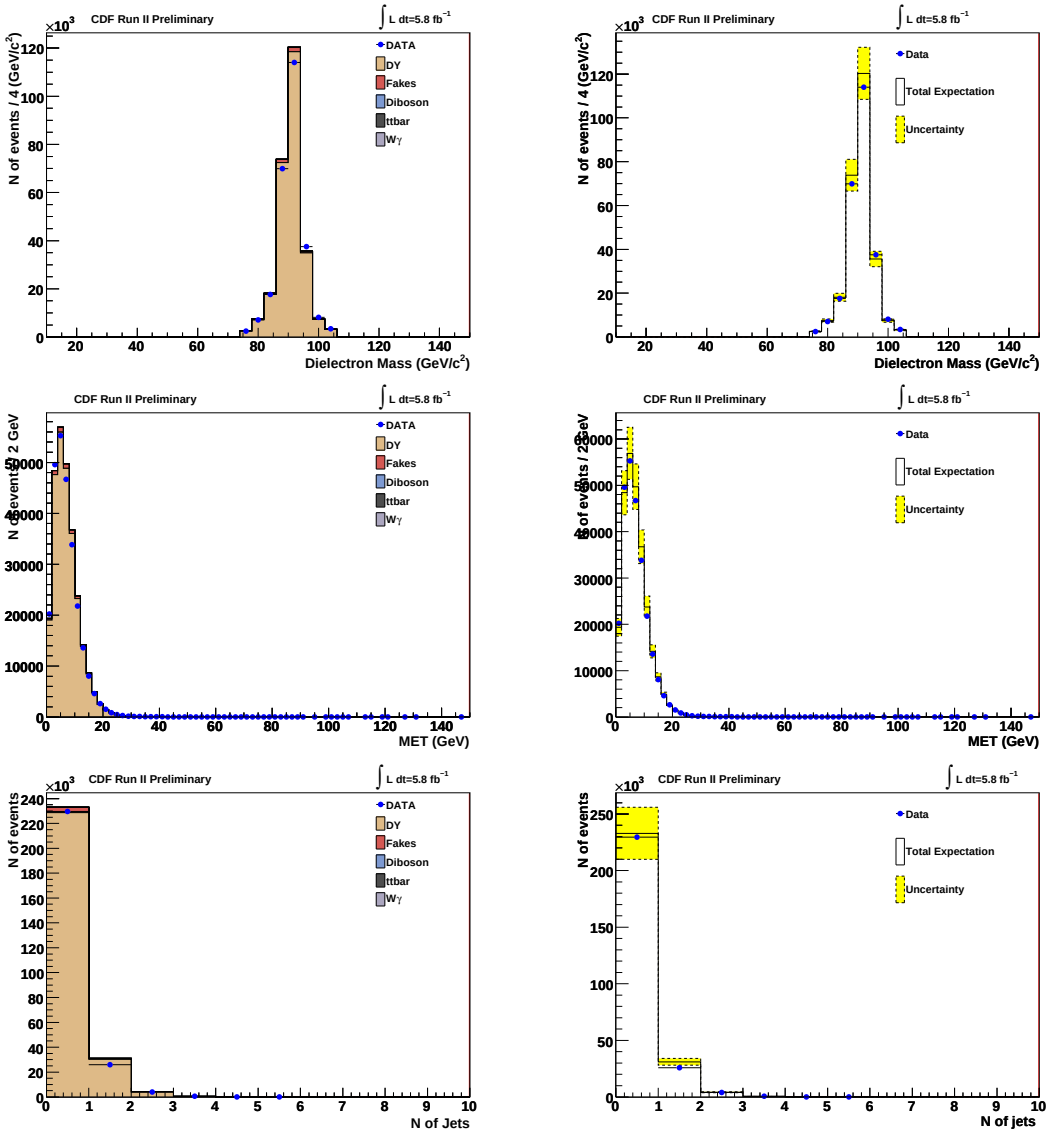

Figure D.66: Dielectron mass, $\not\!\!E_T$ and jet multiplicity for data and SM prediction in region 10 ($Z(OS)$). Plots on the right show the total systematic uncertainty in the expectation (yellow band).

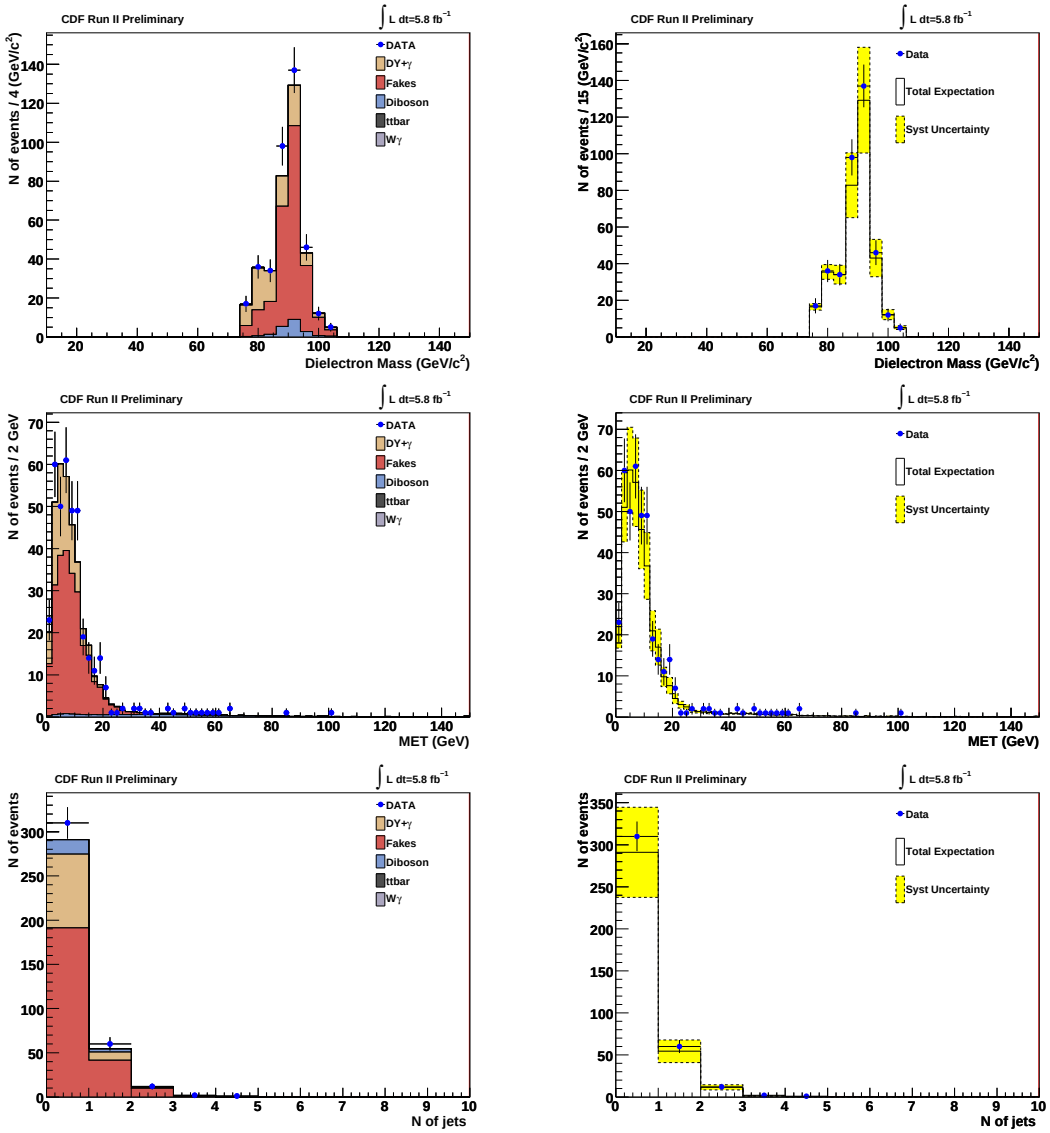

Figure D.67: Dielectron mass, $\not\!\!E_T$ and jet multiplicity of the ee+lepton(e,μ,τ) events for data and SM prediction in region 10 ($Z(OS)$). Plots on the right show the total systematic uncertainty in the expectation (yellow band).

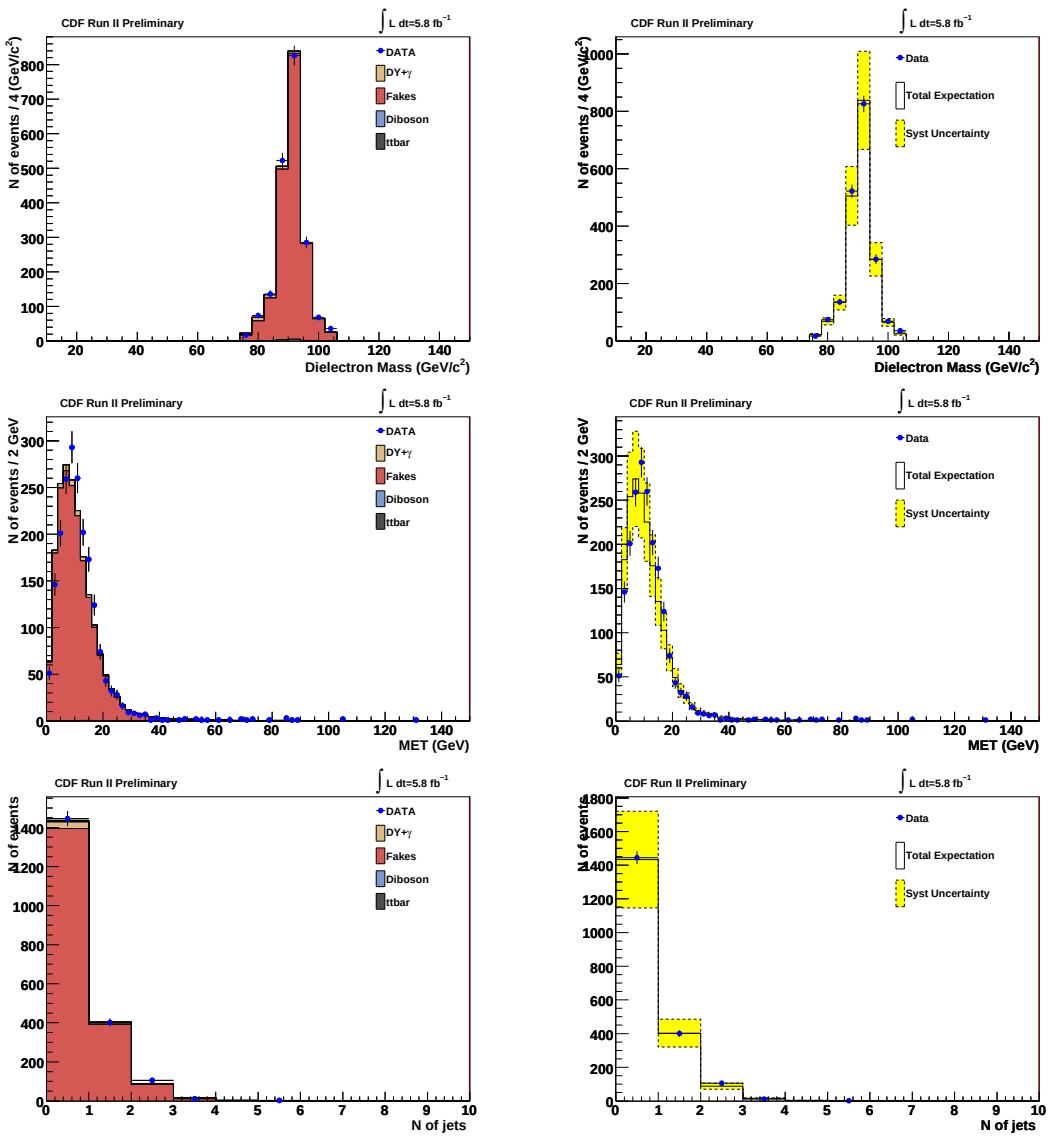

Figure D.68: Dielectron mass, $\not\!\!E_T$ and jet multiplicity of the ee+isotrack events for data and SM prediction in region 10 ($Z(OS)$). Plots on the right show the total systematic uncertainty in the expectation (yellow band).

D.12 Kinematic Variables for Region 11

In this section we show the invariant mass, $\not\!\!E_T$ and jet multiplicity in the inclusive control region (no mass, met or jet multiplicity cuts).

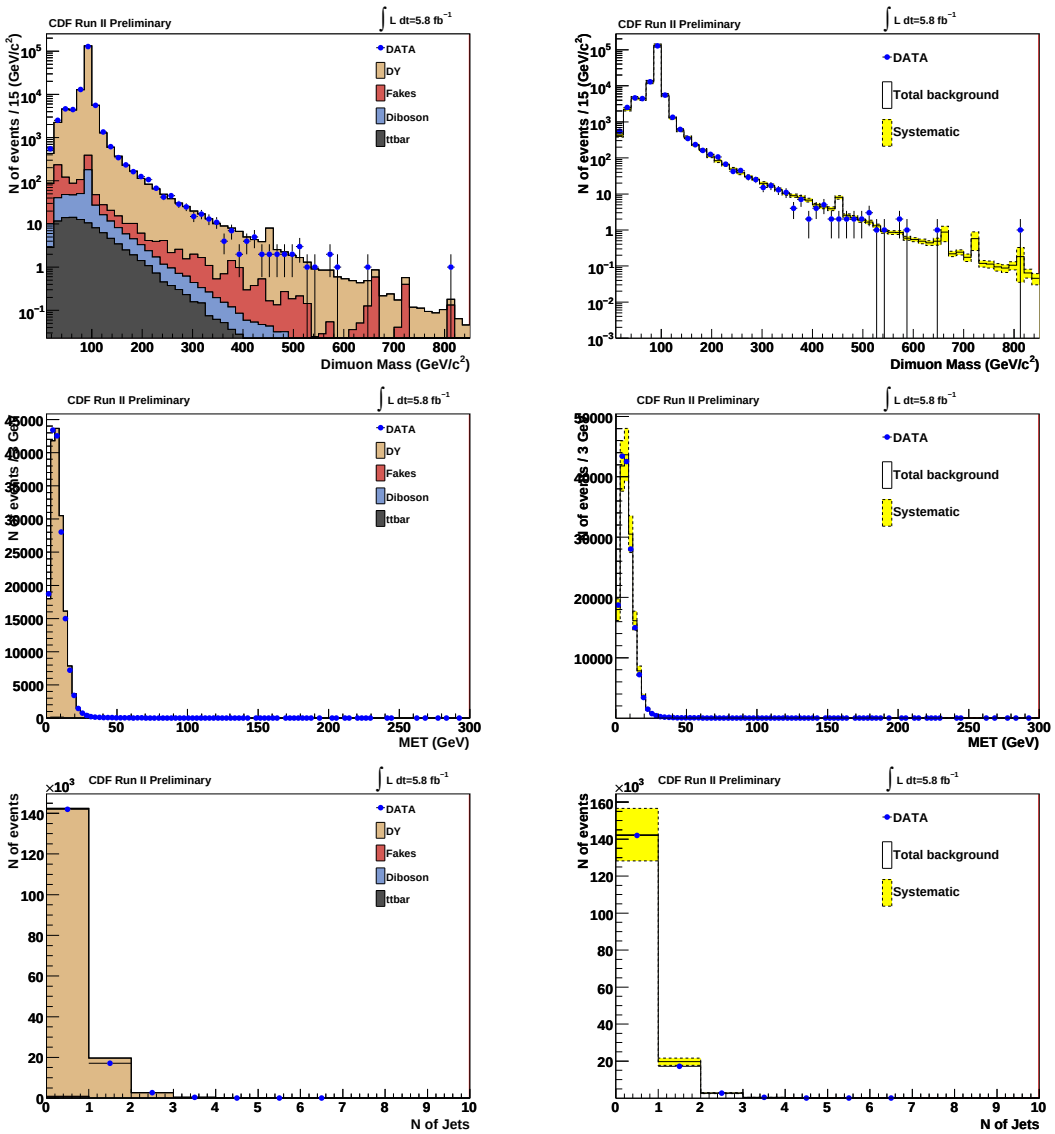

Figure D.69: Dimuon mass, $\not\!\!E_T$ and jet multiplicity for data and SM prediction in region 11 (inclusive). Plots on the right show the total systematic uncertainty in the expectation (yellow band).

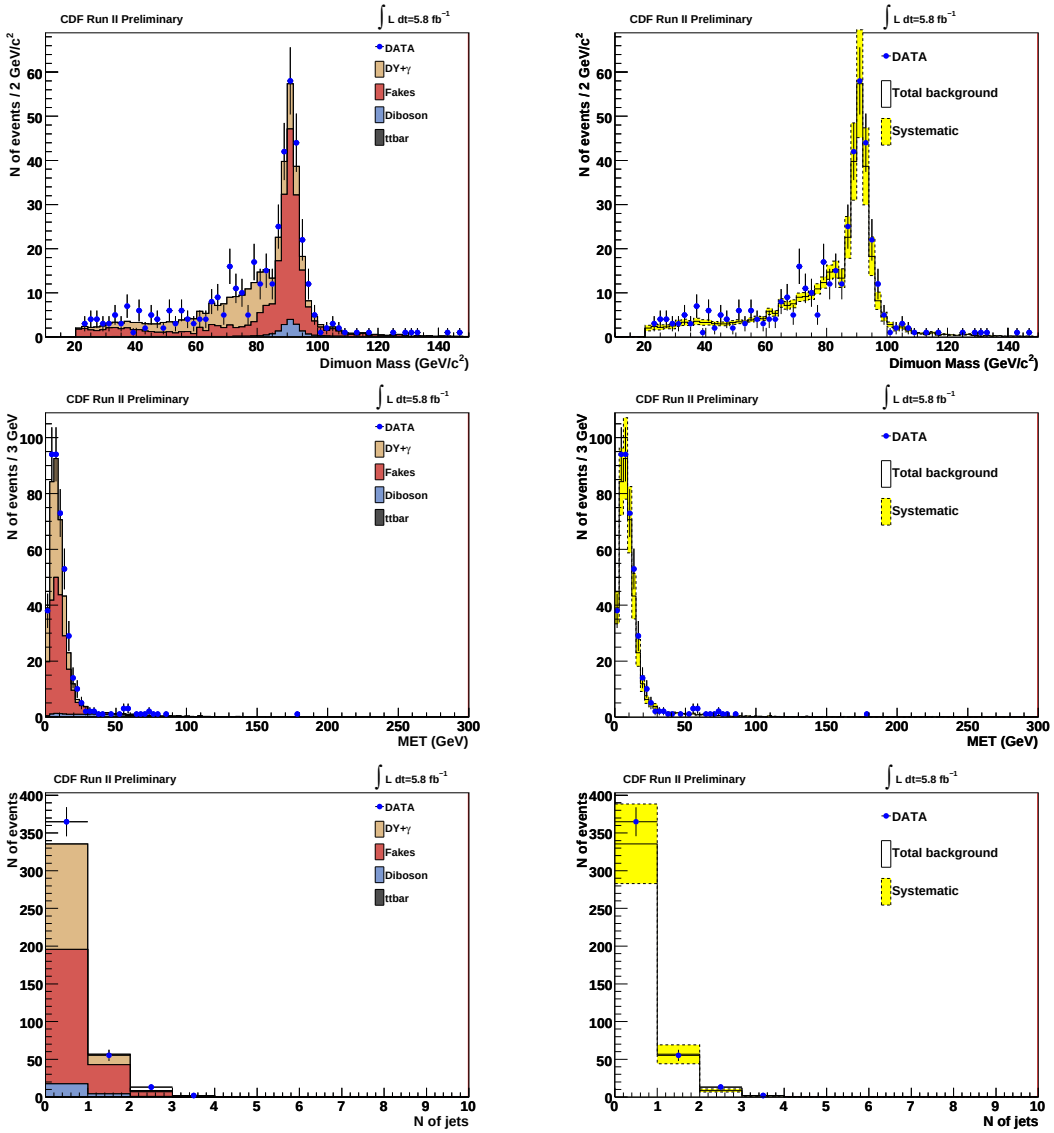

Figure D.70: Dimuon mass, $\not\!\!E_T$ and jet multiplicity of $\mu\mu$+lepton(e,μ,τ) events for data and SM prediction in region 11 (inclusive). Plots on the right show the total systematic uncertainty in the expectation (yellow band).

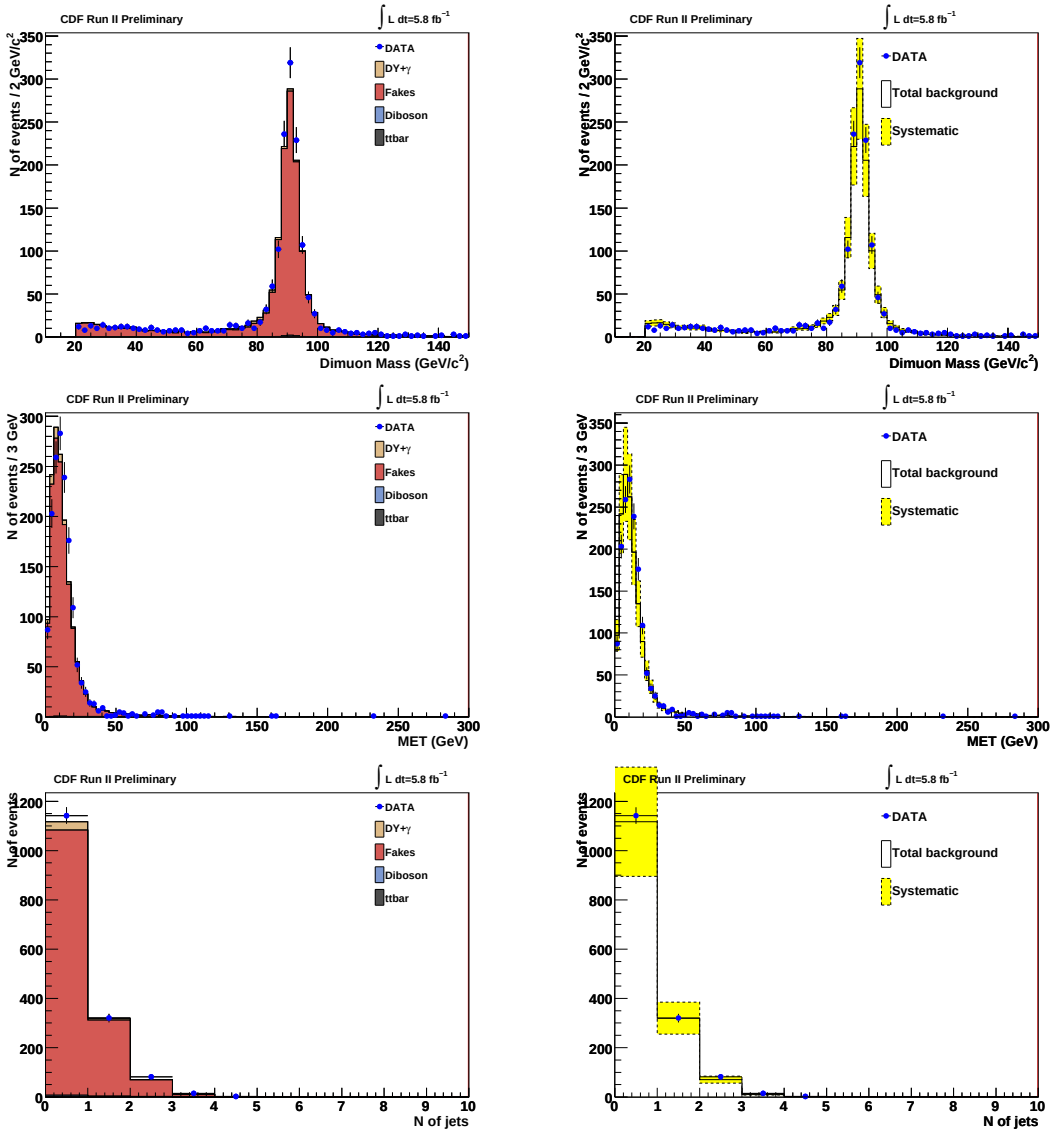

Figure D.71: Dimuon mass, $\not\!\!E_T$ and jet multiplicity of $\mu\mu$+isotrack events for data and SM prediction in region 11 (inclusive). Plots on the right show the total systematic uncertainty in the expectation (yellow band).

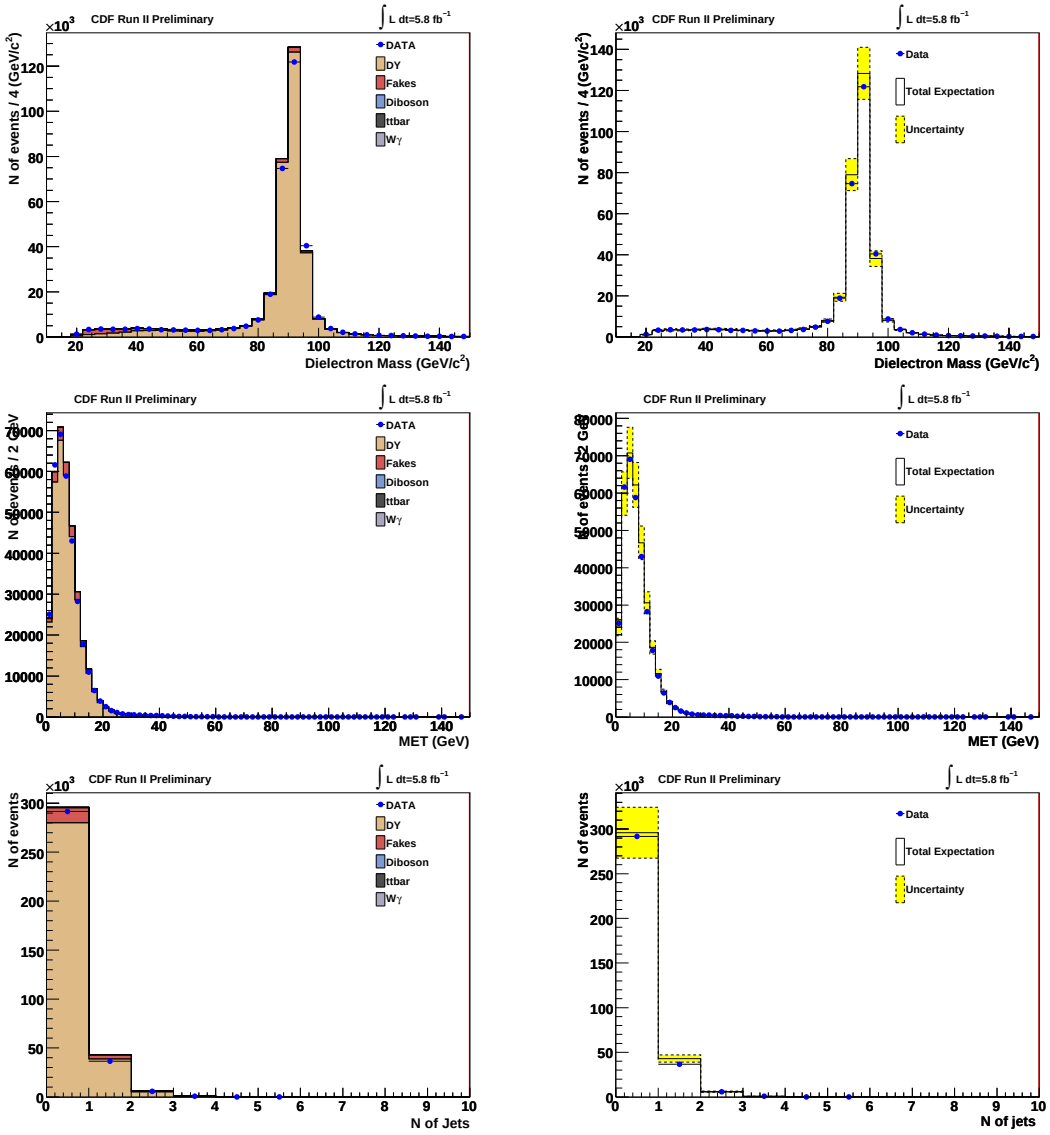

Figure D.72: Dielectron mass, $\not\!\!E_T$ and jet multiplicity for data and SM prediction in region 11 (inclusive). Plots on the right show the total systematic uncertainty in the expectation (yellow band).

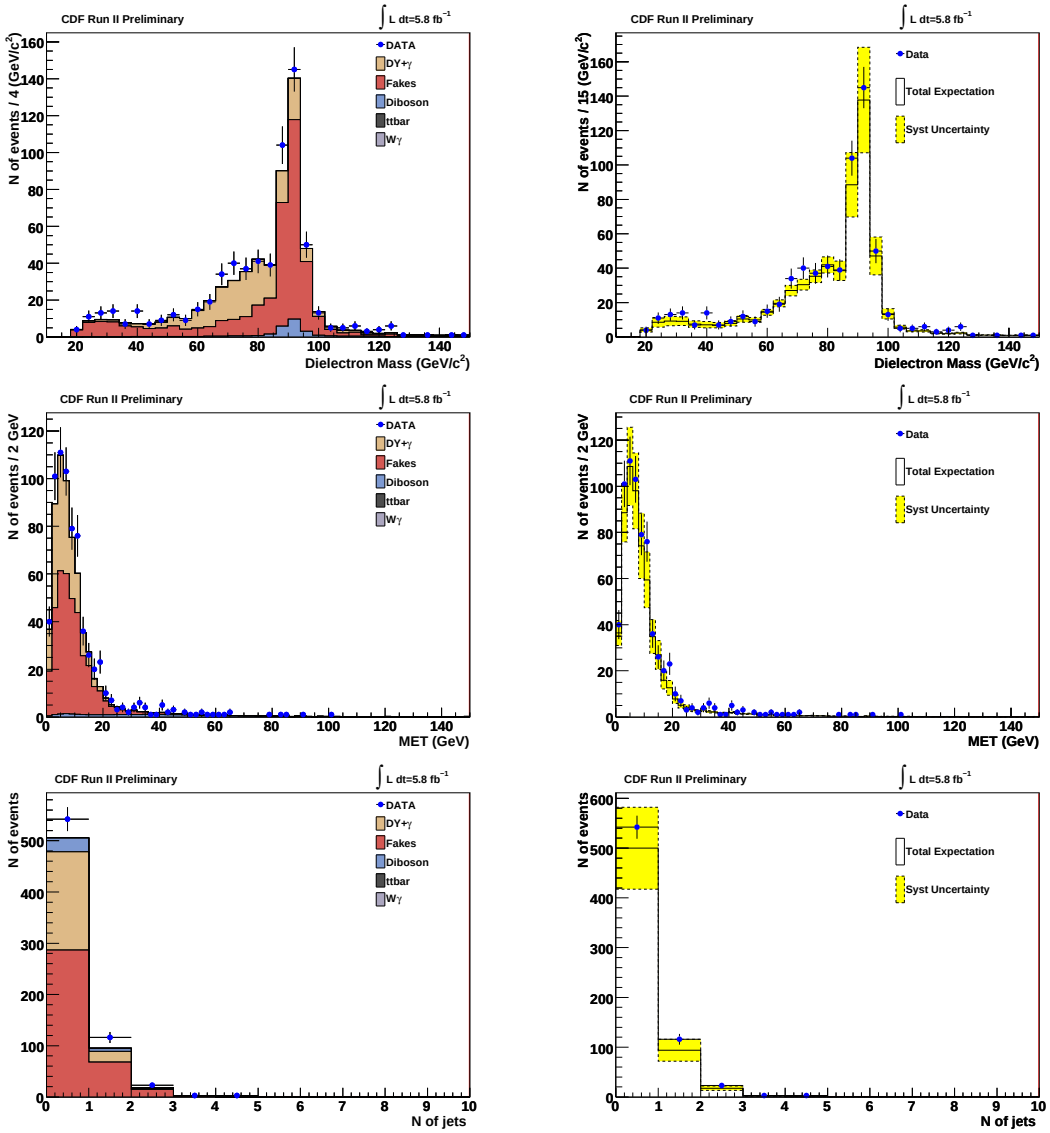

Figure D.73: Dielectron mass, $\not\!\!E_T$ and jet multiplicity of the ee+lepton(e,μ,τ) events for data and SM prediction in region 11 (inclusive). Plots on the right show the total systematic uncertainty in the expectation (yellow band).

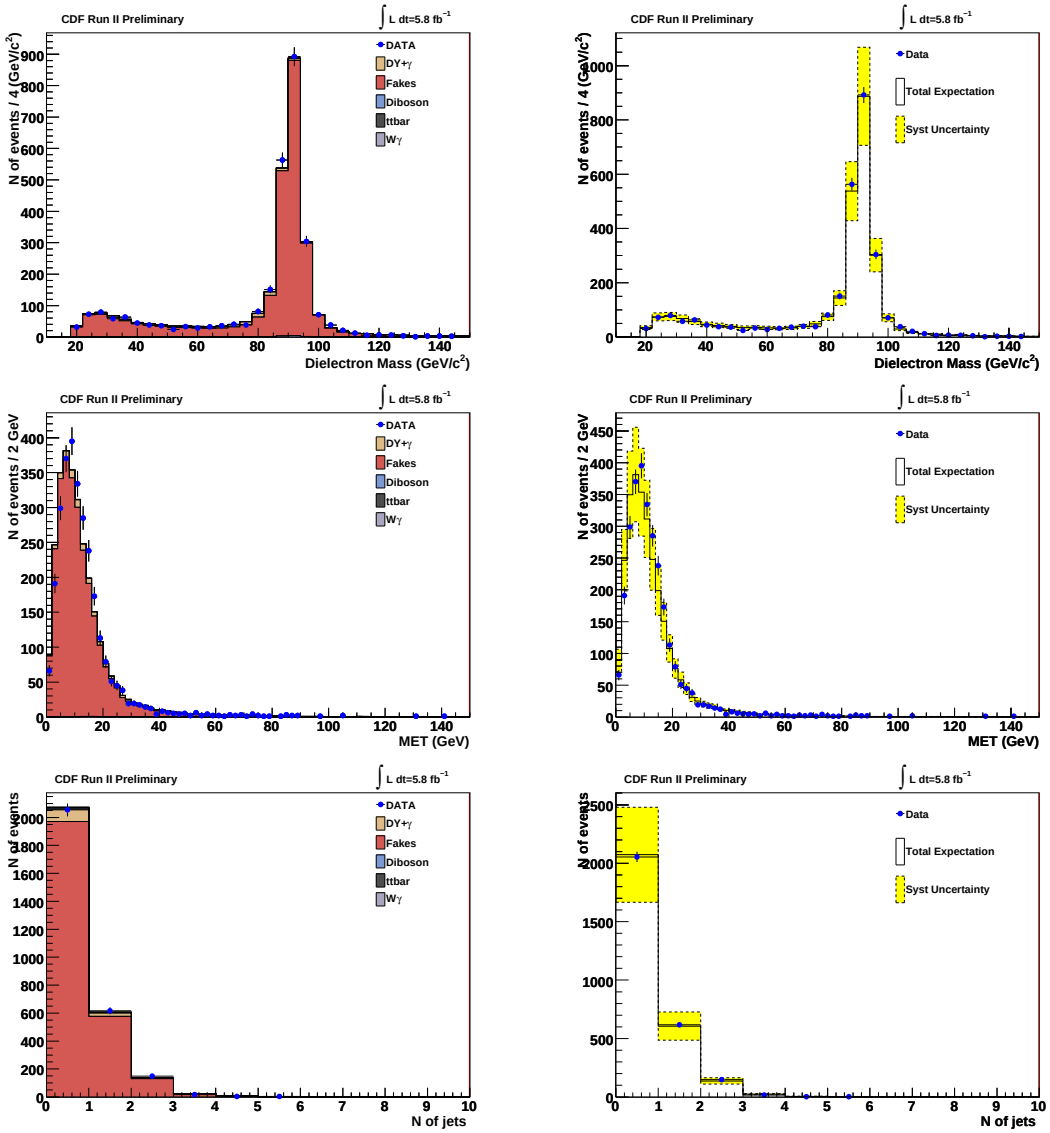

Figure D.74: Dielectron mass, $\not\!\!E_T$ and jet multiplicity of the ee+isotrack events for data and SM prediction in region 11 (inclusive). Plots on the right show the total systematic uncertainty in the expectation (yellow band).